



HAL
open science

Experimental investigation of gas transfer properties and stress coupling effects of salt rocks

Dongmei Zhang

► **To cite this version:**

Dongmei Zhang. Experimental investigation of gas transfer properties and stress coupling effects of salt rocks. Civil Engineering. Centrale Lille Institut, 2021. English. NNT : 2021CLIL0004 . tel-03709711

HAL Id: tel-03709711

<https://theses.hal.science/tel-03709711>

Submitted on 30 Jun 2022

HAL is a multi-disciplinary open access archive for the deposit and dissemination of scientific research documents, whether they are published or not. The documents may come from teaching and research institutions in France or abroad, or from public or private research centers.

L'archive ouverte pluridisciplinaire **HAL**, est destinée au dépôt et à la diffusion de documents scientifiques de niveau recherche, publiés ou non, émanant des établissements d'enseignement et de recherche français ou étrangers, des laboratoires publics ou privés.

N° d'ordre : 423

CENTRALE LILLE

THESE

Présentée en vue
D'obtenir le grade de

DOCTEUR

En

Spécialité: Génie Civil

Par

Dongmei ZHANG

DOCTORAT DELIVRE PAR CENTRALE LILLE

Titre de la thèse

Étude expérimentale des propriétés de transfert de gaz et des effets de couplage dans des roches salines

Soutenue le 25 janvier 2021 devant le jury d'examen

Président	Jian-Fu SHAO, Professeur, Université de Lille
Rapporteur	Albert GIRAUD, Professeur, Université de Lorraine
Rapporteur	Béatrice LEDESERT, Professeur, Université de Cergy-Pontoise
Examineur	Luc DORMIEUX, Professeur, Ecole des Ponts Paris Tech
Examineur	Laura BLANCO MARTIN, Enseignant-chercheur, MINES Paris Tech
Examineur	Laurent JEANNIN, Ingénieur de Recherche, STORENGY
Directeur	Frédéric SKOCZYLAS, Professeur, Centrale Lille

Thèse préparée dans le Laboratoire de Mécanique Multiphysique Multiéchelle (LaMcube)

ED SPI 072 (Université Lille, Centrale Lille, UPHF, UVHC, ULCO, Artois, IMT)

Acknowledgement

Firstly, I would like to express my deepest thanks to my supervisor, Prof. Frédéric SKOCZYLAS. It is a great honour for me to be your PhD student. With your patient guidance, great support and also your interesting ideas during these three years, I was able to complete my thesis work. I have also learned from you to be optimistic and persistent in the face of setbacks. I believe these good qualities will accompany me throughout my entire life.

I would also like to thank the storengy company for their financial and technical support. Special thanks are given to Mr. Laurent JEANNIN from storengy for your extensive experiences and precious advice. I am glad to have this opportunity to work with you on this interesting subject.

I would like to sincerely thank the jury members of my thesis, especially Profs. Béatrice Ledesert and Albert Giraud, for taking on this heavy work of reviewing my thesis as the rapporteurs. I was honored to have Mr. Jianfu SHAO to be the president and also appreciated the advice from Ms. Laura BLANCO MARTIN, Mr. Luc DORMIEUX and Mr. Laurent JEANNIN.

I would like to thank all the members of our laboratory, which is really a great team: Franck AGOSTINI, Thierry DUBOIS, Marie-Claude WILLEMETZ, Ludovic POTIER, Nicolas GAY, Laurent LECONTE and Catherine DAVY for many helps they gave me during these three years. I also thank Zhibo DUAN, Chuanrui WANG, Cong HU, Haifeng YUAN, Takoua LAMOUCHE and Sandy LANIER for all the help during my thesis. I really benefited a lot from this great team.

Many thanks are given to all the friends from Université de Lille for their friendship and the good moments shared with them: Yudan JIN, Meng WANG, Yue SUN, Zhan YU, Jianjian ZHAO, Xi CHEN, Jueliang CHEN and Siyu LIU.

Finally, I would like to deeply thank my family for their continuous support, especially my dear mother. I want to express my gratitude to you with the most beautiful words in the world. This is the end of my doctoral studies, but also the beginning of a new life.

Dongmei ZHANG

Résumé

D'un point de vue technique, la roche saline est généralement considérée comme un milieu imperméable ou ultra-faiblement perméable, capable de supporter une pression élevée et de se cicatriser après avoir été endommagée [1, 2]. Tous ces éléments rendent le stockage souterrain dans la couche de sel très approprié et attrayant. Par conséquence, les cavernes de sel pour le stockage des hydrocarbures tels que le pétrole brut, le gaz de pétrole liquéfié (GPL) ou le gaz naturel [3-5], ainsi que pour l'élimination des déchets nucléaires/radioactifs, ont été développées au cours de plusieurs décennies [3, 6-8].

Dans cette recherche expérimentale, les caractérisations de la roche saline, contenant principalement des propriétés de transfert de fluides et une exploration préliminaire du comportement poromécanique, sont analysées dans le cadre de deux applications. Premièrement, en raison du fluage du sel, certaines cavernes ont perdu leur valeur économique et doivent être abandonnées. Des expériences d'abandon de cavernes de sel [9] démontrent l'existence d'une perméation à l'échelle de la caverne. La caverne est remplie de saumure et scellée pour l'abandon : un équilibre de la pression de la saumure peut être atteint lorsque le fluage de la masse de sel et le retrait de la caverne sont équilibrés par la perméation de la saumure à travers la paroi de la caverne. Cet équilibre est censé être atteint sur une longue période (plusieurs années ou décennies) [10]. Par conséquent, les caractéristiques de transfert de fluide en fonction des contraintes et le comportement de la roche saline en fonction du temps sont essentiels pour cette application. La deuxième application, dans le contexte actuel de transition énergétique, est le stockage de l'hydrogène [11]. L'hydrogène, produit par exemple par l'énergie solaire, peut être stocké dans des cavernes de sel. Dans ce scénario, la perméabilité liée à l'hydrogène doit être évaluée.

La perméabilité au sel n'est pas seulement affectée par l'état de stress, mais elle est également fortement influencée par les effets du temps. D'un point de vue mécanique, le sel gemme est une roche élasto-viscoplastique, qui présente un fort comportement de fluage. Sa réponse instantanée est élastique, tandis que sa réponse mécanique à long terme sous une charge déviatrice constante dépend principalement du temps. Par conséquent, cela peut donc expliquer la perte de volume et la fermeture progressive des cavernes de sel pendant l'opération de stockage du gaz. La variation de la perméabilité lors du fluage du sel devrait donc être détectée [12]. Cependant, il existe peu de recherches antérieures sur l'évolution à long terme de la perméabilité [13, 14].

Par ailleurs, comme la roche saline est peu perméable, la pression interne du fluide peut contribuer à la charge et être impliquée dans la relation contrainte-déformation qui caractérise l'équation d'état du matériau et peut influencer la perméabilité à une charge donnée. Ce phénomène est souvent observé sur d'autres roches sédimentaires plus ou moins perméables, mais, à notre connaissance, il a été peu étudié

pour le sel. La manière dont cette pression interne du fluide est couplée au comportement mécanique mérite d'être explorée et constitue un autre objet clé de cette étude.

Cependant, certains auteurs suggèrent que la perméation, observée lors de tests *in situ* dans les cavernes de sel, a été partiellement induite par la construction de la caverne elle-même, car de fortes contraintes déviatoires se sont développées dans une zone de roche perturbée (appelée DRZ) autour des cavernes [1, 15]. Dans la zone de perturbation rocheuse, des dommages et une dilatation se produisent [16, 17]. La perméabilité augmente en effet de plusieurs ordres de grandeur sous une charge déviatrice, ce qui entraîne un endommagement [14, 18-20]. En tant que facteur essentiel pour évaluer la stabilité dans la ZDR, la variation de la perméabilité en cas de contrainte déviatrice mérite une attention particulière. Un test triaxial avec des mesures de perméabilité peut être effectué pour atteindre cet objectif et obtenir simultanément des échantillons endommagés. Lorsque la caverne saline entre dans une phase de stockage après l'excavation, la perméabilité peut diminuer en raison de la capacité d'auto-guérison. Cela joue également un rôle important dans la conception de l'étanchéité de la caverne de sel. Ces échantillons pré-dommagés peuvent donc être testés sous charge hydrostatique pour étudier les effets des dommages, les propriétés potentielles d'étanchéité/guérison et le couplage poromécanique. En résumé, cette étude expérimentale comprend des tests mécaniques, poromécaniques et de perméabilité (en particulier aux gaz) avec l'effet du confinement ou de la charge axiale. En attendant, il a été décidé de mener des expériences de micro-tomographie aux rayons X pour observer les changements de microstructure interne avant et après les différents tests. Par conséquent, l'objectif principal de cette étude est d'élargir la compréhension du transfert de fluides, du comportement poromécanique et temporel et des propriétés d'étanchéité et de cicatrisation des roches salines.

Les objectifs spécifiques de cette étude sont les suivants :

- Investiguer les propriétés de transport des fluides : perméabilité à la saumure et au gaz, et évaluer l'influence de la contrainte isotrope (et de la pression des pores du gaz) sur la perméabilité en effectuant une série de tests hydrostatiques à l'argon.

- Détecter la perméabilité liée à l'hydrogène et analyser la comparaison entre la perméabilité de l'hydrogène et celle de l'argon.

- Exploration préliminaire des propriétés poromécaniques, c'est-à-dire pour détecter les effets de couplage entre la pression des pores du gaz et le squelette de la roche et pour estimer le coefficient de Biot.

- Investiguer les effets du temps sur la perméabilité sous des contraintes isotropes et déviatoires en effectuant des tests hydrostatiques et triaxiaux respectivement.

-Explorez les propriétés potentielles d'étanchéité/guérison des échantillons pré-dommagés, qui ont été produits par des tests triaxiaux ou uniaxiaux, en mesurant les variations de la perméabilité et de la contrainte volumétrique avec le temps sous une charge hydrostatique.

-Introduire la technique de microtomographie aux rayons X pour détecter les changements de la microstructure interne et quantifier la porosité avant et après différentes charges mécaniques.

Cette étude se compose de cinq chapitres, qui sont organisés comme suit :

1) Le premier chapitre présente le contexte, qui contient le contexte et les objectifs de cette recherche.

2) Le deuxième chapitre est la bibliographie, qui présente une revue des travaux antérieurs sur plusieurs caractéristiques de la roche saline, telles que les propriétés de transport des fluides (gaz et saumure) et les propriétés poromécaniques. Différents processus permettant de caractériser les propriétés de transfert des massifs de sel sont passés en revue, tels que la perméabilité à la saumure et aux gaz et sa dépendance à la contrainte, au temps, au fluage et à 'l'auto-cicatrisation', l'effet Klinkenberg, etc.

3) Le troisième chapitre se concentre principalement sur l'étude expérimentale du transfert de fluides et des propriétés poromécaniques de la roche saline sous charge hydrostatique. Les techniques expérimentales des différents tests sont d'abord présentées et la théorie de base de la poroélasticité (théorie de Biot) est également introduite. Les perméabilités au gaz (et à la saumure) sont ensuite enregistrées pour différents échantillons (provenant de différentes carottes). En parallèle, des tests hydrostatiques sont effectués en conjonction avec la technique des gaz pour étudier les influences du confinement (charge-décharge) et de la pression des fluides (pression effective de Terzaghi) sur la perméabilité aux gaz. Les tests comparatifs de perméabilité (hydrogène v.s. argon) sont effectués. La structure poreuse est également caractérisée par des mesures de porosité et l'analyse de la surface spécifique (SBET) à partir des tests d'adsorption/désorption de gaz. Le comportement poromécanique du sel est détecté au préalable. Comme le sel gemme est une roche élasto-viscoplastique, les effets du temps sur la perméabilité sont également étudiés. De plus, les effets de Klinkenberg à différents niveaux de confinement sont étudiés pour deux échantillons.

4) Le quatrième chapitre est principalement consacré à la mesure des variations de la perméabilité et des couplages lors de différents essais mécaniques, c'est-à-dire des essais hydrostatiques et triaxiaux. Les techniques expérimentales de test tri-/uniaxial et de micro-tomographie aux rayons X sont d'abord présentées. Avant le test tri-/uniaxial, les propriétés hydro-mécaniques sont caractérisées par la réalisation de tests hydrostatiques (**H1**). Les tests triaxiaux sont suspectés d'une part d'étudier la variation de la perméabilité aux gaz avec une charge déviatrice et/ou avec le temps, d'autre part d'obtenir des échantillons endommagés avec des fissures. Les tests hydrostatiques (**H2**) pour ces échantillons pré-

dommagés sont ensuite effectués après les tests triaxiaux/uniaxiaux pour détecter l'effet de dommage et pour caractériser les effets potentiels d'étanchéité/guérison. En parallèle, la technique d'imagerie non destructive par micro-tomographie aux rayons X est introduite pour caractériser les modifications de la microstructure avant et après les différents tests. Par conséquent, ces observations conjointes peuvent être utilisées pour analyser les variations des propriétés de transfert de gaz et les couplages dus aux différentes charges mécaniques d'un point de vue microscopique.

5) Le cinquième chapitre apporte des conclusions et des perspectives. Ce matériau a des propriétés très dispersives. Pour les propriétés de transfert de gaz de la roche saline, la perméabilité est dans une large gamme de 10^{-16} à 10^{-23} m². Les perméabilités mesurées avec l'argon ou l'hydrogène sont proches l'une de l'autre, par conséquent, la perméabilité à l'argon peut être une bonne estimation de la perméabilité à l'hydrogène dans les études pour le développement du stockage de l'hydrogène. La sensibilité de la perméabilité au confinement soutient l'hypothèse que le fluide s'écoule à travers des fissures ou des joints de grains. La perméabilité ne dépend pas seulement de la pression de confinement et de la contrainte axiale, mais évolue également avec le temps pour les essais hydrostatiques et triaxiaux. Pour le couplage poromécanique, l'existence d'un couplage fluide-squelette a été vérifiée en utilisant des techniques de gaz pour différents échantillons, ce qui est une découverte importante. Les tests triaxiaux et uniaxiaux peuvent causer des dommages/fissures, ces échantillons pré-dommagés ont un couplage important dû à l'effet de fissuration. La sensibilité du coefficient de Biot au confinement et à l'effet de fissuration soutient l'hypothèse selon laquelle les couplages sont principalement dus à l'effet de pression des fluides dans les fissures. Les observations de la microtomographie aux rayons X confirment que les fissures étaient (partiellement) fermées dans test **H1**, et deux effets 'antagonistes' dus au test triaxial.

Table of Contents

1. Context	1
2. Bibliography	4
2.1. The fluid transfer properties of salt rock	5
2.1.1. Micro-structure of salt rock	5
2.1.2. Brine permeability of salt	9
2.1.3. Gas permeability of salt	10
2.1.4. Klinkenberg effect	11
2.1.5. Stress and time dependent permeability	13
2.2. Stress couplings (poromechanical properties) of salt rock	14
2.3. Permeability changes in DRZ and sealing/healing properties of salt rock	17
2.3.1. Permeability changes with axial stress in the DRZ	17
2.3.2. Sealing-healing properties	21
2.4. Microstructure observation in damaged and healed salt rocks	24
3. Part I : preliminary study of fluid transfer and poromechanical properties of salt rock under hydrostatic loading	26
3.1. Introduction	26
3.2. Experimental techniques	26
3.2.1. Material used for the experiments	26
3.2.2. Experimental method for brine permeability.....	28
3.2.3. Experimental method for gas permeability	29
3.2.4. Experimental method for porosity	32
3.2.5. Experimental method for biot coefficient.....	34
3.3. Experimental results	36
3.3.1. Brine permeability	36
3.3.2. Confining pressure and Terzaghi effective pressure effects on gas permeability	37
3.3.3. Confining pressure effects on porosity	39
3.3.4. Comparison between argon and hydrogen permeability	41
3.3.5. Time effects on gas permeability	43
3.3.6. Klinkenberg effects	43
3.3.7. Biot coefficient and couplings	49
3.4. Partial conclusion	52
4. Part II : mechanical, poromechanical and gas permeability tests with the effects of confinement and/or axial loading	54
4.1. Introduction	54
4.2. Experimental techniques	55
4.2.1. Material used for the experiments	55

4.2.2.	Experimental method for triaxial test	56
4.2.3.	Experimental method for uniaxial test.....	57
4.2.4.	X-ray microtomography technology	58
4.3.	Permeability evolution in tests H1 before axial loading.....	61
4.3.1.	Time-dependent behavior during hydrostatic test H1	61
4.3.2.	Partial conclusion	67
4.4.	Permeability evolution in triaxial test and sealing/healing effects on five damaged samples (a comparison of hydrostatic tests H1 and H2)	68
4.4.1.	Sample XR02-3: triaxial test and H2 test	68
4.4.2.	Sample XZ25-3: H1 test, triaxial test and H2 test.....	71
4.4.3.	Sample XS01-3: H1 test, triaxial test and H2 test	77
4.4.4.	Sample XR02-4: H1 test, triaxial test and H2 test.....	82
4.4.5.	Sample XS01-4: H1 test, triaxial test and H2 test	95
4.4.6.	Partial conclusion	108
4.5.	Sealing/Healing effects on two damaged samples (uniaxial test and a comparison of hydrostatic test H1 and H2).....	110
4.5.1.	Sample XZ25-5: H1 test, uniaxial test and H2 test	110
4.5.2.	Sample XZ25-4	115
4.5.3.	Partial conclusion	123
5.	Conclusions and perspectives	125
5.1.	Conclusions	125
5.2.	Perspectives.....	127
References	128
Appendix: X-ray microtomography observations.....	137
A.1. Sample XR02-4	137
A.2. Sample XS01-4.....	138
A.3. Sample XZ25-4.....	140

1. Context

From an engineering perspective, salt rock is generally considered to be an impermeable or ultra-low permeable medium, and with the ability to stand high pressure and to heal itself after damage [1, 2]. These all make underground storage in salt layer very suitable and attractive. Therefore, salt caverns for hydrocarbon storage such as crude oil, liquefied petroleum gas (LPG) or natural gas [3–5], as well as for nuclear/radioactive wastes disposal, have been developed over several decades [3, 6–8].

In this experimental research, the characterizations of salt rock, mainly containing fluid transfer properties and a preliminary exploration in poromechanical behavior, are analysed in the context of two applications. Firstly, due to salt creep, some caverns lost their economic value and have to be abandoned. Abandonment experiments of salt caverns [9] demonstrate the existence of permeation at the cavern scale. The cavern is filled with brine and sealed for abandonment: an equilibrium in brine pressure can be reached when salt mass creep and cavern shrinkage are balanced by brine permeation through the cavern wall. This equilibrium is suspected to reach over a long period of time (several years or decades) [10]. Therefore, the stress-dependent fluid transfer characteristics and time-dependent behavior of salt rock are critical for this application. The second application, in the current context of energy transition, can be found as hydrogen storage [11]. Hydrogen, produced for example by solar energy, may be stored in salt caverns. Under this scenario, permeability related to hydrogen needs to be assessed.

Salt permeability is not only affected by stress state, but also is strongly influenced by time effects. On a mechanical point of view, rock salt is an elasto-viscoplastic rock, which exhibits a strong creeping behavior. Its instantaneous response is elastic while its long-term mechanical response under constant deviatoric loading is mainly time-dependent. This can therefore explain the volume loss and the progressive closure of salt caverns during gas storage operation. Hence, the variation of permeability when salt creeps should be detected [12]. However, there are few previous researches on the long-term evolution of permeability [13, 14].

In addition, as salt rock is little permeable, internal fluid pressure may contribute to loading and be involved in the stress-strain relationship characterizing the equation of state of the material and may influence permeability at a given loading. This phenomenon is often observed on more or less permeable other sedimentary rocks, but, to our knowledge, has little been studied for salt. How this internal fluid pressure is coupled with mechanical behavior is worth exploring and is another key object in this study.

However, some authors suggest that permeation, observed during in situ tests in salt caverns, had been partially induced by cavern construction itself, as high deviatoric stresses were developed in a disturb rock zone (denoted DRZ) around caverns [1, 15]. In the DRZ, damage and dilatancy occur [16, 17]. Permeability indeed increases by several orders of magnitude under deviatoric loading, which leads to a damage [14, 18–20]. As an essential factor for evaluating the stability in the DRZ, the permeability

variation with deviatoric stress, deserves special concern. Triaxial test with permeability measurements can be performed to achieve this target and simultaneously get damaged samples. When salt cavern goes into a storage phase after excavation, permeability may decrease due to self-healing capability. This also plays an important role in the seal design of salt cavern. Those pre-damaged samples can therefore be tested under hydrostatic loading to investigate the damage effects, potential sealing/healing properties and poromechanical coupling. To sum up, this experimental study includes mechanical, poromechanical and permeability (especially gas) tests with the effect of confinement or axial loading. Meanwhile, it was decided to conduct X-ray micro-tomography experiments to observe the internal microstructural changes before and after various tests. Consequently, the main goal of this study is to expand the understanding of fluid transfer, poromechanical, time-dependent behavior and sealing/healing properties of salt rocks.

The specific objectives of this study are as follows:

-Investigate fluid transport properties: brine and gas permeability, and evaluate the influence of isotropic stress (and gas pore pressure) on permeability by performing a series of hydrostatic tests using argon.

-Detect the permeability related to hydrogen and analyze the comparison between hydrogen and argon permeability.

-Preliminary investigation of poromechanical properties i.e. to detect coupling effects between gas pore pressure and rock skeleton and to estimate Biot's coefficient.

-Investigate time effects on permeability under isotropic and deviatoric stresses by performing hydrostatic and triaxial tests respectively.

-Explore the potential sealing/healing properties of pre-damaged specimens, which were produced by triaxial or uniaxial tests, by measuring the variations of both permeability and volumetric strain with time under hydrostatic loading.

-Introduce X-ray microtomography technique to detect the changes in internal microstructure and to quantify porosity before and after different mechanical loadings.

This study consists of five chapters, which are organized as follows:

- 1) The first chapter presents the context, which contains the background and objectives of this research.
- 2) The second chapter is the bibliography, which presents a review of previous work on several characteristics of salt rock, such as fluid (gas and brine) transport properties, microstructure, stress couplings and sealing/healing properties.
- 3) The third chapter mainly focuses on the experimental study of fluid transfer and poromechanical properties of salt rock under hydrostatic loading. The experimental techniques for all the different tests are first presented and the basic theory of poroelasticity (Biot's theory)

is also introduced. Gas (and brine) permeabilities are then recorded for different samples (from different cores). In parallel, hydrostatic tests are performed in conjunction with gas technique to investigate the influences of confinement (load-unload) and fluid pressure (Terzaghi effective pressure) on gas permeability. The comparative permeability tests (hydrogen v.s. argon) are performed. The porous structure are also characterized by porosity measurements and the specific surface area analysis (SBET) from gas adsorption/desorption tests. Salt poromechanical behavior is preliminarily detected. Since rock salt is an elasto-viscoplastic rock, time effects on permeability are also investigated. Moreover, Klinkenberg effects at different confinement levels are explored for two samples.

- 4) The fourth chapter is mainly devoted to measure the variations of permeability and couplings during different mechanical tests, i.e. hydrostatic and triaxial tests. The experimental techniques for tri-/uniaxial test and X-ray micro-tomography are first introduced. Before tri-/uniaxial test, hydro-mechanical properties are characterized by performing hydrostatic tests (**H1**). Triaxial tests are suspected on one hand to investigate gas permeability variation with deviatoric loading and/or with time, on the other hand to obtain damaged samples with cracks. Hydrostatic tests (**H2**) for these pre-damaged samples are then performed after the triaxial/uniaxial tests to detect damage effect and to characterize the potential sealing/healing effects. In parallel, the non-destructive X-ray micro-tomography imaging technique is introduced to characterize the microstructure changes before and after various tests. Therefore, these joint observations can be used to analyze the variations of gas transfer properties and couplings due to different mechanical loadings from a microscopic perspective.
- 5) The fifth chapter brings conclusions and perspectives.

2. Bibliography

Salt rocks are generally characterized as: ultra-low porosity and permeability, physical-chemical inertness (or hydrocarbons), very low creep strength under crustal conditions [21], high solubility with water (easy to be leached), abundant geological conditions around world. All these characteristics make a highly suitable geological barrier for underground storage [22]. For around 60 years, numerous salt caverns exist worldwide such as America, Canada, Europe, and Asia [23]. They were leached in deep geological salt formations by injection of water for underground storage [24]. The artificially constructed salt caverns have been used for the storage of not only fossil fuels (hydrocarbons) such as natural gas, crude oil, and petroleum products (refined fuels, liquefied gas), but also for the storage of compressed air and even hydrogen, radioactive wastes [25]. In the 1950s, liquefied petroleum gas (LPG) as well as oil were stored in the first salt caverns in the United States and Europe. The first natural gas cavern was constructed in Marysville, Michigan (United States) in 1961 [26]. Nowadays, there are more than 2000 salt caverns in North America and over 300 salt caverns in Germany for storing energy carriers. By the end of 2012, there are approximately 554 caverns around the world that were used to store natural gas [27]. Fig.2.1 shows the distribution of major salt caverns [28].

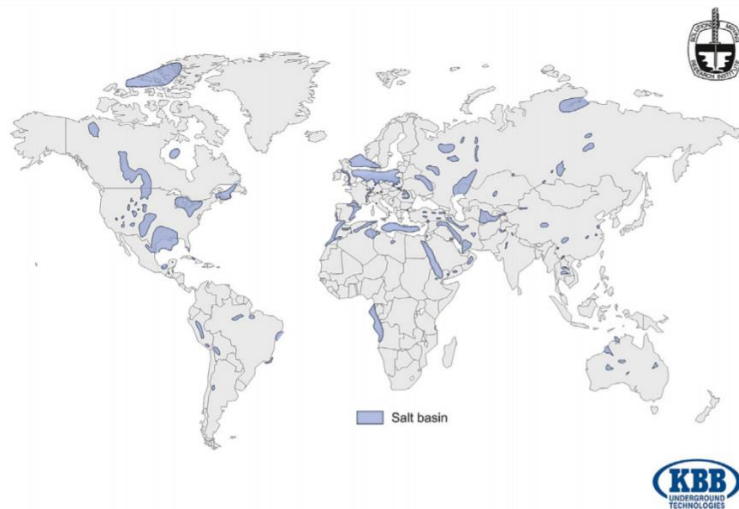


Fig.2.1 Map of underground salt deposits worldwide [28]

From the long-term assessment of salt caverns, specific attention has been paid to their stability and tightness [29, 30]. Even for the abandoned salt cavern, which may someday serve as a repository for hydrocarbon, their safety should deserve the same attention [31, 32]. For most conventional applications, rock salt is considered impermeable within the measurable range. However tightness well tests [25] and abandonment experiments of salt caverns [33] show that, in these particular situations, salt should be regarded as a very low permeable medium. Therefore, the salt permeability cannot be neglected and plays a vital role in the safety assessment of these caverns. For example, in the case of an abandoned salt cavern filled with brine, fluid pressure in the cavern starts to increase due to creep and cavern shrinkage after the cavern is sealed. However, equilibrium is reached when salt mass creep is

balanced by brine permeation through cavern wall. Another example is the application of nuclear waste/radioactive waste disposal. It is critical to quantify permeability far below the conventional ‘impermeable’ limit in the long-term waste isolation [34]. In this context, it is essential to investigate fluid transfer properties and long-term performance.

In addition to permeability, the mechanical properties are generally considered to be the key factors in affecting sealing and storage performance of salt caverns [35]. As salt rock is little permeable, internal fluid pressure may contribute to mechanical loading and be coupled with the mechanical behavior of salt. It is interesting to explore this potential coupling of salt rock as it is often observed on other sedimentary rocks. Due to its ductile rheological properties [36], self-healing/sealing is also another unique characteristic that makes salt rock an excellent seal for underground storage [37]. Therefore, this chapter presents a literature review on the behavior of salt rock in terms of fluid transfer, stress coupling, stress- and time-dependent behavior as well as sealing/healing properties.

2.1. The fluid transfer properties of salt rock

As one of major characteristics, the transport property is of vital importance for design and safety analysis of underground salt caverns [38]. Numerous permeability measurements have been performed on salt rocks from laboratory to in situ conditions using common gases (such as nitrogen [39], helium, argon [40]) and fluid (saturated brine).

In situ permeability tests performed in different salt formations have demonstrated that it is generally considered to be exceedingly low [41]. These tests can be used to detect the permeability of not only DRZ, but also intact or undisturbed salt. While laboratorial testing for undisturbed salt is usually impossible due to disturbance by core drilling.

It is well known that undisturbed salt rock has very low permeability. Based on tests conducted at Waste Isolation Pilot Plant (WIPP) site in New Mexico (USA) [42], it was concluded that the permeability of undisturbed salt is less than 10^{-21} m^2 [15, 40, 43]. Another in situ test in the Amelie salt mine owned by Mines de Potasse d'Alsace (MDPA, France) [39], showed the permeability is in the same order of magnitude as the WIPP site. Wong et al [44] confirmed that the porosity of salt formations is very low, generally less than 1%, with permeability ranging between 10^{-7} and 10^{-4} mD ($9.869\text{E-}23 \text{ m}^2$ and $9.869\text{E-}20 \text{ m}^2$). Such a low gas permeability of undisturbed rock salt is most likely related to the very small porosity (<1%), which is saturated with brine under relatively great pressures. However, in Peach’s tests [34], samples from Asse salt mine in Germany had an initial permeability of 10^{-17} - 10^{-18} m^2 , 3 or 4 orders of magnitude higher than the in situ permeability in MDPA mine and WIPP site.

2.1.1. Micro-structure of salt rock

A saturated porous medium is generally defined as a fluid–solid mixture, composed of a solid matrix phase and of a connected porous space saturated by a fluid mixture (gas or liquid). The matrix

consists of a solid part and unconnected porosity (occluded pores), whether saturated or not, but through which no filtration occurs [45]. The space through which the fluid can actually flow freely is a connected porous part. As shown in Fig.2.2, a porous medium can therefore be considered as a superimposition of two continua, the skeleton continuum and the fluid continuum [45]. The connected porosity is the ratio of the connected porous volume to the total volume.

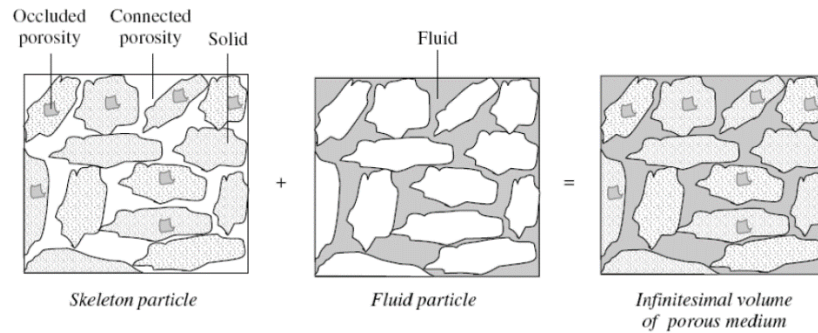


Fig.2.2 The porous medium as the superimposition of two continuous media: a skeleton particle and a fluid particle coincide with the same geometrical infinitesimal volume [45]

Thus, the poromechanical properties depend on solid matrix, connected or occluded pores and fluid (gas or liquid). When a mechanical loading is applied, two essential mechanisms may be coupled between the interstitial fluid and the porous medium. The first is material deformation, which usually brings some changes in porous structure and finally in multiphysical properties, such as the transport properties. The second is the existence of interstitial fluid in porous geomaterials, which modifies mechanical responses of the latter [46]. The fluid transport properties are generally closely related to porosity, pore size and complex pore structure. Therefore, it is indispensable to characterize microscopic pore structure of salt rock.

Natural salt rock is a polycrystalline material. Each salt crystal grain is composed of several smaller parts known as sub-grains [7]. The grain size may range from less than 1 mm to several dm. Salt grains are connected to each other by grain boundaries (i.e. high angle boundaries) while the sub-grains are distinguished from each other by sub-grain boundaries (i.e. low angle boundaries) (see Fig.2.3) [23, 47, 48]. Some scanning electron microscopy (SEM) tests in [49] presented that salt rock is a kind of typical crystallized rock and the inner structure is extremely closed with no obvious pores and cracks (as shown in Fig.2.4). For this polycrystalline material, the porosity typically occurs between the junctions of crystals. For instance, there are pores with size of 20–30 μm observed in the junction of two crystals (see Fig.2.5), which can provide a channel for fluid flow [50].

X-ray computed tomography (CT), has been widely used as a non-destructive technique to characterize the microstructure of salt rocks. 3D- μCT (resolution of 10.3 μm) and -nCT (resolution of 1.7 μm) observations for anhydrite, pore space and fluid inclusions in salt rock, as shown in Fig.2.6 and 2.7 [51]. The pore space (displayed in blue with a total porosity of $0.87 \pm 0.07\%$, see Fig.2.6) consists

of single pores and fractures, which exhibits a moderate distribution anisotropy. The 3D reconstructions of pore space and anhydrite revealed that there is no evident correlation between their spatial distribution (Fig.2.6 (b)). 3D-nCT reconstruction of fluid inclusions along halite grain-boundaries shows various shapes of fluids, including connected and disconnected ones (see Fig.2.7).

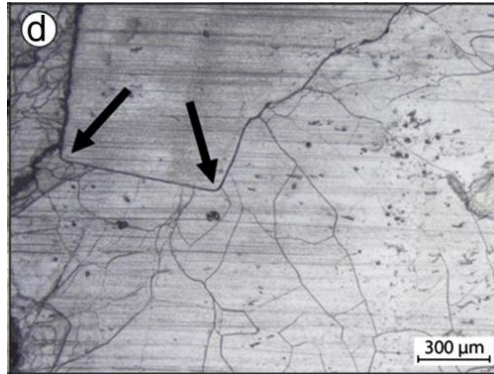


Fig.2.3 Heterogeneous subgrain structure of Gorleben rock salt (from Gorleben salt dome in Northern Germany) separated by high-angle grain boundary (arrows). Subgrain-free halite grain (the upper grain) is adjacent to subgrain-rich halite grains [48]

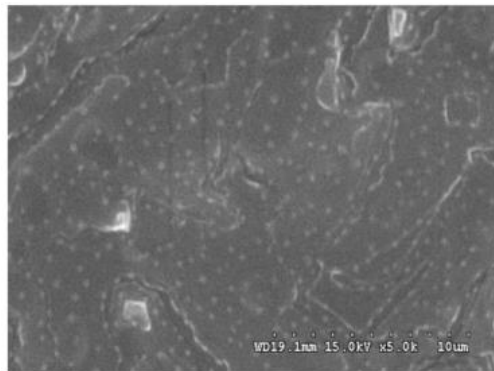


Fig.2.4 SEM picture of pure salt rock crystal (from china) [49]

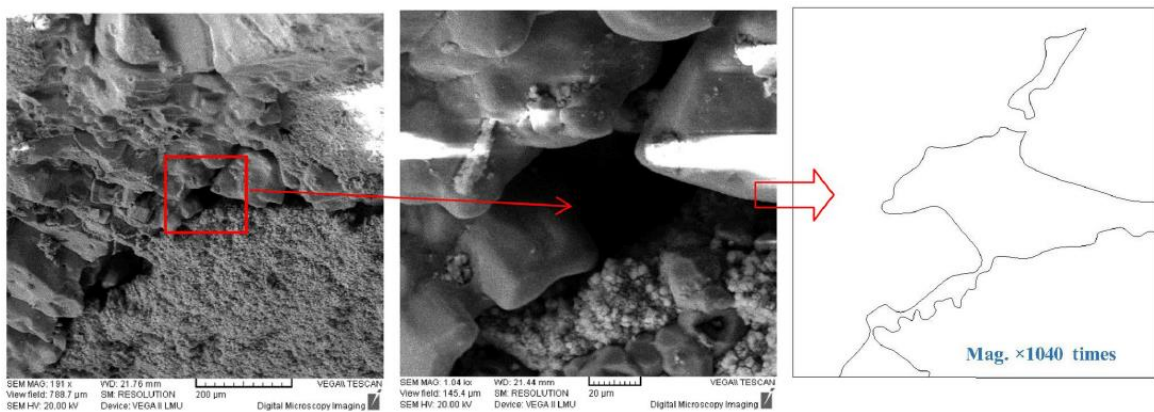


Fig.2.5 SEM results of gray salt rock. A square sodium chloride crystal and a cluster of sodium chloride crystals. The junction of the two has a pore size of 20–30μm, which provides a channel for the upward penetration of the fluid [50].

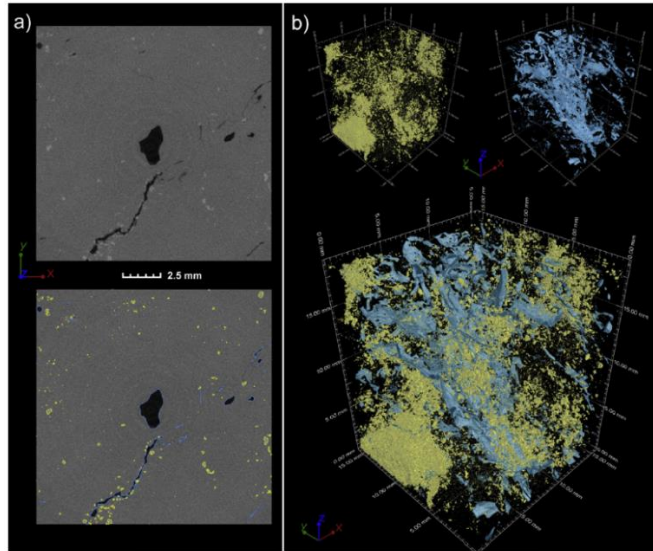


Fig.2.6 (a) Pore space is displayed as dark domains; halite forms the gray matrix. Anhydrite is represented as light gray, small particles. Pore space and anhydrite are captured in two separate volumes illustrated as blue and yellow masks in the lower part. (b) 3D- μ CT reconstruction of pore space (blue) and anhydrite (yellow) based on the raw data set shown in (a). Heterogeneously distributed clusters and scattered crystals of anhydrite (yellow) are quantified with $0.66 \pm 0.25\%$. The pore space (blue) yields $0.87 \pm 0.07\%$. Halite contributes $>98\%$ [51].

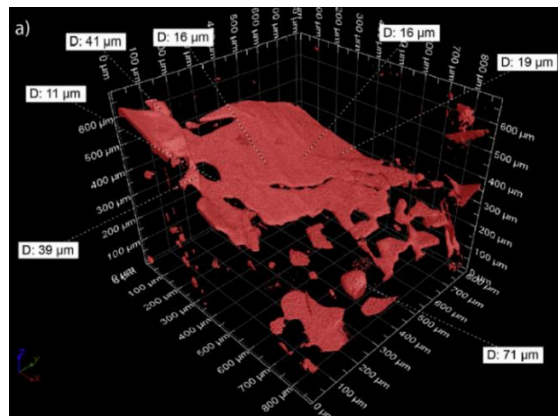


Fig.2.7 3D-nCT reconstruction of fluid inclusions in Asse rock salt (Speisesalz). (a) The 3D-reconstruction (red) shows various shapes of fluids along a halite grain-boundary [51].

Compared to common rock types, the porosity of salt rock is extremely low (usually less than 1%, as previously mentioned). The complicated relationship between salt porous networks and fluid transport properties has been investigated by several authors, but it is difficult to draw conclusions. It was found that the maximum and medium radius of the pore throat (see Fig.2.8) have significant impacts on salt permeability[52]. Porosity is not apparently related to permeability, but the small throat majorly determines the permeability. It has been suggested that permeability evolution during creep is less sensitive to porosity than to void radius and spacing, which control pore connectivity [53]. Renard et al. (2004) [54] presented synchrotron microtomography on experimentally compacted samples with a maximum resolution of $0.7 \mu\text{m}$ to progressively monitor changes in texture and pore space characteristic in halite aggregates. From the microscopic mechanism, it was found that the decrease in permeability

could be linked to changes in halite grain contact, due to grain indentation and pore connectivity reduction by precipitation on free surfaces of pore throats.

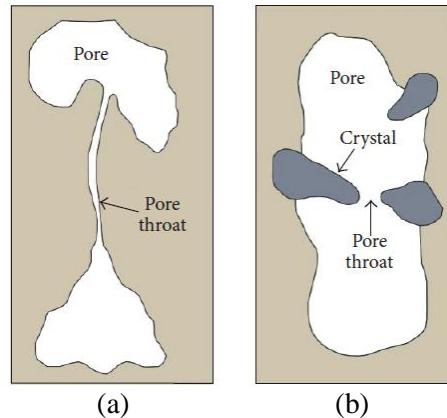


Fig.2.8 A sketch diagram of pore and pore throat in rock salt: (a) demonstrates two pores connecting with a pore throat; (b) displays a pore throat within a single pore [52]

Several methods have been developed to characterize pore properties of porous materials: (1) saturation or imbibition, (2) gas expansion (He porosimetry), (3) gas adsorption/desorption and (4) mercury intrusion porosimetry (MIP) [55, 56]. MIP is one of the most widely used methods for determination of pore size distribution. However, using gas adsorption/desorption makes it possible to quantify the specific surface area (BET theory), the pore volume (Gurvich rule) and the pore size distribution (BJH theory). The other advantage of gas adsorption/desorption over MIP is the ability to quantify fine pores, i.e. micro/meso-pores smaller than 3-6 nm, which are out of measurable range in MIP test.

In the context of physical adsorption, according to the pore size (IUPAC recommendation,1985), they are classified as follows [57]:

- (i) pores with widths exceeding about 50 nm are called macropores;
- (ii) pores of widths between 2 nm and 50 nm are called mesopores;
- (iii) pores with widths not exceeding about 2 nm are called micropores.

The specific surface of a porous material is composed of the external geometric surface and the internal surface developed by the solid, which takes into account all the surface irregularities at the molecular scale and the surface developed by pore wall, all related to the mass unit. It is an essential data of porous materials as it indicates the ‘fineness’ of porous network at a given porosity [58]. Hence, in addition to the porosity measurements (with gas technology), it is also decided to perform gas adsorption/desorption on salt rock to analyse the specific surface area (SBET).

2.1.2. Brine permeability of salt

Understanding brine permeability of salt formation is essential for applications such as monitoring brine leakage during long-term evolution or determining cavern abandonment strategy based on the

magnitude of brine permeability [43]. However, there are not many studies dedicated to characterizing brine transport properties of salt, mainly due to the extremely low permeability and time-consuming.

A finite element formulation for brine transport in rock salt was proposed in [59]: natural salt rock consists of individual crystals gathered together, so only a portion of the crystal faces or grain boundaries contribute to the hydraulically connected pore space. Transport of brine inclusions within a single crystal is considered to be thermally driven, while transport along crystal interfaces or grain boundaries is considered to be pressure driven.

The brine injection measurements performed at the WIPP site [41] and at Mine de Potasse d'Alsace site [60], showed very low brine permeability (10^{-21}m^2). The leakage tests with brine were carried out at a dozen wells at two different sites (Tersanne and Etrez) in France for the duration of 4-305 days. The permeability values of two sites were in the range of $3.2\text{E-}21$ - $8.6\text{E-}22\text{m}^2$ and $1.9\text{E-}20$ - $4.6\text{E-}21\text{m}^2$ respectively. In addition, from the tests conducted in the same cavern but at different pressure levels, it was confirmed that salt permeability increased when cavern pressure was close to geostatic pressure [43].

Some studies focused on the transfer properties of salt rocks by different fluids. Permeabilities measured using brine and silicone as the working fluid were slightly lower than that using comparable gas. No difference was observed between the results using silicone and brine. Tanikawa and Shimamoto [61, 62] measured intrinsic permeability of sedimentary rocks from the western foothills of Taiwan by using nitrogen gas and distilled water as pore fluids. The results proved that gas permeability was larger than water permeability by several times to one order of magnitude, which could be partly explained by Klinkenberg effect. However, H. Loosveldt et al. [63] carried out the gas, water and ethanol (a neutral liquid compared to water) permeability measurements on eight samples cored from the same mortar. The results presented that ethanol permeability values were always intermediate between gas and water values and, when corrected with Klinkenberg effect, were virtually the same as gas permeability results. Therefore, the difference between gas and water permeability have to be explained by other phenomena such as rehydration, dissolution and migration of fine elements or water adsorption in the thinnest pores, while Klinkenberg effect only plays a minimal role.

2.1.3. Gas permeability of salt

Generally, there are two different gas transport mechanisms in a porous network: diffusion and advection. Diffusion is the movement process by which particles are transferred from high molecular concentration to low molecular concentration. It can be described by Fick's first law. While advection is linked to bulk transport of mass (or the motion of particles along the bulk flow) due to a difference in hydraulic pressure (pressure gradient). It is usually described by Darcy's law:

$$V = -(K/\mu) * grad P \quad (2.1)$$

where V is the mean speed of the fluid (in m/s); K is the intrinsic permeability of the material (m^2); μ is the dynamic viscosity of the fluid ($\text{Pa}\cdot\text{s}$); P is fluid pressure (Pa).

During the gas movement, these two types of transfer sometimes can coexist simultaneously. In usual porous media (rocks, concrete) the transport mechanisms under pressure gradient is mainly dominated by advection and the diffusive flow is often neglected. However, for some quasi-impermeable media (salt, epoxy, silicones, etc.) the case seems to be more complicated. Previous permeability measurements are mainly based on the assumption of Darcy's law. The salt permeability can be measured using different methods presented in the literature: mainly the transient pressure pulse-decay methods, and the steady-state method with constant flow. Generally, the constant pressure flow test is used for permeabilities above 10^{-18}m^2 (the lowest value that this method can measure is around 10^{-20}m^2 [64]) and the pressure decay test for smaller permeabilities [15]. Transient permeability test requires an initial constant pore pressure to be established in the sample. A pressure pulse (increment or decrement) is then applied to one side of the sample, and transient flow through the sample is induced [14, 40]. The pressure pulse decay method leads to more rapid determination of the permeability of tight media in comparison to a steady-state experiment that requires the flow rate to stabilize [65].

With the transition from the use of hydrocarbons to renewable energy sources, hydrogen is one of green energy sources, and its storage is the key to the application of hydrogen energy. Salt caverns storage, which have been maturely used for hydrocarbon (especially with the experience of around 50 years of natural gas storage in salt), are considered the most promising technology due to the naturally tightness, large storage capacity, low cost and sealing capacity [66]. However, there are only a few salt caverns for hydrogen storage (such as Teesside in the United Kingdom and Clemens Dome, Spindletop, Moss Bluff in the United States [67]). Although these existing projects can prove that underground hydrogen storage is a technically feasible option, there are still challenges and further research in many aspects is required. From the point of view of salt cavern tightness, salt permeability related to hydrogen should first be evaluated.

As mentioned above, the permeability has been investigated in many experiments using common gases like argon, nitrogen or helium and most have confirmed values of $k < 1\text{E-}20\text{m}^2$ [40]. However, few investigators compare the salt permeability between different gases, and few evaluation of hydrogen permeability of salt rock. Considering very different characteristics of hydrogen (the high mobility and low viscosity), a series of laboratory tests with different gases (hydrogen, methane and nitrogen) were conducted in [68], in order to confirm whether hydrogen is applicable to the same permeability value. The results gave the conclusion that no significant differences in the permeation mechanism through salt rock for hydrogen, methane and nitrogen were observed from these different gas permeability measurements.

2.1.4. Klinkenberg effect

For the flow in micro (or meso) pores medium, it was found that the gas molecules can slide on the pore wall, which contribute to the higher gas permeability than the intrinsic one. This phenomenon, named ‘slip flow’ [69], occurs when the gas pressure is low or the mean free path of the gas molecules and the porous radius are in the same order. This ‘slip flow’ in the pore wall are generally considered to play important roles [39]. Klinkenberg presents the conclusion that the measured gas permeability in the laboratory, which is different from the intrinsic one (a permanent parameter of the porous medium), is a linear function of the reciprocal of the mean gas pressure. It is written by:

$$K_{app} = K_{int} * \left(1 + \frac{\beta}{P_m}\right) \quad (2.2)$$

where K_{app} is the measured permeability and K_{int} is the intrinsic permeability. P_m is the average injection pressure. β is the Klinkenberg factor, which depends on the properties of the fluid (e.g. the kinematic viscosity and the molecular weight) and the properties of the porous medium (e.g. the width of the pores throat) [65]. As these properties is difficult to determine directly, β can be calculated by performing three permeability tests with different mean pressures (the details described in §3.3.6).

The dimensionless Knudsen number (K_n) [70] usually can be used to characterize the gas transport regimes for porous medium in micro-scale, defined as follows:

$$K_n = \frac{\lambda_g}{r} \quad (2.3)$$

where λ_g is the mean free path of gas molecule and r is the average pore radius. Under isothermal conditions, the Knudsen number changes with pressure and permeability. According to the classification of flow regimes by [71, 72], the fundamental flow regimes are described, namely the conditions of continuum fluid flow ($K_n \leq 0.001$), slip flow ($0.001 < K_n < 0.1$), transition flow ($0.1 < K_n < 10$), and free molecular flow ($K_n \geq 10$). Once there is slip flow in the gas flow, the Klinkenberg slip theory can be applied to obtain the intrinsic permeability of medium.

The Klinkenberg effect, has been confirmed by numerous investigations to play an important role on gas flow behavior, especially in low permeability material [62, 73–76]. Usually the Klinkenberg factor is related to complex microscopic mechanisms of porous medium and the mean free path of gas molecules. In recent years, many researchers have devoted to study their connections. Chen et al [77] verified the Klinkenberg effect of concrete. This effect measured by helium is more marked than that measured by argon though permeability tests with these two different gas. Pei [78] presented that the Klinkenberg factor decreases with the intensity of heating by conducting the gas permeability tests on the mortar samples treated at 105, 400 and 500 °C. This phenomenon is mainly driven by the increase in the average pores size due to the generated new cracks and/or widening by the departure of hydrate water. On the contrary, increase in confining pressure leads to an increase in the Klinkenberg factor due to the narrowing cracks. Xiao et al [79] proposed that the intrinsic permeability of tight sandstones was

closely related microstructure (e.g. crack-like pores) though the experimental study. Since the permeability has high sensitivity to confinement in terms of microstructure, it is interesting to explore this effect on salt rocks.

2.1.5. Stress and time dependent permeability

As mentioned before, rock salt can be generally characterized as a quasi-impermeable material under an undisturbed state. It is well known that salt cores decompressed from underground is supposed to have a higher permeability than undisturbed state while hydrostatic confinement can give rise to a reduction in permeability. Besides, the deviatoric stress in the RZD is very likely to increase the salt permeability due to the new micro-cracking created during the excavation process, which will be detrimental to the safety of its storage performance. Therefore, changes in permeability can sometimes be characterized as stress-dependent behavior and its variations related to mechanical (hydrostatic or deviatoric) loads have been studied in numerous experiments [8, 16, 80, 81]. Gas permeability under hydrostatic confinement is often the first case that is investigated. For many geomaterials such as concrete, tight gas sandstones, argillite or shale, permeability has been proven to be strongly sensitive to loading. For salt rocks, permeability measurements under hydrostatic loading generally reveal a strong decrease of the later [38, 80] and combined ultrasonic wave velocities measurements can link its variations with cracks closure (see Fig.2.9). The results illustrate that the flow (mostly) occurred through cracks or grain boundaries [82]. Significant effect of hydrostatic pressure on permeability are also demonstrated in [64]. However, the concept of ‘compression threshold pressure’ is brought to explain that permeability changes exhibit a flat trend when confining pressure exceeds this compression threshold value. The details about salt permeability variation and evolution under deviatoric loading will be described in §2.3.

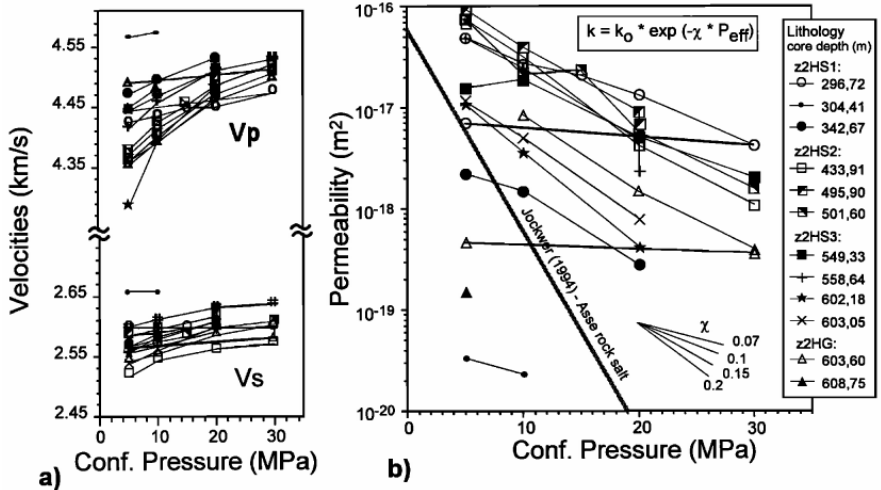


Fig.2.9 Property changes in the rock salt samples during hydrostatic compaction: (a) V_p and V_s v.s. pressure; (b) permeability (k) v.s. pressure. Various slopes of χ are given for comparison, assuming a logarithmic relation between permeability (k) and hydrostatic pressure (P_{eff}) [85]

The elasto-viscoplastic property of salt rock makes it exhibit a strong creeping behavior. During the past several decades, time-dependent behavior on salt has been revealed through many experiments, which led to the establishment of constitutive and computational models [21, 64, 83–86]. A clear time-dependent decrease in permeability of salt rocks can be observed with different gas types (like H₂, CH₄ and N₂) during experimental investigations [68]. The permeability related to hydrogen decreases by two orders of magnitude over a measuring time of about 30 days at P_c=20MPa. The decrease rate of permeability is clearly dependant on the confining pressure (see Fig.2.10), which reveals its crucial role on time dependent permeability [14, 87]. This time dependent behavior also occurs for brine permeability. Several orders of magnitude reduction in brine permeability of hollow spherical samples were observed for several days under quasi-isotropic compressive stresses of 16 MPa to 18 MPa [88]. Understanding time effect on permeability and its reduction may help to predict the time required to reach an impermeable state under the field conditions.

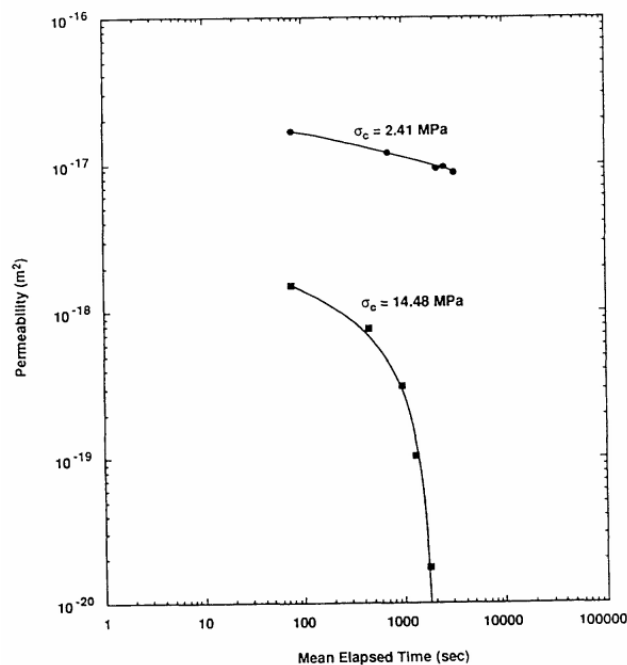


Fig.2.10 Permeability v.s. time data from tests with 2.4 and 14.5MPa hydrostatic stress [14]

2.2. Stress couplings (poromechanical properties) of salt rock

The mechanical behavior of rock salt has been investigated in numerous studies during recent decades [7, 89]. During the excavation of underground storage in salt rocks, changes in external or total stresses will induce pore fluid pressure, which may interact with the mechanical response of this medium. In view of the application of gas storage in salt caverns, it is of great interest to observe if some couplings between pore pressure and rock strains are present. For a linear porous medium, such an interaction (or coupling) between fluid pressure and elastic deformation is known as poroelasticity. Poroelastic analyses of the WIPP to date have considered only the fluid flow induced by the total stress changes [87]. Until now, little is known about the effect of an internal fluid pressure on the mechanical behavior

of salt rocks, especially very few experimental data are available for this coupling. This absence of data can be mainly explained by the great difficulty to perform these kinds of experiments on a very low permeable (and with a very small porosity) rocks. The fluid choice to carry out poro-mechanical tests is also of crucial importance as they need to assess the complete fluid saturation and the homogeneity of pore pressure. Both are very difficult to control in a quasi-impermeable media. It is why, gas was chosen as the saturated fluid to simultaneously measure the rock permeability and the potential occurrence of coupling effects. This will be presented in the following.

In the context of the poro-mechanical approach, a porous material is often assumed to be composed of two parts: the solid matrix which is made up of a solid matrix (solid grain and unconnected pores) and the connected porous network [45, 90] (see Fig.2.2). When associated, the rock matrix and the porous space composed what is called ‘the skeleton’.

The effective stress concept was proposed by [91]. This classic theory is still widely used in soil and sand mechanics. Terzaghi assumed that the solid matrix (grains) of the material is incompressible when compared with the skeleton deformability. When the pore pressure is uniform, the relationship for mean effective stress is defined by [92]:

$$\sigma_{eff} = \sigma - P_i \quad (2.4)$$

where σ_{eff} is the effective stress applied on the porous material; σ is the mean stress, which is very often the total hydrostatic pressure; P_i is pore pressure.

For an elastic isotropic porous medium, the effective mean stress σ_{eff} is calculated as follows:

$$\sigma_{eff} = \sigma - bP_i \quad (2.5)$$

where b is known as the Biot’s coefficient of the material. In the case of a compressible matrix (sometimes comparable to the skeleton compressibility), Biot 1941 [93] had generalized Terzaghi’s concept of effective stress and introduced the ‘famous’ Biot’s coefficient ‘ b ’ to evaluate this stress. Obviously the calculation (and/or the use) of such an effective stress is linked to the presence of coupling effects between pore pressure and skeleton strains. If there is no coupling then the concept of effective stress is useless. It is generally said that the elastic material strains are due to the effective stresses. Generally the Biot theory relates to the strain ϵ of a porous medium due to changes in both the applied stress σ and the pore pressure P_i [94].

In recent years, numerous experimental studies concerning the Biot’s coefficient of different porous media, including mortar [95], concrete [96], sandstones [97, 98], shales [99, 100] etc, have been carried out. They are especially useful for the petroleum industry for example. All these calculated Biot’s coefficients reveal that for these porous mediums, deformation is not only governed by the deformation of the solid phases, but also by changes in porosity [45]. In other words, an internal fluid pressure can

affect rock skeleton deformation. Compared with rock salt, these materials have usually a higher permeability or porosity. Hence it is generally 'relatively easy' to study their poromechanical properties.

There are very few available researches in the literature on the coupling effect between the internal fluid and the skeleton of rock salt. In the very early period, even the concept of effective stress is generally supposed to be not suitable for rock salt due to its extremely low porosity. Detournay et Cheng (1988) [101] got the conclusion that there is almost no deformation of salt rock due to pore pressure, when it's porosity is ultra-low or even 0 (e.g. rock salt with a porosity of less than 1% [87]). However, the effective stress concept may need to be taken into account in the DRZ as the rock salt compressibility is increased due to microcrack occurrence in the DRZ [102]. This kind of phenomenon can also be observed on mortar samples with microcracks created by thermal treatment [95] or drying etc. Mortars heat-treated up to 200 °C and over are significantly more compressible than the intact ones, which can be linked to the increasing microcrack amount at higher heat treatment temperature. Therefore, the decrease in bulk modulus K_b due to thermal damage, to some extent, contributes to the observed increase in Biot's coefficient. The effect of cracks on the coupling can be proved from the reverse side [97] in another study on the cracked sandstone samples. On the opposite, Biot's coefficient decreases with the increase in confining pressure that can be attributed to the closure of microcracks, which as a consequence leads to a K_b increase.

Although low permeability in intact or natural rock salt induces a weak fluid (liquid or gas) flow through it, the fluid can go through new generated cracks due to the occurrence of some damage. Therefore, the presence of fluid in the crack network may affect the behavior of damaged rock salt. In order to investigate this effect on the behavior of dilatant salt rock, two triaxial tests were conducted on the samples subjected to pore pressures of 1 and 2MPa [103]. The results show that for the sample under higher pore pressure, there is an early stage development of dilatancy coming along with a higher value of volumetric strain. The question is now raised as to whether the concept of effective stress applies to describe the influence of pore pressure on dilatancy. On another point of view, it is consistent to suppose that for intact material Biot's coefficient should be null or very low but that it is likely to increase as the damage is evolving (increasing one).

To sum up our present knowledge, the coupling effects between the internal fluid and skeleton were rarely investigated in salt rocks even if such a coupling is likely to occur in the vicinity of dilatancy or disturbed rock zone. This deserves to be explored. As the main question, still under debate, is to identify (or not) whether some coupling effects can modify salt behavior, a large part of this thesis will be devoted to answering this question. A significant numbers of strain measurements due to internal fluid pressure will then be used to detect the existence of a poromechanical coupling. Without having the pretension to carry out a complete poro-mechanical study, brought evidences that there is coupling in salt (i.e. the variations of volumetric strains due to P_i) would be a great step. This could mean that an

estimation of Biot's coefficient can be given (the details of calculation are presented in §3.2.5). As cracks are suspected to lead to significant coupling effects, the characterization of coupling on cracked sample due to deviatoric loading deserves particular investigation. Hence as it is 'a priori' supposed that coupling may occur thanks crack networks, its intensity (i.e. more or less strains due to P_i) under increasing hydrostatic loading is also another interesting research direction.

2.3. Permeability changes in DRZ and sealing/healing properties of salt rock

As mentioned before, low permeability of salt and its remarkable feature of potential self-healing due to its ductile rheological properties [36], make rock salt suitable for underground storage such as compressed air, hydrogen, natural gas and/or nuclear waste. However, even very low permeability may increase due to the occurrence of damage. This can result from cavern construction (i.e. excavation) or internal fluid pressure (i.e. this pressure is applied to the cavern wall) that will lead to tensile orthoradial stresses. The concept of a DRZ around the shafts, underground rooms or adjacent to the excavations [104] has therefore been introduced. The mechanical and fluid transport properties of salt rock may change in this zone. Especially there is a possibility of an increase in permeability due to the generation of microcracking and a potential degradation of the sealing performance. The characterization of such DRZ is complex as the redistribution of the in situ stresses and the reorganization of internal crystal structures are difficult to identify. However they may occur around the excavation or during the healing process after excavation [105]. As the main concern is related to the sealing ability of the underground storage, a large part of researches has been conducted on the transport behavior of salt in the DRZ. In addition, the self-sealing ability of salt must be taken into account. This ability comes from different physical mechanisms like plastic flow and diffusive mass transfer [106]. The existence of healing or sealing around the salt cavern wall can also play an important role in the seal design of the salt cavern and the evaluation of mechanical stability during storage phase. In §2.3.1 and 2.3.2, we will introduce the investigations on these two characteristics (damage and healing/sealing properties) of rock salt in literature.

2.3.1. Permeability changes with axial stress in the DRZ

Some authors have performed tests about the development of salt permeability variations with the distance from excavation zone. Gas and brine permeability measurements were conducted in the DRZ around the intake well (AIS) of WIPP [42]. The results showed that they decreased as the distance from excavation zone increases and could reach an order of magnitude of 10^{-22} - 10^{-23} m² within the radial distance of 3m away from the well wall (see Fig.2.11). The similar variation of gas permeability with the distance from excavation was also found by Peach [13] for another facility (the Asse facility in Germany). Both simulated and measured in-situ permeability showed the influence of excavation damaged zone on fluid transport properties with a decrease with the distance away from cavern wall [19, 41].

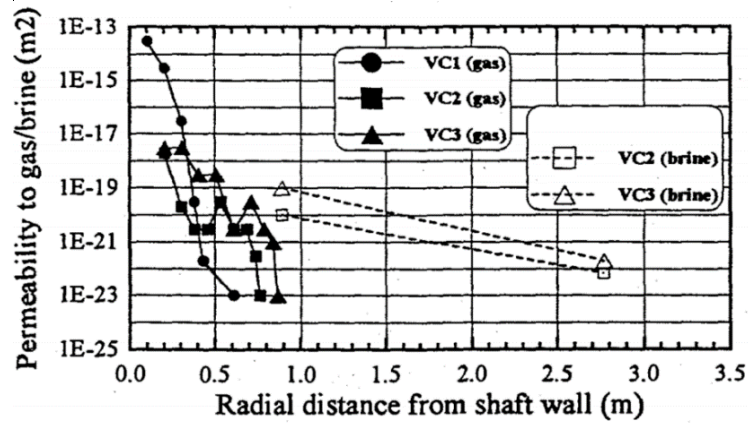


Fig.2.11 Gas- and brine-permeability results from testing conducted at the 629.4 m Horizon [42]

As high deviatoric stresses may develop in DRZ, it is very likely to produce large deformation and/or increased fluid penetration. The variation of salt permeability is generally linked to the development of dilatant deformation. For example in laboratory conditions, it was measured by [13, 107] an increase in permeability (from $<10^{-21}$ to $\sim 2 \times 10^{-16} \text{m}^2$) despite relatively small strains or induced dilatant volume change ($< 0.2\%$) under 5MPa confining pressure.

Prior to the investigation of permeability changes in relation with rock dilatancy, it seems necessary to have a general understanding of its mechanical behavior under deviatoric loading. Some authors gave the stress-strain relationship in triaxial test and an analysis from the perspective of microcrack and damage development, in order to determine the dilatancy boundary [23, 103, 108, 109]. Typical responses of salt rocks observed in short-term strength tests are shown in Fig.2.12.

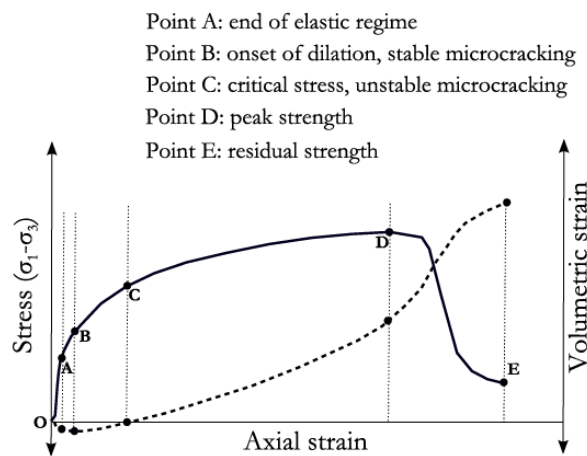


Fig.2.12 Typical responses observed in short-term strength tests; stress vs. strain (solid line) and volumetric strain vs. axial strain (dashed line) [23]

In first stage (point O-A), an initial non-linear stress-strain relationship is mainly attributed to the closure of artificial cracks created during the coring. Then a classic elastic behavior takes place. The Young modulus of samples coming from different sites are obviously different. It is due to the different halite content, or impurity content. For Asse rock salt, the elasticity modulus is 8.5GPa [103]. In the

second stage (point **A-B**), the volumetric strain is still decreasing. This means that the sample is in compaction state. The next step (point **B-C**) is characterized by the beginning of volumetric strain growing. This is generally defined as the onset of dilatancy. Point **B** (i.e. the minimum volumetric strain during whole compression test) is usually called ‘turning point’ from compaction to dilatancy or the compaction-dilatancy (C/D) boundary, indicating a microcrack initiation. At the same time, the initiation of damage occurs due to microcracks occurrence and propagation. The increasing volumetric strain counteracts the previous stage of compaction. Point **C** corresponds to the stress where the volume change is zero, named the critical stress for the dilatancy [109]. At the fourth stage (point **C-D**), the rock exhibits visco-plastic behavior. The continuous increase in axial and volumetric strain indicates the development of microcracks and damage, which is generally considered as irreversible. The peak axial stress is reached at point **D**. Generally, the sample trends to exhibit more ductile-plastic deformation as the minimum principal stress increases [108]. Hence, in view of the close connection between permeability and deformation of rock salt, the influence of minimum principal stress on permeability variations cannot be ignored during conventional compression test. After the peak stress, the last stage is reached until the residual stress at point **E**.

Since understanding the permeability development related to damage or dilatancy is of great significance, some authors have focused on this association with other methods, like acoustic emission (AE is defined as a transient elastic wave generated by the rapid release of energy within the material), ultrasonic technology [38, 107]. A schematic diagram (shown in Fig 2.13) is given in [8] to briefly summarize the changes in volume, permeability, acoustic emission and ultrasonic velocity of rock salt under mechanic loading. Combined with longitudinal P-wave and transverse S-wave velocity measurements, permeability can be (theoretically) linked to the microcracking evolution during loading [110]. An increase in permeability is in fact observed in parallel to the damage caused by the generated microcracks during dilatancy.

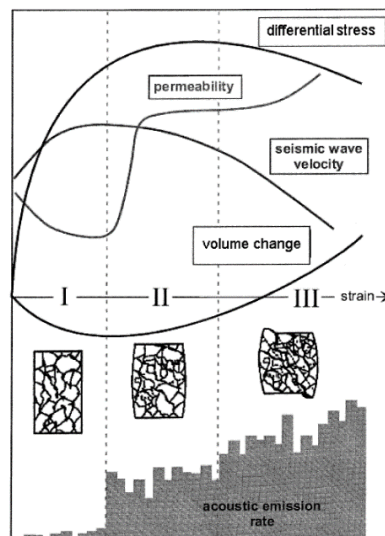


Fig2.13 schematics illustrating changes of physical properties during deformation. Volume change, acoustic emission, permeability, and ultrasonic wave velocity can all be used to monitor dilatancy [8]

AE measurements were performed with the measurements of pore volume (Based on the assumption that the salt matrix is incompressible, the volume change of the sample, measured with the micro-liter pump, was used to calculate porosity changes) and gas permeability changes. During the permeability-dilatancy experimental research on Asse rock salt. Fig.2.14 presents their variations during the compression test. The development of permeability and dilatancy are consistent with the above researches. It should be underlined in Fig.2.14 that a stage of stable permeability is observed at the end of dilatant deformation [19]. Alkan et al [103] defined the dilatancy boundary from the maximum compression on a stress-strain curve during triaxial compression tests, which has a good consistency with the record of variations in acoustic emission.

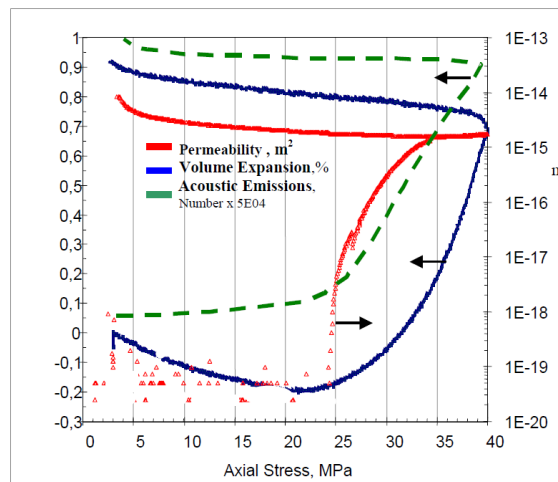


Fig.2.14 Typical compression test of poro-permeability dilatancy with Asse rock salt sample AT3-011, $\sigma_3=3\text{MPa}$, axial stress loading rate = 0.4 MPa/min [19]

Besides, it has been proved by the experimental results of [8, 19, 103] that the minimum principal stress (confining pressure generally) has a significant effect on the extent of increased permeability and damage induced during triaxial tests of porous materials. This is often true for many rocks and cementitious materials. However some unexpected phenomena can be sometimes observed (on a mudstone) [111]: under a confining pressure of 11MPa (this is a fairly high confining pressure, equivalent to a lithological pressure of about 467 m depth), there was no significant increase in permeability even if the sample was fractured at 28 MPa of axial stress. Similar results for bedded salt rocks have been presented in the study of [112]. A series of triaxial tests on different lithotypes of bedded salt rock samples were conducted under confining pressure of 20MPa. Permeability did not increase but on the contrary decreased with the increase in deviatoric stress. This was observed for all the samples for which no obvious dilatancy was recorded, even up to very high differential stress of 55 MPa. On the other hand, such results can also prove that the confining pressure of 20MPa is high enough to avoid the dilatancy even under a high deviatoric loading. Such a phenomenon is positive for the potential sealing of the cavern. Another series of tests was carried out on natural (Asse) rock salt at 150°C under 4 different confining pressures (3, 6.5, 10, 30MPa), in order to provide some systematic investigation of

the effect of P_c on the dilatancy (see Fig.2.15). The results confirm that dilatation is prevented at high confining pressures [113]. But these tests were conducted at quite high temperature. This could have a complementary effect to the hydrostatic pressure effect.

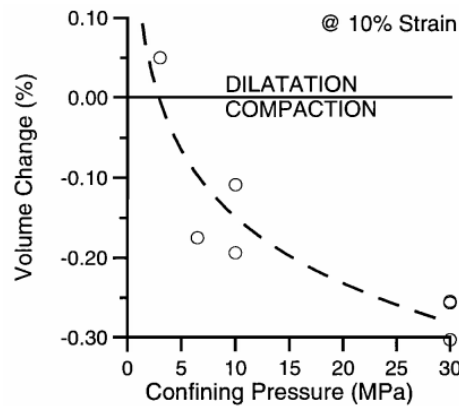


Fig.2.15 Sample volume change v.s. confining pressure plotted at 10% axial strain for all samples. Note the transition from net dilatation at 3 MPa pressure to increasing compaction at pressures of 6.5 MPa and above [113]

2.3.2. Sealing-healing properties

Some authors have revealed that the fluid pathway through salt is cracks or grain boundaries, rather than through crystals [82]. Most cracks are basically closed in the rock salt formations, which is why the undisturbed rock is usually impermeable in ‘in situ’ conditions. As mentioned in the previous section, an increase in salt permeability and damage may occur due to the dilatancy near the excavation zone. However after excavation, the high deviatoric stress will gradually decrease with creep, and a new stress distribution will be established with time during the storage phase [105]. The creep deformation can result in closure of discontinuities due to salt rheological properties [114]. Therefore, re-compaction is very likely to occur and permeability would gradually reduce. This is a kind of self-sealing property, which provides potential guarantee for the safety of underground storage in rock salt [115]. Hence, estimating and observing/monitoring the generation, development and closure of cracks in salt is critical for this context. The crack-sealing or crack-closure of salt can directly induce a reduction in permeability, while, on the contrary, the crack generation can bring an increase. Permeability measurements have been performed in many researches as an experimental analysis method to evaluate the cracks development in rock salt (as well as in many other porous materials).

As shown in Fig.2.16 three different mechanisms for crack sealing are proposed in [36, 106]. The first one (Fig. 2.16 (A)) is a mechanical closure of cracks, which can induce a decrease in permeability in the early stages of healing. This mechanism is mainly due to compaction of the bulk rock leading to elasto-plastic (i.e. not reversible) deformation [12, 116]. The second (Fig. 2.16 (B)) is crack healing by surface-energy-driven processes [36], i.e. fluid-assisted diffusion of transported crystalline media through water films adsorbed on the solid surface or filling the cracks [106, 117]. Actually, this diffusive

mechanism contain chemical processes (dissolution, diffusion and precipitation): salt is dissolved under high stress, transported through brine along grain boundaries and re-precipitated at pore walls under lower stress [105, 106, 118]. Transport of material may be more effective with brine-saturated salt, since this allows the occurrence of chemical process. As a result, not only the permeability decreases, but the strength is also restored by this mechanism [36]. This is known as being a healing process. This mechanism deserves more attention for the long-term behavior of rock salt. The last mechanism (Fig. 2.16 (C)), crack healing by recrystallization, relates to the migration of pre-existing grain boundaries, leading to a new microstructure in salt [113, 119, 120]. This healing process is expected to occur at high temperature or with the presence of fluid film at the boundary.

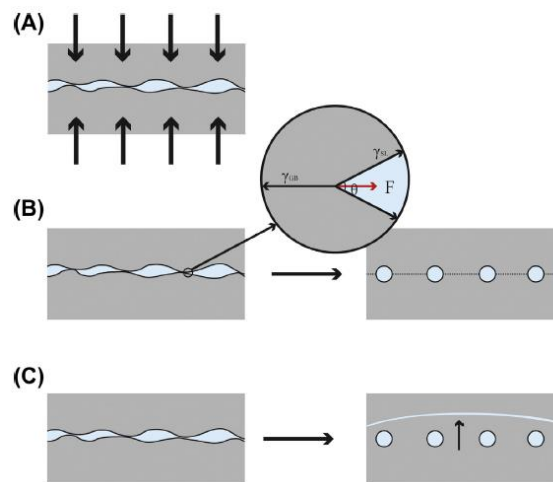


Fig 2.16 Physical mechanisms by which crack healing/sealing and permeability reduction can occur in the EDZ in rock salt. (A) Mechanical closure of cracks in association with compaction of the bulk rock by elastic deformation or plastic flow. (B) Necking down (occlusion) of cracks and pores to form arrays of disconnected tubular and spherical inclusions, by means of surface-energy-driven, diffusive mass transport facilitated by adsorbed water films or free pore brine. (C) Crack and pore occlusion through fluid assisted grain boundary migration (recrystallization) [36, 106].

As the purpose of this experimental study is to investigate the self-sealing capacity on ‘dry’ salt rock samples i.e. with almost no brine and at room temperature, it will mainly focus on mechanical effects toward permeability changes.

Since it is critical to understand self-sealing development in the RDZ to assess the long-term barrier function of salt, investigating the transport properties and their evolutions with time, and stress is of great importance. Crack sealing experiments coming along with permeability measurements have also been investigated on some other geological materials. For argillite, the significant self-sealing properties related to permeability under hydrostatic stress has been reported [121, 122]. In this case, liquid water is needed to ensure sealing.

The healing properties of salt rocks are still under debate and require complementary developments of experimental and modelling research.

Several experimental studies [123, 124] were carried out, with combined ultrasonic wave velocity and volumetric strain measurements as being damage indicators. The details of the overall experimental process and results are presented in [123]. In order to pre-damage samples, triaxial test was conducted under 0.5 MPa confining pressure until axial strain up to 1.5% with a constant strain-rate. The damaged samples were then healed under confining pressure of 15MPa at different recovery temperature 25°C, 46°C, and 70°C. The results showed that damage could be partially healed under hydrostatic compression. This was evaluated with volumetric strains and compressional wave characteristics which were close to the values of the undamaged state. The damage recovery process was faster at higher temperatures. However, the recovery tests were performed at 15MPa hydrostatic stress, which did not allow to study the influence of different loadings.

The self-healing capacity of rock salt damage was investigated under different experimental conditions (with different initial damage, temperature, humidity), combined with the ultrasonic technology to estimate damage recovery [120]. A rapid recovery of damage in the first 200h is observed, then followed by a phase of gradual stabilization. Water in rock salt plays a key role in the effect of temperature on damage recovery: temperature has an inhibitory effect when water evaporates, while an accelerated effect is recorded with liquid water present in the rock.

Another experimental assessment of healing of fractures in rock salt was conducted by [125]. The healing of three different fracture types formed by Brazilian tension test, saw-cut surfaces and polished surfaces was investigated under uniaxial and radial load. The results indicated that the origin of fracture has significant impact on the healing effectiveness. Both pressure and time are important factors for the healing of salt fractures. In addition, the closure of salt fractures is related to visco-plastic deformation on both sides of fracture, while the healing involves the mechanical bonding between the two surfaces.

In a recent MSc thesis [115], time-lapse X-ray tomography were used to investigate the micro-cracking evolution and healing of compacted (i.e. cracked) salt aggregates in the presence of brine with time. The reduction in crack size observed with comparisons between successive scans of the same samples demonstrated the development of healing over time. Grain boundary migration and grain recrystallization occurred during the healing process.

Caverns are expected to be submitted to re-pressurization by the surrounding salt, which leads to the closure of void spaces in the DRZ. To evaluate the seal design and its performance, it is necessary to be able to identify the behavior of the DRZ coupled with the sealing kinetics of the re-pressurized fractures initially formed [123].

The development of salt rock healing modelling will be presented as below. In order to simulate healing behavior of damaged intact WIPP salt, a constitutive model was incorporated with a healing term under hydrostatic pressure [116, 126]. Since the permeability changes with damage had not been identified, this new model cannot predict salt permeability. Hunsche U and Hampel A [7] described the

mechanical properties considering different mechanical effects (dilatancy, damage, healing, failure and deformation) by an elasto-viscoplastic constitutive equation. However, the relationship between dilatancy/healing and permeability has not been particularly established.

Chan KS et al [12] proposed the Multi mechanism Deformation Coupled Fracture (MDCF) model, incorporated with the functional relationship between permeability and damage. The calculations of this model showed a great agreement with experimental data from WIPP salt. Moreover, this model can predict salt laboratory behavior subjected to either damaging or healing condition.

Combining thermodynamic equations, a microphysical model for the healing of single crack in salt rock was proposed by [36] to predict healing in halite. It was revealed that a fluid-filled crack healing was mainly controlled by diffusion of adsorbed water films or brine. In addition, this model could also give an estimation of healing times: at laboratory humidity level cracks healing or disconnection is suspected to occur in several years, while under very dry conditions the healing time will be longer due to the thin adsorbed aqueous films.

Based on the proposed thermo-mechanical model [127], Zhu et Arson [128] presented the continuum Damage Mechanics model coupling damage and healing. It was assumed in the modelling that healing is mainly controlled by Diffusive Mass Transfer (DMT). It was demonstrated that the increase in temperature could promote healing processes. The results also showed that permeability variations was mainly dominated by crack connectivity.

Consequently, the direct estimation for the healing/sealing behavior of cracked salt from the experimental perspective is nevertheless rare. It is necessary to explore the healing/sealing effects on permeability and on compressibility properties, which is a very difficult task.

2.4. Microstructure observation in damaged and healed salt rocks

Since the permeability changes are strongly related to the connected porosity and microcracking, tensile cracks or grain boundaries sliding can cause an increase in permeability when exceeding the dilatancy boundary [8, 14]. Studying salt rock microstructures can help verify/identify damage and healing mechanisms, and characterize microcracks propagation (closure or generation, i.e. the development of potential pathways for fluid transfer). Compared with the electron microscopy techniques, such as Scanning Electron Microscopy (SEM), X-ray microtomography can give a direct observation of internal microstructure. As a non-destructive imaging technique, it is widely used in microscopic analysis of geotechnical material [129–132]. This technology also allows to accurately quantify and visualize porosity structure. In addition, the variation of internal structure of the sample during the compression test, impossible to observe before, is now accessible by the in situ x-ray microtomography technique to characterize the microstructure evolution of geomaterials under mechanical loads [54, 133]. There is however some limitations with this technics that are due to the

device resolution i.e. the sizes of observable pores and cracks. For example, the LaMcube X-Ray microtomography gives a resolution of 40 μm if large samples (centimetric size) have to be tested. This means that very small pores and/or cracks can not be observed. This is an important current limitation of this kind of technics.

In any case, X-ray microtomography studies on the microscopic investigation of salt rock are few. The pore space have been characterized and quantified based on the CT scanning [134, 135]. Thiemeyer [48, 51, 134] revealed the deformation mechanism of salt rock from the microscopic images obtained by X-ray tomography. The significant confining pressure effect on microscopic damage of salt during triaxial tests was revealed by [136], using CT scanning technique. Both the quantity of cracks and porosity decreased with the increasing confining pressure. The healing of compacted salt aggregates in brine over time was investigated using X-ray tomography [115]. The reduction in crack size could be observed from the comparisons between scans of the same sample at different days. X-ray synchrotron microtomography method with the resolution of 4.92 and 0.7 μm was used on (very small) compacted samples (in saturated solution) [54]. This technique allowed to incrementally monitor changes of the matrix and pore space in halite aggregates. It was revealed that halite grain contact changes could result in decreasing permeability due to grain indentation and pore connectivity reduction by precipitation of dissolved salt on free surfaces of pore throats (see Fig.2.17).

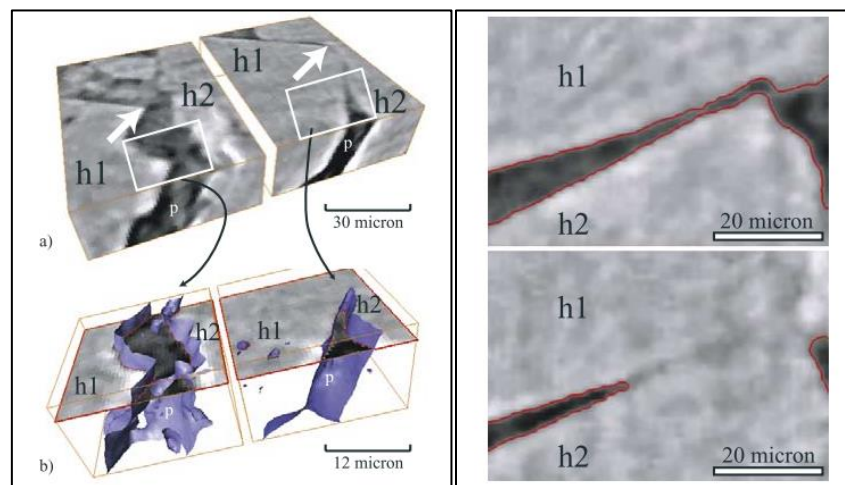


Fig.2.17 Left figure: a) Two grains of halite before (left, initial aggregate) and after (right, 11% deformation) indentation by pressure solution. The arrows indicate the indentation of grain h1 into grain h2. The pore space (p) appears darker. b) Extraction of the pore surface on two subvolumes showing that the grain contact has disappeared and contact healing has occurred. Right figure: Two grains of halite (h1 and h2) before (top) and after (bottom) pressure solution. The pore throat between the two grains has closed by precipitation on the free surface, without any relative displacement or indentation between the two grains [54].

In our study, the damage due to deviatoric stress and sealing mechanism under isotropic stress will be systematically investigated from not only laboratorial experiments but also with microscopic images based on the X-ray microtomography. Visualization and quantification of the pores space or cracks propagation after different mechanical tests (hydrostatic, triaxial and uniaxial tests) will also be achieved.

3. Part I: preliminary study of fluid transfer and poromechanical properties of salt rock under hydrostatic loading

3.1.Introduction

This chapter mainly focuses on the experimental study of salt rock under hydrostatic loading. The material used in this study and the sample preparation are first described. The experimental techniques for all the different tests, such as brine and gas permeability tests, porosity tests, and poromechanical tests, are then presented. Two methods used for gas permeability testing are described: pulse decay pressure method and steady state flow method. The basic theory of poroelasticity (Biot's theory) is also introduced in detail.

The experimental study in this part is dedicated to the measurements of the main characteristics of salt rock: the (gas and brine) permeability under confinement and preliminary characterizations of poromechanical behavior. Hydrostatic compression tests were performed to investigate isotropic stress (load-unload) and fluid pressure (or Terzaghi effective pressure) influences on permeability and porosity. The poromechanical behavior is preliminary characterized under different confinement levels for different samples. Since rock salt is an elasto-viscoplastic rock, the time-dependent effects on permeability were also investigated. The comparative permeability tests (hydrogen v.s. argon) are performed for samples from different cores (or different sites). Thus, the results allow comparing the permeability of the two gases. Moreover, the low permeability of salt makes it necessary to explore Klinkenberg effects.

3.2.Experimental techniques

3.2.1. Material used for the experiments

The salt rock cores, shown in Fig.3.1, come from a cenozoic sedimentary basin located in three different sites of France (XR02 from Southern France, XS01 from Eastern France, XZ24/XZ25 from Southeastern France), about 1000 to 1500m depths from ground. Sample preparation was the first difficult task as salt rocks cannot be cored with water that dissolves the material. Air coring had been unsuccessful (cutting tool generates particles, that agglomerate and do not allow further cutting) and it was neither possible to core with a hydrocarbon fluid in our laboratory.

It was finally chosen a coring with saturated brine by modifying the water supply circuit of our corer. This was successful and cores could be obtained close to the required diameter of 65mm to match with our experimental cells. As it is shown in Fig.3.1, the salts used are composed of large crystals (centimetric size), which lead to a heterogeneous material. Different gauge sizes were hence tested and this surprisingly showed that the strain results were not significantly influenced by gauge size. For practical reasons, the best choice revealed to be the use of crossed gauges of 20mm length (Fig.3.1 (d)).

Two sets of gauges were glued at diametrically opposed positions on the cylindrical surface of the specimen. Before gluing gauges a thin layer of fast-cured epoxy was applied to the sample to smooth its rough surface and then polished. A thin layer of silicone sealant was then applied on the sample surface to protect the gauges. The sample was then sealed by a rubber membrane and placed into the cell. The experimental apparatus consisting of a confining cell, which can reach confining pressures P_c as high as 100 MPa, together with a gas injection device, are shown in Fig.3.3 (a). The confining pressure was controlled by a Gilson pump. The gas used in this experiment is 99%-pure Argon (or sometimes hydrogen) and the value of gas pressure is continuously recorded using a LabView system.

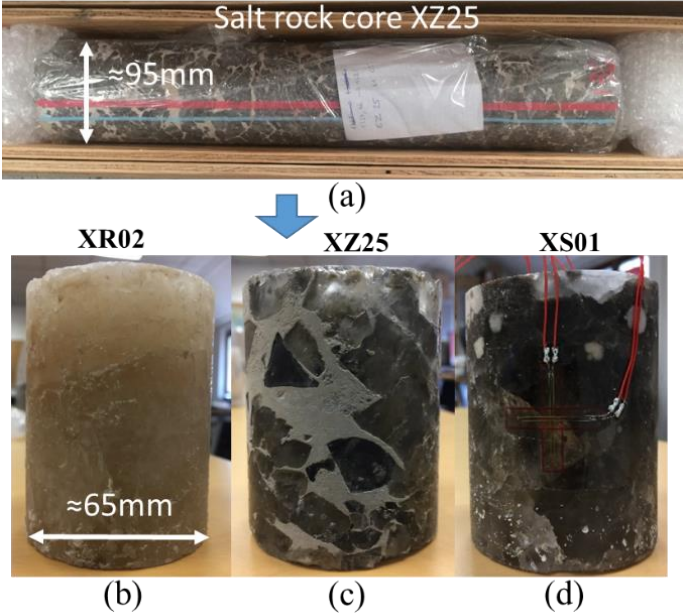


Fig.3.1 Salt rock core and samples (with gauges)

Table 3.1 Description and experiment schedule of salt rock samples

Salt sample	Height (mm)	Diameter (mm)	Weight (g)	Test	Time
XS01-2	63.29	64.50	446.75	Brine permeability	16/01/2018 - 27/02/2018
XZ24-1	61.10	63.80	425.42	Test 1 (pulse permeability + porosity)	25/06/2018 - 02/07/2018
				Test 2 (pulse permeability)	05/07/2018 - 20/07/2018
XZ24-2	52.03	64.43	356.93	Test 1 (pulse permeability + porosity)	28/09/2018 - 26/10/2018
				Test 2 (pulse permeability)-unloading	19/11/2018 - 05/12/2018
				Hydrogen and argon permeability test	07/11/2018 - 19/11/2018
XZ25-3	81.80	64.59	594.49	Hydrogen and argon permeability test	11/02/2019 - 19/02/2019
XS01-3	81.04	64.28	579.43	Hydrogen and argon permeability test	13/05/2019 - 16/05/2019
XS01-4	83.51	64.53	589.15	Porosity (time effect)	16/10/2019 - 04/11/2019
XR02-4	82.81	64.77	587.00	Porosity (time effect)	05/11/2019 - 20/11/2019
XZ25-4	80.06	64.94	572.39	Porosity (time effect)+Klinkenberg effect	27/11/2019 - 11/12/2019
XS01-5	76.41	64.94	558.38	Klinkenberg effect+ Porosity (time effect)	09/01/2020 - 04/02/2020
XS01-1	63.44	64.86	449.18	Poro-mechanical test1(Biot)	23/10/2017 - 27/10/2017
				Poro-mechanical test2(Biot)	14/03/2018 - 06/04/2018
XS01-2	63.29	64.50	446.75	Poro-mechanical test (Biot)	29/11/2017 - 08/12/2017
XZ24-1	61.10	63.80	425.42	Test 1 (Biot)	25/06/2018 - 02/07/2018
				Test 2 (Biot)	05/07/2018 - 20/07/2018

3.2.2. Experimental method for brine permeability

Concerning brine, as the flow rate is very low, an Isco type pump with a resolution of less than one nanoliter is used for brine permeability measurements. To avoid damaging the pump, as shown in Fig.3.2, a buffer tank of 300mL filled with saturated brine is placed between the pump and the cell. The supply pipes reaching the sample were also filled with brine. Thus the liquid entering the material is saturated and does not dissolve the material. The injected volumes are directly followed by a LabView type acquisition connected to the pump.

Considering brine, permeability K_{brine} is estimated by Darcy's law :

$$K_{brine} = \frac{\mu Q}{A} \frac{L}{(P_i - P_0)} \quad (3.1)$$

where μ is the brine viscosity and Q injection flow rate.

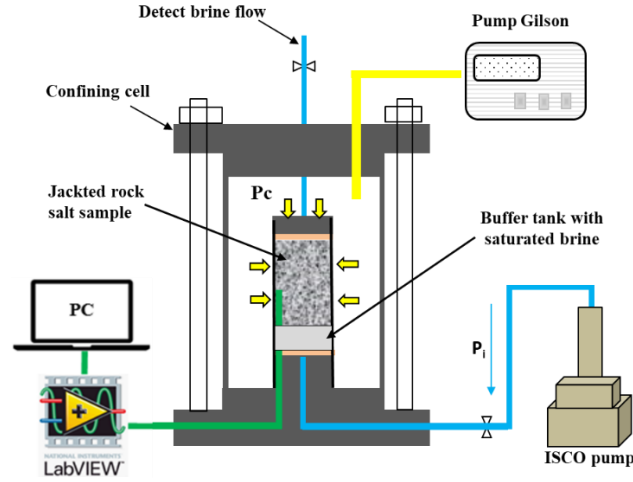


Fig.3.2: Brine permeability with confining pressure

3.2.3. Experimental method for gas permeability

3.2.3.1. Pulse-decay pressure method

For extremely low permeability materials, the transient pulse decay method is convenient instead of the steady state flow method. An initial pore gas pressure P_{i0} was applied firstly to both sides of the sample. Then, a small pressure increase ΔP_0 at one end of the sample for this initial gas pressure P_{i0} [137–140]. The advantage is undeniable here as P_{i0} can also be used as the pore fluid pressure that has been established steadily in the sample, intended to detect potential coupling effects. A small gas flow was observed due to the pressure difference between two sides of this sample. The schematic diagram of this method is shown in Fig.3.3 (b). An initial pressure difference ΔP_0 between the upper and lower surfaces of the sample is applied (at the upper one) and then slowly decreases with the flow. Walder and Nur (1986) [141] stated that the decrease in pressure difference ΔP obeys the following power function:

$$\Delta P(t) = \Delta P_0 e^{-ct} \quad (3.2)$$

$$c = \frac{A * K}{\mu * L} P_f \left(\frac{1}{V_1} + \frac{1}{V_2} \right) \quad (3.3)$$

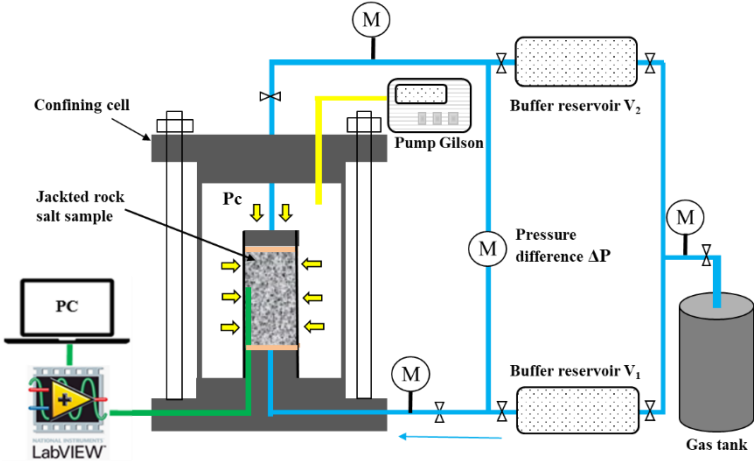
where c depends on the: permeability K , sample dimensions L (length) and A (section surface), reservoir volumes V_1 and V_2 , gas viscosity μ (2.2×10^{-5} Pa·s) for Argon at room temperature. P_f is the final equilibrium pressure, which can be calculated from

$$P_f = P_{i0} + \frac{V_1 * \Delta P}{V_1 + V_2} \quad (3.4)$$

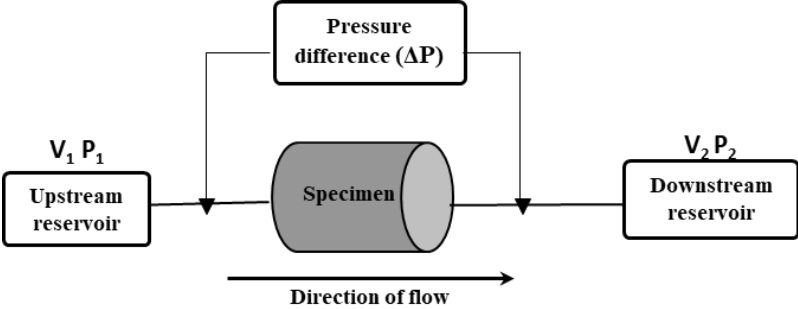
where P_{i0} is the homogeneous initial pressure. The gas permeability is obtained according to relations (3.2), (3.3) and (3.4):

$$K = \frac{c * \mu * L}{A * P_f} \left(\frac{V_1 * V_2}{V_1 + V_2} \right) \quad (3.5)$$

Note: This method (with the use of rel. (3.2), (3.3), (3.4)) is considered to be valid if ΔP is small compared to P_{i0} , generally less than 5% of P_{i0} and if the sample porosity volume is weak compared to the reservoir volumes. It will be seen in the following that the material porosity is less than 1%, the second condition is therefore easy to be fulfilled. On another end, the analysis of such a test is based on the validity of Darcy’s law. The latter is assumed despite the very low values of the gas permeability obtained. Obviously those very low values rule out the occurrence of turbulent flow. As it will be seen in the following, the gas flow is likely to occur in cracks or grain joints. The level of permeability will be therefore assumed to mainly depend on crack density and not on the flow nature through the crack. As a consequence, the assumption of a laminar flow (i.e. Darcy’s law validity) remains consistent.



(a) The experimental apparatus



(b) Schematic diagram

Fig.3.3 Transient pulse decay method

3.2.3.2. Steady state flow method

The steady-state flow method to measure the permeability of salt rock is described as below. As show in Fig.3.4, a buffer reservoir is installed between the gas tank and the salt sample. The gas was firstly injected from the upstream side. After a period of time, a steady-state gas flow is assumed through the sample at time t with a pressure P_i at the sample upstream side and P_0 at the downstream side. A pressure increase ΔP_0 (from P_0 to $P_0 + \Delta P_0$) was measured in the downstream “reservoir” during the

time variation Δt . All tests are conducted in a thermally insulated room at constant temperature. According to Darcy's law, the average volume flow rate Q_{mean} for a one-dimensional flow is:

$$Q_{mean} = -\frac{A * K_x}{\mu} \frac{dP(x)}{dx} \quad (3.6)$$

where K_x is permeability along axis x , and μ is the fluid viscosity; A is the sectional area of the sample.

Since the permeability of salt rock usually varies between several orders of magnitude, it is not easy to find the standard flowmeters in the range of flow rates and pressure used. Therefore, in our tests the variable Q_{mean} should be measured without flowmeter. According to the schematic diagram of this method, as shown in Fig.3.4 (b), a special device is designed to allow quasi-stationary test to be performed by using downstream flow rate measurements. By connecting a gas pressure manometer at the sample downside to collect gas and measuring gas pressure, the flow rate Q_{mean} can therefore be measured at the specimen outlet. This manometer and the tube at the downstream side of the sample can be regarded as a special 'reservoir' with a very small volume. It is also possible to use the upstream reservoir (upstream technics) to measure the entering flow. This technics is theoretically equivalent to the downstream one. On a practical point of view, the downstream technics is preferable as to measure the inlet flowrate, it is necessary to use a high level of gas pressure. For ultra-low permeability, the slightest leak can cause significant error or uncertainty. The downstream technics does not have this disadvantage as it allows to work at low gas pressure (atmospheric pressure), which eliminates the leak risk. The mean volume flow can be deduced from perfect gas assumption and the ideal gas law:

$$Q_{mean} = \frac{V_r \Delta P_0}{\Delta t P_m} \quad (3.7)$$

where V_r is the volume of downstream 'reservoir'; ΔP_0 is the gas pressure increase at downstream during Δt ; the gas flow is assumed stationary at an average pressure P_m the mean outlet gas pressure $P_m = (P_0 + (P_0 + \Delta P_0))/2 = P_0 + \Delta P_0/2$.

The pressure variation in the direction x is the inner gas pressure in the sample and is assumed to be a function of coordinate x and time t [142]:

$$P(x, t) = \sqrt{P(0, t)^2 \left(1 - \frac{x}{h}\right) + P(h, t)^2 \frac{x}{h}} \quad (3.8)$$

where h is the height of rock salt sample; $P(0, t) = P_i$ and $P(h, t) = P_m$. Consequently, according to the equations above, the permeability is derived from Q_{mean} measurements as shown below:

$$K = \frac{\mu Q_{mean}}{A} \frac{2hP_m}{(P_i^2 - P_m^2)} \quad (3.9)$$

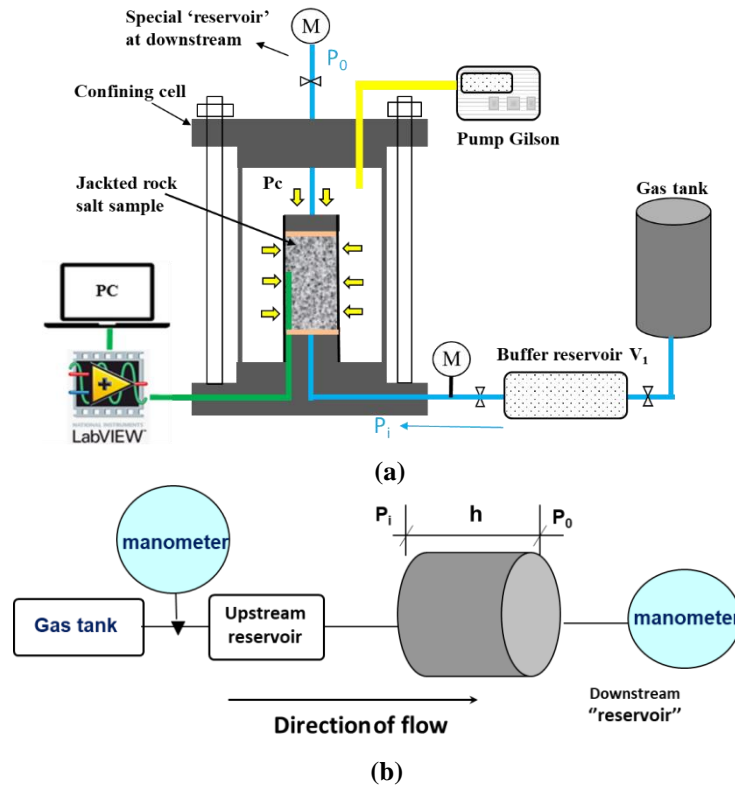


Fig.3.4 (a) The experimental apparatus (b) Schematic diagram of the steady-state flow method

Remark: It is generally asserted, for very low gas permeability measurements, that the pulse technics is more efficient than the steady state one (especially to gain time for the measure). Our point of view is less affirmative as the used of relation (3.2) (i.e. $\Delta P(t) = \Delta P_0 e^{-ct}$) derives from the hypothesis that the transient flow rate is a succession of steady flow rates: ($P(x, t)$ is given by relation (3.8)), which can be assumed if the pore volume is negligible compared to the buffer reservoir volume. Moreover, before the ΔP_0 loading, a certain time is needed to obtain a uniform value of pressure P_{i0} inside the sample. Our own experimentations have therefore often shown that the steady flow rate technics, with a very small downstream reservoir, is a better choice than the pulse technics. In the present study, the main advantage of the pulse test was the possibility to use P_{i0} as the pore pressure applied to detect potential coupling. Despite this advantage, it will be seen in the following that, after an initial use of pulse tests, it was then chosen to perform steady state technics: gain of time (thanks to the small reservoir volume) and gain in accuracy (for the same reason).

3.2.4. Experimental method for porosity

3.2.4.1. Porosity measurement with gas technology

The gas-accessible porosity test is a highly useful tool designed in our lab for studying the variations of porosity under different confinement (or loading). This test can be carried out in a confining (or triaxial) cell and allows the variations in pore volume to be measured under loading or unloading. The sample, for which pore volume is V_{pore} , is connected to the experimental set-up consisting of a buffer

reservoir and tubes having a calibrated volume V_t (Fig.3.5). The test is carried out under isothermal conditions, and, over the range of gas pressure used, the ideal gas law applied:

$$PV = nRT \quad (3.10)$$

The reservoir is set with an initial gas pressure P_{ini} . The valve (Fig.3.5) is opened and the gas pressure is continuously monitored by a LabView system until stabilization. The pressure settles to a final value P_f such as:

$$P_{ini}V_r = nRT = P_f(V_r + V_t + V_{pore}) \quad (3.11)$$

where V_r is the volume of the reservoir, V_t is the volume of different connected tubes and the dead volume of the cell. Both are carefully calibrated before the test. P_f is the final stable gas pressure value. According to relation (6), V_{pore} can be calculated and leads to the connected “gas porosity”:

$$\Phi = \frac{V_{pore}}{V_{sample}} \quad (3.12)$$

Note 1: As previously mentioned the relation (3.10) only applies under isothermal conditions. This was ensured by placing the whole device in a big climatic chamber in which the temperature was regulated at 21°C for the whole test duration (generally several weeks).

Note 2: It will be seen in the results that the porosity measured (with such a technics) is extremely low (generally less than 1%). This means that, despite all precautions taken to perform accurate measurements, the absolute porosity value should be almost used to describe general tendencies i.e. decrease or increase for example. A ‘0’ porosity value will mean that it is not measurable with the technics used.

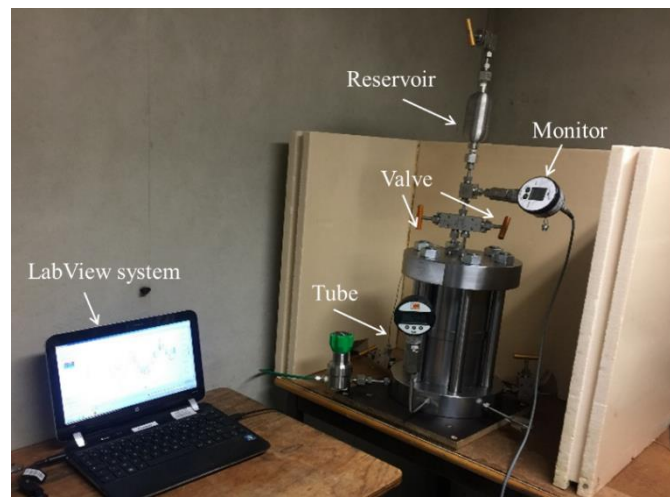


Fig.3.5 Device for the measurement of porosity

3.2.4.2. Specific surface analysis (SBET)

The gas (nitrogen) adsorption/desorption test is performed by using an ASAP 2020 (MICROMERITICS brand, see Fig.3.6) in our laboratory. This test is estimated from the quantity of nitrogen adsorbed in relation to its pressure at the boiling point of liquid nitrogen and at normal atmospheric pressure. The specific surface area (SBET) can be interpreted by the Brunauer - Emmett – Teller theory [143] which is based on multi-layer adsorption model. It can relate the volume of adsorbed molecules to the pore surface of solid. The SBET of other porous materials (concrete and mudstone) from our laboratory allow a comparison with the results of salt rock, which are presented in §3.3.3.2.



Fig.3.6 MICROMERITICS ASAP 2020

3.2.5. Experimental method for biot coefficient

Most studies of the poromechanical behavior of rocks are based on works initiated by [93] and [91] for fully-fluid saturated porous media. Both mechanical stress $\boldsymbol{\sigma}$ and internal fluid pressure P_i contribute to loading. For an elastic porous medium, the effective stress $\boldsymbol{\sigma}'$ is defined as follows, in which isotropic or orthotropic behavior is assumed:

$$\boldsymbol{\sigma} = \boldsymbol{\sigma}' - \mathbf{B}P_i \quad (3.13)$$

\mathbf{B} is known as the Biot's tensor of the material. A common expression for soil is Terzaghi's effective stress tensor $\boldsymbol{\sigma}' = \boldsymbol{\sigma} + \mathbf{1}P_i$. For materials with a compressible solid phase, Biot had generalized Terzaghi's concept leading to the use of the 2nd tensor \mathbf{B} .

The first state equation of poroelasticity can be written in the form:

$$\boldsymbol{\sigma} = \mathbb{C}_d : \boldsymbol{\varepsilon} - \mathbf{B}P_i \quad (3.14)$$

where $\boldsymbol{\varepsilon}$ is the strain tensor, \mathbb{C}_d is the drained stiffness tensor of the porous material. For a unit change of pore (respectively confining) pressure, two strain tensors are obtained:

$$\boldsymbol{\varepsilon}_1(P_c = 1) = -\mathbb{C}_d^{-1} : \boldsymbol{\delta} ; \boldsymbol{\varepsilon}_2(P_i = 1) = \mathbb{C}_d^{-1} : \mathbf{B} \quad (3.15)$$

It is therefore obvious that pore pressure coupling effects take place if ϵ_2 is not null for an increase in pore pressure. A large part of our strategy is based on the ϵ_2 measurement. Is it null or not when gas pore pressure varies?

For an isotropic material the Biot tensor $\mathbf{B} = b\mathbf{1}$, ‘b’ is known as the Biot’s coefficient and can be estimated from two tests: hydrostatic loading and pore pressure variation, which give respectively the drained bulk modulus K_b and the H modulus such as:

$$\Delta P_c = -K_b \Delta \epsilon_v \quad (3.16)$$

in which ΔP_c is a variation in confining pressure and $\Delta \epsilon_v$ the resultant volumetric strain.

$$\Delta P_i = H \Delta \epsilon_v \quad (3.17)$$

in which ΔP_i is a variation in pore pressure and $\Delta \epsilon_v$ the resultant volumetric strain. The Biot’s coefficient “b” can then be calculated by the ratio K_b/H .

In its initial version, the Biot’s theory can be applied for an elastic medium only. It is why, the Biot’s coefficient measurements, based on the use of K_b and H , need unloading step for P_c and loading step for P_i . Both of these steps lead to a decrease in effective confining pressure, which is likely supposed to result in elastic strains. The behavior of the rock salt is unlikely to be elastic and its isotropy is still to be evidenced. This second assumption is far below the scope of this study. It is however necessary to process to unloading in P_c or to pore pressure P_i increases to benefit from some elastic behavior of the material. On another hand, it must be pointed out that, as mentioned before, coupling effects have almost never been really investigated in salt (to our knowledge). The purpose of this work is to evidence that, in some cases, fluid-skeleton couplings can occur, which is the most important point. As a consequence, the Biot’s coefficient calculations, proposed in the following, will be mainly done to answer single questions: is there coupling or not? Is it “strong” or not? Hence, the calculations will be based on the evaluation of the ratio $-\Delta \epsilon_v(\Delta P_i = \Delta P_c)/\Delta \epsilon_v(\Delta P_c)$, which is equivalent to the ratio K_b/H for isotropic material. On another hand, this ratio would lead to an “apparent” Biot’s coefficient, which can mainly be used to highlight the fluid-skeleton coupling intensity.

Note: a direct experiment conducted with $P_i = P_c$ is commonly known as being the “unjacketted” compressibility test. The resulting volumetric strain is then generally assumed to be the one of the material solid phase i.e. solid matrix only and the non connected porosity that may be included inside it.

For a given value of P_c , we proceed as follows:

Step1: An initial confining pressure ($P_c = 5MPa$) is applied. Then, porosity experiment is carried out under the corresponding stress.

Step2: The same gas pressure P_i is applied on both sides of the sample, which allows the strains to be measured to evaluate (possible) coupling effects. It can then be proceeded to the transient pulse decay method (see §3.2.3.1) and to evaluate the salt permeability. When the steady state flow method is used, as described in §3.2.3.2, the gas pressure is injected from the upstream side after this step.

Step3: The confining pressure is unloaded P_c from 5MPa to 0MPa and strains are measured. Next steps are then performed at higher P_c values ($P_c = 7,10,14,18,22MPa$).

3.3. Experimental results

3.3.1. Brine permeability

As expected, the injected volumes are very low and the experiment for brine is time-consuming. The brine permeability of sample XS01-2 is $4.31E-21m^2$ under 30 bars of confining pressure and $6.46E-22m^2$ under 60 bars of confining pressure. Assuming that the material is fully saturated with brine between 30 to 40days, the brine permeability is $6.5E-22m^2$ under 6MPa confining pressure, as shown in Fig.3.8.

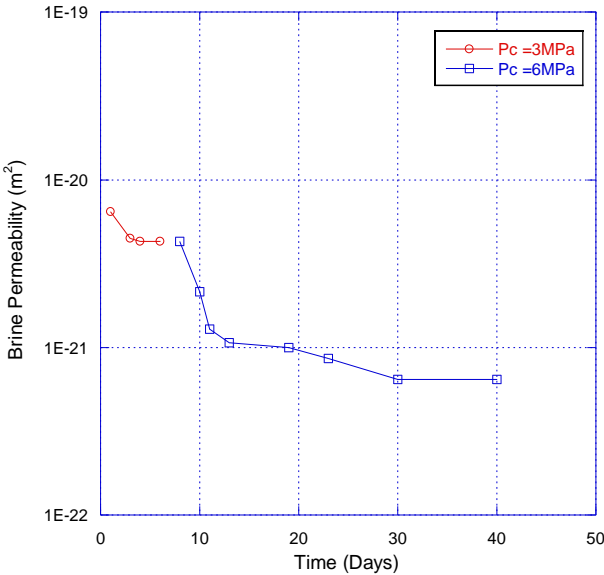


Fig.3.8 Brine permeability under two confining pressure levels

Gas permeability for salt rock is generally several orders of magnitude higher than brine permeability: this phenomenon is also observed with other porous materials such as concrete, argillite, shales [61, 62, 144, 145]. This difference for low permeable materials is generally attributed to physico-chemical effects and/or hydration of pore walls [63, 121]. Considering this possible interaction between salt and brine, and long time consumption of brine permeability test, in the following experimental studies, we will mainly devote to the gas instead of brine permeability measurements. Another advantage of gas permeability is its high level of sensitivity to change in confining pressure, which means that this property is a better tool to evaluate cracking. In parallel gas pressure is also used to perform poro-

mechanical experiments as it is almost not possible to consider water for this purpose (permeability to brine and porosity are too low) and it would never be really possible to assess complete saturation level of the sample.

3.3.2. Confining pressure and Terzaghi effective pressure effects on gas permeability

A series of hydrostatic tests were performed for two samples (XZ24-1 and XZ24-2) to investigate isotropic stress (load-unload) and fluid pressure (or Terzaghi effective pressure) influences on permeability. These two samples were extracted from the same plug XZ24. For each sample, two tests (test 1 and test 2) were carried out. For test 1 on sample XZ24-1, gas permeability were detected at different confinements (P_c up to 14MPa), and different gas pore pressures were applied at each confinement to record permeability. It is the same experimental schedule for test 2 on sample XZ24-1, except P_c was increased until 22MPa. For sample XZ24-2, test 1 was performed during the loading phase (up to 22MPa) while test 2 was conducted during the unloading phase from 22 to 5MPa. The whole set of operating conditions and results are given in Table 3.2.

Fig.3.9 below sums up the results of gas permeability measurements under different P_c and P_i for two samples and for the two tests. The initial permeability of these two samples at 3MPa of confining pressure is comparable ($6.36E-18m^2$ and $1.43E-17m^2$). A strong effect of confining pressure, leading to a global reduction of gas permeability by almost three orders of magnitude, can be observed for both samples at the end of test 2. The large amount of impermeable crystals in salt rocks makes the permeability closely related to cracks or joints. At this scale, the closure of joints around crystals are likely to play a key role on the flow. As increasing confining pressure will cause the closure of cracks, the latter induces a strong permeability decrease. The influence of the mean pore pressure P_i is clearly not systematic. On the first hand, if present this effect leads to an increase in permeability when P_i is increased, which excludes a potential Klinkenberg effect (the details can be seen in §3.3.6). This means that there is a coupling effect, which can be attributed to a crack (or joint) aperture effect. On the second hand, the P_i effect is sometimes present (Fig.3.9 (b) or (d)), partial (Fig.3.9 (a)) or negligible (Fig.3.9 (c)) and varies with times as it can be absent for test 1 and present for test 2. The effect of time is commented in the following (§3.3.5).

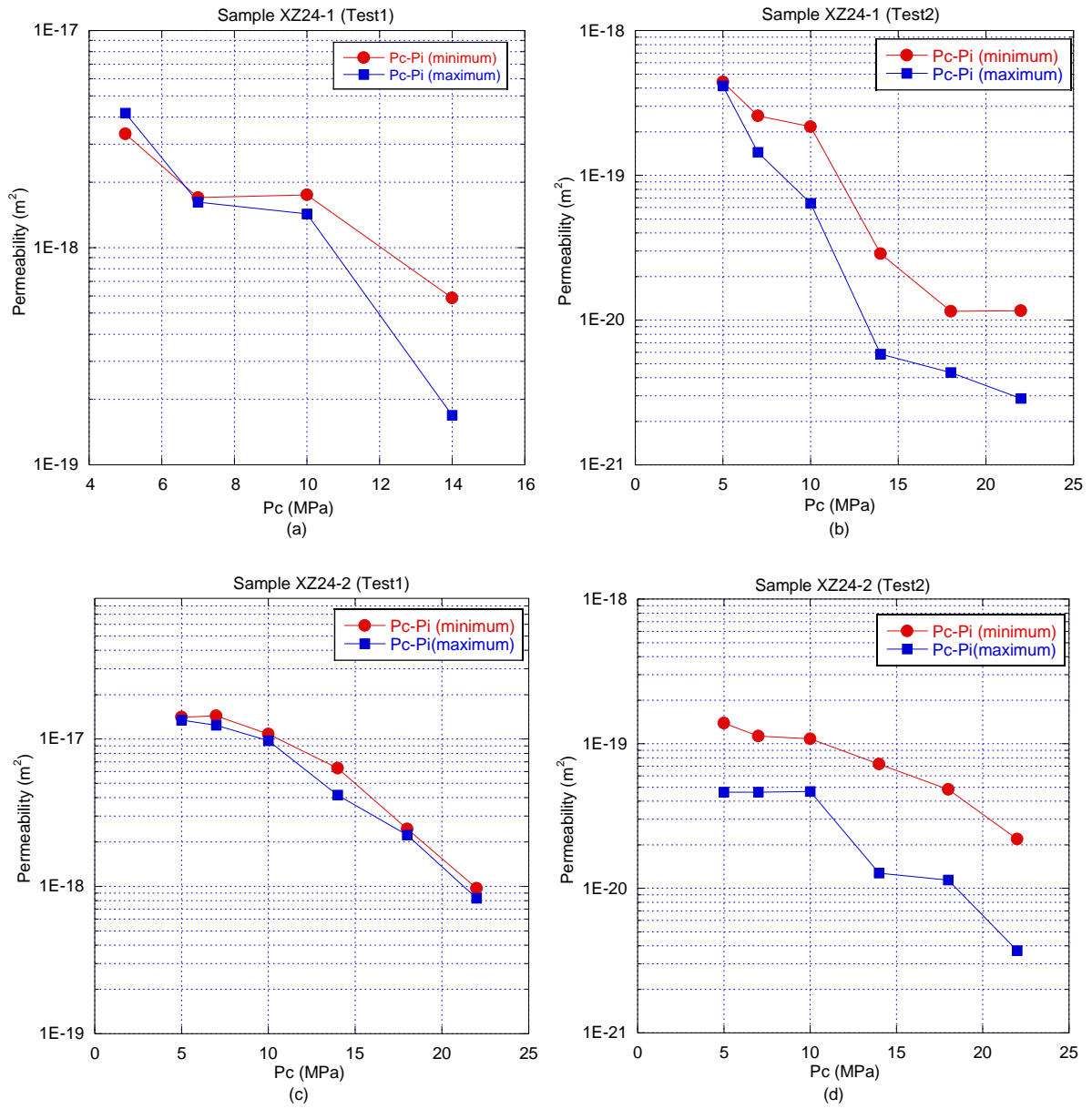


Fig.3.9 Effect of confining pressure and Terzaghi effective pressure on gas permeability

Table 3.2 Gas permeability measurements under different P_c and P_i for two samples

P_c (MPa)	P_i (MPa)	K(m ²) - Sample XZ24-1		K(m ²) - Sample XZ24-2	
		Test 1-load P_c (5 to 14MPa)	Test 2-load P_c (5 to 22MPa)	Test 1-load P_c (5 to 22MPa)	Test 2-unload P_c (22 to 5MPa)
5	1	4.17E-18	4.13E-19	1.34E-17	4.61E-20
5	3	3.34E-18	4.42E-19	1.40E-17	8.15E-20
5	4			1.41E-17	1.39E-19
7	2	1.62E-18	1.44E-19	1.24E-17	4.62E-20
7	4	1.70E-18	2.58E-19	1.14E-17	6.97E-20
7	5			1.43E-17	1.13E-19
10	2	1.43E-18	6.41E-20	9.73E-18	4.66E-20
10	4	1.70E-18	7.46E-20	7.19E-18	6.94E-20
10	6	1.74E-18	1.14E-19	9.40E-18	9.42E-20
10	8	1.75E-18	2.17E-19	1.08E-17	1.08E-19
14	2	1.69E-19	5.81E-21	4.16E-18	1.27E-20
14	4	1.70E-19	8.14E-21	4.28E-18	2.08E-20
14	6	2.31E-19	1.12E-20	4.79E-18	4.27E-20
14	8	3.05E-19	1.26E-20	3.66E-18	3.60E-20
14	10	3.50E-19	1.72E-20	5.81E-18	5.77E-20
14	12	5.86E-19	2.87E-20	6.34E-18	7.22E-20
18	2		4.35E-21	2.23E-18	1.14E-20
18	4		6.39E-21	2.20E-18	2.76E-20
18	6		5.51E-21	3.41E-18	1.89E-20
18	8		8.49E-21	3.27E-18	2.15E-20
18	10		1.03E-20	2.93E-18	2.90E-20
18	12		1.15E-20	2.45E-18	4.83E-20
22	2		2.88E-21	8.30E-19	3.70E-21
22	4		4.78E-21	8.13E-19	3.77E-21
22	6		4.41E-21	8.57E-19	1.90E-20
22	8		4.45E-21	8.22E-19	2.17E-20
22	10		6.82E-21	8.67E-19	2.03E-20
22	12		1.16E-20	9.72E-19	2.19E-20

3.3.3. Confining pressure effects on porosity

3.3.3.1. Porosity measured with gas

As seen before, gas permeability revealed to be highly sensitive to confining pressure. Porosity measurements (described in §3.2.4) at different confinements were therefore performed for seven samples and the results are given in Fig.3.10 (a). The porosity values are in fact very low since the highest one was 1% at 5MPa confining pressure (see the following SBET results). The sensitivity to the confining pressure is very high as the porosity is almost 0 (or not measurable) for samples XZ24-1, XZ25-3 at 7MPa and at 14MPa for XZ24-2. Some interesting deductions can be drawn from such a sensitivity and relative porosity reduction. The first one is that the salt cannot be considered as a common porous material. If the pores were like ‘classical’ ones in usual rocks, the porosity variation would be in

the relative order of a few percent, and not almost one percent as it is observed on the salt. The second one, which is a consequence of the first one, is that the (very) small measured pore volumes can only be constituted of cracks or grain joints between non-porous crystals. This has been confirmed by SBET analysis (in the next section §3.3.3.2) that gave almost no porosity and no specific surface, which evidenced the fact that there are no pores in the usual meaning. This single porosity measurement confirms that fluids can only flow between the crystals and coupling effects would be likely to take place through these interfaces. Cracking can be then considered as producing new interfaces.

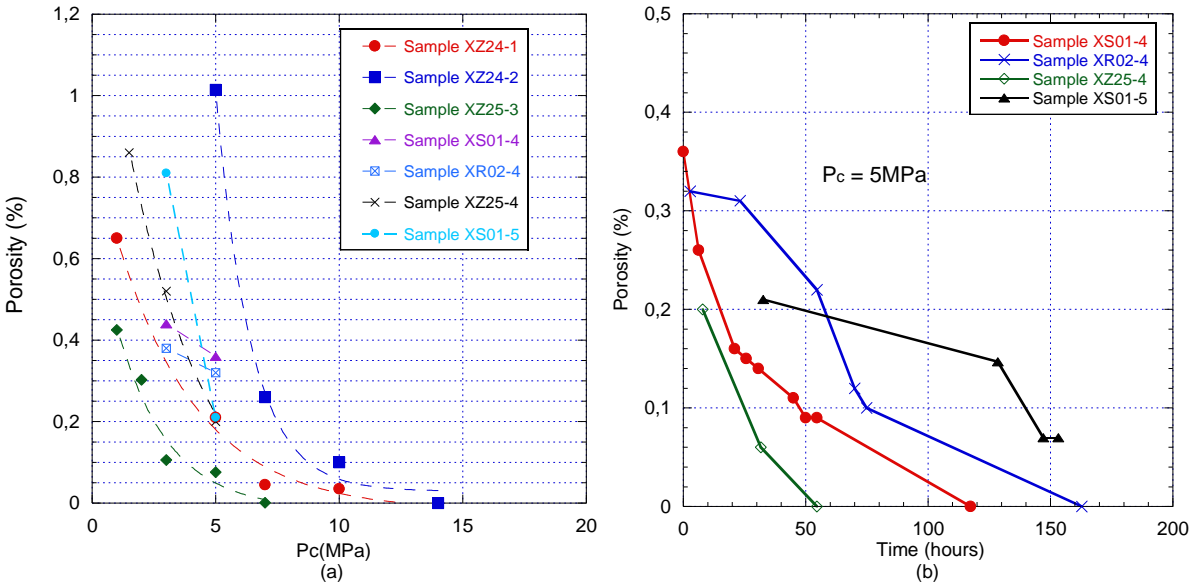


Fig.3.10 Variation of porosity with P_c (a) and with time (b)

Not only salt porosity varies with confining pressure but also with time. As shown in Fig.3.10 (b), a decrease in porosity with time was detected for four samples at a moderate value $P_c=5\text{MPa}$. It can be underlined that the decrease rate is high as, for three samples, the porosity has reached a non-measurable value in 160 hours (maximum value). As mentioned before, the porous structure is mostly constituted of cracks or grain joints between crystals. The porosity decrease with time can indicate that there is a crack sealing or a tighter connection between crystals. This phenomenon is consistent with following observations on gas permeability (time effects on gas permeability) in §3.3.5.

3.3.3.2. SBET results (specific surface area analysis)

Several nitrogen adsorption/desorption tests were performed on three salt samples from different cores, with emphasis on the specific surface area analysis (SBET). This gas adsorption technics allows the measurement of adsorbed nitrogen on the pore surface. It is generally admitted that more adsorbed gas means a higher specific surface (or a finer porosity). The SBET results for salt rock can be compared to results for two other typical materials (concrete and argillite) in our laboratory.

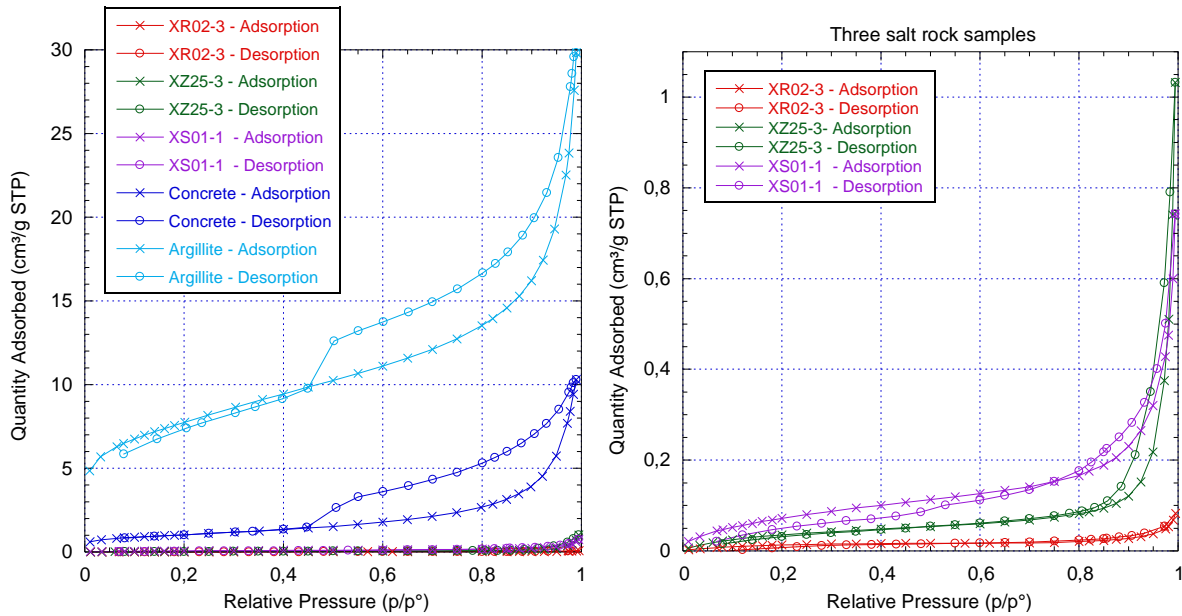


Fig.3.11 Raw results of SBET for three salt rocks (right), concrete and argillite (left)

Table 3.3 SBET results and porosity, permeability of different materials

Rock material	BET Surface area (m ² /g)	Pore volume (cm ³ /g)	Mean pore diameter (nm)	Porosity (%)	Gas Permeability (m ²)
Salt (XR02-3)	0.05	0.00013	15	~ 0	10 ⁻²³
Salt (XZ25-3)	0.15	0.0016	37.6	~ 0.3	10 ⁻²¹ ~ 10 ⁻²²
Salt (XS01-1)	0.19 ~ 0.3	0.0011	15.2 ~ 17.2	~ 1	10 ⁻¹⁸
Concrete	5 ~ 22	0.02 ~ 0.04	7 ~ 15	8 ~ 16	10 ⁻¹⁵ ~ 10 ⁻¹⁸
Argillite Cox	30 ~ 40	0.05 ~ 0.06	5 ~ 7	13 ~ 19	10 ⁻¹⁸ ~ 10 ⁻²¹

These results are very revealing as they are out of the range of significance of SBET measurements for which several m² are needed to be analyzed. The results in bold-red in Table 3.3 indicate that they are far below this value. This is confirmed by Fig.3.11 that gives the comparison of total adsorbed nitrogen v.s. relative pressure for salt, concrete and argillite. These raw results clearly show that the quantity of adsorbed gas for salt is very low compared with the two other materials. This simply means that there is no significant surface for the gas to adsorb on it, which also implies that the salt porosity is very small. To conclude there are some ‘voids’ in the salt but with no specific surface, this is in complete agreement with the fact that salt ‘porosity’ is composed of cracks or joint grains.

3.3.4. Comparison between argon and hydrogen permeability

As mentioned in the introduction, salt gas cavern could be used as hydrogen storage facilities. It is well known that experiments with hydrogen require safety disposal and precautions, which are not always available in rock mechanics laboratories. Leakage of permeability devices is also among issues that are met with this gas. It is therefore very useful to compare the permeability values obtained with this gas and a more convenient one like argon. Three tests were performed on samples having (ultra)

low (XZ25-3), intermediate (XZ24-2) and high (XS01-3) gas permeability. The results are presented in Fig.3.12. The hydrogen permeability was always the first one to be measured. The process for the sample XZ24-2 was to confine it at 22MPa and get the permeability during the unloading phase. For the two other samples, classical loading-unloading phases were applied. Tests with hydrogen were performed prior to those with argon. First of all these results confirm the great sensitivity of salt permeability to confining pressure and its irreversibility due to crack closure, which is visible on the unloading paths (Fig.3.12 (b) and (c)). As a consequence, hydrogen and argon permeability comparisons have to be compared at the highest confining pressure. What can be drawn from these results is that permeability obtained with both gas are very close to each other and can be considered as being virtually the same. **This interesting result evidences that argon gas can be chosen to evaluate the hydrogen permeability with no significant differences. This is also true whatever the order of magnitude of the initial permeability.** The considerable differences obtained on this material (with permeability being in the range 10^{-16} to $10^{-23}m^2$) underline the material's dispersion and/or its initial state of cracking.

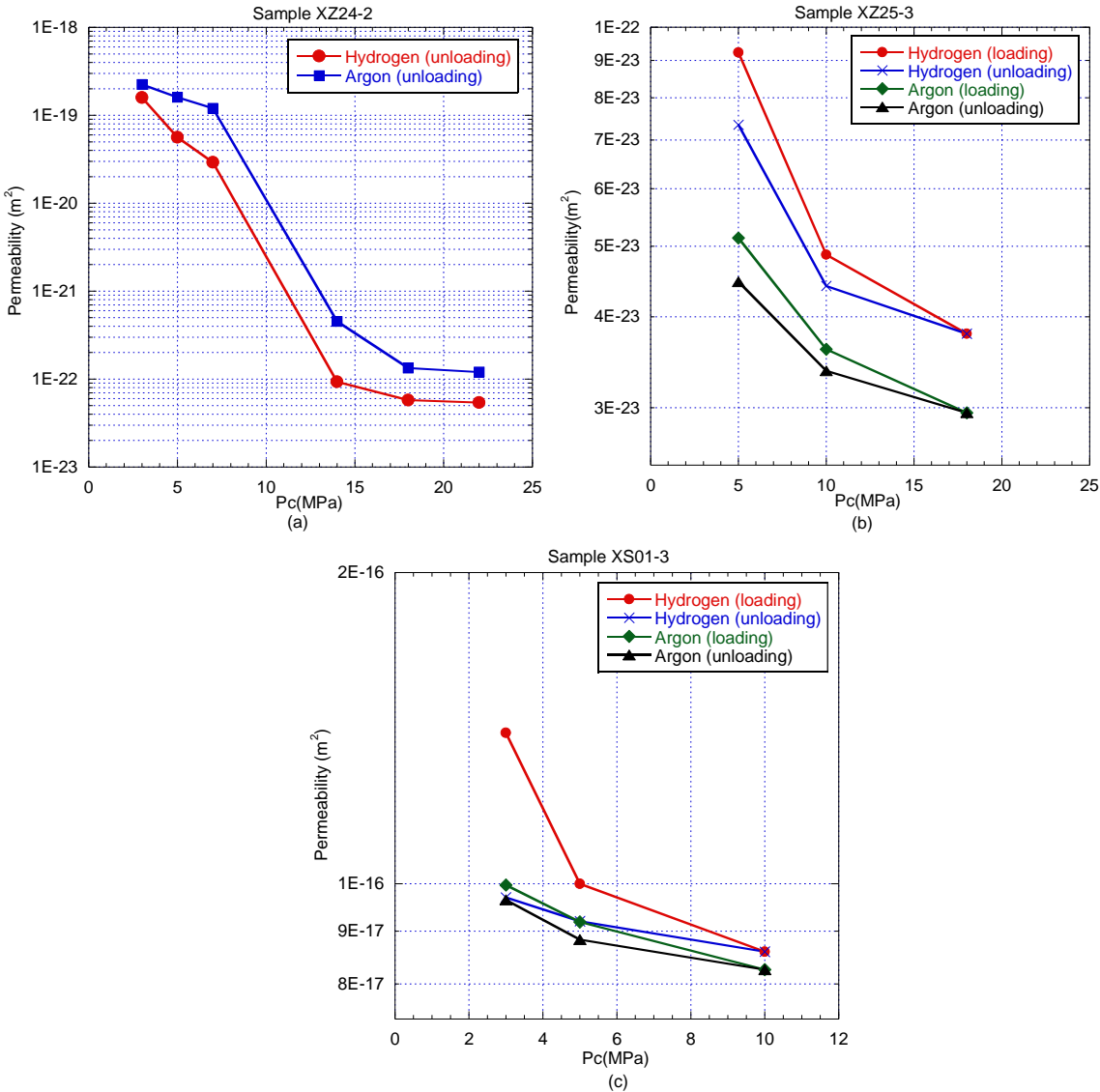


Fig.3.12 Comparison between argon and hydrogen permeability

3.3.5. Time effects on gas permeability

The time effect, which is illustrated in Fig.3.13, is clearly visible as gas permeability, recorded for the test2 is systematically lower, by one to two orders of magnitude, than for test1. This can be especially underlined at 14MPa of confining pressure (in Fig.3.13 (a)) and at 22MPa (in Fig.3.13 (b)), which were the highest confining pressure values reached in test1 for the corresponding samples. In fact, the differences observed with lower confining pressures cannot be only attributed to the time effect as the hydraulic material's behavior depends on crack closure, which is generally not reversible. This kind of time effect is consistent with what is generally reported in the literature [13, 14, 68, 146]. The time-dependent behavior of salt rock had been demonstrated through many experiments, which led to constitutive and computational models [21, 83–86, 147]. More hydrostatic tests were carried out to investigate this time effects under two levels of confinement (low and high confining pressure), described in §4.3.

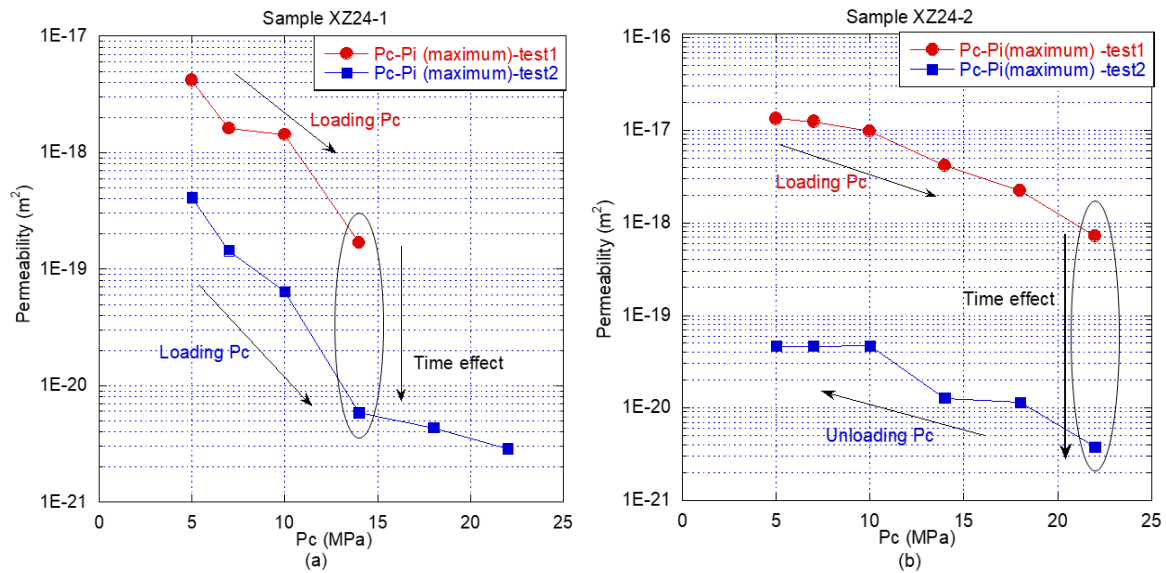


Fig.3.13 Comparison of permeability under different P_c between test 1 and test 2

3.3.6. Klinkenberg effects

There is a perturbative effect for porous medium gas flow, the slipping or Klinkenberg effect [69]. Gas flow in the porous materials is mainly due to two forms of gas molecular movement: gas molecules collide with each other, and gas molecules collide with the pore wall. When the gas pressure is low and the mean pore radius is close to the free mean path of gas molecule, the effective molecular collisions are those with the pore wall rather than with other gas molecules. This phenomenon is called ‘slip flow’ and will make the measured permeability higher than the intrinsic one.

The Klinkenberg slip theory [69] exhibits a relation between the measured gas permeability variations of an idealized porous medium towards the reciprocal of the average pore pressure. Klinkenberg formula is given by

$$K_{app} = K_{int} * \left(1 + \frac{\beta}{P_m}\right) \quad (3.18)$$

where K_{app} is the measured permeability and K_{int} is the intrinsic permeability. P_m is the mean gas pressure. β is the Klinkenberg factor, which can be calculated by performing three (or four) permeability tests with different mean pressures, as described below. Usually β is mainly related to the microscopic pore structure of porous medium, especially the mean pore (radius) size. It is assumed that the larger the β , the smaller the pore size. Since the permeability has high sensitivity to confinement in terms of microstructure, it is interesting to study this effect on β .

Sample XZ25-4 was used to detect the Klinkenberg effect during hydrostatic test (this test was conducted simultaneously to investigate time effects, see in §4.3). Three different injection gas pressures (0.5, 1, 1.55MPa) were considered at each level confinement (3, 5, 10MPa). According to Fig.3.14, a clear Klinkenberg effect on permeability occurs. This led to the Klinkenberg factor β calculation (as shown in Table 3.4). They show an increase in β with confinement, this simply indicates and confirms that there is gradual crack closure (reduction of pore size (or narrowing pore wall)). On another end, the increase in β is from 0.65 at 3MPa to 4.2 at 10MPa, revealing a strong reduction of porosity, so consistent with the previous results on this property and also with the significant volumetric strain change. If we assume that (this is often done) β is proportional to $1/r$ or $1/e$ for crack (being the mean crack aperture), then the crack volume reduction would be $4.2/0.65 \approx 6.5$. This is also consistent with the porosity variations observed in Fig.3.10.

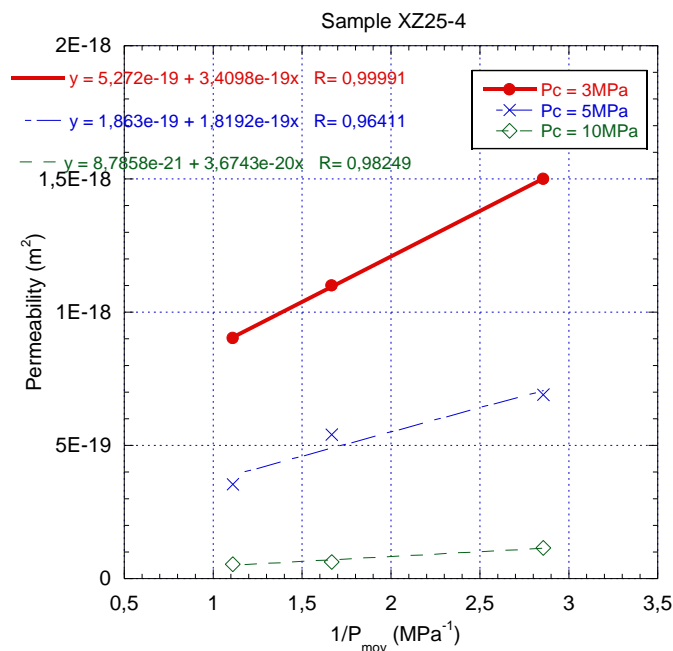


Fig.3.14 Variations of permeability with pore pressure at different confining pressure

Table 3.4 Values of the Klinkenberg factor β and intrinsic permeability of sample XZ25-4

P_c (MPa)	3	5	10
β (MPa)	0.65	0.98	4.18
K_{int} (m ²)	5.3E-19	1.9E-19	8.8E-21
ϵ_v (10 ⁻⁶)	217	413-440	738

Another hydrostatic test on sample XS01-5 was devoted to study not only confining pressure but also time effects on the Klinkenberg factor β . First, the permeability measurements with different mean gas pressure were carried out at $P_c=3$ MPa. Then the confinement was increased and maintained at 5MPa for 120hours. The permeability evolutions were daily measured. The same type of measurements were then performed at 10MPa of confinement. According to our knowledge, it is the first time that such experiments, including evolution of Klinkenberg factor β , are carried out on salt. The last step was to unload the sample to investigate irreversibility.

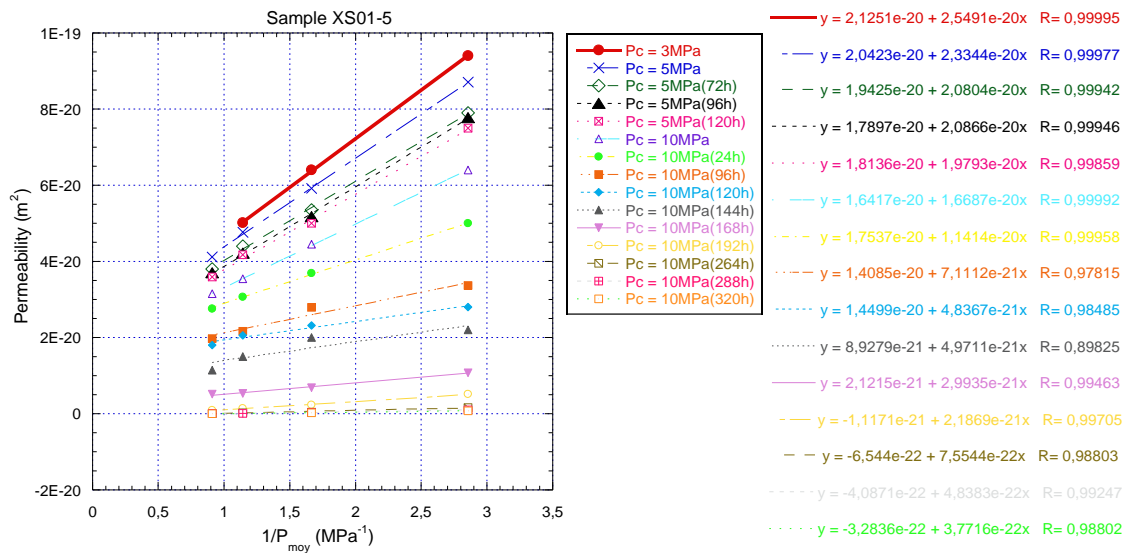


Fig.3.15 Variations of permeability with pore pressure and time at different confining pressures

The whole set of results (for the loading phases) is given in Fig.3.15 and tabulated in Table 3.5. A first comparison with the results (Table 3.4) shows that the initial permeability is (at 3MPa) lower than for the previous sample, by one order of magnitude. On another hand, the permeability is now less sensitive to the confining pressure as at 10MPa both sample permeabilities are comparable. This may evidence that there were more cracks (or with a higher aperture) in the sample XZ25-4. Combined with changes of volumetric strain with time at different P_c (see Fig.3.17 (b)), things are less simple for sample XS01-5 and:

-the confining pressure effect is not significant between 3 and 5MPa confining pressure and at the same time the volumetric strain change is very low.

-there is a slight effect of time whatever the injection pressure is at 5 MPa confining pressure with a small permeability decrease, which is coming along with a negligible volumetric strain evolution ($\Delta\epsilon_v=31.10^{-6}$ with time).

-the confining pressure effect is not significant between 5 and 10MPa confining pressure. This is surprising as there is a significant effect of confining pressure on the volumetric strain ($\Delta\epsilon_v=413.10^{-6}$ with time).

-there is a strong effect of time at 10MPa confining pressure with a permeability reduction by 2 or 3 orders of magnitude, which is coming along with a moderate evolution of volumetric strain ($\Delta\epsilon_v=66.10^{-6}$ with time).

-there is an effect of injection pressure amplitude i.e. reduction of permeability as P_i is increased. This is observed for every test and can be attributed to the Klinkenberg effect. On the other hand the β calculations did not lead to significant variations, contrary to the previous case (see Table 3.6). This can be regarded as quite logical as from 3 to 10MPa, the permeability decreased is very little. One can nevertheless mention that, at 10MPa and 168h of test duration, there is a sudden drop in permeability linked to an increase in the Klinkenberg coefficient.

-between 0 and 144h, there is a decrease in the Klinkenberg coefficient that can be artefact as it is unlikely possible that the time effect led to crack opening.

-after 168h to 320h, there is a (strong) continuous decrease in permeability by 2 orders of magnitude. But the Klinkenberg coefficient calculation did not lead to any valuable results and even to negative intrinsic permeability. It can be assumed that the latter is now almost 0 (or non measurable) and the negative value is then artefact.

Table 3.5 Changes in permeability of sample XS01-5 with gas pressure and time at different confining pressure – unloading step (in blue) was from 10MPa confining pressure

XS01-5 P_i (MPa)	$1/P_{moy}$ (MPa^{-1})	P_c (3MPa)		P_c (5MPa)							
		load	Unload	0h	72h	96h	120h	Unload			
0.5	2.86	9.4E-20	5.6E-22	8.7E-20	7.9E-20	7.8E-20	7.5E-20	5.1E-22			
1	1.67	6.4E-20	2.6E-22	5.9E-20	5.4E-20	5.2E-20	5.0E-20	2.8E-22			
1.55	1.143	5.0E-20	9.8E-23	4.8E-20	4.4E-20	4.2E-20	4.2E-20	1.2E-22			
2	0.91			4.1E-20	3.8E-20	3.7E-20	3.6E-20	8.8E-23			
ϵ_v (10^{-6})		271	466	305	318	300	336	584			
P_i (MPa)	$1/P_{moy}$ (MPa^{-1})	P_c (10MPa)									
		0	(24h)	(96h)	(120h)	(144h)	(168h)	(192h)	(264h)	(288h)	(320h)
0.5	2.86	6.4E-20	4.8E-20	3.4E-20	2.8E-20	2.2E-20	1.1E-20	5.2E-21	1.6E-21	1.0E-21	7.8E-22
1	1.67	4.5E-20	3.7E-20	2.8E-20	2.3E-20	2.0E-20	6.8E-21	2.3E-21	4.6E-22	3.5E-22	2.3E-22
1.55	1.143	3.5E-20	3.0E-20	2.2E-20	2.1E-20	1.5E-20	5.4E-21	1.4E-21	2.2E-22	1.1E-22	
2	0.91	3.2E-20	2.8E-20	2.0E-20	1.8E-20	1.1E-20	5.2E-21	9.6E-22	1.1E-22	9.2E-23	5.5E-23
ϵ_v (10^{-6})		749	766	822	820	819	829	823	834	827	815

As mentioned before, Fig.3.16 and Table 3.6 highlight time effects on Klinkenberg factor, on measured permeability (K_{app}) with maximum pore gas pressure P_i and intrinsic permeability (K_{int}). This observation indicates that time-dependent behavior at $P_c=10\text{MPa}$ is stronger than at 5MPa (weak decrease from $4.1\text{E-}20$ to $3.6\text{E-}20\text{m}^2$ in 120 hours). A large decrease in permeability is observed with time at 10MPa , but this occurred after 168h of test (it is not an immediate phenomenon) and coming along with a weak volumetric strain changes (see Table 3.5). This makes us think to a possible clogging, which may illustrate the time dependant sealing. This time effect on permeability is basically consistent with the observation of the other two samples XZ24-1 and XZ24-2 in §3.3.5.

It is therefore very interesting to evaluate the unloading effect from 10 to 5 and then 3MPa (Table 3.6 and Fig.3.17). This unloading did not induce a significant increase in permeability and a high level of irreversibility was captured. As a whole, and despite a visible sample expansion ($\Delta\varepsilon_v=349.10^{-6}$ due to unloading from 10 to 3MPa , see the unloading phase in Fig.3.17 (b)), the intrinsic permeability remained almost 0. This can be seen in Fig.3.17 (a). Under $P_c=3\text{MPa}$, the permeability after the unloading phase ($9.8\text{E-}23\text{m}^2$) is more than two orders of magnitude lower than the one after the first loading step ($5.0\text{E-}20\text{m}^2$). This phenomenon is generally attributed to irreversible crack closure during unloading but, in the present case, there is maybe an additional irreversible sealing effect. It is therefore difficult to make a distinction between both possibilities.

Table 3.6 Klinkenberg factor β , K_{int} and K_{app} of sample XS01-5

$P_c= 3\text{MPa}$			$P_c= 5\text{MPa}$			$P_c= 10\text{MPa}$				
$\beta(\text{MPa})$	$K_{int} (\text{m}^2)$	$K_{app} (\text{m}^2)$ (max P_i)	Time (hours)	$\beta(\text{MPa})$	$K_{int} (\text{m}^2)$	$K_{app} (\text{m}^2)$ (max P_i)	Time (hours)	$\beta(\text{MPa})$	$K_{int} (\text{m}^2)$	$K_{app} (\text{m}^2)$ (max P_i)
1.20	2.13E-20	5.0E-20	0	1.14	2.04E-20	4.1E-20	0	1.02	1.64E-20	3.2E-20
			72	1.07	1.94E-20	3.8E-20	24	0.65	1.75E-20	2.8E-20
			96	1.17	1.79E-20	3.7E-20	96	0.50	1.41E-20	2.0E-20
			120	1.09	1.81E-20	3.6E-20	120	0.33	1.45E-20	1.8E-20
							144	0.56	8.93E-21	1.1E-20
							168	1.41	2.12E-21	5.2E-21
							192	-1.96	-1.12E-21	9.6E-22
							264	-1.15	-6.54E-22	1.1E-22
							288	-1.18	-4.09E-22	9.2E-23
							320	-1.15	-3.28E-22	5.5E-23
$P_c= 3\text{MPa}(\text{unload})$			$P_c= 5\text{MPa}(\text{unload})$							
-1.36	-1.96E-22	9.8E-23		-1.94	-1.14E-22	8.8E-23				

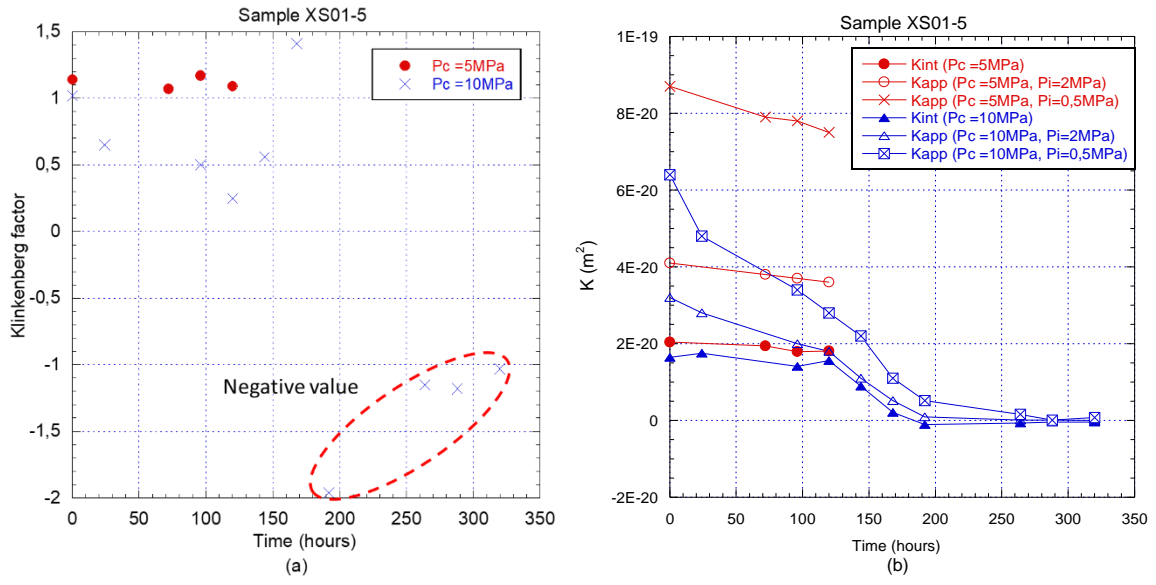
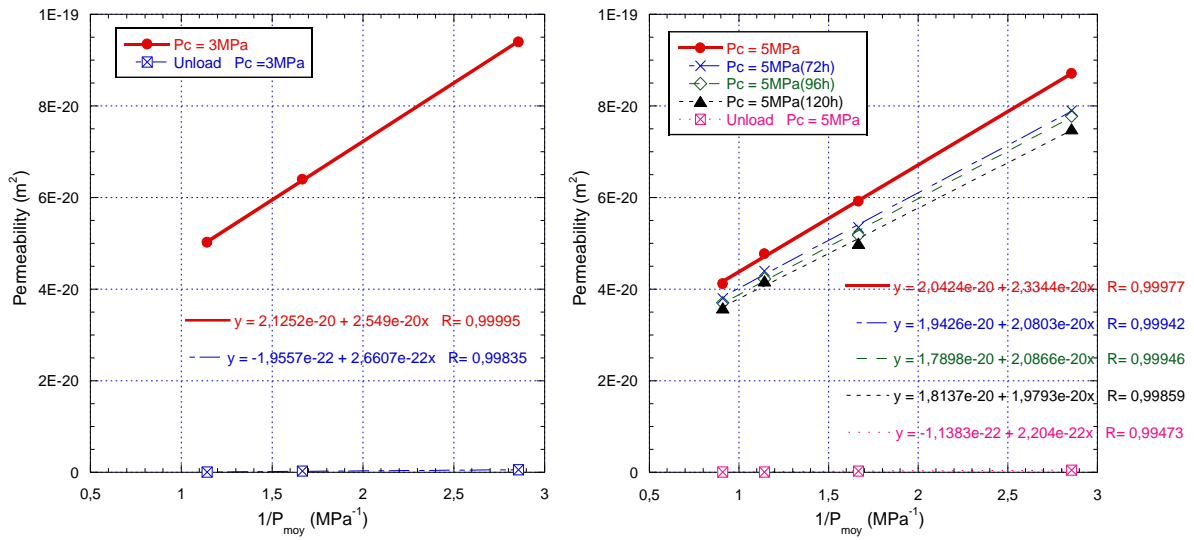
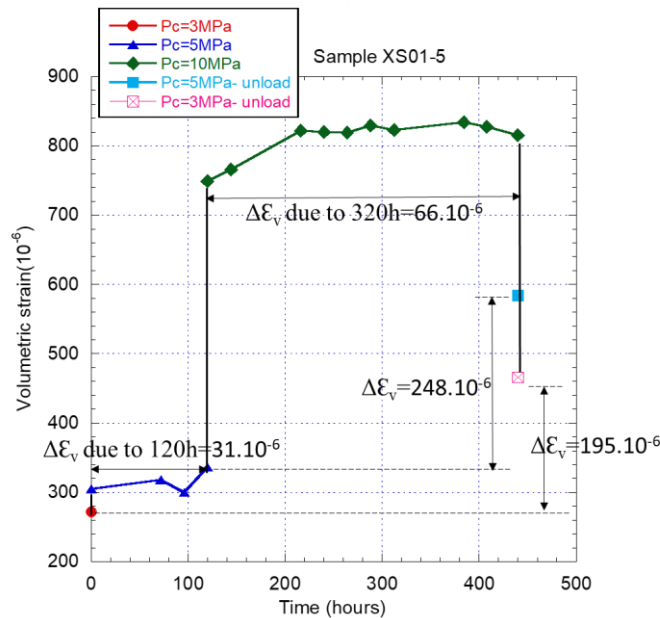


Fig.3.16 Variations of Klinkenberg factor (a) and permeability (b) with time at different P_c



(a)



(b)

Fig.3.17 (a) Variations of permeability with pore pressure (loading-unloading phase); (b) Variations of ϵ_v with time and P_c (loading-unloading phase)

3.3.7. Biot coefficient and couplings

As mentioned in §3.2.5, the ratio between the volumetric strain due to an increase in pore pressure with that due to a confinement (during an unloading phase) can be calculated to evaluate the ‘apparent’ Biot’s coefficient. The term ‘apparent’ is used here as to calculate the Biot’s coefficient with this ratio, the material must be isotropic and the strains have to be elastic. Both of these conditions are difficult to assess and we must keep in mind that the present Biot’s coefficient calculation will simply indicate that there is a coupling effect and/or that this effect is more or less intense. In Fig.3.18 can be observed the volumetric strain measured on two samples (XS01-1 and XS01-2), under three different levels of confinement and for a unit change of 1MPa of pore pressure. There is clear sample expansion due to this pore pressure increase, which evidences a poro-mechanical coupling. Increasing the confining

pressure always leads to a reduction of this expansion. As a consequence, when combined to the volumetric strains due to a confining pressure decrease (plotted in Fig.3.19), it was possible to calculate apparent Biot's coefficients (also indicated in Fig.3.18).

The coefficients obtained are quite low but far from marginal since they approximately vary from 0.37 to 0.04 under the range of confinement used. The increase, from 7 to 17MPa, in confining pressure results in a reduction in the Biot's coefficients, which is currently associated with a less and less fragmented material, and is likely to be associated to closure of grain boundaries or cracks. The time effect is evidenced by comparison of the results given by two successive identical tests (1 and 2) for the sample XS1. Hysteretic effects are present at 7 and 12MPa, between test1 and test2, that can be interpreted by the loading history i.e. 17MPa were applied during test1. Such a value might have led to an irreversible closure of cracks inducing a lower Biot's coefficient at 7 and 12MPa for test 2. On another hand the coefficients, compared at 17MPa for both tests, are very different (0.24 at test 1 and 0.04 at test 2). Such a difference can logically be attributed to the time effect and is consistent with what was observed for the gas permeability (see Fig.3.14 for example).

The results of these experiments allow the evaluation of the bulk modulus K_b and expansion (due to pore pressure P_i) modulus H. Their variations v.s. confining pressure are plotted in Fig.3.19. They clearly indicate that, whatever is the confining pressure, the K_b modulus weakly varies in the range [20-30GPa] since there is a considerable increase in the H modulus within the range [50-600GPa]. The confining pressure is supposed to be linked to crack closure effects. The results seem to indicate that, for these samples, this crack closure phenomenon has moderate effects on modulus K_b . This would mean that these samples are initially weakly cracked or that the crack network has little influence on the skeleton compressibility, which seems logical as regards its very low porosity. On another hand, the crack closure effect leads to less and less material expansion due to pore pressure. This is consistently linked to the significant increase in the H modulus. To sum up the Biot's coefficient decrease (i.e. less coupling effect) is mainly due to the H modulus variation and not to dramatic changes in K_b .

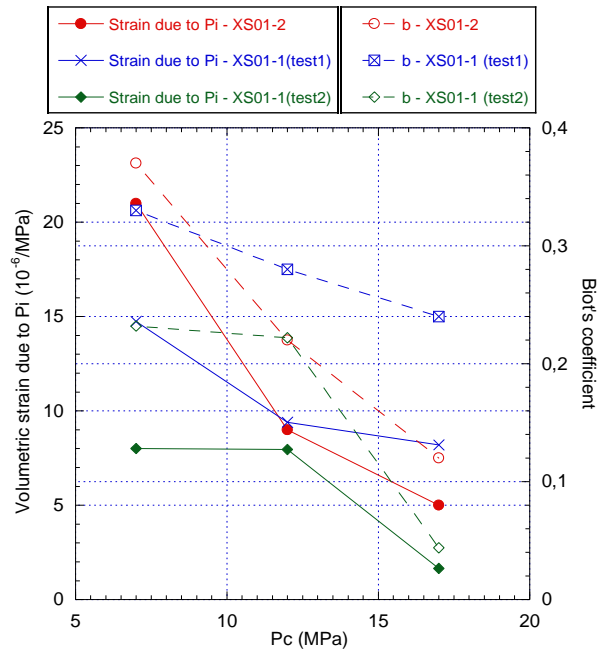


Fig.3.18 Biot coefficient and volumetric strain due to P_i

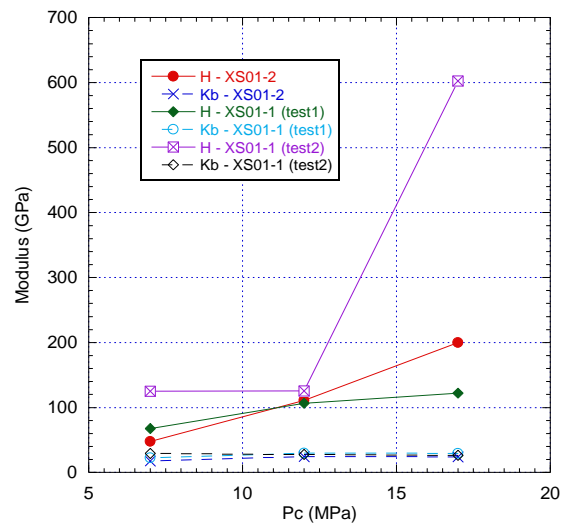


Fig.3.19 Variations of moduli H and K_b due to confining pressure

These results were confirmed by other tests on sample XZ24-1. Fig.3.20 and Fig.3.21 plot the results. The volumetric strains are given v.s. Terzaghi effective pressure for different levels of confining pressure (Fig.3.20). At a fixed value of the latter one can observe the slope ε_v according P_c - P_i . A negative slope means that there is expansion due to an increase in ' P_i '. A null (or quasi null) one is relative to an absence of coupling. The coupling for test 1 is clear (Fig.3.20 (a)) and allowed several 'apparent' Biot's coefficients to be calculated (Fig.3.21) whereas it completely vanishes for test 2 (Fig.3.20 (b)). This is a new evidence of the combination of irreversible crack closure and time effect. It can also be noted in Fig.3.20 (b) (compared with Fig.3.20 (a)) that there is a strong material stiffening as the level of strain ε_v is lower for test 1 than for test 2. For example it is $-800\mu\text{m/m}$ in test 2 and $-1300\mu\text{m/m}$ in test 1 at $P_c=14\text{MPa}$ ($P_i=0$).

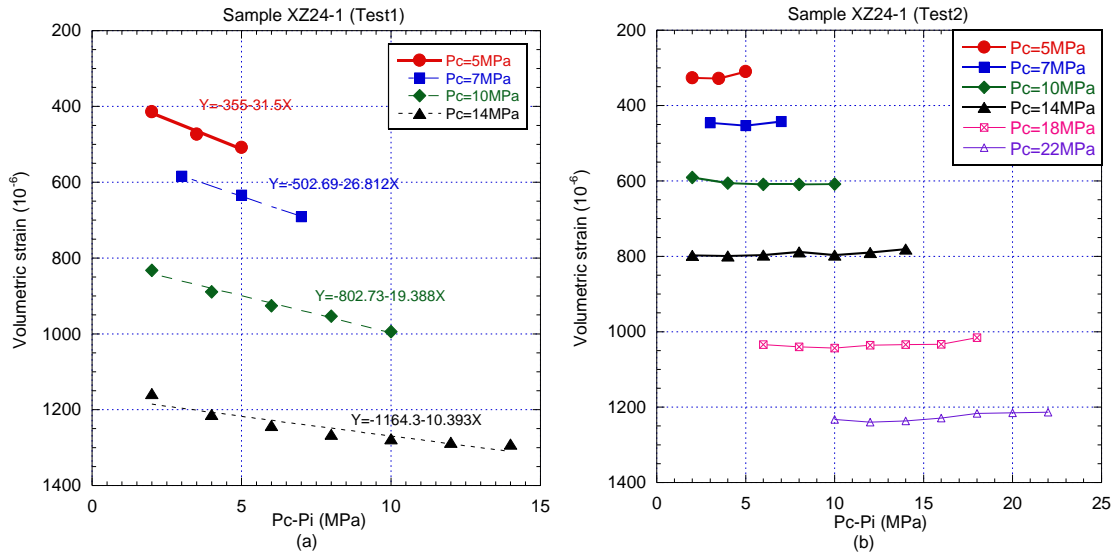


Fig.3.20 Variation of ε_v with $(P_c - P_i)$ - for a given value of P_c there is only a P_i variation

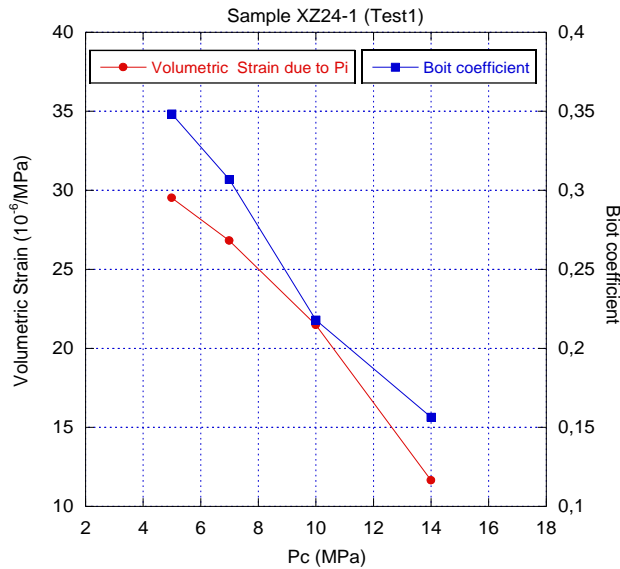


Fig.3.21 Biot coefficient and volumetric strain due to P_i

3.4. Partial conclusion

In this part, the experimental methods for permeability, porosity and Biot's coefficient were first introduced, and then their results were presented. Salt gas permeability was measured under hydrostatic loading for different kind of samples. Different behaviors in term of permeability can be observed. For samples XZ24-1 and XZ24-2 from Southeastern France, the permeability is of an intermediate order of magnitude 10^{-17} - 10^{-18} m². For samples XZ25-3, the permeability is of a (ultra) low order of magnitude 10^{-22} - 10^{-23} m². For sample XS01-3 from Eastern France the permeability is of a high order of magnitude 10^{-16} m² while it is 10^{-20} for XS01-5 (The permeability here is the 'initial' one at low confining pressure). This shows a very high level of dispersion as XS01-5 and XS01-3 come from the same big core. Generally, the same kind of material is supposed to have similar gas transport properties due to the

similar structure. However, from the above experimental results, it can be obviously seen that even three samples of the same material (i.e. same in-situ location - XZ24-1, XZ24-2, XZ25-3) can have very different properties. This may be a natural dispersion and/or a damage due to coring or to sample preparation. The presented results also reflect that, even if salt is a complex material and very difficult to characterize, some general tendencies can be put in light especially about self-sealing.

Regardless of the different levels of permeability, all the recorded porosities were very small -less than 1%. The permeability is not only dependent on confinement but it also evolves with time because of the viscous effects, even under isotropic loading. Beyond that, permeabilities measured with argon or hydrogen are close to each other, and argon permeability may be therefore a good estimate of hydrogen permeability in studies for hydrogen storage development. This result will allow easier measurements of gas permeability that will be involved in the hydrogen storage concept.

Klinkenberg effect (i.e. decrease in apparent permeability when there is a pore pressure increase) was clearly observed on two different samples (XZ25-4 and XS01-5). The first sample was just submitted to an increase in confining pressure that lead in the Klinkenberg coefficient increase. This simply reflects crack closure. The second case is trickier than the first as there is very little variation of the Klinkenberg coefficient. It nevertheless indicate that, with time, there can be a strong permeability decrease that is not linked to volumetric strain evolution: pure sealing.

Pore pressure coupling effects, between internal fluid pressure and volumetric strain, were evidenced on samples XS01-1, XS01-2 and XZ24-1, which simultaneously led to a rough estimation of Biot's coefficient (apparent). For samples XS01-1 and XS01-2 (from East France), Biot's coefficients are 0.33 and 0.37 at P_c of 7MPa respectively, while for sample XZ24-1 (from Southeast France), Biot's coefficient is 0.31. These results show no significant difference between these two families. The apparent Biot's coefficients were found to be sensitive to confinement and could almost reach '0' at 17MPa. They are lower than usual values measured for permeable or low permeable sandstones, shales or other sedimentary rocks [97, 100, 148] but they are significant. This experimental study, conducted with gas, has thus verified that there are couplings effects in salt rock, which is an important finding.

At a microscopic scale, the results of SBET analysis confirmed a very small porosity, which is consistent with porosity measurements (less than 1%). Moreover, the sensitivity to confinement of permeability and of Biot's coefficient support the hypothesis that fluid flows through cracks or boundaries between salt grains and that coupling are only due to (fluid) pressure effect into those cracks. Following experiments were conducted with the main goal to verify this hypothesis.

4. Part II: mechanical, poromechanical and gas permeability tests with the effects of confinement and/or axial loading

4.1. Introduction

As cracks are suspected to lead to significant coupling effects, conventional (on a mechanical point of view) triaxial/uniaxial tests were carried out on seven samples. The purpose of triaxial tests is on one hand to investigate gas permeability variation with deviatoric loading and/or with time, on the other hand to obtain damaged samples with cracks. As mentioned before, it has been demonstrated that the higher the confining pressure, the more difficult is the initiation and opening of fractures during triaxial test [134]. This is in fact a general observation that can be made on different porous materials. It is the reason why uniaxial tests were sometimes performed instead of triaxial tests. The influence of confinement on gas permeability evolution was simultaneously examined by performing triaxial tests under different confinements (2MPa, 7MPa and 10MPa).

H1 type hydrostatic test was conducted **before** the triaxial/uniaxial tests. Hydro-mechanical properties (the gas transfer properties and couplings) were first characterized with tests **H1**. The variations in these properties as function of P_c had been investigated on samples XS01-3 and XZ25-3. In the previous part I, it has been underlined that the gas transfer properties are time-dependent under isotropic loading. Hence, in this part, hydrostatic tests **H1** on samples XS01-4, XR02-4 and XZ25-4 were carried out to systematically explore time effects on the gas transfer properties under two levels of confinement (5MPa and 10MPa).

The hydrostatic tests **H2** were performed **after** the triaxial/uniaxial tests to detect the influence of the potential damage on gas permeability and couplings with internal gas pore pressure. They were also used to characterize the potential sealing/healing effects on those samples damaged for triaxial test.

The non-destructive X-ray micro-tomography imaging technique was used to capture the microcrack/pore evolution due to these different mechanical loadings (hydrostatic stress and deviatoric/uniaxial stress). Three-dimensional (3D) visualization of pore/crack space of one entire sample and sub-volume can be identified: their distribution, shape and size. In addition, the quantitative analysis on the volume of pore/crack was done through the results obtained with the mechanical tests (hydrostatic tests and triaxial/uniaxial tests).

The experimental techniques for all the different tests in this chapter are first described in §4.2, including triaxial/uniaxial test and X-ray micro-tomography technique. The results of tests **H1** for four samples, which was specifically used to investigate time effects on permeability, are presented in §4.3. In the next section §4.4, the results of triaxial tests are presented first, followed by a comparison of tests

H1 and **H2** for five samples. In §4.5, the results of uniaxial tests and the comparison of tests **H1** and **H2** for two samples are given.

4.2. Experimental techniques

4.2.1. Material used for the experiments

The whole set of tests and their duration are indicated in Table 4.1 below.

Table 4.1 Description and experimental schedule of salt rock samples

Salt sample	Height (mm)	Diameter (mm)	Weight (g)	Test	Time
XR02-3 §4.4.1	83.18	64.41	588.04	Triaxial test	09/01/2019 - 18/01/2019
				Hydrostatic test (permeability + coupling)(with time)	08/03/2019 - 28/03/2019
XZ25-3 §4.4.2	81.80	64.59	594.49	Hydrostatic test (H1) (permeability + coupling) (with P_c)	12/12/2018 - 30/01/2019
				Triaxial test (with time effects)	24/04/2019 - 04/06/2019
				Hydrostatic test (H2) (permeability + coupling) (with P_c)	17/06/2019 - 09/07/2019
XS01-3 §4.4.3	81.04	64.28	579.43	Hydrostatic test (H1) (permeability + coupling) (with P_c)	16/05/2019 - 28/05/2019
				Triaxial test	15/07/2019 - 19/07/2019
				Hydrostatic test (H2) (permeability + coupling) (with P_c)	21/08/2019 - 29/08/2019
XR02-4 §4.3 and §4.4.5	82.81	64.77	587.00	Scan 1°	
				Hydrostatic test with time (H1)	05/11/2019 - 20/11/2019
	82.15			Scan 2°	
				Triaxial test (with time effects)	28/11/2019 – 19/12-2019
	76.49			Scan 3°	
				Hydrostatic test with time (H2)	06/06/2020 – 02/07/2020
XS01-4 §4.3 and §4.4.4	83.51	64.53	589.15	Scan 1°	
				Hydrostatic test with time (H1)	16/10/2019 - 04/11/2019
	82.97			Scan 2°	
				Triaxial test (with time effects)	05/11/2019 - 27/11/2019
				Scan 3°	
				Hydrostatic test with time (H2)	03/07/2020 - 31/08/2020
XZ25-4 §4.3 and §4.5.2	80.06	64.94	572.39	Scan 1°	
				Hydrostatic test with time (H1)	27/11/2019 -11/12/2019
	60.80			Uniaxial test (U1)	03/03/2020
				Hydrostatic test (Biot and K) (H2)	04/03/2020 - 16/03/2020
				Hydrostatic test (reload) (H3)	25/05/2020 - 06/06/2020
				Scan 2°	
	60.30			Uniaxial test (U2)	29/06/2020
				Scan 3°	
XZ25-5 §4.5.1	81.84	65.03	598.3	Biot and K at P_c =3MPa (H1)	05/02/2020
				Uniaxial test	06/02/2020
				Hydrostatic test (Biot and K) (H2)	06/02/2020 - 03/03/2020

Table 4.1 gives information on all the samples used in this section, including their size and the schedule for different tests. As shown in this table, five samples (XR02-3, XZ25-3, XS01-3, XS01-4 and XR02-4) were tested as described below: a series of hydrostatic tests (**H1**) were first carried out to detect the permeability and coupling variations with different levels of confining pressure – before (tri)-axial test. (Sample XR02-3 excepted for which the triaxial cell was also used to measure initial permeability under isotropic stress then submitted deviatoric loading). Following **H1**, triaxial tests were carried out with the purpose to damage the sample. These (supposed to be) damaged samples were then tested again with hydrostatic tests (**H2**). The main idea was to evaluate the differences in the results given by (**H1**) and (**H2**) and to observe the cracking influence on different properties. Things are nevertheless not easy as there are also time effects during triaxial testing, which can lead to sealing/healing of cracks. In order to investigate the time influence (for example the permeability evolution during creep), it was decided to keep constant the deviatoric stress for a given time (usually several days) and to periodically measure the permeability variation (for samples XZ25-3, XS01-4 and XR02-4).

The two other samples (XZ25-4 and XZ25-5) were just submitted to uniaxial stress as it was supposed to be more efficient to produce damage.

Hydrostatic tests (**H2**) (samples XS01-4, XR02-4, XZ25-4 and XZ25-5), aimed at measuring the permeability evolution to explore the time-dependent effects under isotropic loading and/or the potential crack sealing, were carried out after axial test.

4.2.2. Experimental method for triaxial test

The experimental apparatus used for triaxial test is shown in Fig.4.1. It includes a triaxial cell, which is similar to the hydrostatic one but equipped with a piston to apply axial stresses and a gas injection device intended to gas permeability measurements. The confining pressure is controlled by a Mini single pump, which can accurately maintain a constant confining pressure. The gas pressure value is continuously recorded using a LabView system. Axial stresses are applied with a mechanical press Zwick/Roell Z250.

As mentioned before, triaxial test was performed to investigate the evolution of permeability under deviatoric stress for five samples. Three of these (XZ25-3, XS01-4 and XR02-4) were used to simultaneously study the ‘creep’ influence. Experimental procedures for these samples are described in §4.4.

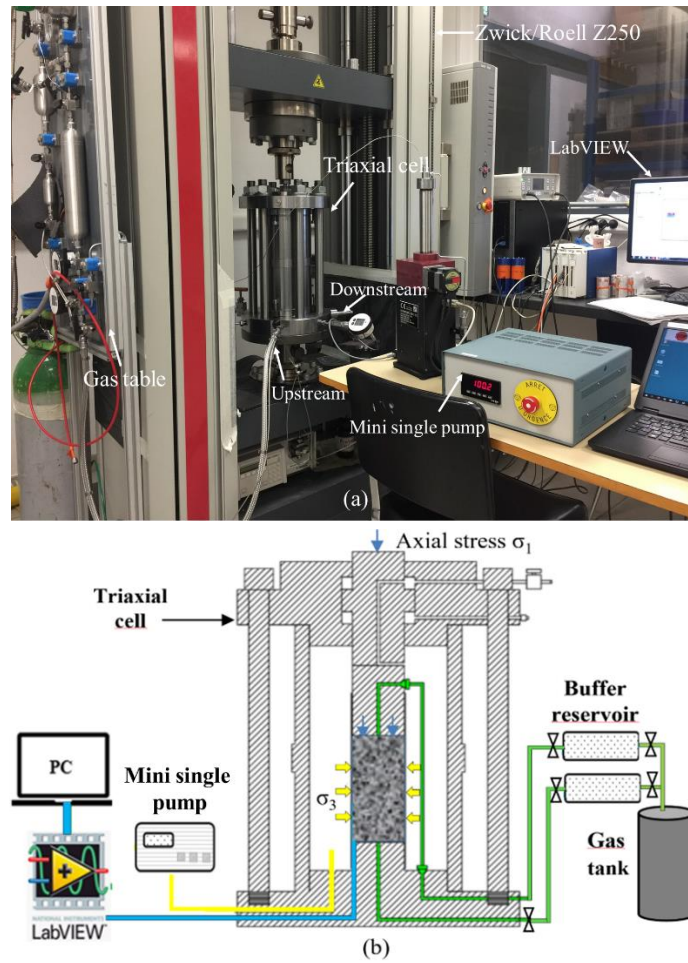


Fig.4.1 The experimental apparatus

4.2.3. Experimental method for uniaxial test

Uniaxial tests were also performed for the purpose of damaging sample XZ25-4 and XZ25-5 without confinement. The machine used to load axial stress is the same as for the triaxial test, shown in Fig.4.2. The procedures of these two uniaxial tests are described in §4.5.



Fig.4.2 The experimental apparatus

4.2.4. X-ray microtomography technology

Recently, the in-situ x-ray tomography technique, scanning internal structures of materials under progressive loading has become available in our laboratory. However, the permeability measurements under the complex mechanical loading (isotropic and triaxial loads) make this new technique unavailable in our tests. Therefore, X-ray microtomography experiments were performed before or after different mechanical tests (hydrostatic and triaxial/uniaxial test) for three different samples (XR02-4, XS01-4 and XZ25-4). When a (specific) test is completed, the sample is removed from the cell and sent to the CT room for scanning. These scans were carefully conducted to be able to observe some identical parts of the same sample before and after the various tests. This allows to follow the crack evolution over time (closure, opening or sealing due to different loadings) and also the visible porosity. As shown in Fig.4.3, the first scan was performed to present the initial state just after coring. The second scan was carried out after test **H1** whereas the third one was conducted on damaged sample obtained after triaxial/uniaxial test.

As the X-ray microtomography equipment was not operational during tests on sample XZ25-4, the first uniaxial test (**U1**) was carried out after test **H1** without scanning between **H1** and **U1**. The following hydrostatic tests **H2** and **H3** were used to heal the damaged specimen. The second scan was done after test **H3**. The third scan was performed after the second uniaxial test (**U2**) in order to observe the microstructure changes due to uniaxial stress (see Fig.4.3).

The results of X-ray microtomography experiments allow quantitative analysis of the pore/crack size or volume, as well as their distribution but, as already mentioned, the whole set of pores and cracks can not be observed due to limitation of resolution. On a global point of view, these observations are very useful to visualize the microstructure changes induced by the different mechanical loadings and can help to confirm (or not) assumptions based on macroscopic experiments and results. With X-ray micro-CT, it is possible to focus on the distribution and development of microcrack/pore due to high deviatoric loading and healing. These micro-observations are expected to be consistent with the transport property variations during hydrostatic and triaxial tests.

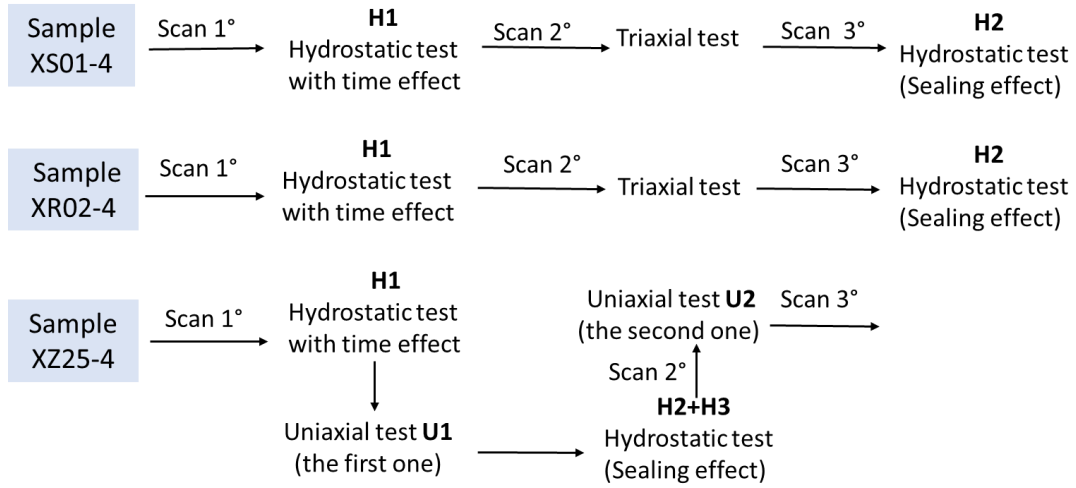


Fig.4.3 Scheme of X-ray micro-tomography experiments for three samples

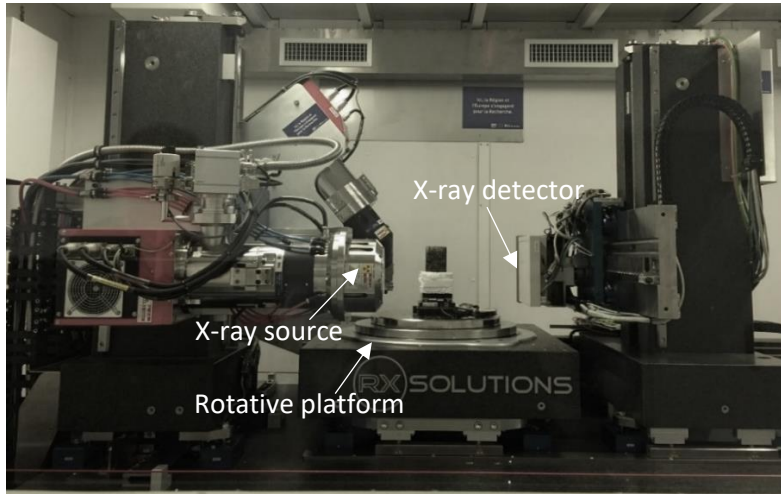


Fig.4.4 X-ray micro-tomography device

As shown in Fig.4.4, X-ray micro-tomography is mainly composed of X-ray source and detector. The principle of this technology is to use X-rays to penetrate through an object. The detector collects the attenuated X-rays. Attenuation depends on the different components of the object because their heterogeneity induces different absorption rates of X-ray. Then they are converted into images. After the X-ray emitted by the signal source penetrates the sample, the attenuated signal satisfies the following attenuation equation [149].

$$I = I_0 \exp(-\mu d) \quad (4.1)$$

where: I is the attenuated intensity of X-ray, $J/(\text{cm}^2 \cdot \text{s})$; I_0 is the incident intensity of X-ray, $J/(\text{cm}^2 \cdot \text{s})$; μ is the absorption coefficient of the substance irradiated by X-ray, d is the thickness of the object.

The key technology lies in the 3D reconstruction from the projection obtained during rotation of the object. This can lead to realistic 3D imaging of whole material. The CT image reconstruction is therefore based on the attenuation degree of the X-ray beam in each voxel to obtain what is called

reconstruction matrix. These calculated attenuation values are then represented as gray levels in a two-dimensional image of the slice [150]. 3D images can be obtained after stacking all the 2D images in order. The spatial resolution of X-ray microtomography can generally vary from several hundred nanometers to several hundred microns, which mainly depends on the distance between the sample and the X-ray source: the shorter the distance (i.e. the smaller the scanning volume), the higher the resolution. Therefore, the scan resolution is mainly related to sample size. In this X-ray microtomographic experiment, as the sample diameter is 65mm, the best expected resolution is around 40µm. Hence, pore/crack smaller than 40µm cannot be detected. This can be considered as being a binding limitation but the following will evidence that, despite this limitation, important phenomena could have been captured.

Reconstruction of the tomographic data is performed with a filtered back-projection algorithm using X-act software [151]. AVIZO 9.0 software is used for the processing of micro-tomographic images. Fig.4.5 summarizes the major processing steps of these two software. As raw data coming from micro-tomographic acquisitions are mainly noisy, it is first necessary to apply ‘Median Filter’, a denoising operation. The operation ‘Register and Resample Transformed Image’ allows to automatically spot on the same slice of sample despite the sample irreversible deformation due to different mechanical loadings. This is obviously the prerequisite for the comparison of the same horizontal or vertical slices.

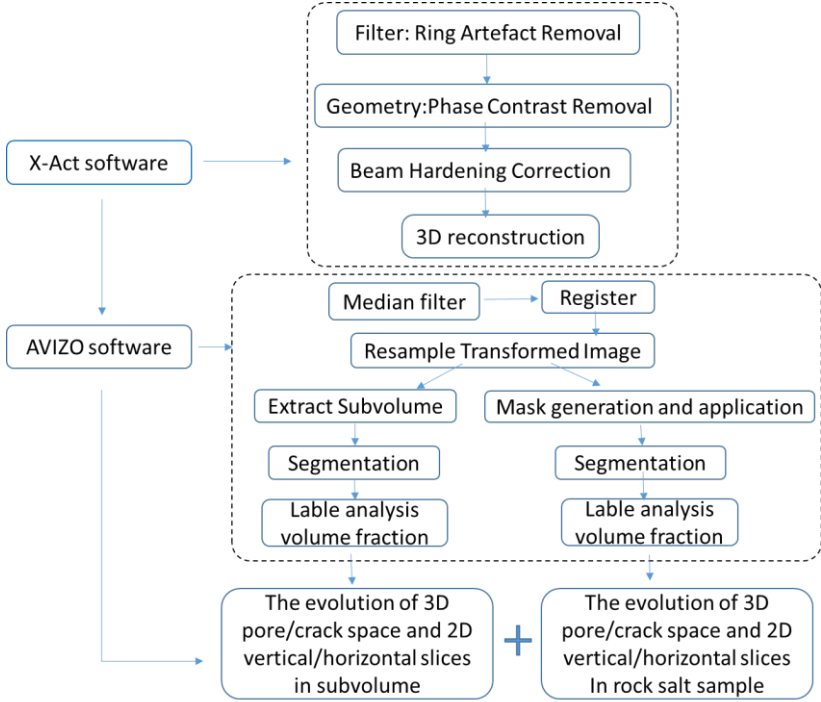


Fig.4.5 The detailed image process by AVIZO and X-Act software

A segmentation (gray levels discrimination) can help to identify (a part) of the porosity (the black ones); it is based on the gray values of the image data. However, when dealing with a volume, the external surface sample (background) is also considered as a part of porosity. This necessitates to

generate a 3D mask to identify the inside and outside parts of the sample, i.e. to separate sample from background. Fig.4.6 gives an example of this operation performed on sample XZ25-4. The ‘Arithmetic’ module is used to carry out this phase. As a result, internal volume of sample is obtained to do a segmentation without the interference from outside of sample. “Volume fraction” module can provide an accurate quantification of pore/crack volume, taking sample’s internal volume as the mask volume.

The ‘extract subvolume’ procedure allows to extract the zone we want to focus on. This extracted 3D volume will undergo a segmentation in order to draw a 3D pore and crack scheme. Then, the Label Analysis allows to process to a wide range of volume measurements to quantify pore and crack. And ‘Volume fraction’ module can also give an estimated porosity.

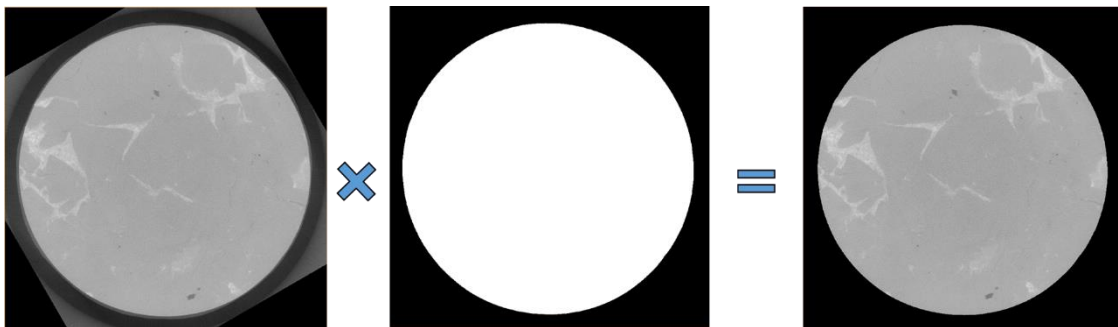


Fig.4.6 Mask application by taking 2D slice of sample XZ25-4 as an example

4.3. Permeability evolution in tests **H1** before axial loading

4.3.1. Time-dependent behavior during hydrostatic test **H1**

Since time effects on permeability had been preliminary underlined on the samples XZ24-1 and XZ24-2, a systematic study of time effects was conducted. Therefore, a series of hydrostatic tests **H1** were performed to measure both permeability and volumetric strain with time at two different levels of $P_c=5\text{MPa}$ and 10MPa for four samples (XR02-4, XS01-4, XZ25-4 and XS01-5). The results are presented in this section. For sample XS01-5, which was used to investigate Klinkenberg effect in §3.3.6, the results with 2MPa gas pressure were selected to detect time effects.

The ‘initial’ permeability and porosity were measured at $P_c=3\text{MPa}$. The confining pressure was then increased to 5MPa and kept constant in order to measure the changes in permeability, porosity and volumetric strain with time. The next step was to increase P_c to 10MPa , and the same measurements were performed (such as at $P_c=5\text{MPa}$). Table 4.2 - 4.5 gives the results of tests **H1** for four samples. The variations of permeability and volumetric strain with time at the two levels of confinement are plotted in Fig.4.7.

There is first a general tendency that can be observed in the whole set of results, which evidence the time effect under hydrostatic loading:

- A decrease in porosity that always starts from a low value and becomes almost non measurable (with our gas technics) after a time less than 1 week.
- A parallel decrease in permeability, which is quite logical.
- A strain effect that is not systematic i.e. sometimes strains evolved with time and sometimes not (see comments after Fig.4.7)

Table 4.2 Variations of permeability (K), porosity (ϕ) and volumetric strain (ϵ_v) with time for sample XS01-4 at different P_c

XS01-4	$P_c = 5\text{MPa}$				Time (hours)	$P_c = 10\text{MPa}$		
	K(m ²)	$\epsilon_v(10^{-6})$	$\phi(\%)$	K/K ₀		K (m ²)	$\epsilon_v(10^{-6})$	K/K ₀
	2.12E-16	272.25	0.36	1.0000	167.58	8.10E-17	572.25	0.3821
	2.01E-16	286.50	0.26	0.9481	174.92	6.10E-17	583.00	0.2877
	1.89E-16	320.25	0.16	0.8915	189.42	5.04E-17	579.75	0.2377
	1.86E-16	321.00	0.15	0.8774	193.92	4.93E-17	595.50	0.2325
	1.86E-16	337.50	0.14	0.8774	198.67	4.80E-17	583.50	0.2264
	1.85E-16	341.50	0.11	0.8726	214.00	3.90E-17	582.75	0.1840
	1.80E-16	343.00	0.09	0.8491	218.75	3.86E-17	595.50	0.1821
	1.78E-16	348.00	0.09	0.8396	222.75	3.79E-17	597.75	0.1788
	1.46E-16	360.75	0	0.6887	285.58	2.13E-17	626.25	0.1005
	1.45E-16	359.25		0.6840	290.25	2.02E-17	639.00	0.0953
	1.43E-16	372.50		0.6745	294.92	2.03E-17	650.25	0.0958
	1.40E-16	372.75		0.6604	308.83	1.93E-17	672.00	0.0910
	1.39E-16	368.25		0.6557	312.58	1.87E-17	655.50	0.0882
					319.25	1.89E-17	663.75	0.0892
					333.25	1.82E-17	654.75	0.0858
	$P_c = 3\text{MPa}$ (initial loading)				338.42	1.77E-17	671.25	0.0835
	2.48E-16	178.5	0.44		343.58	1.76E-17	699.00	0.0830
					359.25	1.63E-17	695.25	0.0769
					366.25	1.63E-17	707.25	0.0769
					453.08	1.64E-17	706.50	0.0774

The results for this sample, especially for its porosity, are a little bit weird. Its permeability is very high (10^{-16}m^2 order of magnitude), compared to the other ones. On the other hand, its initial porosity (0.36%) is comparable with that of the other samples. Such a surprising low value had been checked several times to verify if this was not an artefact or an experimental issue. All the results had shown the same range of porosity (between 0.3 and 0.6%). This kind of value made us think about a cracked network that could lie through the whole sample. For example a diametral crack, with an aperture of $5\mu\text{m}$, throughout the sample would lead to 10^{-16}m^2 (order or magnitude) permeability. Such a crack has dramatic effect on permeability but is negligible on a porosity point of view. It will be seen later that 0.3% porosity is consistent with micro-CT observations (but with a low resolution). At this stage, the only plausible explanation of such a high permeability is ‘cracking’. In parallel the confining pressure effect on permeability and its evolution with time are present but far from being spectacular. From 5 to 10MPa (at the end of the tests) the permeability starts at $2.12 \cdot 10^{-16}$ to end at $1.64 \cdot 10^{-17}\text{m}^2$. This fact is

not really consistent with the (mentioned before) cracking, which should be highly sensitive to confining pressure. What is nevertheless surprising is that, after 100 hours at 5MPa, the porosity is not measurable while the permeability is still of $10^{-16}m^2$ order of magnitude. At this stage, it is very difficult to find a logical explanation i.e. porosity close to zero and high permeability value.

Table 4.3 Variations of permeability (K), porosity (ϕ) and volumetric strain (ϵ_v) with time for sample XR02-4 at different P_c

XR02-4 Time (hours)	$P_c = 5MPa$				Time (hours)	$P_c = 10MPa$		
	K(m ²)	$\epsilon_v (10^{-6})$	ϕ (%)	K/K ₀		K(m ²)	$\epsilon_v (10^{-6})$	K/K ₀
2.75	1.22E-19	701.25	0.32	1.00000	180.00	1.71E-22	1322.3	0.00140
23.17	8.70E-20	860.25	0.31	0.71311	190.00	5.28E-23	1584.8	0.00043
48.67	3.34E-20	930.75	0.28	0.27377	210.83	3.77E-23	1605.7	0.00031
55.00	3.07E-20	930.00	0.22	0.25164	234.83	3.70E-23	1618.8	0.00030
70.00	6.83E-21	934.50	0.12	0.05598	258.72	3.66E-23	1633.3	0.00030
75.00	4.40E-21	940.00	0.1	0.03607	306.70	3.34E-23	1675.5	0.00027
162.80	1.28E-21	943.50	0	0.01049	331.68	3.22E-23	1706.3	0.00026
172.00	1.10E-21	939.75		0.00902	359.01	3.18E-23	1728.0	0.00026
	$P_c = 3MPa$ (initial loading)							
	2.33E-19	399.75	0.38					

The porosity values for XR02-4 are similar as for the previous sample. The time effect leads to a ‘zero’ porosity value after 160 hours at 5MPa. While observing permeability, its evolution is now consistent with porosity changes. The initial permeability is moderate to low ($10^{-19}m^2$) and the variation with time is spectacular as it reached $10^{-21}m^2$ after 160 hours. Loading from 5 to 10MPa has strong additional effects and led to a loss of one order of magnitude. A supplementary wait of 16 hours at 10MPa induced a new loss as the permeability now reached $3.9 \cdot 10^{-23}m^2$, then stabilized with time (final value at $3.2 \cdot 10^{-23}m^2$). Such a low value can be related to an almost non-permeable material.

Table 4.4 Variations of permeability (K), porosity (ϕ) and volumetric strain (ϵ_v) with time for sample XZ25-4 at different P_c

XZ25-4 Time (hours)	$P_c = 5MPa$				Time (hours)	$P_c = 10MPa$		
	K(m ²)	$\epsilon_v (10^{-6})$	ϕ (%)	K/K ₀		K(m ²)	$\epsilon_v (10^{-6})$	K/K ₀
7.98	8.56E-19	413.25	0.20	1.0000	294.85	5.44E-20	738.00	0.0636
31.73	7.00E-19	425.25	0.06	0.8178	313.85	3.38E-20	753.00	0.0395
54.68	3.54E-19	428.25	0	0.4136		Oil leakage in sample		
126.68	3.03E-19	453.75		0.3540				
145.68	2.61E-19	444.00		0.3049				
171.68	2.98E-19	441.00		0.3481				
194.77	2.77E-19	441.75		0.3236				
223.18	2.75E-19	440.25		0.3213				
280.00	2.85E-19	440.00		0.3329				
	$P_c = 3MPa$ (initial loading)							
	9.03E-19	217	0.52					
	$P_c = 1.5MPa$ (initial loading)							
		90.75	0.86					

There was an experimental issue with sample XZ25-4 and the test had to be stopped before the end. The confining pressure effect (from 1.5 to 5MPa) is very strong on the initial porosity that started at 0.86% to be 0.2% at 5MPa. After 55 hours waiting it was virtually zero. On certain extents, there are similarities with sample (Table 4.2). The initial permeability is lower ($8.6 \cdot 10^{-19} \text{m}^2$) for this new sample and the relative permeability decrease is 0.42 when the measured porosity is 0. For sample XS01-4 and XS01-5 (same origin, see Table 4.2 and 4.5), it was 0.69 and 0.88 respectively (at 0 porosity). This decrease can be compared with the one of sample XR02-4 that was recorded at 0.009 (under the same conditions: from initial porosity to 0).

Table 4.5 Variations of permeability (K), porosity (ϕ) and volumetric strain (ϵ_v) with time sample XS01-5 under different P_c

XS01-5 Time (hours)	$P_c = 5\text{MPa}$				Time (hours)	$P_c = 10\text{MPa}$		
	K(m ²)	$\epsilon_v (10^{-6})$	ϕ (%)	K/K ₀		K(m ²)	$\epsilon_v (10^{-6})$	K/K ₀
0.00	4.1E-20	305	0.21	1.0000	141.83	3.2E-20	749	0.7805
70.96	3.8E-20	318	0.20	0.9268	165.41	2.8E-20	766	0.6829
95.92	3.7E-20	300	0.15	0.9024	237.91	2.0E-20	822	0.4878
115.00	3.6E-20	336	0.06	0.8780	263.41	1.8E-20	820	0.4390
					288.66	1.1E-20	819	0.2683
					309.75	5.2E-21	829	0.1268
					329.75	9.6E-22	823	0.0234
	$P_c = 3\text{MPa}$ (initial loading)				402.00	1.1E-22	834	0.0027
	5.0E-20	271	0.81		422.00	9.2E-23	827	0.0022
					454.00	5.5E-23	815	0.0013

The sample XS01-5 was extracted from the same plug used for the XS01-4. The first observation that can be made is that its initial permeability is very low (10^{-20}m^2) compared to XS01-4 (10^{-16}m^2 order of magnitude), almost four orders of magnitude lower. This could evidence that the XS01-4 sample is atypical but the permeability of XS01-3 (see Fig.3.12) was found to be the same order of magnitude as XS01-4. The present results may be seen as highlighting the strong dispersion of salt properties. Once again there is a strong confining pressure effect from 3MPa to 5MPa on porosity (0.81 to 0.21%), but not on permeability ($5 \cdot 10^{-20}$ to $4.1 \cdot 10^{-20} \text{m}^2$). This is a common phenomenon observed for all the samples. Fig.4.7 (a) gives a comparison of both material behaviors.

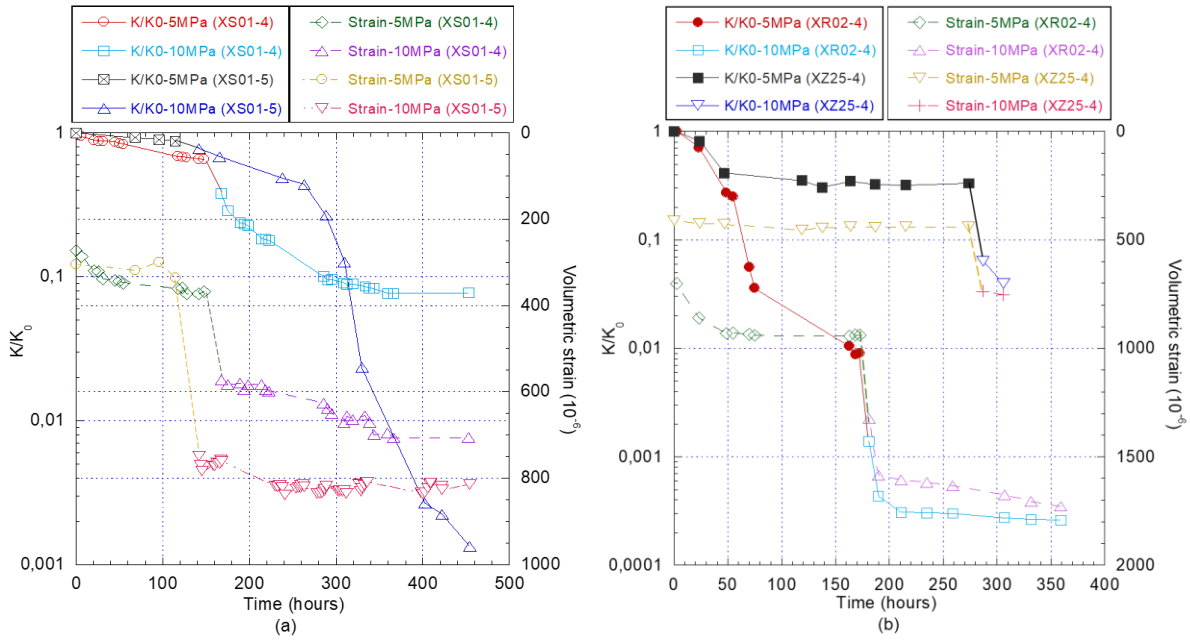


Fig.4.7 Variations of permeability and volumetric strain with time for four samples

This is an interesting comparison as these two materials are of the same nature. It was chosen to plot the permeability variation as its ratio K/K_0 (K_0 is the 'initial' permeability at 5MPa). Volumetric strains are plotted v.s. time. At $P_c=5\text{MPa}$, volumetric strains are comparable for both samples. They are different at 10MPa (but nevertheless comparable - $700\mu\text{m/m}$ v.s. $800\mu\text{m/m}$ at the end of the tests). Their evolution with time are similar. The major difference can be seen in the permeability ratio evolution. There is a constant and smooth decrease for sample XS01-4, which is also observed for XS01-5 at the beginning. However, (at around 300h) a rapid and sharp decrease was recorded for XS01-5 despite a quasi-constant volumetric strain. A similar phenomenon was also detected for sample XR02-4 at 5MPa (see Fig.4.8) with a sharp decrease in permeability from 50 to 173h while there was no variation in volumetric strains. It must be underlined that this sample is much more deformable than the three other ones, which are comparable on this aspect.

It is therefore useful to examine Fig.4.8 in which permeability variations are plotted v.s. volumetric strains.

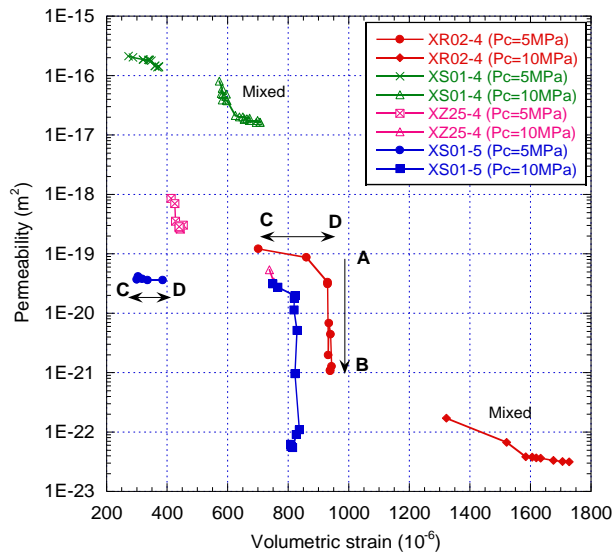


Fig.4.8 Permeability variations v.s. volumetric strains four four samples

Results presented in Fig.4.8 reveal two different kind of behaviors, which can possibly be mixed:

-a strong decrease in permeability while the volumetric strain is almost constant (**A** to **B**). This can be observed at 5 or 10MPa confining pressure.

-a quasi-constant value despite a volumetric strain evolution (**C-D**), this is observed at 5MPa confining pressure. It cannot be assessed if this phase would not be followed by a ‘**A-B**’ phase if the waiting time was longer.

The mixed behavior is a continuous decrease in permeability v.s. volumetric strains. This was observed at 10MPa confining pressure.

There are not enough tests to conclude but they clearly indicate that there is sealing phenomena in the permeability reduction. It can be assumed that this sealing is evidenced by the ‘**A-B**’ phase i.e. negligible strains and strong permeability reduction. The mixed phases describe a logical process: increase in compaction and decrease in permeability. Such a decrease could be the superposition of crack closure and/or sealing. The **C-D** phase is more difficult to analyse as it would mean that despite material compaction, the porous structure remained (almost unchanged). In every case the material porosity is close to 0 and gas is supposed to flow through cracks with a negligible porosity (i.e. crack volume is very small compared to the sample volume). The (quasi) constant permeability would indicate that a ‘particular’ compaction phase could occur without significant closure of crucial cracks. A hypothetical scheme could be imagined with a crack, which would be stiffened by rigid material (see Fig.4.37 in §4.4.5.1). Such a scheme is consistent with the fact that, sometimes, increase in confining pressure does not lead to (significant) reduction of permeability.

It is also interesting to compare time-dependent properties at different P_c . The results are shown in Table 4.6 below. As mentioned before, although sample XS01-4 and XS01-5 are from the same salt

core, they exhibit quite different gas transfer properties and different time-dependent behaviors. To sum up, time effects on permeability were observed for all samples (strong for samples XR02-4, XS01-5 but weak for the other two samples).

Moreover, the evolution of permeability and volume strain sometimes exhibit inconsistencies. At $P_c=5\text{MPa}$, there is a significant decrease (two orders of magnitude) in permeability and a large deformation for sample XR02-4. While the other three samples exhibit weak time-dependent behavior. However, at $P_c=10\text{MPa}$, the result illustrates a time-dependant sealing for sample XS01-5: a significant decrease (three orders of magnitude) in permeability came along with very small volumetric strains.

Table 4.6 Comparison between different samples: variations of permeability and volumetric strain with time under $P_c=5$ and 10MPa

	$K_g(\text{m}^2)$	$\varepsilon_v(10^{-6})$	$K_g(\text{m}^2)$	$\varepsilon_v(10^{-6})$
XS01-4	$P_c = 5\text{MPa} (\Delta t = 147.8\text{hours})$		$P_c = 10\text{MPa} (\Delta t = 285.5\text{hours})$	
	2.12E-16 ~ 1.39E-16	272.25 ~ 368.25	8.10E-17 ~ 1.64E-17	572.25 ~ 706.50
	$\Delta K_g \approx 0$	$\Delta \varepsilon_v = 96$	$\Delta K_g < 1$ order of magnitude	$\Delta \varepsilon_v = 134$
XR02-4	$P_c = 5\text{MPa} (\Delta t = 172.6\text{hours})$		$P_c = 10\text{MPa} (\Delta t = 178\text{hours})$	
	1.22E-19 ~ 1.10E-21	701.25 ~ 939.75	1.71E-22 ~ 3.18E-23	1322.3 ~ 1728.0
	$\Delta K_g \approx 2$ orders of magnitude	$\Delta \varepsilon_v = 238.5$	$\Delta K_g < 1$ order of magnitude	$\Delta \varepsilon_v = 405.7$
XZ25-4	$P_c = 5\text{MPa} (\Delta t = 281.9\text{hours})$		$P_c = 10\text{MPa}$	
	8.56E-19 ~ 2.85E-19	413.25 ~ 440.00	5.44E-20 ~	738 ~
	$\Delta K_g < 1$ order of magnitude	$\Delta \varepsilon_v = 26.75$		
XS01-5	$P_c = 5\text{MPa} (\Delta t = 120\text{hours})$		$P_c = 10\text{MPa} (\Delta t = 320\text{hours})$	
	4.10E-20 ~ 3.60E-20	305 ~ 336.0	3.20E-20 ~ 5.50E-23	749 ~ 815
	$\Delta K_g \approx 0$	$\Delta \varepsilon_v = 31$	$\Delta K_g \approx 3$ orders of magnitude	$\Delta \varepsilon_v = 66$

4.3.2. Partial conclusion

This section mainly explored the time-dependent behavior from the measurements of volumetric strain, permeability and porosity at two confinement levels (5 and 10MPa). Four different samples were used for this investigation. For all samples, no matter permeability is high or low, the porosity is extremely low, in the range of 0.86-0%. This was also observed on the tested samples in chapter 3. The porosity decreased to 0 (non-measurable) with time at confining pressure of 5MPa for all samples. The results confirmed that porosity of salt rock is sensitive to confinement and decreased with time under hydrostatic loading.

The time effects on permeability decrease has been clearly evidenced from the above results, except the very weak decrease for samples XS01-4 and XS01-5 at 5MPa confining pressure. This difference can be mainly attributed to the confining pressure level and the strong dispersion of salt properties. Different samples exhibit considerably different time-dependent behaviors. For example, there is a sealing with time (i.e. significant decrease in permeability but with small changes in volumetric strain)

for sample XR02-4 at $P_c=5\text{MPa}$, and for sample XS01-5 at $P_c=10\text{MPa}$. Another observed phenomenon is a quasi-constant permeability despite a volumetric strain evolution. Sometimes, a mixed behavior of both can also be observed.

In the following section, these samples were loaded with (tri)-axial loadings (triaxial tests for XR02-4 and XS01-4; uniaxial test for XZ25-4). The investigation of potential sealing of cracks with time for these damaged samples were then carried out with hydrostatic test **H2**. The comparison of time effects between these intact and damaged samples is shown in §4.4 and 4.5.

4.4. Permeability evolution in triaxial test and sealing/healing effects on five damaged samples (a comparison of hydrostatic tests H1 and H2)

Triaxial tests were performed on five samples to investigate permeability variation with deviatoric stress. For samples XZ25-3, XR02-4 and XS01-4, a particular attention was paid to evaluate time effects on permeability during triaxial test (by measuring permeability evolution at different constant deviatoric stresses).

H1 type hydrostatic test was conducted **before** the triaxial tests (except for sample XR02-3– which had not been submitted to **H1**). For samples XS01-3 and XZ25-3, tests **H1** were devoted to investigate the variations of permeability and couplings with P_c . Whereas, as described in §4.3, tests **H1** for XR02-4 and XZ25-4 were dedicated to exploring time effects on these properties under two confinement levels (5MPa and 10MPa).

After triaxial tests, these five samples were taken out and re-placed into hydrostatic cell to perform a new hydrostatic test (**H2**). The purpose was to detect (by comparing with **H1** results) whether potential damage had induced effects on permeability, porosity and couplings (except for sample XR02-3). They were also used to characterize the potential sealing/healing effects on those pre-damaged samples.

This section introduces these three tests (**H1**, triaxial test and **H2**) for each sample. For each specimen, the triaxial test is presented first, followed by a comparison of tests **H1** and **H2**. The results of X-ray microtomography experiments for samples XR02-4 and XS01-4 are also given in this section.

4.4.1. Sample XR02-3: triaxial test and H2 test

4.4.1.1. Triaxial test for sample XR02-3

The results of triaxial test for sample XR02-3 presented in Fig.4.9 were obtained under different steps of testing. The initial permeability values, recorded at step 1 with $P_c=3\text{MPa}$ and at step 2 with $P_c=5\text{MPa}$ are already extremely low, respectively $6.1\text{E-}23\text{m}^2$ and $5.7\text{E-}23\text{m}^2$, which are virtually the same. At step 3, the confining pressure was 7MPa and the deviatoric loading was started, the permeability fell to $2\text{E-}23\text{m}^2$. The following steps were conducted with this constant confining pressure

and the sample degradation can be observed with the regular increase in permeability, by two orders of magnitude, due to the axial stress increase, up to 51MPa. Despite this growing, the sample’s gas permeability remains low: $5E-21m^2$, which is likely to indicate a small damage. The sample was then dismantled and placed into a hydrostatic cell in order to performed test **H2**, described in next section §4.4.1.2.

Fig.4.10 gives the stress-strain curves of this triaxial test. The occurrence of dilatancy was observed after a deviatoric stress up to 35MPa. This dilatancy came along with a significant increase in permeability (more than one order of magnitude). However, in contrast to other materials (such as granite, concrete, etc.), this increase led the salt sample to remain of very low permeability.

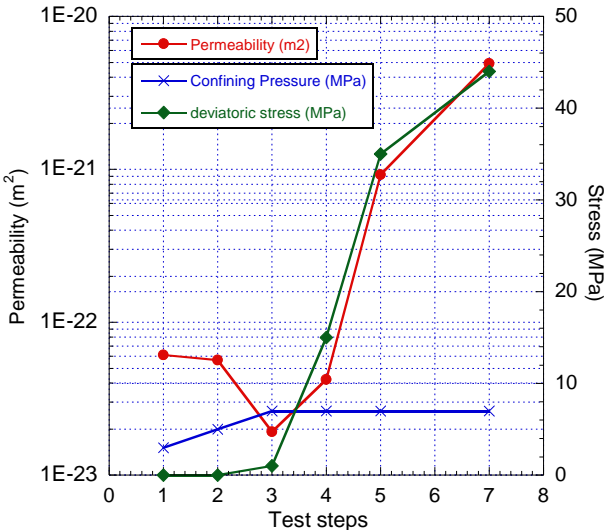


Fig.4.9 Permeability measurements during triaxial test

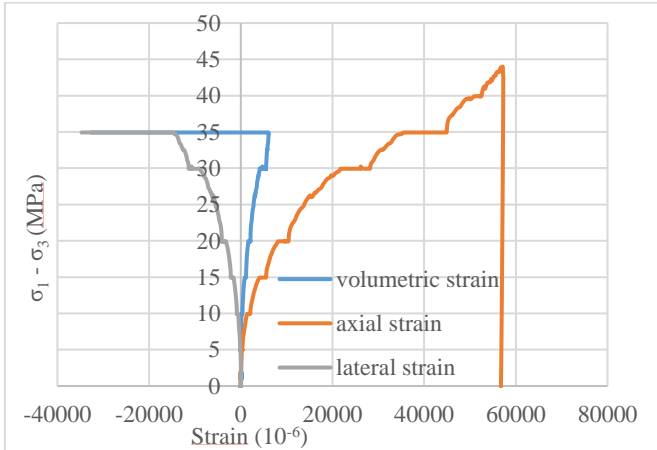


Fig.4.10 Stress-strain curves of triaxial test for sample XR02-3

4.4.1.2. Hydrostatic test H2 for sample XR02-3

Hydrostatic test **H2** was then carried out on this sample (XR02-3). Gas permeability was measured and coupling effects were estimated at 6 levels of confining pressure (from 3 to 20MPa). It was also decided to observe the time effect at $P_c=14MPa$. The results for gas permeability can be found in Fig.4.11

and the time effects in Fig.4.12. At $P_c=3\text{MPa}$ the permeability is now $2.8\text{E-}19\text{m}^2$ (point C in Fig.4.11). This value can be compared to the first one (point A in Fig.4.11), measured before deviatoric loading during the triaxial test, which was around $6.1\text{E-}23\text{m}^2$. Such an increase, by 4 orders of magnitude, indicates that the sample was seriously damaged and that multiple cracks had been produced. This new result can be considered as a little bit surprising as, at the end of the deviatoric test, the permeability was around $5\text{E-}21\text{m}^2$ at 51MPa axial stress (point B in Fig.4.11). Dismounting the sample (so no confining pressure for two months) brought back a high permeability value. This can be attributed to crack opening and **evidences here that the sealing is valid under stress but is likely to vanish when the material is no longer stressed. This is an interesting result.** There is then a classical decrease in permeability with the increase of confining pressure but it can be underlined that 20MPa of confining pressure are necessary to recover the initial sample permeability i.e. to close the cracks due to deviatoric stress. The time effect is still present as it is shown in Fig.4.12, which illustrates the recording of volumetric strains and permeability varying with time, at 14MPa . There is a first phase of permeability reduction, which is quite sharp at the beginning, followed by a plateau. This phenomenon is consistent with the volumetric strain evolution, which also reached a plateau at the end of this phase.

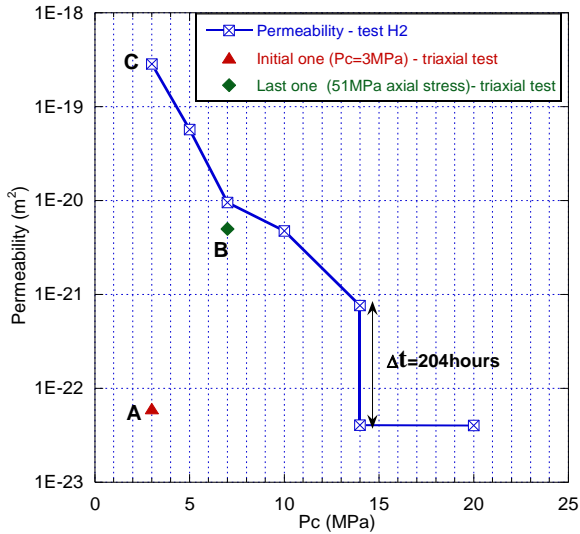


Fig.4.11 Variation of permeability with P_c /time

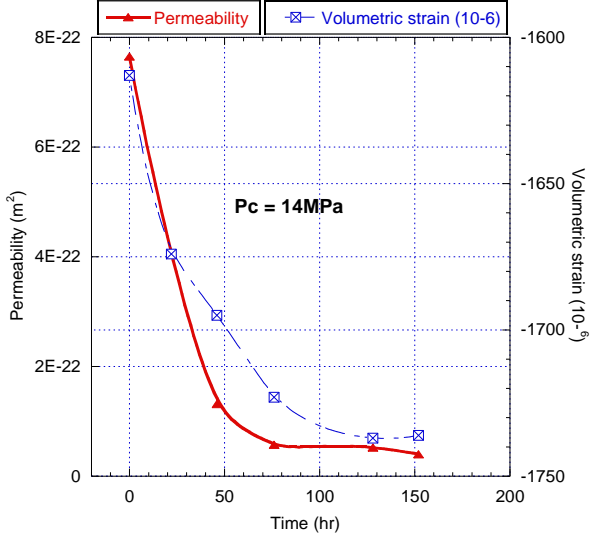


Fig.4.12 Variations of K and ϵ_v with time

Results on coupling effects and the resulting apparent Biot’s coefficient are given in Fig.4.13 and Fig.4.14. As for the previous experiments, the potential coupling effect was detected by a progressive increase in gas pore pressure, while the confining pressure is fixed at a constant value. At the highest confining pressure (20MPa) almost no coupling was observed i.e. the volumetric strain due to P_i is virtually 0. For the other confining pressures (3 to 14MPa), there is a clear coupling which is illustrated both in Fig.4.13 and Fig.4.14. The effect of Terzaghi effective pressure is also present (Fig.4.13) as there is a stronger coupling for the lowest values (i.e. high P_i level) than for the highest ones. There is an apparent threshold at 7MPa , which is only indicative here. The volumetric strains due to P_i and the apparent Biot’s coefficient can be observed in Fig.4.14. The confining pressure level and the crack

closure induced have a strong reduction effect of the volumetric expansion due to P_i , which exhibits a continuous decrease. This kind of phenomenon was also observed on cracked sandstone samples [97]. Combined with the progressive material stiffening, this leads to a stable value on the apparent Biot's coefficient, lying in the range of 0.35-0.3 (excepted at 5MPa, which is maybe artifact). This Biot's coefficient value is significantly higher than for the previous experiments (for the other samples that were not (a priori) damaged), especially at medium confining pressure (7-14MPa). This confirms that coupling effects occur through cracks i.e. gas pressure into cracks or joint grains can induce material expansion. Damage logically amplifies this effect.

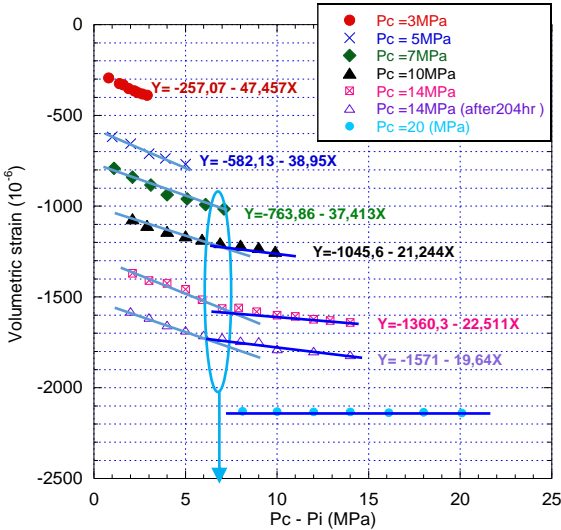


Fig.4.13 Variation of ϵ_v with $(P_c - P_i)$

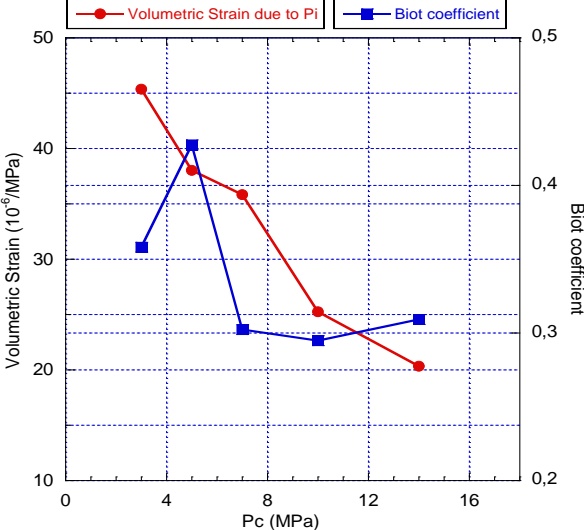


Fig.4.14 Variations of Biot and $\Delta\epsilon_v$ due to P_i with P_c

4.4.1.3. Partial conclusion for sample XR02-3

Triaxial test was first performed for XR02-3. The initial permeability values was extremely low ($6.1E-23m^2$). Axial loading up to 51MPa led to a significant increase in permeability (two orders of magnitude). Dismounting the sample brought a higher permeability value at the beginning of test **H2**, compared to the last value of triaxial test. The initial permeability in **H2** was much higher than the one at the end of triaxial test, which can reveal that multi-cracks had been produced by axial loading. Time effects on permeability and strains were clearly observed at $P_c=14MPa$ during **H2**. Permeability and couplings decreased with confining pressure. From the point of view of permeability and coupling, the confining pressure of 20MPa is high enough to close the cracks due to deviatoric stress. It is also confirmed that poro-mechanical coupling may occur through cracks and is reduced with confining pressure increase.

4.4.2. Sample XZ25-3: H1 test, triaxial test and H2 test

4.4.2.1. Triaxial test for sample XZ25-3

A **H1** type test had been carried out on sample XZ25-3 prior to triaxial test, in which permeability decreased from $1.33\text{E-}21$ to $1.28\text{E-}22\text{m}^2$ with P_c increasing from 2 to 22MPa (see the details in §4.4.2.2). During the triaxial test, before loading deviatoric stress, the initial permeability was $2.78\text{E-}22\text{m}^2$ at 7MPa confining pressure. Then, the confining pressure was kept constant at 7MPa and the deviatoric stress was progressively increased, as shown in Fig.4.15. At the beginning of axial loading and up to 7MPa deviatoric stress (total axial stress was 14MPa) there was a strong decrease in permeability (almost unmeasurable so close to 0). For the next steps, the permeability remained extremely low (out of measurement) until axial stress reached 24MPa. Even under this loading, the sample volumetric strain indicated ‘compaction’ (see Fig.4.15 (a)). Dilatancy and resultant potential increase in permeability may not occur even under very high deviatoric stress at this confining pressure (7MPa) for this sample. It was therefore decided to unload the sample. The deviatoric stress was first put down to 0MPa, then the confinement was decreased from 7 to 2MPa. This was expected to more easily produce visible damage. This global unloading brought an immediate increase in permeability from ≈ 0 to $4.03\text{E-}23\text{m}^2$. It can be assumed that this increase was mainly due to confining pressure unloading.

As a consequence, the following measurements were carried out at $P_c=2\text{MPa}$. The first increase in deviatoric stress from 0 to 17MPa did not cause a significant increase in permeability (from $4.03\text{E-}23$ to $5.21\text{E-}23\text{m}^2$, see Fig.4.16). And the sample was still in compaction (see Fig.4.15 (b)). It can also be observed in Fig.4.15 (b) that at 22MPa (and over) deviatoric stress some dilatancy was recorded. It was thus decided to evaluate the time effects at two constant deviatoric stresses (22 and 27 MPa). The results are shown in Fig.4.16 (A-B at 22MPa and C-D at 27MPa).

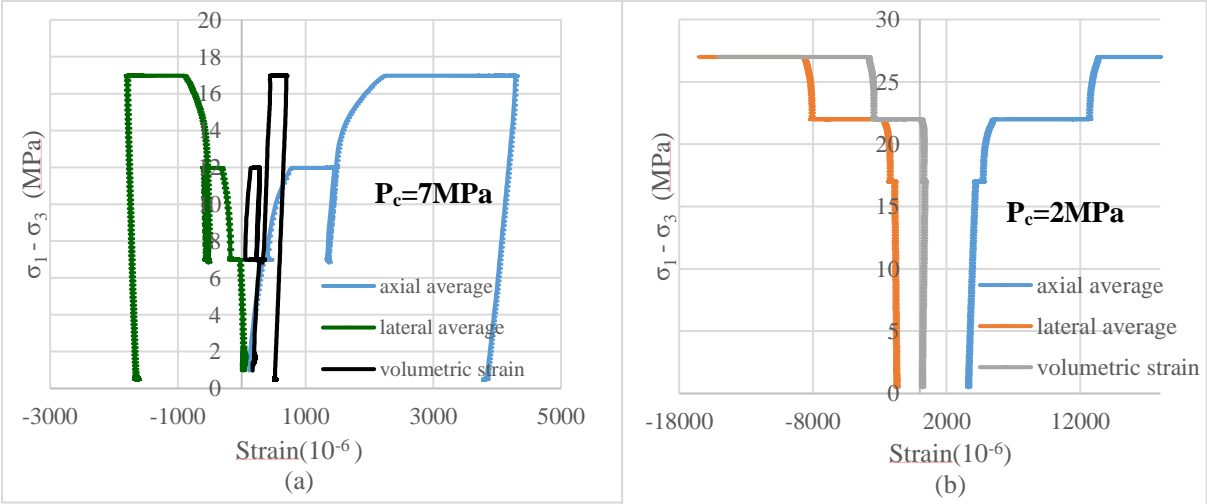


Fig.4.15 Stress-strain curves of triaxial test for sample XZ25-3

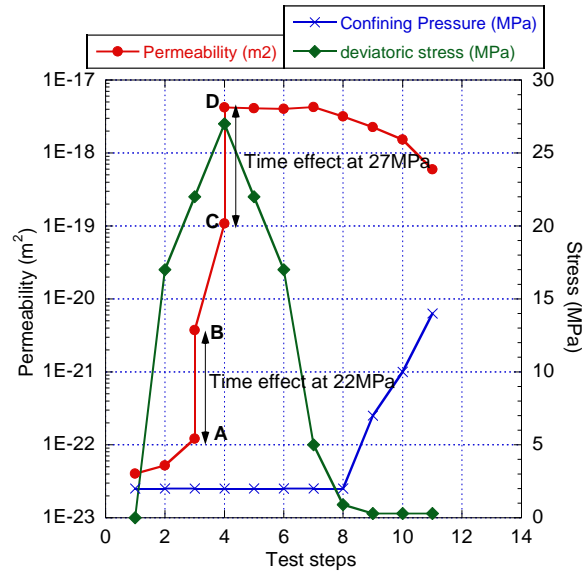


Fig.4.16 Variations of permeability and deviatoric stress (and P_c) during triaxial test

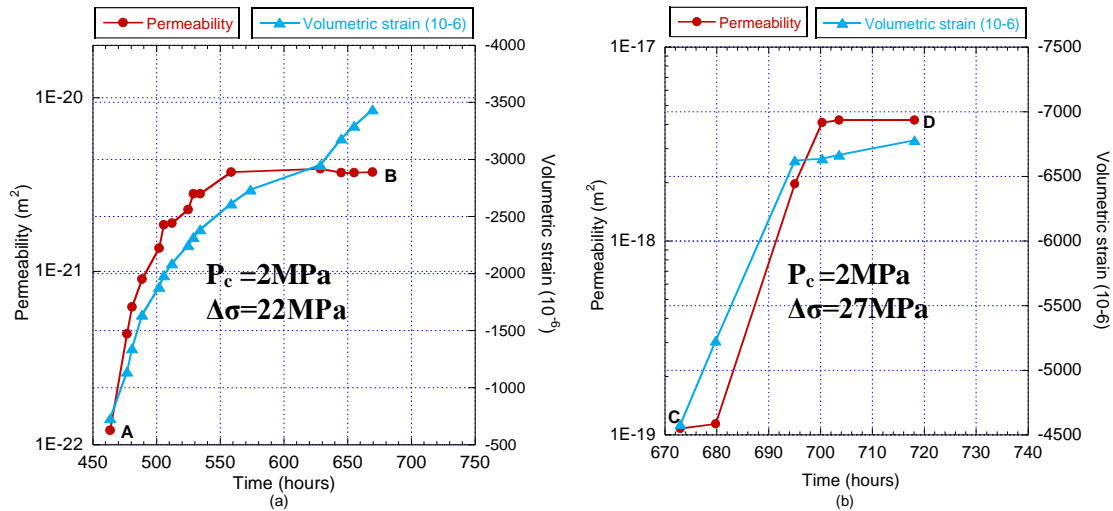


Fig.4.17 Variations of K and ϵ_v with time at $P_c=2\text{MPa}$ and $\Delta\sigma=22\text{MPa}$ (a); 27MPa (b) – negative volumetric strain indicates expansion

The deviatoric stress was kept constant at 22MPa for 7 days. As shown in Fig.4.17 (a), it can be observed that the permeability increased from $1.2\text{E-}22$ to $3.7\text{E-}21\text{m}^2$ within the first 4 days, then followed by a plateau. In parallel, the volumetric strain exhibited continuous expansion with time during this phase. In other words, the permeability increased by more than one order of magnitude, and came along with dilatancy ($\Delta\epsilon_v=0.3\%$). When deviatoric stress was increased to 27MPa, the permeability sharply increased by almost 2 orders of magnitude (from $3.7\text{E-}21$ to $1.08\text{E-}19\text{m}^2$). Then the time effects on both permeability and volumetric strain were observed, as shown in Fig.4.17 (b). The results are similar to the ones recorded at 22MPa. The permeability continuously increased and then remained constant at around $4.2\text{E-}18\text{m}^2$. As a whole, both loading and time effects led to four orders of magnitude increase in permeability, which is quite spectacular.

During deviatoric stress unloading to 0MPa, the permeability remained almost unchanged, which shows the irreversibility. This means that if cracking occurred, unloading the sample did not result to significant crack closure. A following increase in confining pressure was then applied, from 2 to 14MPa. This induced a logical decrease in permeability and as shown in Fig.4.16, it was from $3.2\text{E-}18$ to $6.0\text{E-}19\text{m}^2$ due to the increase of P_c . The damage can be considered to be partially healed from a permeability point of view as initial permeability values are far to be recovered.

4.4.2.2. Hydrostatic tests **H1** and **H2** for **XZ25-3**

Hydrostatic tests **H1** and **H2** were performed **before and after** triaxial test for this sample. The permeability, porosity and couplings were measured at different levels of confining pressure (from 2 to 22MPa) in both **H1** and **H2**. Table 4.7 presents the main results. A strong damage was observed for the triaxial test as permeability at P_c of 2MPa increased by five orders of magnitude, from $4\text{E-}23$ to $3\text{E-}18\text{m}^2$. The initial permeability value at $P_c=2\text{MPa}$ was respectively $1.33\text{E-}21\text{m}^2$ in test **H1** and $1.45\text{E-}17\text{m}^2$ in test **H2**. This difference reveals the strong damage caused by triaxial test. One can also notice that, due to the sample dismounting, a permeability evolution occurred again between the end of triaxial test and the beginning of **H2**. The effect of triaxial test is clearly a strong damage for this sample.

Fig.4.18 shows the variations of permeability and porosity with P_c in tests **H1** and **H2**. For test **H1**, the permeability sharply dropped (from $1.33\text{E-}21$ to a low value $2.52\text{E-}22\text{m}^2$) with P_c from 2 to 3MPa, then slowly decreased on a plateau. The porosity decreased from 0.3 to 0% when P_c increased to 10MPa. In test **H2**, it can be observed that the initial permeability is now $1.45\text{E-}17\text{m}^2$ and continuously decrease, with confining pressure, down to $4.30\text{E-}23\text{m}^2$. Gas permeability reveals now more sensitive to confining pressure increase (see also K/K_0 in Fig4.18 (b)). According to previous experiments conducted in our laboratory, such greater decrease and sensitivity of permeability can mainly be attributed to crack closure and to the occurrence of many new cracks due to triaxial test. The rearrangement of the grain boundaries or shapes of voids during triaxial test may not be excluded at this stage (such a rearrangement will be observed for other sample in the following). At the end of confinement (22MPa), the permeability reached a lower value than at the end of **H1**. This indicates that the damage/cracks created by deviatoric stress had been completely closed.

The damage had also a significant effect on porosity as it increased from 0.3 to 1.12%, which is consistent with the observed dilatancy during triaxial testing. The effect of confining pressure remains similar as this 'new' porosity vanished at 22MPa.

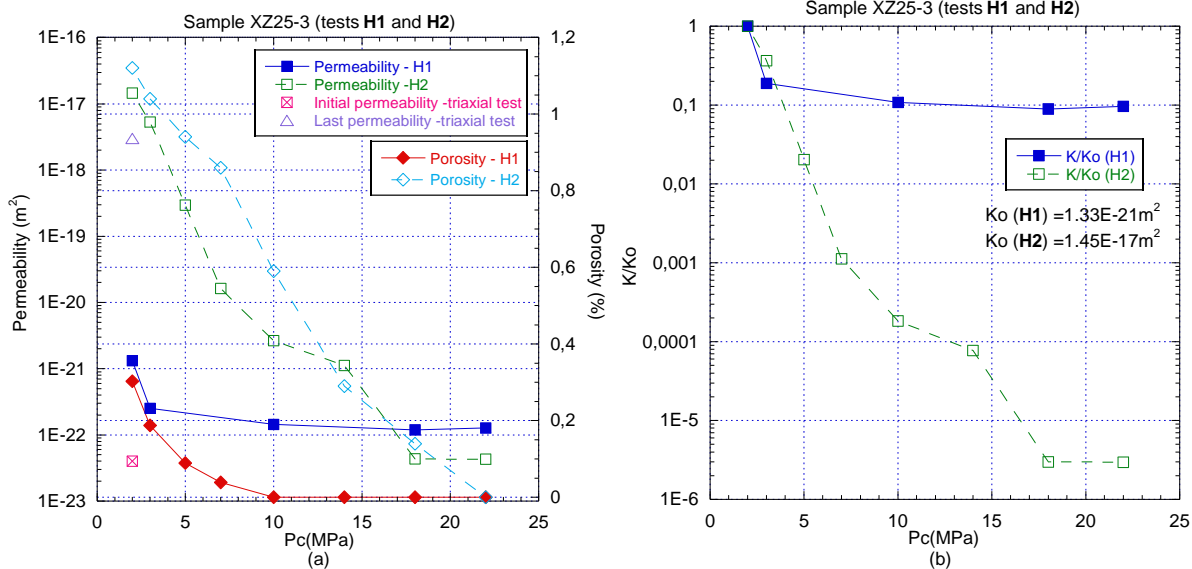


Fig.4.18 (a) changes in permeability and porosity with P_c in tests **H1** and **H2**; (b) changes in normalized permeability with P_c in tests **H1** and **H2**

Table 4.7 Changes in permeability and porosity with P_c in test **H1**, **H2** (and triaxial test)

XZ25-3	Permeability(m ²)				Porosity(%)		
	P_c (MPa)	Before (test H1)	Triaxial test (initial one)	Triaxial test (last one)	After (test H2)	Before (test H1)	After (test H2)
	2	1.33E-21	4.03E-23	3.20E-18	1.45E-17	0.3	1.12
	22	1.28E-22			4.30E-23	0	0

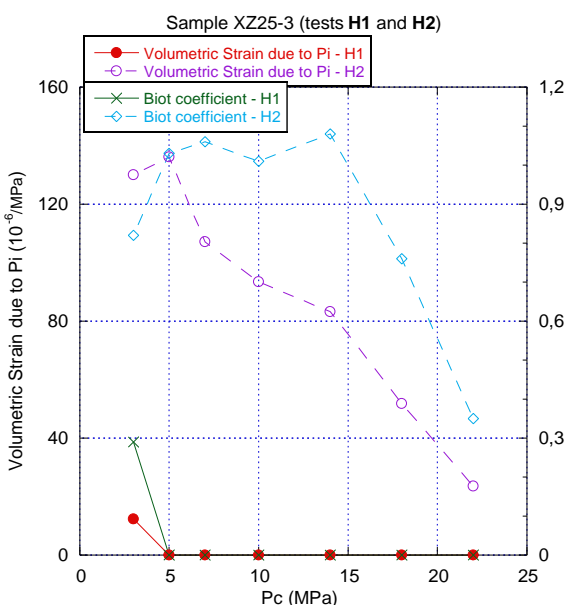


Fig.4.19 Biot and $\Delta\epsilon_v$ due to P_i for tests **H1** and **H2**

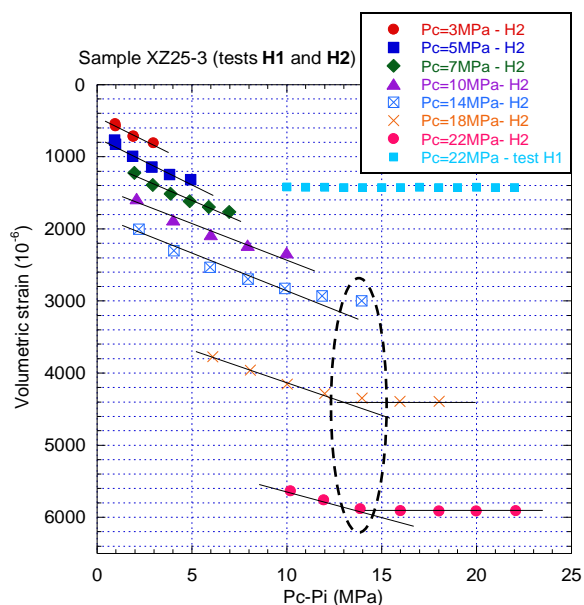


Fig.4.20 Variation of ϵ_v as the function of $P_c - P_i$

It is therefore not surprising to record a strong effect of the damage on Biot's (apparent) coefficient. Before axial test the latter was quite weak (**0.3**) at $P_c=3$ MPa then negligible at higher P_c values. After

the triaxial test, the Biot's coefficient exhibits a spectacular increase to a value close to **0.9**. If experimental artifacts (or strain measurements inaccuracies) are put aside, the Biot's coefficient remains almost constant (close to **1**) from $P_c=3$ to 14MPa (see Fig.4.19). This phase is interesting as, during the same time, there were important permeability and porosity decreases. As this indicates a crack closure, this means that coupling effects can take place even in a particular case i.e. presence of closed cracks. At a certain level of crack closure there is a logical decrease in the Biot's coefficient to around **0.3** at 22MPa. This decrease occurred at $P_c=14$ MPa and over.

The volumetric strain changes due to P_i were also recorded at different levels of P_c (as shown in Fig.4.20). This figure clearly indicates that:

- For P_c less than 14MPa, there is an immediate coupling due to internal gas pressure
- For P_c greater than 14MPa the coupling is delayed as a certain amount of internal gas pressure is needed to induce couplings i.e. volumetric strains due to P_i are negligible until P_i reaches a certain value.

This can be highlighted with the Terzaghi effective pressure effect that shows a weak coupling when P_c-P_i is high (i.e. low P_i level). The apparent threshold for this sample is 13-14MPa (it is 7MPa for sample XR02-3). It should also be underlined that the sample is much more deformable during P_c loading after the triaxial test. At $P_c=22$ MPa, the maximum ϵ_v reached $5909 \cdot 10^{-6}$ in test **H2**, while it was only $1427 \cdot 10^{-6}$ in test **H1** (see Fig.4.20). The whole compressibility of sample has significantly increased, which can be attributed to the cracking coming from triaxial test.

Table 4.8 Changes in $\Delta\epsilon_v$ due to P_i/P_c , modulus H and Biot's coefficient with different P_c in tests **H1** and **H2** for sample XZ25-3 (Measured with unloading phases for $\Delta\epsilon_v$ due to P_c)

P_c (MPa)	$\Delta\epsilon_v$ due to P_i ($10^{-6}/\text{MPa}$)		$\Delta\epsilon_v$ due to P_c ($10^{-6}/\text{MPa}$)		H (GPa)		Biot	
	H1	H2	H1	H2	H1	H2	H1	H2
3	12.375	130.08	42.75	159.42	80.81	7.69	0.29	0.82
5	0	136.14	38.82	132.36	—	7.35	0.00	1.03
7	0	107.15	33	100.64	—	9.33	0.00	1.06
10	0	93.44	37.5	92.66	—	10.70	0.00	1.01
14	0	83.30	31.14	77.37	—	12.01	0.00	1.08
18	0	51.80	36.75	69.66	—	19.31	0.00	0.74
22	0	23.59	31.32	68.01	—	42.39	0.00	0.35

Table 4.8 shows results from tests **H1** and **H2**, including $\Delta\epsilon_v$ due to pore pressure or confining pressure, apparent modulus H and Biot's coefficient. It can first be observed that in test **H1**, no coupling effects were detected from confining pressure higher than 5MPa. The triaxial test has completely changed this situation as, in test **H2**, a coupling effect was visible for the whole range of confining pressure. Both $\Delta\epsilon_v$ due to P_i and P_c were significantly higher than for **H1** ($\Delta\epsilon_v$ due to P_i increased from

12.4 $10^{-6}/\text{MPa}$ to 130.1 $10^{-6}/\text{MPa}$ at $P_c=3\text{MPa}$, meanwhile $\Delta\varepsilon_v$ due to P_c increased from 42.8 $10^{-6}/\text{MPa}$ to 159.4 $10^{-6}/\text{MPa}$). This is linked to a greater sample deformability, which is attributed to damage and newly created cracks induced by triaxial test. Increase in confining pressure closes cracks and leads to sample stiffening. As a consequence, $\Delta\varepsilon_v$ due to P_i or P_c (in test **H2**) sharply decreased with P_c . On the other hand, it must be highlighted that the ratio $\Delta\varepsilon_v(P_i)/\Delta\varepsilon_v(P_c)$, which is assumed to be a good evaluation of apparent Biot's coefficient, remains almost constant between $P_c=5$ and 14MPa. What is surprising in this case is the high Biot's coefficient b value, almost equal to 1. The numerical results even indicate that b is slightly greater than 1. As this case is not valid on a poro-mechanical point of view, it can be assumed that this is due to artefact or inaccuracy. What is to be kept in mind is the very high value of this coefficient after damage, which is consistent with previous hypotheses made on the role of cracks in coupling effects.

4.4.2.3. Partial conclusion for XZ25-3

For the triaxial test, the permeability increased by five orders of magnitude (from $4\text{E}-23$ to $3\text{E}-18\text{m}^2$) due to time effects and axial loading (up to 29MPa), and coming along with a dilatancy. As for the previous sample XR02-3, this sample dismounting also brought an increase in permeability. The damage caused by triaxial test had a strong effect on permeability and coupling, i.e. permeability and Biot's coefficient were spectacularly increased in test **H2** compared to the ones in **H1**. A logical decrease in permeability with P_c was observed in test **H2**. The greater deformability and higher sensitivity of permeability to confining pressure revealed that new multi-cracks (or damage) had been produced by triaxial test. From the permeability point of view, new cracks had been completely closed by 22MPa confining pressure.

4.4.3. Sample XS01-3: H1 test, triaxial test and H2 test

4.4.3.1. Triaxial test for sample XS01-3

Similar to the previous sample XZ25-3, test **H1** had been carried out on this sample prior to triaxial test (see §4.4.3.2). During test **H1**, the permeability varied from $9.7\text{E}-17$ to $2.1\text{E}-18\text{m}^2$ with P_c increasing from 3 to 24MPa. The permeability of this sample was not very sensitive to confining pressure from 3 to 10MPa but it appears to be (sensitive) if the confinement is increased to 24MPa. It must be mentioned here that this sample has been previously tested for the comparative tests hydrogen v.s. argon, up to $P_c=10\text{MPa}$. At that time, its argon permeability was recorded at around $1\text{E}-16\text{m}^2$ at 3MPa and $8\text{E}-17\text{m}^2$ at 10MPa.

The triaxial test was conducted at 7MPa confining pressure. Deviatoric stress was first increased to 7MPa and followed by steps of 5MPa until 37MPa. Fig.4.21 presents the strains and permeability variations with deviatoric stress. The variations of volumetric strain indicated that the sample is still in compaction (about 0.14%) until 32MPa deviatoric stress. A weak dilation phase occurred in the last

loading step from 32 to 37MPa. As shown in Fig.4.22, there were only moderate changes in permeability. Its initial value was $2.7E-18m^2$, then it was observed a slight decrease to $1.35E-18m^2$ up to 32MPa deviatoric loading. This certainly means that compaction takes precedence over damage during this loading phase. From 32 to 37MPa, the slight sample dilation led to a not significant increase in permeability, from $1.35E-18$ to $1.5E-18m^2$. On a permeability point of view, it can be said that this axial loading phase did not bring damage. The unloading phase to 0MPa brought the sample in global compaction, which is nevertheless very low: the remaining volumetric strain being 0.02%. As a logical consequence, the final value of permeability ($1E-18m^2$, see Fig.4.22) is lower than the initial one. This is consistent with the absence of obvious dilatancy (negative volumetric strain).

Two poro-mechanical results could be obtained with the measurements of volumetric strain due to 5MPa pore pressure loading at $P_c=7MPa$. They were recorded before and after deviatoric loading. It was found that the two coupling effects were both very weak and nearly the same ($\Delta\epsilon_v$ due to $P_i \approx 9 \cdot 10^{-6}/MPa$). Such low values often led to a very small Biot's coefficient. This can be regarded as a clue that almost no new cracks (or damage) were caused by deviatoric stress. This phenomenon is consistent with the previous results of gas permeability variations and confirms the absence of significant damage.

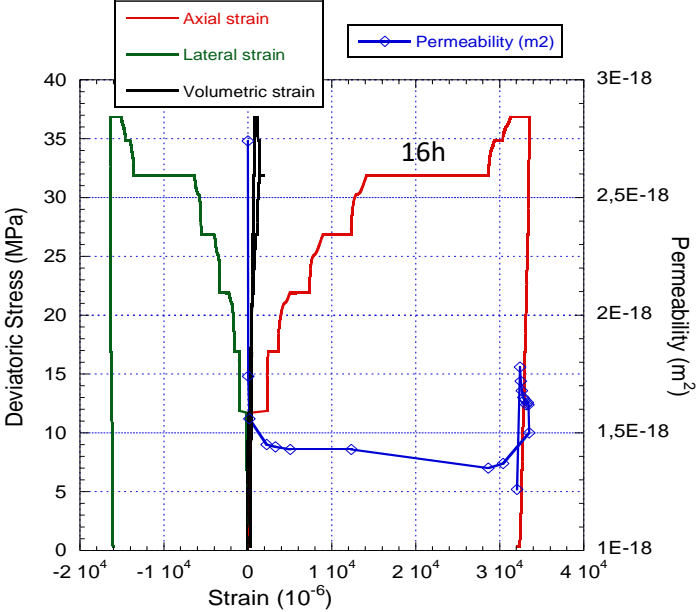


Fig.4.21 Stress-strain curves (and K_g -axial strain) of triaxial test for sample XS01-3

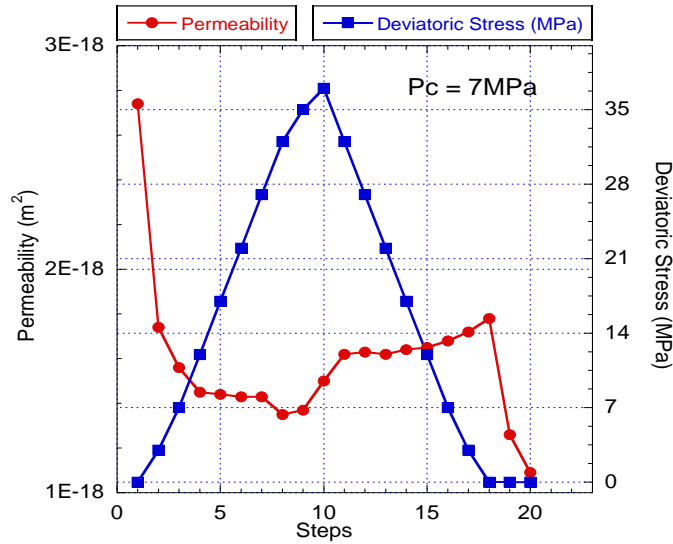


Fig.4.22 Variations of permeability and deviatoric stress during triaxial test

4.4.3.2. Hydrostatic tests H1 and H2 for XS01-3

For test **H1** on this sample, a loading from $P_c = 3$ to 24MPa and then an unloading were performed. The variation of permeability was measured in the loading-unloading phase, while porosity was only recorded in the unloading phase. A significant reduction of permeability can be observed in test **H1** (from $9.65E-17$ to $2.1E-18m^2$ with P_c increasing from 3 to 24 MPa), as presented in Table.4.9 and Fig.4.23. It was also found that the permeability reduction due to P_c is quite weak at the beginning then is amplified from $P_c=17$ MPa. This is consistent with observations made in previous comparative tests hydrogen v.s. argon (see §3.3.4). It was assumed that this sample was especially sensitive to high confining pressure ($P_c > 10$ MPa). Unloading did not bring back significant increases in permeability and porosity. The last permeability value is $3.1E-18m^2$ almost two orders of magnitude lower than the initial one ($9.65E-17m^2$ at 3MPa). This revealed a strong irreversibility.

After axial testing, the **H2** test showed a permeability decrease from $2.8E-17$ to $1.1E-19m^2$ (by more than two orders of magnitude) with P_c varying from 3 to 22MPa. There is now a more significant confining pressure effect on permeability after triaxial test than before. This phenomenon was similar for the previous sample XZ25-3. The sample damage is finally masked by high confining pressure, as the gas permeability between 14 and 22MPa is lower than the one measured (at the same stress level) during **H1** test (see comparison between point **D** and **E** in Fig. 4.23).

The porosity before triaxial test during the unloading phase was 0.1% at 3MPa. In test **H2**, it was 0.4% at $P_c=3$ MPa after damage, which is still extremely low. On this point of view, the damage has virtually no effect on porosity. The permeability value at 3MPa is $2.81E-17m^2$ (point **B** in Fig.4.23) is one order of magnitude higher than the last one at unloading phase (point **C**), but still lower than the initial one (point **A**) ($9.65E-17m^2$) in test **H1**. The small increase, recorded between **C** and **B**, eventually indicates that damage caused by 37MPa deviatoric stress is not really significant.

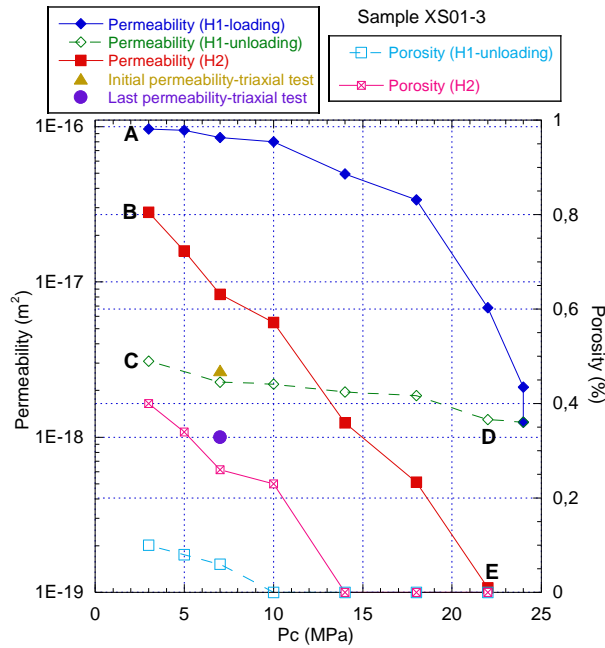


Fig.4.23 Changes in permeability and porosity with P_c in tests **H1** and **H2** (and triaxial test)

Table 4.9 Changes in permeability and porosity with P_c before (**H1**) and after (**H2**) triaxial test

XS01-3 P_c (MPa)	Permeability(m^2)			Porosity(%)	
	H1 -loading (from 3-24MPa)	H1 -unloading (from 24-3MPa)	H2 -loading	H1 -unloading (from 24-3MPa)	H2 -loading
3	9.65E-17	3.09E-18	2.81E-17	0.10	0.4
5	9.45E-17		1.58E-17	0.08	0.34
7	8.51E-17	2.26E-18	8.31E-18	0.06	0.26
10	7.98E-17	2.20E-18	5.49E-18	0	0.23
14	4.97E-17	1.95E-18	1.24E-18	0	0
18	3.38E-17	1.85E-18	5.12E-19	0	0
22	6.81E-18	1.30E-18	1.07E-19	0	0
24	2.10E-18	1.25E-18			

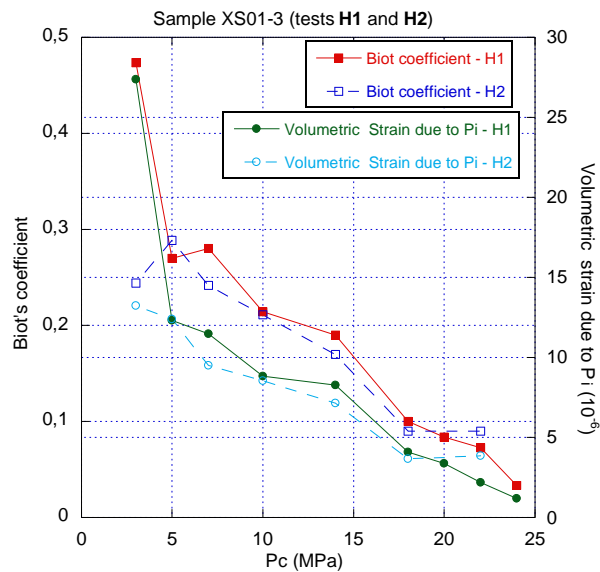


Fig.4.24 Biot's coefficient and $\Delta \epsilon_v$ due to P_i at different P_c for tests **H1** and **H2**

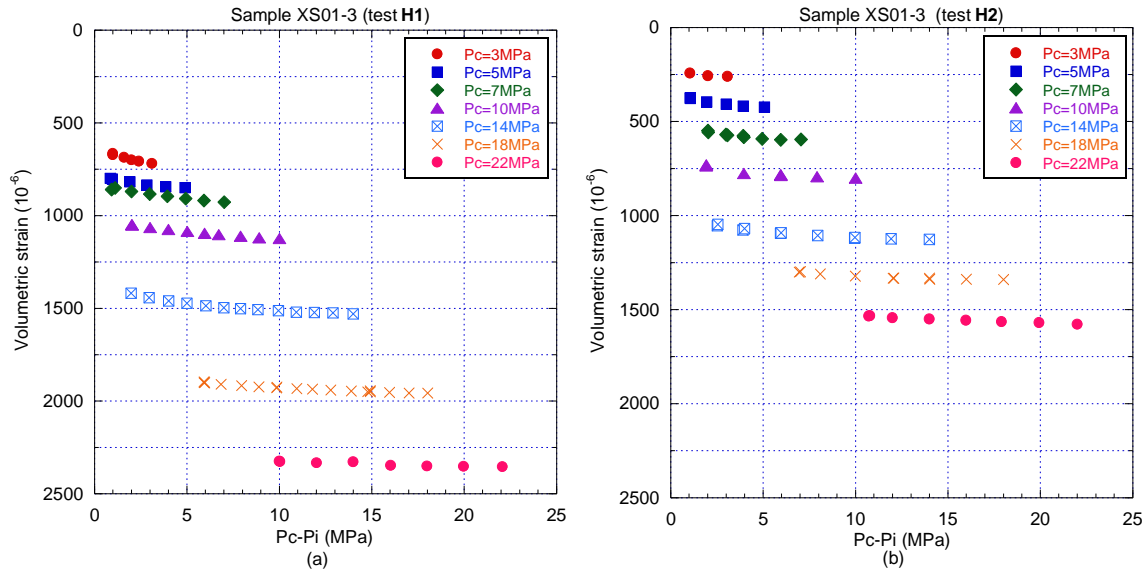


Fig.4.25 Variation of ϵ_v as the function of P_c - P_i : (a) test **H1**; (b) test **H2**

Table 4.10 gives the results of tests **H1** and **H2** ($\Delta\epsilon_v$ due to P_i and P_c , apparent modulus H , K_b and Biot's coefficient). The variations of Biot's coefficient and $\Delta\epsilon_v$ due to P_i with P_c in tests **H1** and **H2** are plotted in Fig.4.24. Excepted for the lowest P_c (3MPa), the Biot's coefficients are found to be similar for both tests **H2** and **H1**. They are very sensitive to confining pressure (as well as volumetric strain due to P_i). Biot's coefficient decreased down to 0.1 with P_c increasing to 22MPa for the two tests **H1** and **H2**. In parallel, a significant decrease in permeability was detected (as mentioned before, see Fig.4.23). It is logical as this phenomenon can be attributed to crack closure effects. The comparison of couplings in tests **H1** and **H2** eventually reveals that there was no significant damage caused by triaxial test.

When compared to Fig.4.20, Fig.4.25 highlights that there is not significant material expansion due to gas pore pressure for both tests **H1** and **H2**. This is consistent with the above observation (low Biot's coefficient). Under P_c loading it can be mentioned that the sample is less deformable after the triaxial test. At $P_c=22$ MPa, the maximum ϵ_v reached 2355 10^{-6} in test **H1**, while it was only 1578 10^{-6} in test **H2**. This phenomenon (a lower compressibility in **H2**) is in contrast to the previous sample XZ25-3. It should be underlined here that, despite less compressibility in test **H2**, the values of $\Delta\epsilon_v$ due to P_c unloadings at different P_c levels are basically the same in **H2** and **H1**, as shown in Table 4.10. ($\Delta\epsilon_v$ due to P_c was recorded during an unloading phase to evaluate the moduli K_b). As K_b is almost constant with P_c , the decrease in Biot's coefficient can be attributed to the increase in 'H' modulus i.e. decrease in $\Delta\epsilon_v$ due to P_i when P_c is increased. On a 'coupling' point of view, the triaxial test has not significantly modified the sample behavior.

Table 4.10 Changes in $\Delta\epsilon_v$ due to P_i and P_c , H , K_b and Biot's coefficient with confining pressure in tests **H1** and **H2** for the same sample XS01-3

P_c (MPa)	$\Delta\epsilon_v$ due to P_i ($10^{-6}/\text{MPa}$)		$\Delta\epsilon_v$ due to P_c ($10^{-6}/\text{MPa}$)		$H(\text{GPa})$		$K_b(\text{GPa})$		Biot	
	H1	H2	H1	H2	H1	H2	H1	H2	H1	H2
3	27.38	13.25	57.81	54.21	36.53	75.50	17.30	18.45	0.47	0.24
5	12.32	12.39	45.02	42.92	81.20	80.71	22.21	23.30	0.27	0.29
7	11.48	9.50	40.97	39.35	87.15	105.32	24.41	25.42	0.28	0.24
10	8.84	8.55	42.99	40.50	113.19	116.96	23.26	24.69	0.21	0.21
14	8.28	7.14	42.95	40.92	120.77	140.06	23.29	24.44	0.19	0.17
18	4.08	3.66	41.01	39.17	245.10	273.22	24.38	25.53	0.10	0.09
22	2.19	3.87	32.75	43.62	456.62	258.40	30.54	22.93	0.07	0.09

4.4.3.3. Partial conclusion for XS01-3

During the triaxial test, deviatoric stress (up to 37MPa) brought a small decrease in permeability on a whole from $2.7\text{E-}18$ to $1.5\text{E-}18\text{m}^2$. The sample dismounting also brought an increase in permeability (by comparing the last value of triaxial test and the first one of test **H2**). Contrary to the previous two samples, this one was less compressible in test **H2** than in **H1**. From the comparison of permeability and coupling in tests **H1** and **H2**, it can also be indicated that triaxial test did not cause significant damage. It can then be logically supposed that the triaxial test brought a predominant sample compaction.

4.4.4. Sample XR02-4: H1 test, triaxial test and H2 test

4.4.4.1. Triaxial test for sample XR02-4

Prior to the triaxial testing, this sample had been submitted to permeability measurements (with time effect) at $P_c=5$ and 10MPa (see §4.3.1). Its permeability was very sensitive to both confinement and time (see Table 4.11 (a) - test **H1**). It also revealed to be the most deformable sample among the tested ones. The sample was dismantled from the hydrostatic cell to be scanned (with micro-CT) and then installed in the triaxial cell. These operations had lasted 8 days, during which the sample was unconfined. A gradual deviatoric loading was then performed under 10MPa confinement, with loading steps of 5MPa (except for the first one at 10MPa). A systematic effect of time was targeted for each step, during which permeability and volumetric strain evolutions were recorded. Fig.4.26 shows the stress-strain curves of this triaxial test. It must be underlined that dilatancy occurred over 15MPa of deviatoric stress, so quite earlier than for the previous samples.

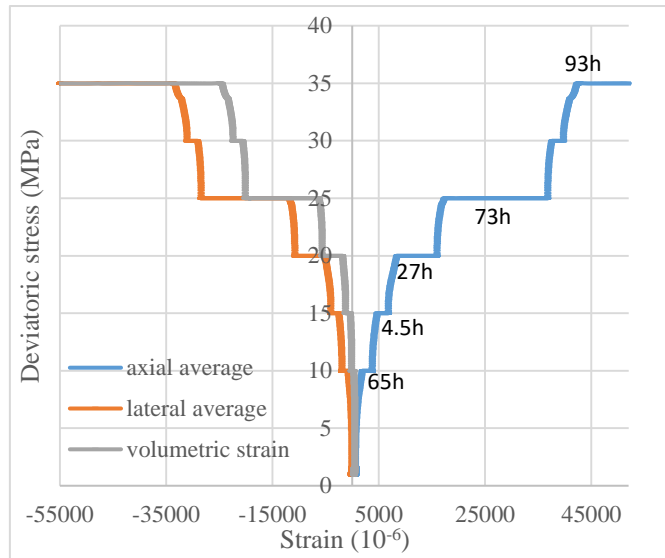


Fig.4.26 Stress-strain curves of triaxial test for sample XR02-4

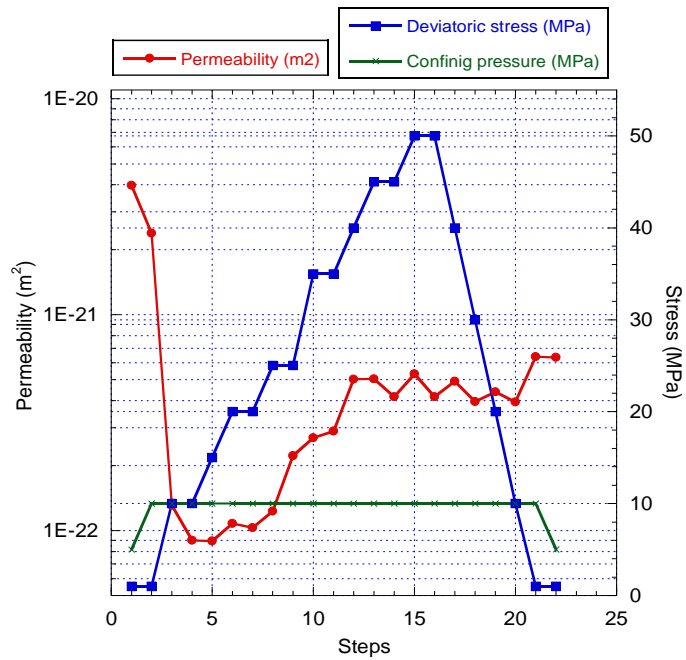


Fig.4.27 Changes in permeability during triaxial test

Table 4.11 Variation of permeability with deviatoric stress/time during test **H1** (a) and triaxial test (b)

(a)

P _c = 5MPa (Δt =172.6hours)		P _c = 10MPa (Δt =178 hours)	
Permeability (m ²)	ε _v (10 ⁻⁶)	Permeability (m ²)	ε _v (10 ⁻⁶)
1.22E-19 ~ 1.10E-21	701.25 ~ 939.75	1.71E-22 ~ 3.18E-23	1322.3 ~ 1728.0
ΔK _g ≈ 2 orders of magnitude	Δε _v = 238.5	ΔK _g < 1 order of magnitude	Δε _v = 405.7

(b)

Steps	P _c (MPa)	Δσ (MPa)	K (m ²)	ε _v (10 ⁻⁶)	Steps	P _c (MPa)	Δσ (MPa)	K (m ²)
1	5	0	3.98E-21	252	12	10	40	5.03E-22
2	10	0	2.39E-21	469	13	10	45	5.04E-22
3	10	10	1.31E-22	251	14	10	45(60h)	4.17E-22
4	10	10(65h)	9.01E-23	-102	15	10	50	5.31E-22
5	10	15	8.93E-23	-428 ~ -1267	16	10	50(120h)	4.17E-22
6	10	20	1.08E-22	-1864	17	10	40	4.91E-22
7	10	20(27h)	1.03E-22	-5658	18	10	30	3.96E-22
8	10	25	1.23E-22	-6323	19	10	20	4.39E-22
9	10	25(73h)	2.22E-22	-20119	20	10	10	3.94E-22
10	10	35	2.69E-22	-25068	21	10	0	6.39E-22
11	10	35(93h)	2.89E-22	~ -∞	22	5	0	6.34E-22

Table 4.11 presents the variations of permeability and volumetric strain with deviatoric stress and time during this triaxial test and recalls the previous **H1** results. The first observation to be made is the permeability difference at P_c=10MPa at the end of **H1** and at the beginning of the triaxial test i.e. 3.2E-23 compared to 2.4E-21m². This is likely to indicate that the sealing observed during **H1** is temporary and remains present as long as the sample is loaded. On the other hand, this would mean that the crack closure is partially reversible. The difference is less spectacular at P_c=5MPa but the new loading, from 5 to 10MPa, leads to a permeability variation from 4 to 2.4E-21m². The obtained difference in **H1** was from 1.1E-21 to 1.7E-22m² (one order of magnitude). As a whole, this confirms a partial but not total crack re-opening.

As shown in this Table, the starting permeability value is 2.39E-21m² at P_c=10MPa and before deviatoric loading. The first effect of axial loading was a decrease in permeability to its lowest value 8.93E-23m² at 15MPa deviatoric stress. This is due to global sample compaction. Then the permeability started to increase with deviatoric stress. Based on the volumetric strain changes (Fig.4.26), the sample started to dilate from 10MPa and more of deviatoric stress. Therefore, no immediate increase in permeability was observed as 15MPa deviatoric stress was found to be necessary to get a (slight) permeability growing. Even at the last deviatoric loading step (up to 50MPa), the permeability slightly increased to 5.31E-22m², less than one order of magnitude higher than the lowest value. Such a low difference means that, if cracks were created, they are few and weakly open. Unloading the sample came along with a permeability plateau, that finally reached 6.34E-22m² at P_c=5MPa, which is still lower than the initial one 3.98E-21m². To sum up, even if the axial loading led to some increase in volumetric

strains i.e. to damage, no significant increase effect in permeability was detected. As a whole, all is happening as if sample compaction was predominant.

After this triaxial test, the sample was dismantled again for scanning. It had been unconfined for six months (*due to Covid*) before being installed in the hydrostatic cell to perform **H2** experiment. The initial **H2** permeability values at $P_c=3$ or 5MPa were found to be slightly higher than the ones measured for **H1**. This is quite a surprising result that is commented further.

Variations of permeability and volumetric strain with time at different levels of deviatoric stress are plotted in Fig.4.28. At the first level of deviatoric stress (Fig.4.28-10MPa), there was a small reduction of permeability for 65hours. The specimen expansion was really visible at 25MPa of deviatoric stress: the volumetric strain significantly decreased by $\Delta\varepsilon_v=-1.38\%$ (from around -0.63% to -2.01%) in 73hours, but the permeability varied only from $1.2E-22$ to $2.2E-22m^2$ and with almost no time effect (Fig.4.28). The same phenomenon was observed at 35MPa of deviatoric stress (Fig.4.28): the volumetric strain decreased by $\Delta\varepsilon_v=-3.14\%$ (from -2.51% to -5.65% - the maximum range of gauges) for the first 17hours but with virtually no increase in permeability during the whole 93h period at this constant deviatoric stress. After the last deviatoric loading step up to 50MPa, the permeability slightly increased to $5.3E-22m^2$. To sum up, it was found that the deformation with time was much larger at high deviatoric stresses (25 and 35MPa) than at low ones (10 and 20MPa). Even if there was a large dilatancy at $\Delta\sigma=25$ and 35MPa (obvious viscoplastic deformation), permeability did not significantly increase with time effects.

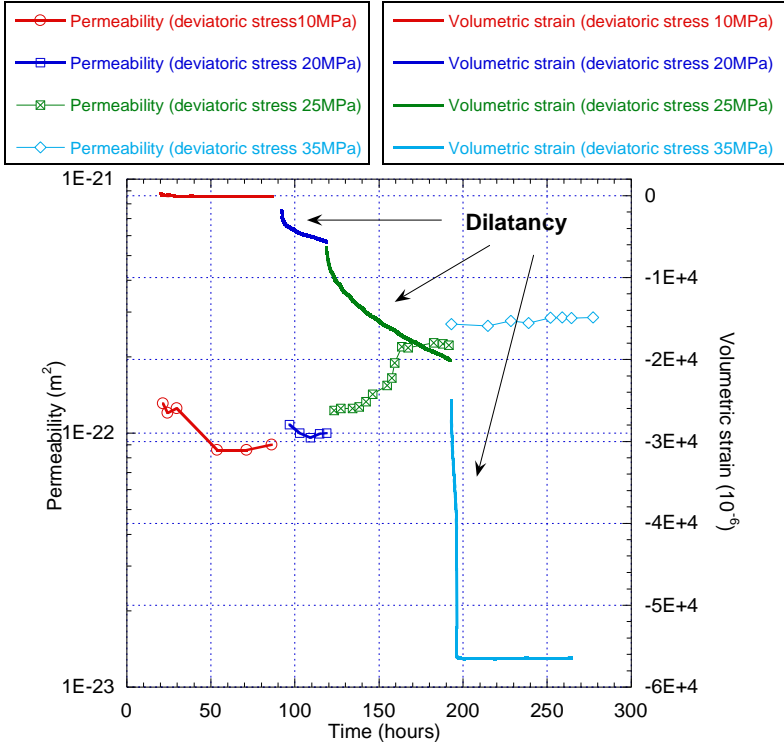


Fig.4.28 Variations of permeability and volumetric strain with time at $\Delta\sigma=10, 20, 25$ and 35MPa

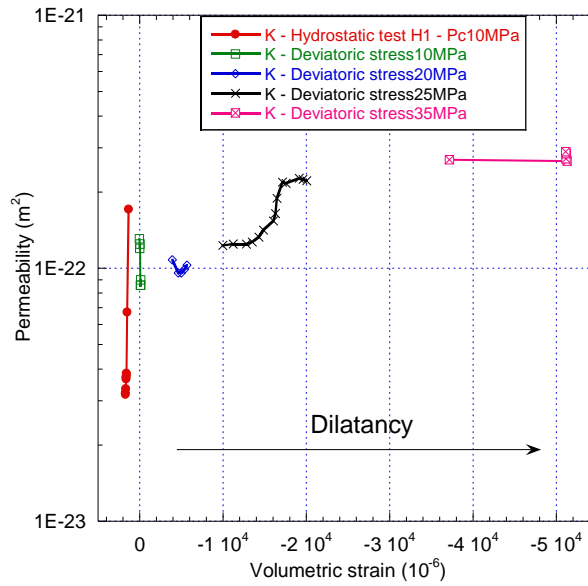


Fig.4.29 Variation of permeability with volumetric strain for the same sample (under both hydrostatic **H1** and triaxial test)

Permeability and volumetric strain are related, during hydrostatic **H1** test or triaxial test, in Fig.4.29. As mentioned before, the permeability decreased from $1.7E-22$ to $3.2E-23m^2$ at constant P_c of 10MPa in 178hours during hydrostatic test (**H1**) (see Table 4.11 (a)). In parallel, the volumetric strain only varied by a small $\Delta\varepsilon_v=0.0406\%$ (it is called a ‘mixed behavior’: a continuous decrease in permeability v.s. volumetric strains in Fig 4.8). The first ε_v evolution at $\Delta\sigma=10MPa$ in triaxial test is -0.0353% in 65h with a small decrease in permeability. In the following and despite significant dilatancy, the permeability slightly increased or remained almost constant. All these results underline the preponderant role played by hydrostatic pressure and the fact that this stress is likely to mask potential cracking.

Fig.4.30 (a) shows the variation of normalized permeability K/K_0 with a K_0 ‘initial’ value ($2.39E-21m^2$ at $P_c=10MPa$ - before deviatoric loading) due to deviatoric stress and time. This representation is interesting as it shows that, at the end of deviatoric loading (and despite dilatancy), the permeability had decreased by almost 80%. To highlight the dilatancy effects, Fig.4.30 (b) takes $K_0=8.93E-23m^2$ (15MPa deviatoric stress) as the ‘initial’ state. The permeability increased by nearly 6 times with deviatoric loading up to 50MPa but its absolute variation remains very low.

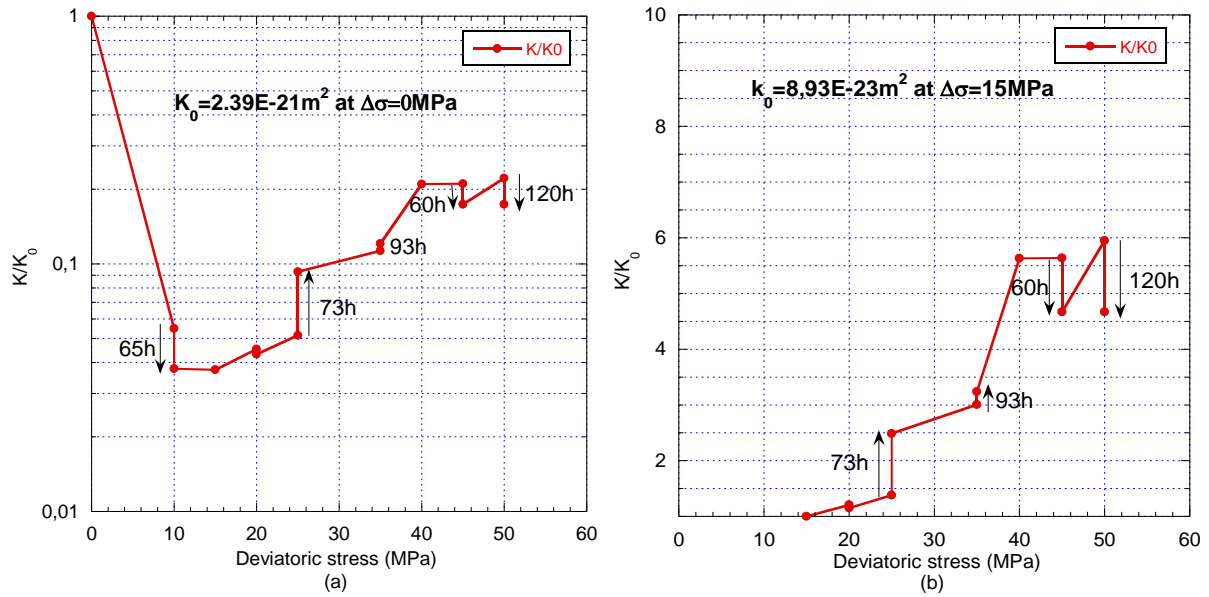


Fig.4.30 Normalized permeability under deviatoric stress

4.4.4.2. Hydrostatic tests H1 and H2 for XR02-4

Hydrostatic test (**H2**) on ‘damaged’ sample XR02-4 caused by deviatoric stress was expected to investigate sealing/healing properties with time at two levels of confinement (5MPa and 10 MPa). It was also intended to compare time-dependent behavior for tests **H1** and **H2** (before and after triaxial test). For test **H2**, variations of permeability, porosity and volumetric strain with time at $P_c=5$ and 10MPa are presented in Table 4.12 and Fig.4.31 (a). The comparative results are shown in Fig.4.31 (b), (c) and Table 4.13.

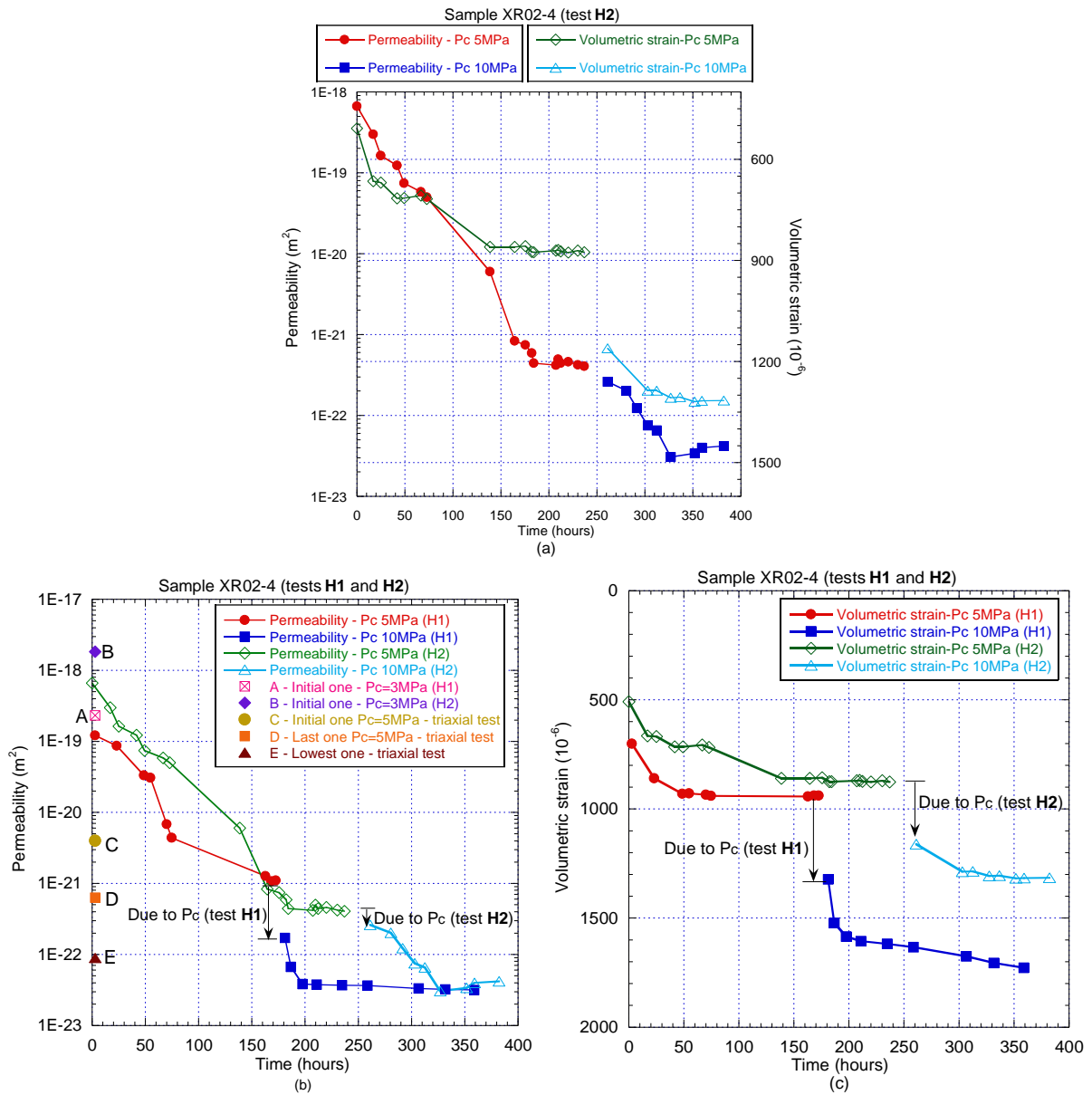


Fig.4.31 Variations of permeability and volumetric strain with time (a); (b) and (c): comparison

Table 4.12 Variations of permeability (K), porosity (ϕ) and volumetric strain (ϵ_v) with time under different P_c (after triaxial test – **H2** test)

XR02-4 Time (hour)	$P_c = 5\text{MPa}$			Time (hour)	$P_c = 10\text{MPa}$	
	K(m ²)	$\epsilon_v (10^{-6})$	ϕ (%)		K(m ²)	$\epsilon_v (10^{-6})$
0.00	6.67E-19	508.5	0.30	261.13	2.62E-22	1161
16.97	3.00E-19	665.25	0.15	280.63	2.03E-22	
25.05	1.63E-19	669	0.17	291.63	1.23E-22	
41.72	1.23E-19	715.6	0.09	303.13	7.50E-23	1287
49.22	7.46E-20	715.07	0.05	312.47	6.56E-23	1286.75
66.63	5.83E-20	708	0.03	327.63	3.06E-23	1308
72.80	5.00E-20	717.75		351.63	3.40E-23	1319.0
138.63	8.49E-21	859.87		359.30	4.00E-23	1317.0
164.47	8.33E-22	860		382.30	4.20E-23	1316.0
175.47	7.43E-22	858				
182.13	5.91E-22	875				
184.30	4.44E-22	875.5				
207.30	4.17E-22	871.2				
209.80	4.97E-22	869.25				
212.30	4.42E-22	873.7				
220.13	4.62E-22	876.75				
230.30	4.23E-22	870.75				
236.97	4.07E-22	876				
	$P_c = 3\text{MPa}$ (initial loading)					
	1.83E-18	334.5	0.53			

During triaxial test (see §4.4.4.1), there was an obvious reduction of permeability from 3.98E-21 (point **C** in Fig.4.31 (b)) to the lowest value 8.93E-23m² (point **E**). Then it slightly increased to 6.34E-22m² (point **D**) at the end of triaxial test. It indicates (a priori) that cracks were firstly closed and then new cracks were created with axial loading. As mentioned before, the ‘initial’ permeability in test **H2** was 1.83E-18m² at 3MPa (point **B**), almost one order of magnitude higher than **H1** (2.33E-19m², point **A**). This difference can evidence a small damage caused by triaxial test. The dismounting operation after triaxial test (i.e. the sample had been unconfined for 6 months and then submitted to test **H2**) brought a significant increase in permeability from 6.34E-22 to 1.83E-18m², (see Fig.4.31 (b) from point **D** to **B**). This phenomenon was also observed for samples XR02-3, XZ25-3 and XS01-3, and can be attributed to crack opening after dismounting.

As shown in Fig.4.31 (a), significant time effects on permeability and volumetric strain were detected in **H2**. The dependence between permeability and volumetric strain corresponds to the so called mixed behavior in §4.3.1. At both $P_c= 5$ and 10MPa, the permeability first sharply dropped with time, then followed by a plateau. The permeability continuously decreased by three orders of magnitude (to 5.91E-22m²) in one week at low confinement of 5MPa. And it decreased by one order of magnitude in 3 days at $P_c=10\text{MPa}$. The evolution of volumetric strain is similar with that of permeability.

The comparison of time-dependent behavior in tests **H1** and **H2** is presented in Fig.4.31 (b) and (c). On a global point of view, the two observed behaviors are not very different. Permeability obtained at the end of both **H1** and **H2** tests are virtually the same. One can nevertheless find some differences in volumetric strains as they are greater in **H1** than in **H2**. This means that the sample have gained some stiffness between the both tests. This is confirmed by the volumetric strain difference due to the loading $P_c=5$ to 10MPa. On a mechanical point of view, it can be said that the triaxial test led to a more compacted sample.

Table 4.13 Comparison of changes in permeability, porosity, coupling with P_c /time, and volumetric strain due to time in tests **H1** and **H2**

XR02-4	Permeability(m ²)		Porosity(%)		$\Delta\epsilon_v$ due to time (10 ⁻⁶)		$\Delta\epsilon_v$ due to P_i (10 ⁻⁶ /MPa)	
	H1	H2	H1	H2	H1	H2	H1	H2
P_c (MPa)								
3	2.33E-19	1.83E-18	0.38	0.53				
5	1.22E-19	6.67E-19	0.32	0.3	238.5	367.5	11.3	29.26
5	1.10E-21	4.07E-22	0	0	(172hours)	(237hours)	0	25.37
10	1.71E-22	2.62E-22	0	0	405.7	158	0	
10	3.18E-23	4.20E-23	0	0	(178hours)	(121hours)	0	8.7

Some complementary results are presented in Table 4.13. The absence of an unloading phase at $P_c=5$ MPa resulted in the inability to estimate the corresponding modulus K_b and Biot's coefficient. Therefore, variation of volumetric strain due to gas pore pressure can be used to characterize the coupling effects. After triaxial test, at $P_c=5$ MPa, there is a more significant coupling than before, i.e. $\Delta\epsilon_v$ due to P_i increased from 11 10⁻⁶ in test **H1** to 29 10⁻⁶/MPa in **H2**. It indicated that multiple-cracks, produced by deviatoric loading, could lead to easier expansion due to gas pore pressure. This observation is consistent with the changes in permeability and porosity between **H1** and **H2**. As a whole, in test **H2**, loading (to 10MPa) and time effects eventually bring the value of $\Delta\epsilon_v$ due to P_i decreased to 8.7 10⁻⁶/MPa (very weak but not 0). On the coupling point of view, the 'damaged' sample was not perfectly healed (unlike in **H1**, $\Delta\epsilon_v$ due to P_i decreased to 0).

4.4.4.3. Microstructure observations from X-ray microtomography for sample XR02-4

The variations of permeability, porosity (and the ones obtained based on micro-CT) and couplings for sample XR02-4 during different tests are presented in Table 4.14. (The slices at the top and bottom of the sample are generally with noise. In order to reduce the effect of noise, they are not selected during the procedure of porosity extraction.) Hence, the 3D pore space of sample XR02-4, as shown in Fig.4.32, is extracted from the volume close to the entire sample. As mentioned in §4.2.4, the first scan was performed on this sample at its initial state, scan 2° was after test **H1**, and scan 3° after triaxial test. (Big) Cracks can be clearly observed in scan 1° followed by their closure observed in scan 2° (see Fig.4.32). This evidences that the reduction of permeability (amplified with time) in test **H1** can be associated with crack closure. This is not new. Scan 3° is very instructive. As it concerns the 'whole' sample, the compaction due to axial loading is visible, which was anticipated with the **H2** test results. On the other

hands, no new cracks can be (easily) detected from scan 3°. This is why more accurate visualisation were made on 3D sub-volumes i.e. easier to detect cracks.

Remark: It must be reminded that porosity, extracted from micro-CT scans, depends on the test resolution. This means that this porosity is logically less than the total porosity. On the other hand, the micro-CT porosity is the total one i.e. including connected and non-connected one. The gas porosity gives the only connected one and it is measured under confinement, which has a considerable reduction effect.

Table 4.14 Variations of permeability, porosity (and the ones obtained based on micro-CT) and couplings for sample XR02-4 during different tests

XR02-4	Mechanical loadings	K (m ²)	Porosity (%)	$\Delta\varepsilon_v (P_i)$ 10 ⁻⁶ /MPa	Modulus H (GPa)
Scan 1° (0.381%)					
Hydrostatic test (H1)	P _c =3MPa	2.33E-19	0.38		
	P _c =10MPa (last one)	3.18E-23	0	0	
Scan 2° (0.238%)					
Triaxial test $\sigma_{\max} = 50\text{MPa}$	P _c =5MPa; $\Delta\sigma=0\text{MPa}$	3.98E-21			
	P _c =10MPa; $\Delta\sigma=15\text{MPa}$	8.93E-23 (the lowest one)			
	P _c =5MPa; $\Delta\sigma=0\text{MPa}$	6.34E-22			
Scan 3° (0.228%)					
Hydrostatic test H2	P _c =3MPa	1.83E-18	0.53	35	28.57
	P _c =10MPa (last one)	4.20E-23	0	8.7	114.94

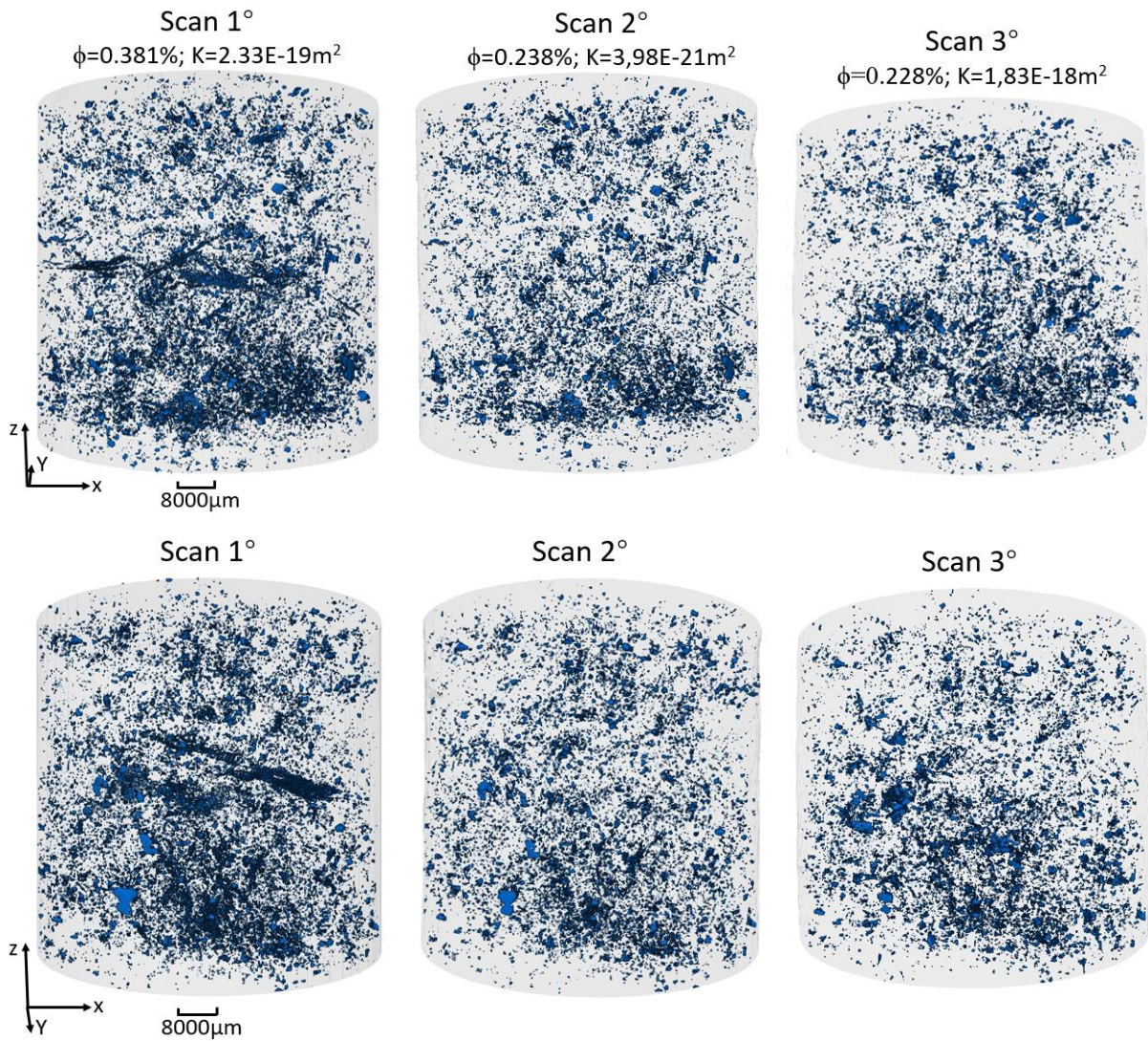
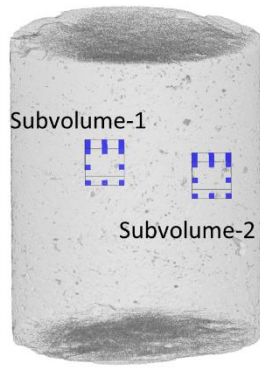


Fig.4.32 3D pore space of sample XR02-4 from different scans

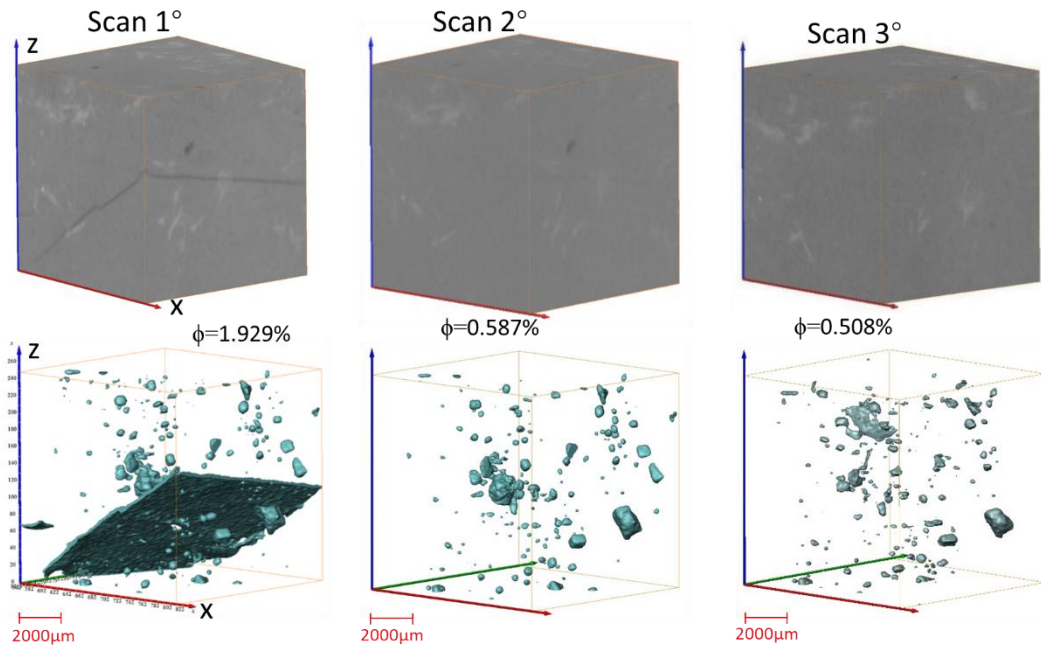
Two 3D sub-volumes (10mm×10mm×10mm) and their pore space were extracted from three scans, as shown in Fig.4.33. Slices of sub-volumes from different scans are presented in Fig.4.34, in order to investigate the microstructure changes in horizontal and vertical directions. To facilitate the analyses, the comments are directly done on the pictures (scan). To sum up they indicate without any doubt that:

- **H1** test led to crack closure.
- Triaxial test has two ‘antagonistic’ effects: a compaction one that makes pores smaller (and further crack closure) and produces new cracks (anticipated by a small permeability increase and mainly a higher sensitivity to internal gas pressure (coupling effect)).

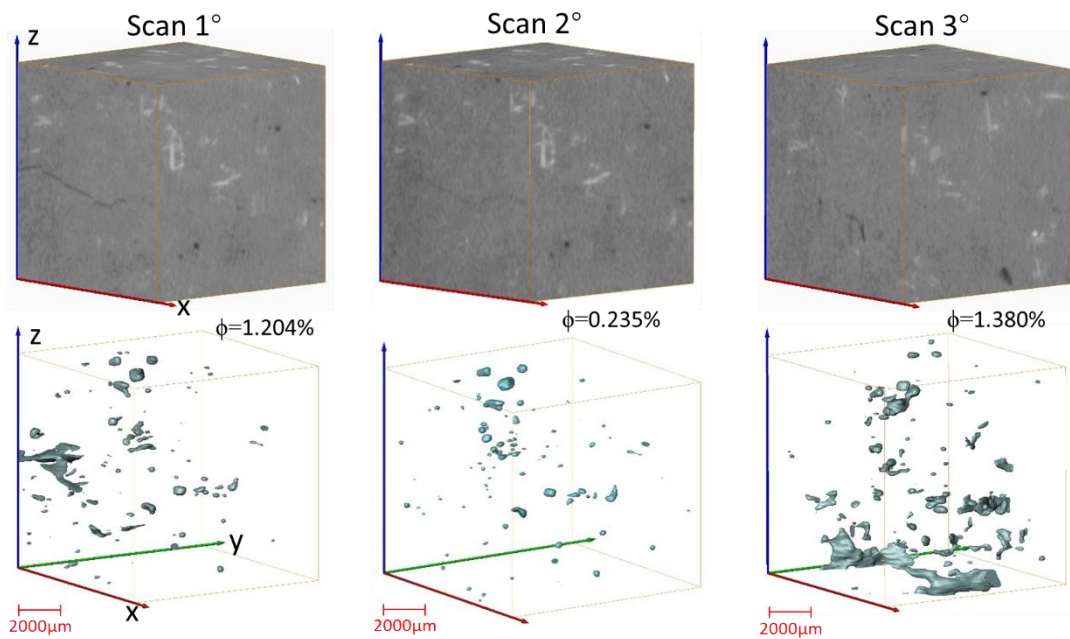
Since the permeability in test **H2** was higher than **H1**, it can be indicated that the new crack effect on transfer property is more significant than the compaction effects.



(a) Location of 3D subvolume-1 and subvolume-2 of sample XR02-4 from scan 1°



(b) 3D subvolume-1 (10mm×10mm×10mm)



(c) 3D subvolume-2 (10mm×10mm×10mm)

Fig.4.33 Two 3D sub-volumes and pore space extracted from three scans of sample XR02-4

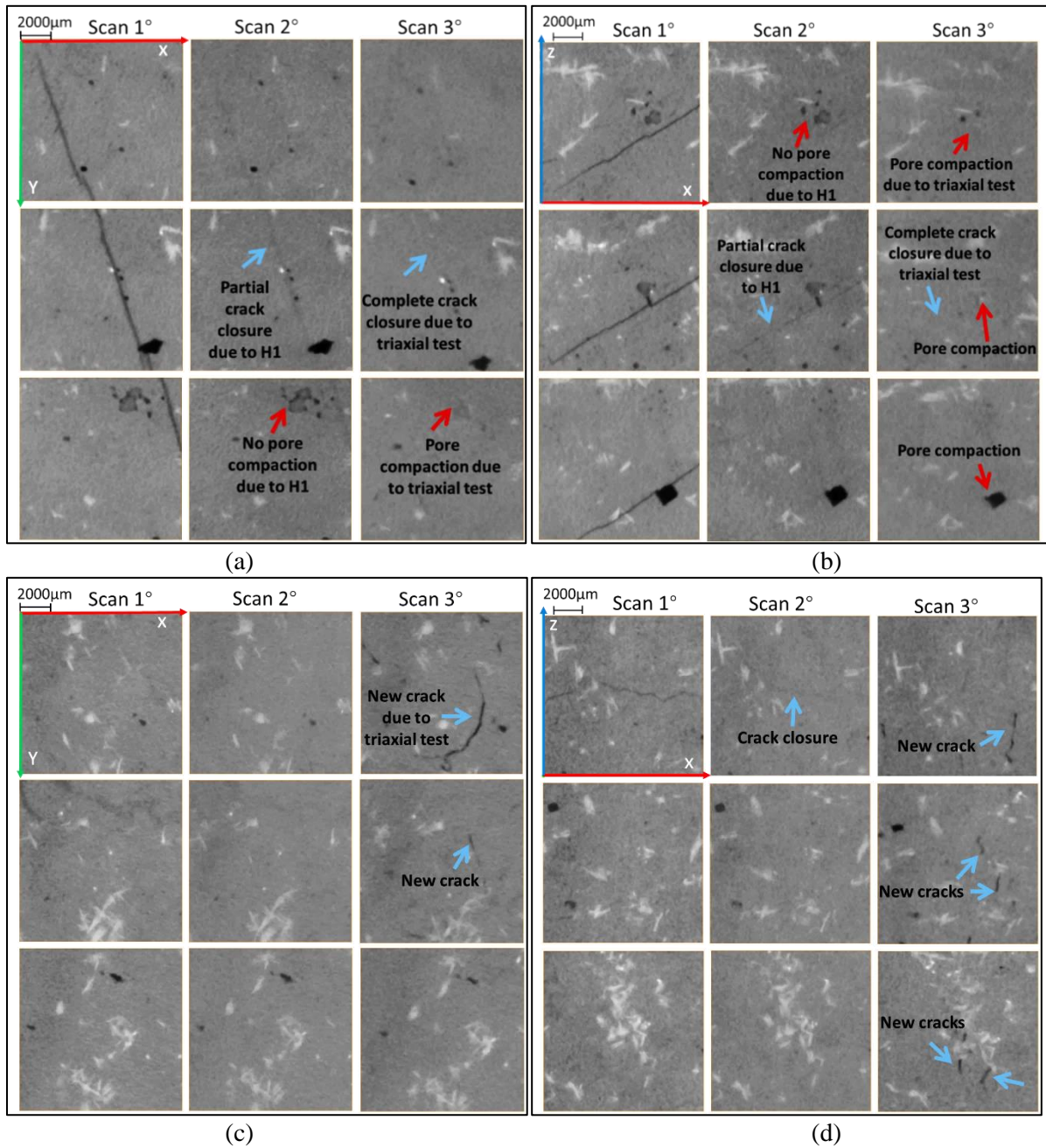


Fig.4.34 The microstructure development (crack: blue arrows; pore: red arrows) of slices in two subvolumes with different scans of sample XR02-4 ((a) and (b): the horizontal and vertical slices of subvolume-1, (c) and (d): the horizontal and vertical slices of subvolume-2)

4.4.4.4. Partial conclusion for sample XR02-4

For the triaxial test, the permeability first decreased and then slightly increased with deviatoric stress. However, this small increase in permeability came along with a significant dilatancy. The time effects had a weak influence on permeability but an evident influence on strains during triaxial test. While for tests **H1** and **H2**, time effects on both permeability and volumetric strain were significant. There were higher permeability and stronger couplings in test **H2** than in **H1**, which can indicate that

new cracks (or damage) had been created by triaxial test. However, lower compressibility in **H2** indicates a compaction due to triaxial testing. The observations from micro-CT scans, i.e. crack closure (and smaller pores) and new cracks in scan 3° after triaxial test, gave evidence to verify these two ‘antagonistic’ effects. Furthermore, in terms of the measured permeability, the new crack effect is more prominent than the compaction effect. It can be inferred that new cracks were weakly open or remained close during triaxial test as the permeability did not significantly increase. They could open after the dismounting operation as the beginning permeability value of test **H2** was three orders of magnitude higher than the last one of triaxial test. On a global point of view, micro-CT experiment revealed that triaxial test is able to significantly change the porous network.

4.4.5. Sample XS01-4: H1 test, triaxial test and H2 test

4.4.5.1. Triaxial test for sample XS01-4

The experimental process of this triaxial test was the same as for sample XR02-4. For hydrostatic test (**H1**) prior to the triaxial test, the permeability decreased from 2.12E-16 to 1.64E-17m² due to both confinement (up to P_c=10MPa) and time effects (see §4.3.1), which was considered to be a small variation. Then, this sample was dismounted to be scanned. It was not loaded for just one day and then placed into the triaxial cell. The triaxial test was conducted at P_c=10MPa for 23days. The main purpose was to investigate permeability variations with deviatoric stress and time at different levels of loadings. Fig.4.35 shows the stress-strain curves of this triaxial test.

At 35MPa deviatoric stress (after 14days), one axial strain was close to the limit of measurable gauge range (around 5.6%). The two axial strains reached the limit at 40MPa while the lateral strain reached the limit at 45MPa deviatoric stress. A high level of dilatancy can then be observed at 35MPa and more.

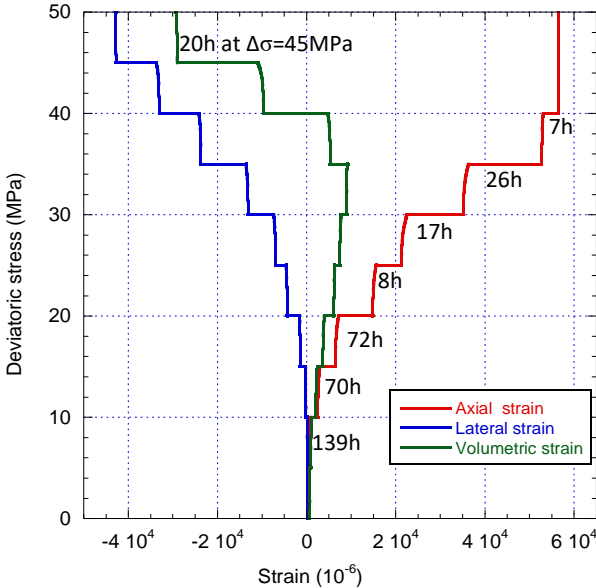


Fig.4.35 Stress-strain curves of triaxial test for sample XS01-4

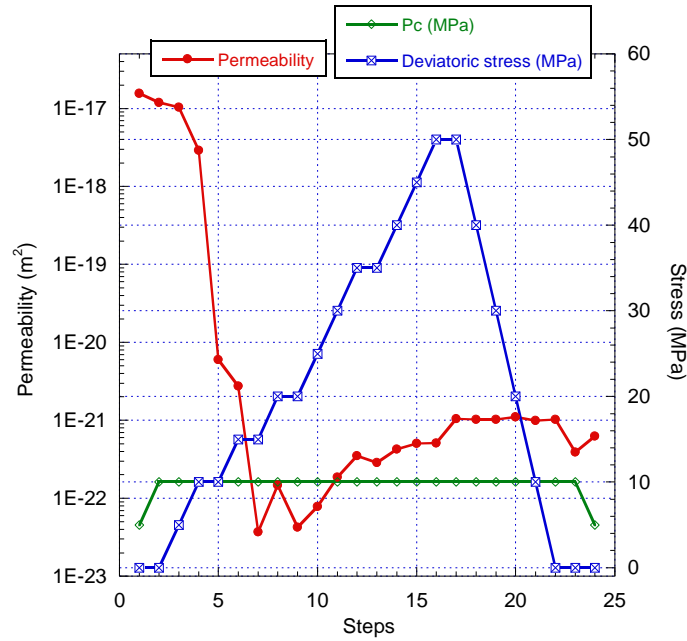


Fig.4.36 Changes in the permeability during the triaxial test

Table 4.15 Variation of permeability with deviatoric stress/time during test **H1** (a) and triaxial test (b)

(a)

P _c = 5MPa (Δt =147.8hours)		P _c = 10MPa (Δt =285.5hours)	
Permeability (m ²)	ε _v (10 ⁻⁶)	Permeability (m ²)	ε _v (10 ⁻⁶)
2.12E-16 ~ 1.39E-16	272.25 ~ 368.25	8.10E-17 ~ 1.64E-17	572.25 ~ 706.50
ΔK ≈ 0	Δε _v = 96	ΔK < 1 order of magnitude	Δε _v = 134

(b)

Steps	P _c (MPa)	Δσ(MPa)	K (m ²)	ε _v (10 ⁻⁶)
1	5	0	1.56E-17	330
2	10	0	1.19E-17	623
3	10	5	1.04E-17	738~903
4	10	10	2.89E-18	1256
5	10	10(139h)	5.98E-21	2093
6	10	15	2.74E-21	2414
7	10	15(70h)	3.70E-23	3613
8	10	20	1.48E-22	3959
9	10	20(72h)	4.25E-23	6081
10	10	25	7.86E-23	6347~7408
11	10	30	1.87E-22	7749~8950
12	10	35	3.50E-22	9100
13	10	35(26h)	2.87E-22	5293
14	10	40	4.25E-22	4635 ~ -9645
15	10	45	5.07E-22	-11106 ~ -∞
16	10	50	5.12E-22	
17	10	50(115h)	1.05E-21	
18	10	40	1.02E-21	
19	10	30	1.02E-21	
20	10	20	1.10E-21	
21	10	10	9.90E-22	
22	10	0	1.03E-21	
23	10	0	3.90E-22	
24	5	0	6.28E-22	

Table 4.15 presents the variation of permeability with deviatoric stress and time during this triaxial test (b), and the results of test **H1** (a). The ‘initial’ permeability ($1.56\text{E-}17\text{m}^2$ - step 1 - table 4.15 (b)) at $P_c=5\text{MPa}$ is lower than the initial one ($2.12\text{E-}16\text{m}^2$) found in **H1** test. This difference revealed that this sample had been sensitive to its previous hydrostatic test up to $P_c=10\text{MPa}$ with a significant irreversibility – supposed to come from the partial reopening of cracks and joints. On another hand the permeability at $P_c=10\text{MPa}$ ($1.19\text{E-}17\text{m}^2$ - step 2 – Table 4.15 (b)) is close to the one ($1.64\text{E-}17\text{m}^2$) at the end of **H1**. This phenomenon seems logical but totally different from what was observed on the previous sample XR02-4.

The time effect under hydrostatic loading was very weak for this sample (see Table 4.2) and coming along with a negligible (small) permeability evolution. This is completely different under axial loading (see Fig.4.36 and Table 4.15 (b)). The increase in axial stress led first to some compaction and logical small permeability decrease but, with time, there is a following decrease of the latter by two or three orders of magnitude. This is especially true at 10, 15 and in a lower extent at 20MPa deviatoric stress. At this level, the gas permeability can go down to $4\text{E-}23\text{m}^2$. Six orders of magnitude have therefore been lost. The deviatoric stress leads to shear stresses that seem to produce a strong effect on the gas flow i.e. on the existing cracks (see Fig.4.37 that is a conceptual scheme able at explaining this phenomenon). In details, the permeability decreased by almost one order of magnitude (from $1.19\text{E-}17$ to $2.89\text{E-}18\text{m}^2$) due to (0 to) 10MPa deviatoric loading – instantaneous effect. Keeping constant this stress, the permeability evolved by losing three orders of magnitude for 139hours (from $2.89\text{E-}18$ to $5.98\text{E-}21\text{m}^2$). For the same time, the volumetric strain only increased by $\Delta\varepsilon_v=0.08\%$ (from 0.126% to 0.209%), which is considered to be a small compaction of volume as shown in Fig.4.38. The same tendency occurred from 10 to 15MPa deviatoric stress and time effects were also observed. The permeability decreased by almost two orders of magnitude, for 70 hours, to reach its lowest value $3.7\text{E-}23\text{m}^2$. This decrease also came along with a small compaction of volume: volumetric strain increased by $\Delta\varepsilon_v=0.12\%$ (from 0.241 to 0.361% in Fig.4.38). The permeability really started to (weakly) increase at 20MPa and more. Even at 35MPa and more, which showed dilatancy, (beginning of expansion, see point **A** in Fig.4.38), nothing spectacular was detected on permeability. A small increase in permeability (from $2.87\text{E-}22$ to $5.12\text{E-}22\text{m}^2$) was recorded as the deviatoric stress increased to 50MPa and it continued to slightly increase up to $1.05\text{E-}21\text{m}^2$ for 115hours. The deviatoric unloading did not bring any change in permeability that remained very low. All this is detailed in Fig.4.38 to 4.40.

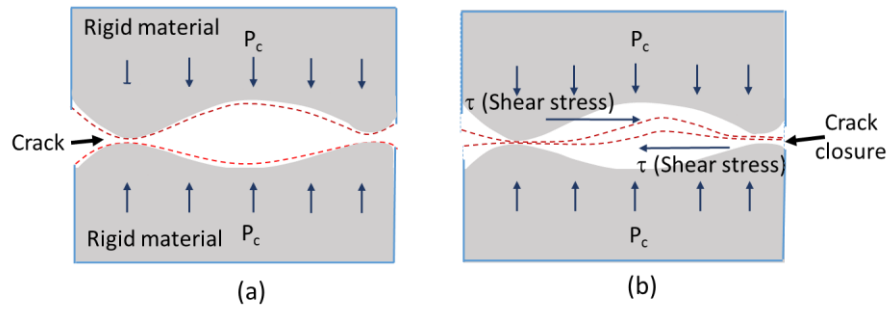


Fig.4.37 Conceptual scheme: the influence of isotropic and deviatoric stress on cracks

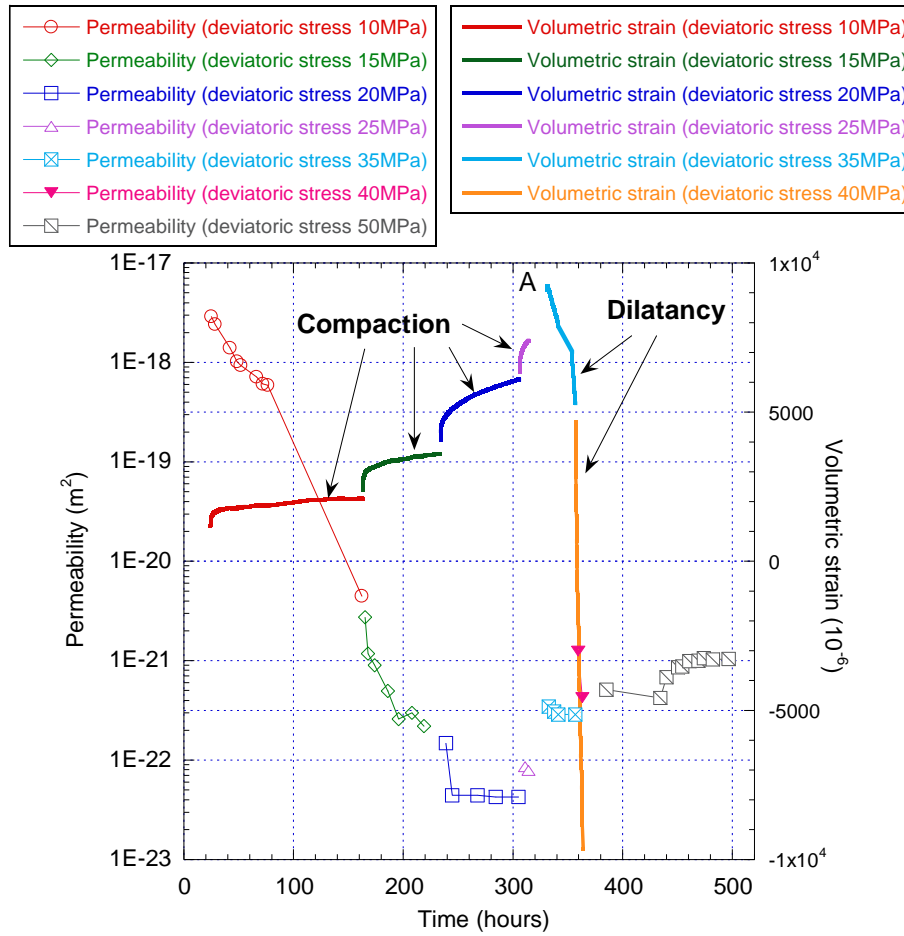


Fig.4.38 Variations of permeability and volumetric strain with time at $\Delta\sigma=10, 15, 20, 25, 35, 40, 50$ MPa

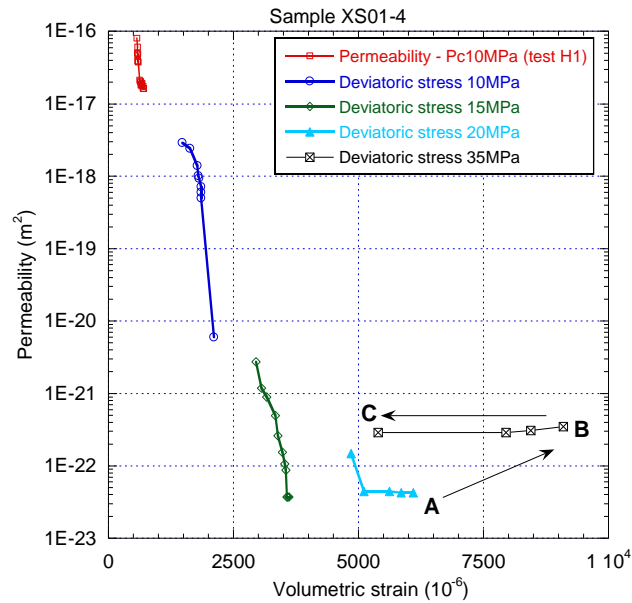


Fig.4.39 Permeability v.s. volumetric strains for both hydrostatic and triaxial test

Fig.4.39 also allows a summary of permeability variations for hydrostatic test **H1** and triaxial test. During test **H1**, the permeability decreased from $8.1E-17$ to $1.64E-17m^2$ (less than one order of magnitude) at $P_c=10MPa$ for 285 hours, which was the lowest value under isotropic loading. However, during the following triaxial test, the permeability significantly decreased (from $2.89E-18$ to $5.98E-21m^2$, almost three orders of magnitude in 139hours) at deviatoric stress of 10MPa. Such a considerable reduction with time can illustrate that time effects are more intense at 10MPa deviatoric stress than at 10MPa isotropic stress. X-ray microtomography experiments on this sample gave an evidence to verify this result from a microscopic scale (see §4.4.5.3). A sealing was observed at $\Delta\sigma=10$ and 15MPa i.e. a significant decrease in permeability came along with a small compaction. It was found that a mixed behavior (i.e. a continuous decrease in permeability v.s. volumetric strain) occurred at $\Delta\sigma=20MPa$ (and at $P_c=10MPa$ in test **H1**). There was also a quasi-constant permeability despite a significant volumetric strain evolution (decreased from 0.9% to 0.54%, point **B** to **C** in Fig.4.39) at $\Delta\sigma=35MPa$.

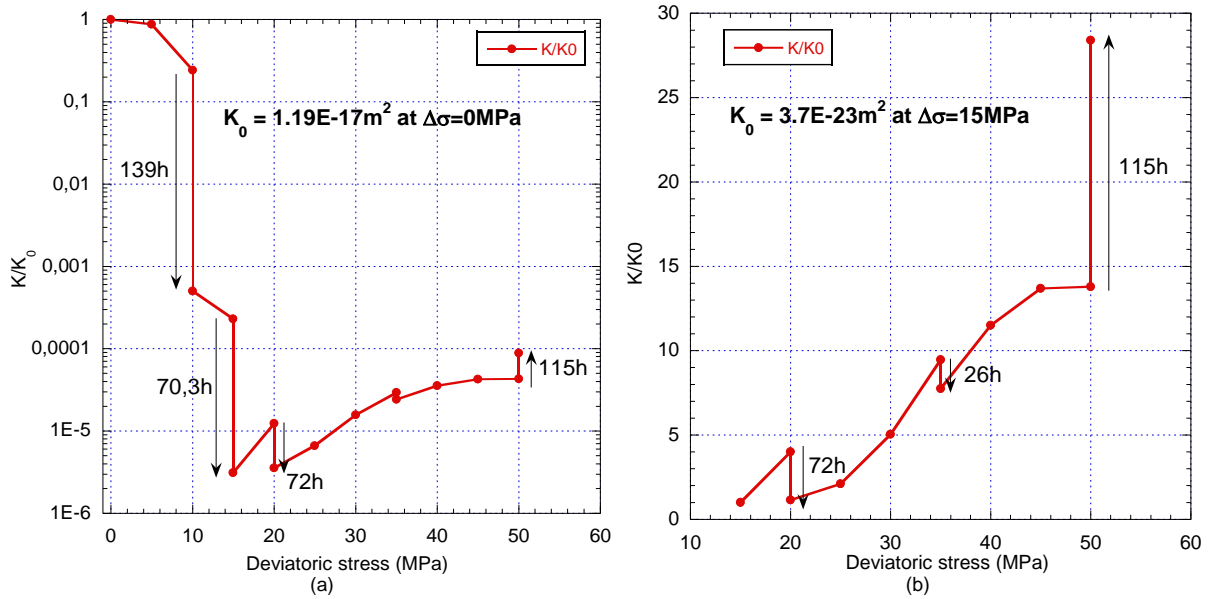


Fig.4.40 Normalized permeability under deviatoric stress

Fig.4.40 (a) shows the variations of normalized permeability K/K_0 ($K_0=1.19E-17m^2$, the value before applying deviatoric loading). Deviatoric stress increase, from 0 to 15 MPa, significantly decreased the permeability by more than five orders of magnitude due to both loading and time effects. It can be underlined that the time effects (at $\Delta\sigma=10$ and 15MPa) makes a significant contribution to this reduction (bringing almost four orders of magnitude decrease). At 20MPa, the permeability began to increase before the ‘turning point’ (dilatancy after deviatoric stress of 35MPa). Fig.4.40 (b) shows the normalized permeability using the lowest permeability (at 15MPa deviatoric stress), $K_0=3.70E-23m^2$. The permeability increased by 14 times (by more than one order of magnitude) with deviatoric loading up to 50MPa. A remarkable time effect on permeability (by 15 times increase) was found at $\Delta\sigma=50$ MPa. Despite these relative increases, the gas permeability remains very low. This means that even if cracks occurred, they had a weak effect on gas flow.

4.4.5.2. Hydrostatic tests H1 and H2 for XS01-4

During the triaxial test of this sample (see §4.4.5.1), the ‘initial’ permeability value at $P_c=5$ MPa was $1.56E-17m^2$ before axial loading (see point C in Fig.4.41 (b)). It reached the lowest one $3.70E-23m^2$ at $\Delta\sigma =15$ MPa (point D). At the end of triaxial test, it increased to $6.28E-22m^2$ (point E). Such a significant variation of permeability illustrates a visible change in the gas transfer path.

After triaxial test, this sample was taken out for scanning and replaced in hydrostatic cell to perform another hydrostatic test (H2). This hydrostatic experimental process was the same as for sample XR02-4. It was expected to evaluate the damage recovery (sealing/healing properties) of this sample with time at $P_c =5$ and 10 MPa respectively. Table 4.16 and Fig.4.41 (a) present the variations of permeability, porosity and volumetric strain with time. Besides, the comparative results for tests H1 and H2 are shown in Fig.4.41 (b), (c) and Table 4.17.

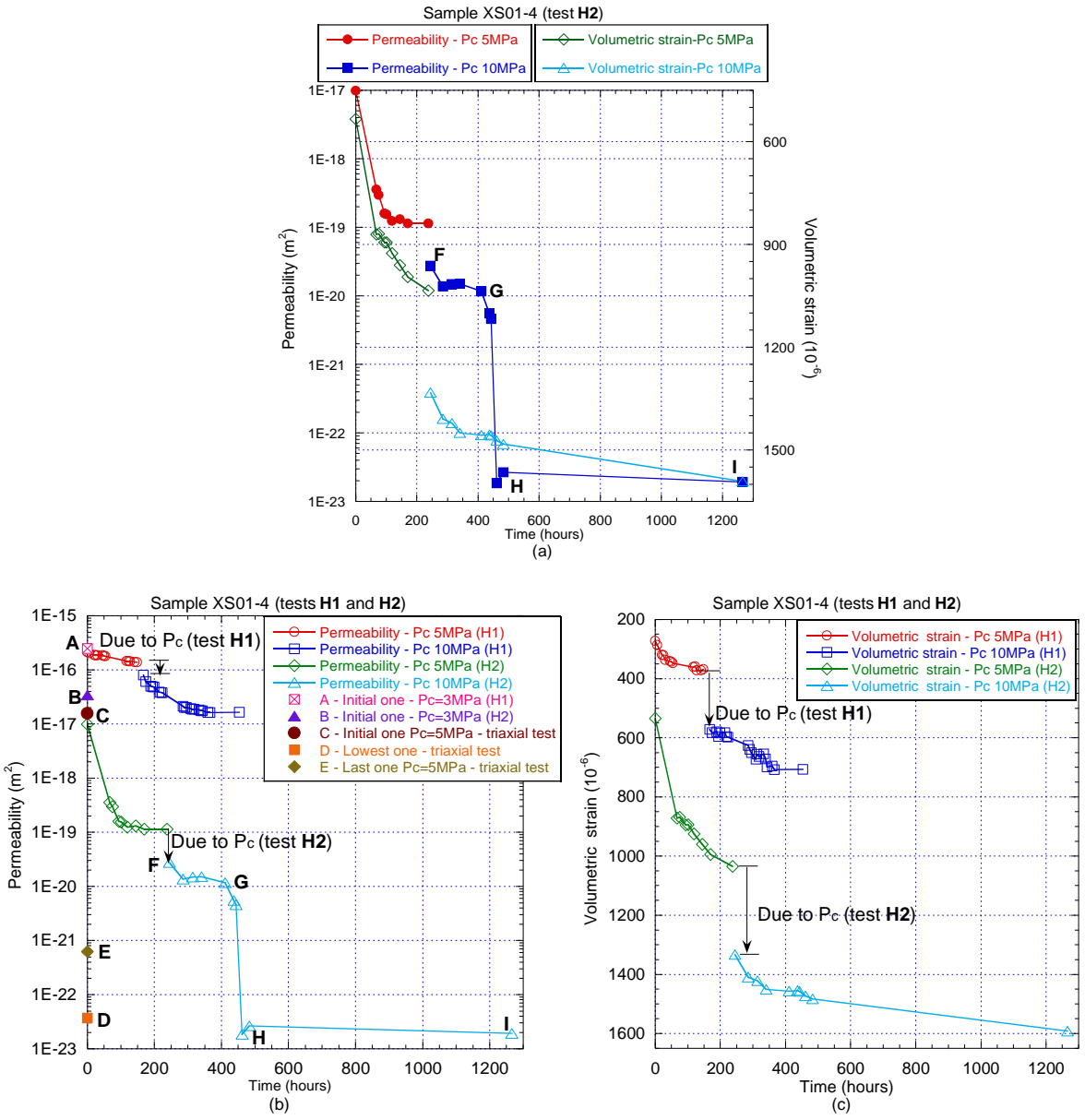


Table 4.16 Variations of permeability(K), porosity (ϕ) and volumetric strain (ϵ_v) with time under different P_c (test **H2**–after triaxial test)

XS01-4 Time (hours)	$P_c = 5\text{MPa}$			Time (hours)	$P_c = 10\text{MPa}$	
	K(m ²)	ϵ_v (10 ⁻⁶)	ϕ (%)		K(m ²)	ϵ_v (10 ⁻⁶)
0.00	9.85E-18	534.75	0.06	244.92	2.76E-20	1332.75
67.17	3.56E-19	871.5	0	285.33	1.37E-20	1409.25
75.10	2.98E-19	869.25		314.67	1.49E-20	1422
94.17	1.58E-19	894.75		340.67	1.50E-20	1450.5
101.00	1.55E-19	894		411.17	1.17E-20	1457.25
119.00	1.24E-19	925.5		437	5.53E-21	1455
144.52	1.31E-19	960.75		443	4.58E-21	1458
169.83	1.14E-19	995.25		461	1.85E-23	1473
237.50	1.09E-19	1035		483	2.66E-23	1482.75
				1266	1.92E-23	1591.65
Unloading						
	$P_c = 3\text{MPa}$ (initial loading)			$P_c(5\text{MPa})$	1.63E-22	1290
	3.41E-17	310.5	0.50	$P_c(3\text{MPa})$	3.21E-22	1116.75

At P_c of 3MPa in test **H2**, the initial permeability value was $3.41\text{E-}17\text{m}^2$ (point **B**), almost five orders of magnitude higher than the last measurement (point **E**, $6.28\text{E-}22\text{m}^2$ at $P_c=5\text{MPa}$ and $\Delta\sigma=0\text{MPa}$) in triaxial test. As mentioned before (in §4.4.5.1), axial loading did not cause a significant increase in permeability during triaxial test. Based on the comparison of permeability between point **B** and **E** in Fig.4.41, it can be inferred that new micro-cracks, generated due to deviatoric stress, remained closed in triaxial test, but can reopen after all external stresses were removed. Therefore, such an increase in permeability can be mainly attributed to the reopening of new micro-cracks. This hypothesis can be verified from the microstructure observation of scan 3° after triaxial test, as shown in Fig.4.43 and 4.44,

It can be observed that the initial permeability in test **H2** is lower than in **H1** (see point **B** and **A**). This difference of permeability in **H1** and **H2** progressively increased with time, especially at $P_c=10\text{MPa}$. This phenomenon is quite different with sample XR02-4, for which the permeability in test **H2** was higher than **H1**. At $P_c=5\text{MPa}$, the permeability decreased from $9.85\text{E-}18$ to $1.09\text{E-}19\text{m}^2$ in 238hours (sharply dropped with time in the first 94hours, then remained stable). The loading of P_c from 5 to 10MPa led to a bigger decrease in permeability than during test **H1**, as shown in Fig.4.41 (b). It decreased to $1.92\text{E-}23\text{m}^2$ in the next 1021hours (42days) at $P_c=10\text{MPa}$. The permeability evolution during this time can be divided into 3 parts: a smooth and continuous decrease from 250 to 450h (point **F** to **G** in Fig.4.41 (a)) followed by a sharp drop at constant volumetric strain (**G** to **H**) and then a long plateau until 1250h (**H** to **I**) during which the volumetric strains increased very little.

The permeabilities during the P_c unloading phase are shown in Table 4.16 (in bold). It increased by one order of magnitude (to $3.21\text{E-}22\text{m}^2$) with P_c unloading to 3MPa. It is five orders of magnitude lower than the initial one at $P_c=3\text{MPa}$ ($3.41\text{E-}17\text{m}^2$, point **B**), which presents a strong irreversibility.

Table 4.17 Comparison of changes in permeability, porosity, coupling with P_c /time, and volumetric strain due to time before (**H1** test) and after triaxial test (**H2** test)

XS01-4	Permeability(m^2)		Porosity(%)		$\Delta\epsilon_v$ due to time (10^{-6})		$\Delta\epsilon_v$ due to P_i ($10^{-6}/MPa$)	
	H1	H2	H1	H2	H1	H2	H1	H2
P_c (MPa)								
3	2.48E-16	3.41E-17	0.44	0.5				
5	2.12E-16	9.85E-18	0.36	0.06	96	500.25	1.84	
5	1.39E-16	1.09E-19	0	0	(148hours)	(238hours)	1.31	24.75
10	8.10E-17	2.76E-20	0	0		150	0.84	
10	1.64E-17	1.92E-23	0	0	134.25	(238hours)	0	23.65
					(286hours)	258.9		
						1021hours		

Table 4.17 gives the comparative results of $\Delta\epsilon_v$ due to time in tests **H1** and **H2**. At $P_c=5MPa$, $\Delta\epsilon_v$ due to time (238hours) in test **H2** was $500 \cdot 10^{-6}$, while it was only $96 \cdot 10^{-6}$ (148hours) in test **H1**. ($\Delta\epsilon_v$ due to a time of **145hours** in test **H2** was $426 \cdot 10^{-6}$, which is still considerably higher than the value of $96 \cdot 10^{-6}$ in test **H1**). On a whole, this sample is more deformable (under confining pressure) after triaxial test than before (see Fig.4.41 (c)). Porosity and permeability are in parallel more sensitive to this loading.

The variations of volumetric strain due to gas pressure were recorded to characterize coupling effects between pore fluid pressure and rock skeleton (due to the absence of an unloading phase as sample XR02-4). $\Delta\epsilon_v$ due to P_i was tenuous ($1.3 \cdot 10^{-6}/MPa$) at $P_c=5MPa$ in test **H1** so almost negligible. The behaviour is very different after triaxial test since the coupling effects became significantly stronger: $\Delta\epsilon_v$ due to P_i is $25 \cdot 10^{-6}/MPa$ (after 238hours at $P_c=5MPa$). This phenomenon can be attributed to the production of multi-cracks under deviatoric loading. In fact, two phenomena (already observed) can be involved in triaxial loading: compaction and cracking. This means that the porous network is profoundly changed and this is why the occurrence of cracking is not visible on permeability value (before and after triaxial test) but makes it very sensitive to confining pressure (in **H2**). On the other hand, the new cracking is also evidenced by coupling effects i.e. sensitivity to pore pressure is increased. It is also consistent with observation from X-ray micro-tomography (see Fig.4.44 in the next section §4.5.5.3).

4.4.5.3. Microstructure observations from X-ray microtomography for sample XS01-4

The porosity of this sample XS01-4 from three scans, as shown in Fig.4.42, is composed of pores and cracks. The pore/crack volume in the range of $1 \sim 3.54e+5$ voxels in scan 1° and $1 \sim 1.08e+6$ voxels in scan 3°, which reveals visible new generated cracks due to triaxial test. Some cracks closure are observed in scan 2°. A significant compaction of the whole sample due to axial loading is found in scan 3°. In order to obtain more accurate visualisation of crack/pore changes, two sub-volumes and their 3D pore space were extracted from three scans (scan 1° the original state, scan 2° after test **H1** and scan 3° after triaxial test, see Fig.4.43 (b) and (c)). Their location in the sample is shown in Fig.4.43 (a). Subvolume-1 ($12mm \times 12mm \times 10mm$) is chosen to mainly present the development of pore while

subvolume-2 (10mm×10mm×10mm) mainly shows crack changes. The microstructural changes in horizontal and vertical slices of two sub-volumes are shown in Fig.4.44.

Table 4.18 Variations of permeability, porosity and coupling of sample XS01-4 during different tests

XS01-4	Mechanical loadings	K (m ²)	Porosity (%)	$\Delta\varepsilon_v (P_i)$ 10 ⁻⁶ /MPa	Modulus H (GPa)
Scan 1° (0.358%)					
Hydrostatic test (H1)	P _c =3MPa	2.48E-16	0.44	2	500
	P _c =10MPa	1.64E-17	0	0	+∞
Scan 2° (0.290%)					
Triaxial test $\sigma_{max} = 50MPa$	P _c =5MPa; $\Delta\sigma=0MPa$	1.56E-17			
	P _c =10MPa; $\Delta\sigma=15MPa$	3.70E-23 (the lowest one)			
	P _c =5MPa; $\Delta\sigma=0MPa$	6.28E-22			
Scan 3° (0.327%)					
Hydrostatic test (H2)	P _c =3MPa	3.41E-17	0.50		
	P _c =10MPa	1.92E-23	0	23.65	42.28

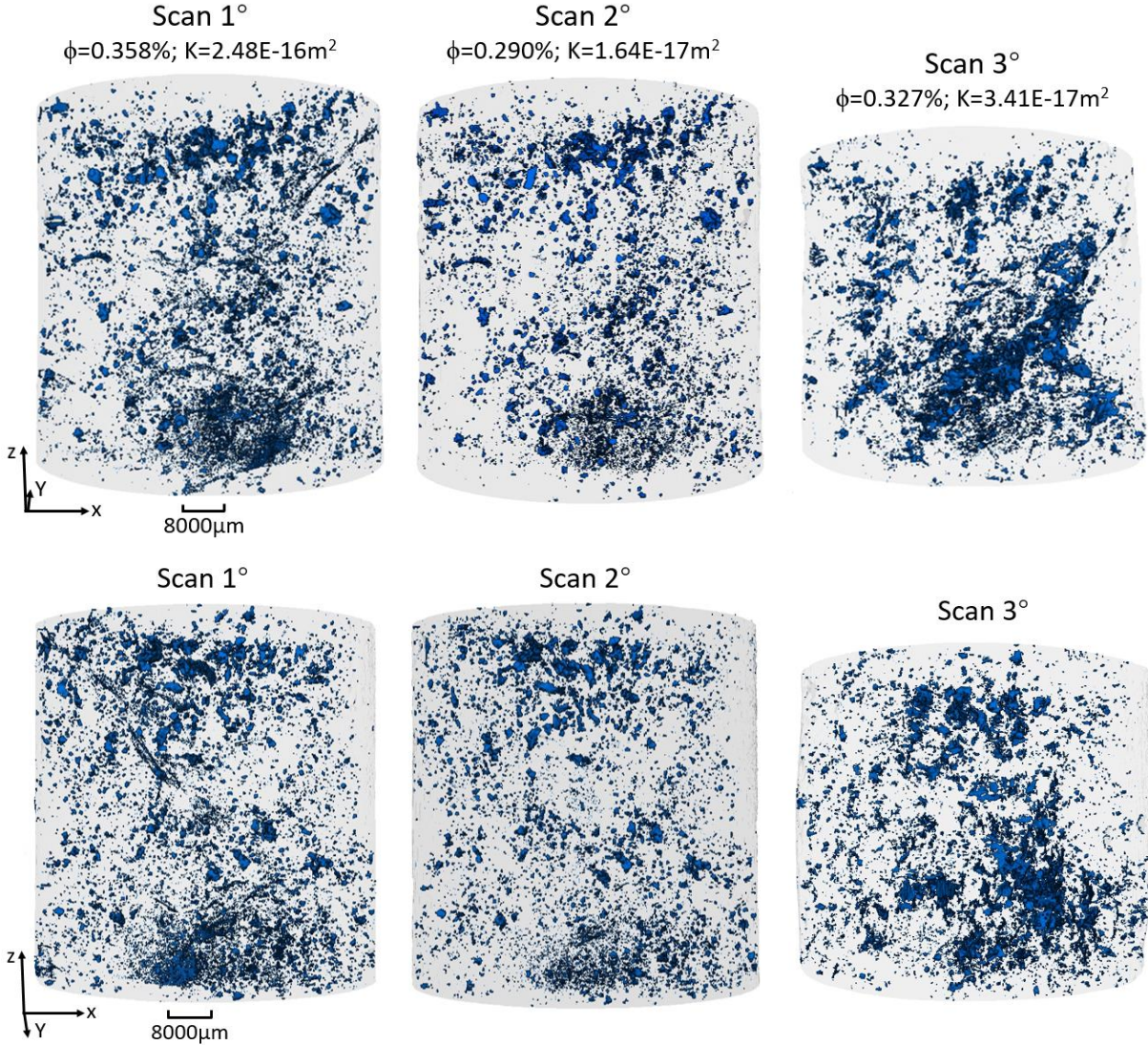
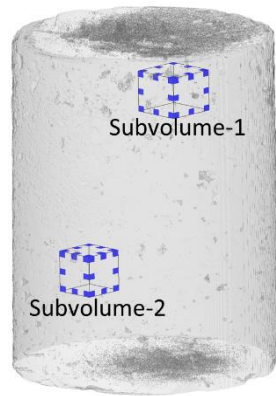


Fig.4.42 3D pore space of sample XS01-4 from different scans

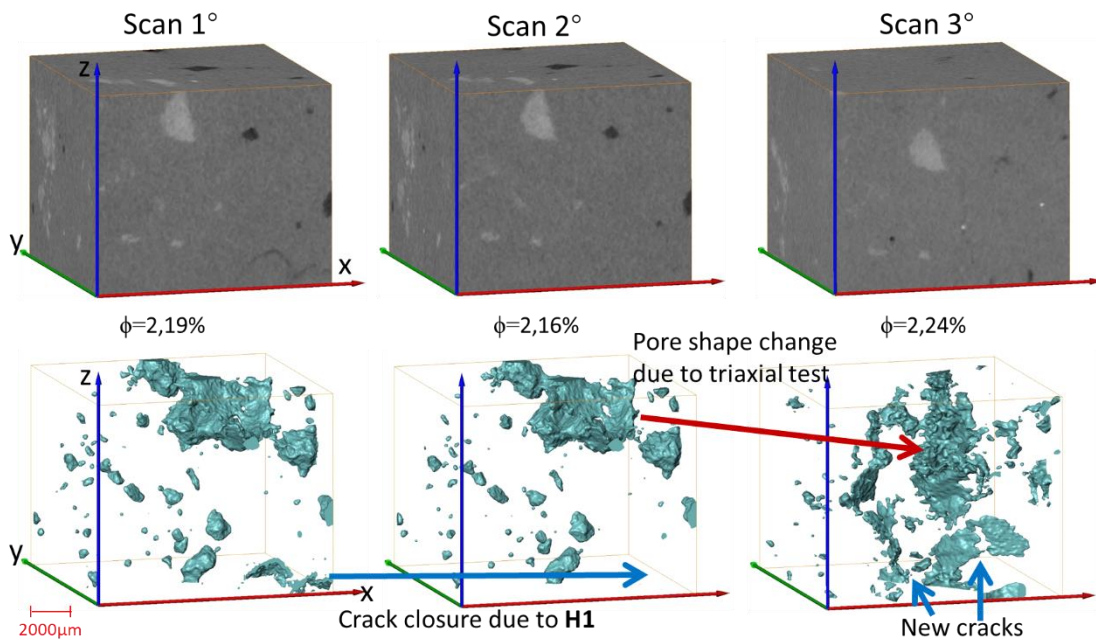
Some comments are directly given on Fig.4.43 and 4.44 to facilitate the analyses (the same as sample XR02-4). To sum up, the pore/crack changes for three scans are as follows:

- It can be observed from scan 1° to 2° that **H1** test led to (partial) crack closure, but with virtually no changes in pores volume
- Triaxial test has two ‘competitive’ effects (observed from scan 2° to 3°): significant loss of pores volume (compaction of some pores, they were significantly changed from a pore shape to flat/crack shape) and new multi-cracks.

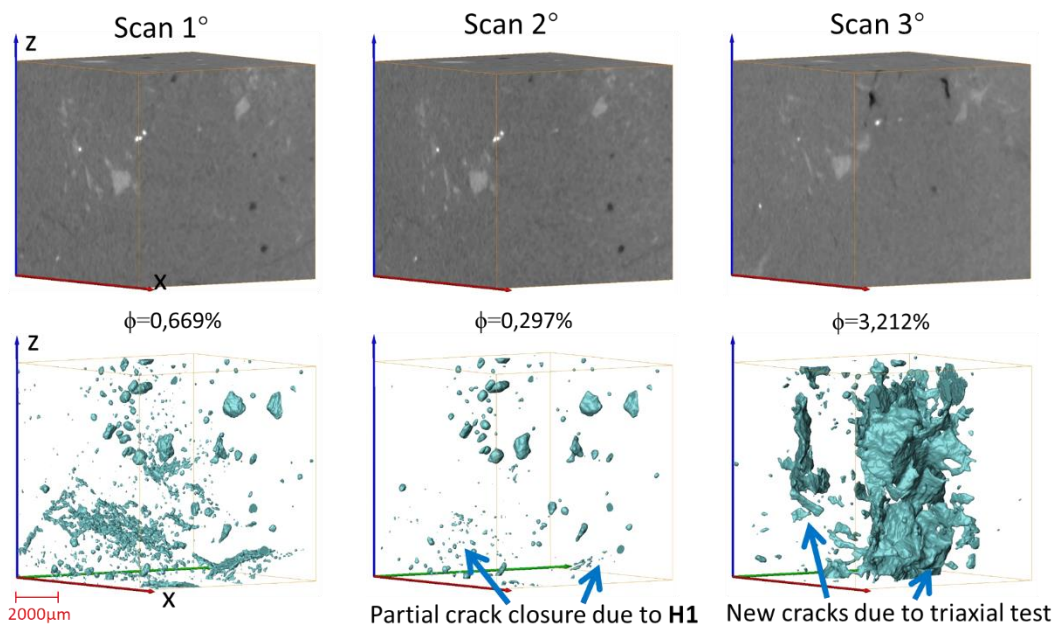
It should be noted that, the loss of porosity from scan 1° to 2° (by 0.03% in subvolume-1 and 0.37% in subvolume-2) is mainly due to crack closure. On a whole, if crack closure effect was not visible in test **H1**, the small decrease in permeability observed during test **H1** is therefore logical. Despite multi-cracks due to axial loading, the initial permeability in test **H2** (see point **B** in Fig.4.41 (b)), was lower than the one (point **A**) in test **H1**. The compaction effect is dominant in terms of permeability.



(a) Location of 3D subvolume-1 and subvolume-2 of sample XS01-4 from scan 1°



(b) 3D subvolume-1 (12mm×12mm×10mm)



(c) 3D subvolume-2 (10mm×10mm×10mm)

Fig.4.43 Two 3D sub-volumes and pore space extracted from three scans of sample XS01-4

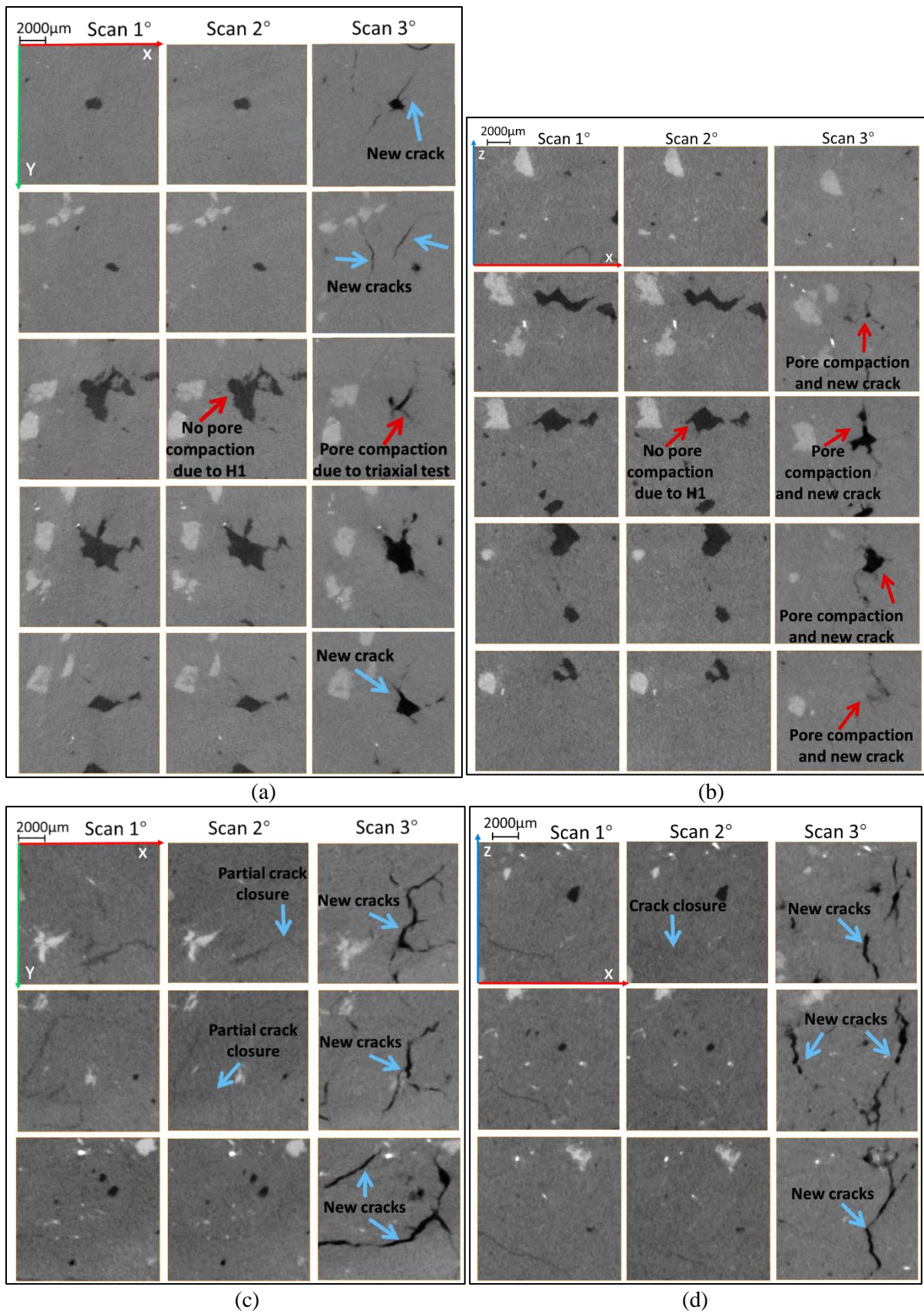


Fig.4.44 The microstructure development (crack: blue arrows; pore: red arrows) of slices in two subvolumes with different scans of sample XS01-4 ((a) and (b): the horizontal and vertical slices of subvolume-1; (c) and (d): the horizontal and vertical slices of subvolume-2)

Such substantial changes in pore's shape make it more sensitive to confining pressure or time effects than before (i.e. these flat pores are easier to be closed with time under confinement). This new microstructure of 'damaged' sample can therefore explain the significant decrease in permeability in test **H2** (reaching an order of magnitude 10^{-23}) with time at $P_c=10\text{MPa}$ (6 orders of magnitude lower than the lowest one ($1.64\text{E-}17\text{m}^2$) achieved in test **H1**). On the other hand, it is consistent with the increase in sensitivity to pore pressure.

Based on the crack development in three scans (see Fig.4.44 (a), (c) and (d)), it can also be found that cracks were partially closed after test **H1**, and this effect continued (both in horizontal (c) and vertical (d) direction) during deviatoric test. This additional closure resulted in a blockage of gas transfer pathway. Coupled with the pores compaction, it led to a significant decrease in permeability during triaxial test.

At the edges of pores, where the stress concentration occurred (relatively sharp parts), some new cracks were generated due to deviatoric stress (see Fig.4.44 (a) and (b)). These new cracks are supposed to be opened after dismounting, this can be due to stress relaxation coupled with non-homogeneous strain recovery. Most of these cracks were kept in a closure state and did not provide effective channel or pathway for gas transfer in triaxial test.

4.4.5.4. Partial conclusion for sample XS01-4

The time effect on permeability was found to be remarkable during triaxial test: the permeability significantly decreased with time in the compaction phase (at $\Delta\sigma=10$ and 15MPa) and increased with time in the dilatancy phase (at $\Delta\sigma=50\text{MPa}$). As a whole, the permeability first decreased by five orders of magnitude and then increased by one order of magnitude due to deviatoric loading and time.

The permeability value at the beginning of **H2** was four orders of magnitude higher than the last one of triaxial test due to the sample dismounting. This proved that the triaxial test had created multi-cracks, which remained close under confinement but could open after all stresses were removed. It is surprising that the permeability in test **H2** was significantly lower than in **H1**, which can be attributed to the compaction effect caused by triaxial test. The time dependent behaviors were highly different: very weak in test **H1** but strong in **H2**. For 'damaged' sample XS01-4, the lowest permeability in test **H2** can even reach six orders of magnitude lower than the lowest one in test **H1**. **This means that its porous network is profoundly changed.** However, both the stronger coupling and more sensitivity of permeability to confining pressure in **H2** revealed the occurrence of a cracking effect. Furthermore, these two effects due to triaxial test have been validated by the observations of micro-CT scans.

4.4.6. Partial conclusion

Triaxial tests on five different samples were performed to investigate permeability variations with deviatoric stress and time. A significant increase in permeability (or damage), almost five orders of

magnitude, with deviatoric loading/time was evidently observed at low confinement (2MPa) for sample XZ25-3. While the permeability increase for other samples at 7MPa confining pressure are much smaller than this one (e.g. two orders of magnitude increase for XR02-3 and basically no changes for XS01-3). At high confinement (10MPa), permeability (first significantly decreased and then) moderately increased for XS01-4, and only slightly increased for XR02-4. The difference in permeability variations revealed that the generation and development of cracks are suspected to be highly dependent on different applied P_c . Therefore, it can be inferred that during triaxial test the confining pressure has a crucial effect on dilatancy or damage, which is also consistent with those in literature.

Time effects on permeability were observed to be different under different levels of constant deviatoric stress. In the compression phase (usually at low deviatoric stress), the permeability decreased with time due to crack closure. When sample went into the dilatant phase (usually at high deviatoric stress), the permeability increased with time due to crack generation. The permeability variations cannot be attributed to changes in volumetric strain alone, as for sample XR02-4 a large volumetric dilatancy (5.65%) did not cause a significant increase in permeability. Obviously, these permeability measurements were all performed at the time scale of tens of days. In the future, it may be interesting to conduct triaxial test with the purpose of estimating time effects during a period of months.

Even if the permeability had reached a 'stable' value during relatively 'long-term' (around 2 weeks) hydrostatic pressure in test **H1**, it still significantly decreased (6 orders of magnitude for sample XS01-4) due to deviatoric loading and time effects. This result reveals that permeability is not only sensitive to isotropic loading, but also strongly influenced by deviatoric loading and creep. The permeability of salt in DRZ may vary under deviatoric stress and with time.

After triaxial tests, these five 'damaged' samples were used to perform a new hydrostatic test (**H2**). The first interesting observation is that, for all samples, the first permeability value at test **H2** was higher than the last one of triaxial test. This is mainly attributed to the opening of new cracks (due to deviatoric stress) after the sample dismounting. It is likely to show that sealing effects are temporary i.e. can vanish when the material is completely unloaded. A higher permeability and stronger coupling than in **H1** were detected in **H2** for samples XR02-3, XZ25-3 and XR02-4. However, there is only a small increase in permeability for sample XS01-3 and even lower permeability in **H2** than in **H1** for XS01-4. For these two sample, there was a more significant confining pressure effect on permeability after triaxial test than before. This phenomenon reveals cracking due to triaxial test.

The permeability variation in **H2** indicates that the damaged samples can achieve a good sealing i.e. recover the initial permeability before axial loading. In other words, cracks caused by high deviatoric loading can be closed with isotropic stress and time. In addition, significant time effects on permeability decrease were observed in the healing (damage recovery) phase for samples XR02-4 and XS01-4.

The results of X-ray microtomography experiments confirm that cracks were (partially) closed, but pores were basically unchanged during test **H1**. Two ‘antagonistic’ effects due to triaxial test can be observed from micro-CT scans: the first is the compaction effect that makes pores smaller (and further crack closure); the second is the cracking effect. For sample XR02-4, the cracking effect is suspected to play a dominant role because of a small permeability increase and stronger coupling effects in **H2**. On the contrary, for sample XS01-4, the compaction effect dominates in terms of permeability, as permeability was decreased in **H2** compared to **H1**, even with higher sensitivity to confining pressure. What is nevertheless clear and indicated by micro-CT is that deviatoric loading leads to spectacular changes in the porous structure. Shape of pores is modified and cracks disappear while new ones are created.

4.5. Sealing/Healing effects on two damaged samples (uniaxial test and a comparison of hydrostatic test H1 and H2)

The sealing/healing properties of ‘damaged’ rock salt are also evaluated in this section. However, the damaged samples XZ25-4 and XZ25-5 were obtained by performing uniaxial tests. As mentioned before, the damage caused by conventional triaxial test under 10MPa confining pressure was not very significant on a permeability point of view. A uniaxial test was therefore conducted since a stronger damage (without confinement) was expected. Subsequently, hydrostatic tests (**H2**) were conducted on these two ‘damaged’ samples to investigate potential sealing/healing effects on permeability and couplings (Biot’s coefficient and H modulus). Time effects were also estimated but only at the highest/last confinement level (20MPa) during test **H2**. In addition, permeability was also measured during the unloading phase.

4.5.1. Sample XZ25-5: H1 test, uniaxial test and H2 test

For this sample XZ25-5, hydrostatic test (**H1**) was first carried out to get the initial properties (such as permeability, porosity, and couplings). The results are presented in Table 4.19. The initial permeability at $P_c=3\text{MPa}$ is $1.29\text{E-}19\text{m}^2$ and the porosity is 0.6%. As expected, Biot’s coefficient is 0.2, this is still very low if compared to other sedimentary rocks. It was then decided to perform uniaxial test to obtain a cracked sample.

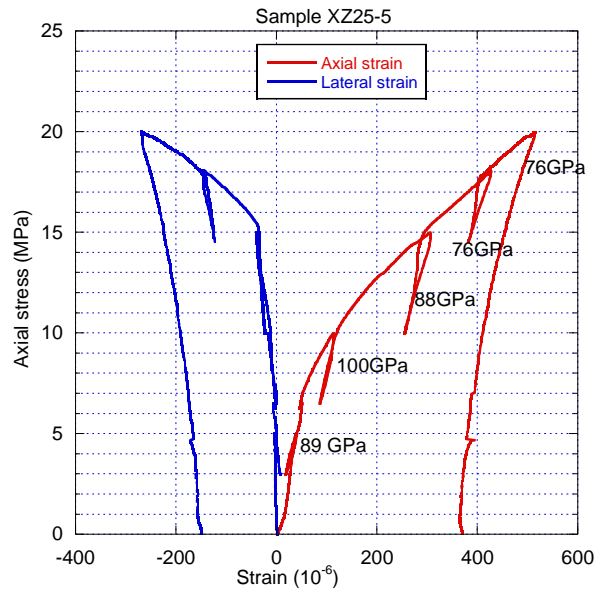


Fig.4.45 Stress-strain curves of uniaxial test

The maximum axial stress was limited to 20MPa. As shown in Fig.4.45, four unloadings were performed to evaluate Young's moduli. It is probable that a small compaction phase occurred and linked to a first Young's modulus increase (89 to 100GPa). The sample was then likely to be damaged as in the following there was a decrease in Young's modulus.

Permeability, porosity, volumetric strain and couplings v.s. confining pressure and/or time were measured during test **H2**. These measurements were conducted at 7 levels of confinement (from 3 to 20 MPa). The time effects were estimated at the last level of $P_c=20$ MPa to explore the potential sealing with time at high confining pressure. All the results are shown in Table 4.19 and 4.20.

Table 4.19 Variation of ϕ , biot, K_b , H, $\Delta\varepsilon$ due to P_i , K_g and ε_v with P_c for the same sample before (**H1**) and after (**H2**) uniaxial test

XZ25-5	P_c (MPa)	porosity (%)	Biot	K_b (GPa)	H (GPa)	$\Delta\varepsilon_v(P_i)$ $10^{-6}/\text{MPa}$	K (m^2)	$\varepsilon_v(10^{-6})$
Test H1	3	0.6	0.205	20.77	101.23	9.88	1.29E-19	199
Test H2	3	1.45	0.62	11.11	18.39	54.37	3.73E-16	749
	5	1.13	0.55	13.42	24.30	41.15	2.23E-16	1066
	7	0.99	0.41	16.36	39.84	25.10	1.05E-16	1318
	10	0.80	0.397	18.64	46.93	21.31	2.52E-17	1713
	13	0.76	0.396	19.86	50.15	19.94	1.17E-17	1982
	16	0.70	0.351	20.13	57.4	17.42	5.50E-18	2297
	20	0.47	0.277	22.28	80.57	12.41	1.17E-18	2621
	20(74hr)	0.23	0.262	22.65	86.32	11.59	1.52E-19	2805
	20(336hr)	0	0.226	22.34	98.79	10.12	2.40E-20	2930
Test H2 -Unload	10			17.24			2.83E-20	2417
	3			13.85			1.70E-19	1961

Table 4.20 Variation of ϕ , K_g , ϵ_v at P_c of 20MPa with time after uniaxial test

XZ25-5	Time (hours)	porosity (%)	K (m ²)	ϵ_v (10 ⁻⁶)
Time effects at $P_c=20$ MPa After uniaxial	0	0.47	1.17E-18	2621
	74	0.23	1.52E-19	2805
	91	0.25	9.05E-20	2808
	102		7.02E-20	2827
	118	0.09	5.83E-20	2839
	128		5.61E-20	2863
	135		4.47E-20	2868
	139	0.07	3.65E-20	2882
	148		4.80E-20	2965
	153		4.73E-20	2945
	158		3.93E-20	2935
	163	0.04	3.39E-20	2920
	174		4.07E-20	2900
	236		3.24E-20	3012
	241	0	3.60E-20	2973
	246		3.39E-20	2965
	259		2.93E-20	3000
	265		2.79E-20	2964
	270		2.62E-20	2960
	283		2.45E-20	2926
	291		2.64E-20	2926
	294		2.43E-20	2930
	315		2.40E-20	2930
407		2.01E-20	2948	
413		1.95E-20	2952	

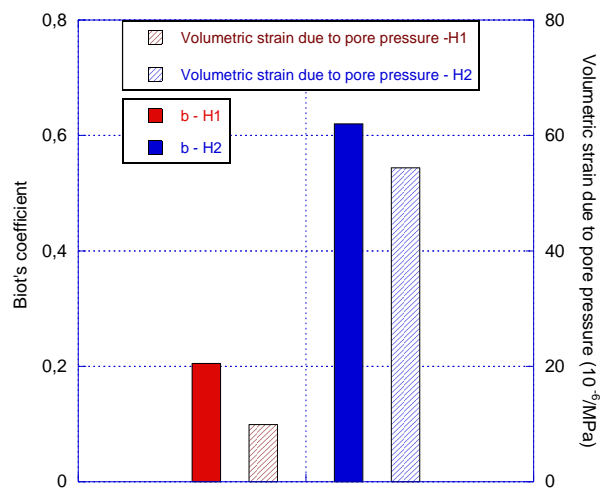


Fig.4.46 Comparison of Biot's coefficient and $\Delta\epsilon_v$ due to P_i at $P_c=3$ MPa in tests **H1** and **H2**

At $P_c=3\text{MPa}$, the permeability value is $3.73\text{E-}16\text{m}^2$, almost 3 orders of magnitude higher than the ‘initial’ value $1.29\text{E-}19\text{m}^2$ in test **H1**. Meanwhile the porosity significantly increased from 0.6% to 1.45%. Despite this porosity is still very low compared to other rock, such a large increase is higher than for the other samples. In addition to these two phenomenon, the variation of volumetric strain due to pore gas pressure also considerably increased from 10 to $54 \cdot 10^{-6}/\text{MPa}$ (as shown in Fig.4.46). This is linked to a larger material expansion due to pore pressure (H decrease). In parallel, it was observed a decrease in K_b , after uniaxial test, the material is more deformable. This logically led to a Biot’s coefficient increase from 0.2 to 0.6 (as shown in Fig.4.46), which illustrates much more couplings caused by pore pressure than before. All these results can indicate that the sample had been strongly damaged and that new cracks had been produced by axial stress. The micro-observation from X-ray microtomography of another sample XZ25-4, which was used for similar tests (see §4.5.2.2), demonstrated the multiple-cracks caused by axial stress. The spectacular ‘b’ increase confirms that the coupling can only be produced through cracks (or mainly produced).

The permeability variation with P_c in test **H2** is shown in Fig.4.47, it decreased with confining pressure. At $P_c=20\text{MPa}$ the permeability was $1.17\text{E-}18\text{m}^2$ (point **B**). This value cannot meet the ‘initial’ one $1.29\text{E-}19\text{m}^2$ in test **H1** (point **E**), which indicates the cracks caused by axial stress of 20MPa had not been completely closed at high confining pressure of 20MPa.

Time effects at $P_c=20\text{MPa}$:

The confining pressure was maintained constant at 20MPa, the variations of permeability and porosity with time were measured, as well as the volumetric strain evolution. The results are shown in Table 4.20 and Fig.4.50. The permeability decreased to $1.95\text{E-}20\text{m}^2$, by almost two orders of magnitude, after 413hours. In parallel, the volumetric strain varied from 2621 to 2952 $\mu\text{m}/\text{m}$. The evolution of volumetric strain seems to be stable at the end (except for a small fluctuation). As shown in Fig.4.49, the permeability variation with volumetric strain exhibits the so called ‘mixed behavior’ (see §4.3.1).

After 17days of constant 20MPa confinement, an unloading was processed. The permeability and volumetric strain were recorded at 10 and 3MPa respectively in the unloading phase. The results are shown in Fig.4.47, Fig.4.48 and Table 4.19. A significant hysteretic behavior is observed as after unloading, the last permeability value at 3MPa ($1.70\text{E-}19\text{m}^2$, point **D**), was three orders of magnitude lower than the first measurement at $P_c=3\text{MPa}$ (point **A**). The corresponding volumetric strain also exhibits an irreversibility (see point **A** and **D** in Fig.4.48). Such a high irreversibility shows that the closure of some cracks produced in uniaxial test is, in a large part, irreversible.

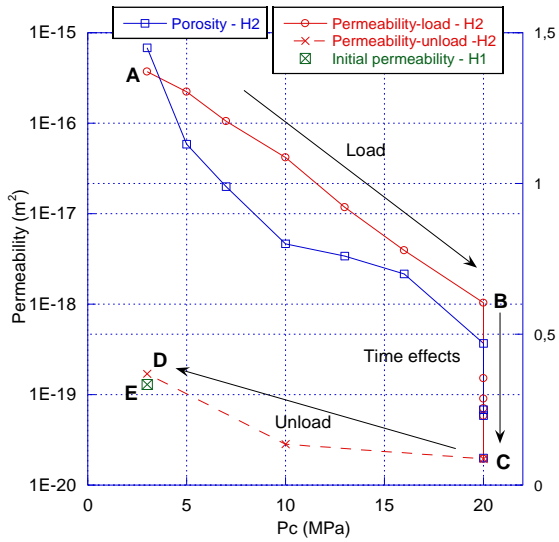


Fig.4.47 Changes in K_g and ϕ with P_c in test H2

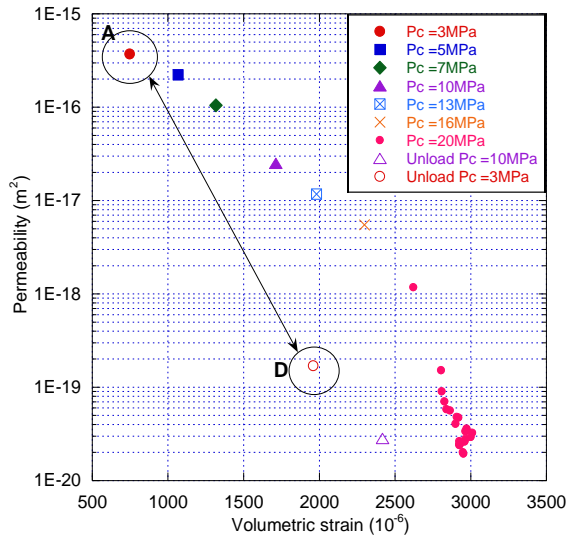


Fig.4.48 K_g as a function of ϵ_v (load and unload)

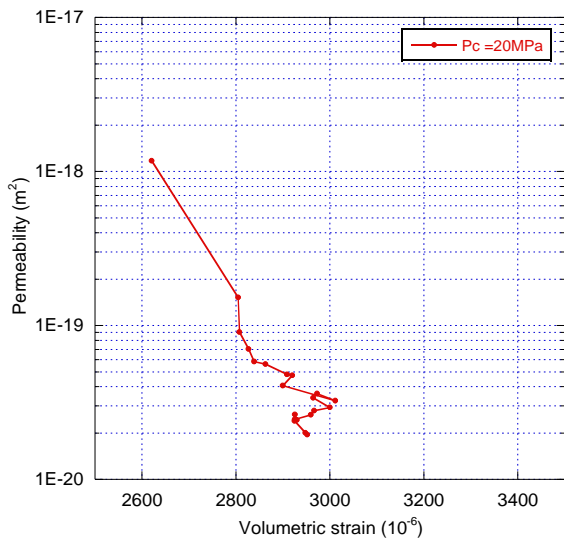


Fig.4.49 K_g as a function of ϵ_v at $P_c=20MPa$

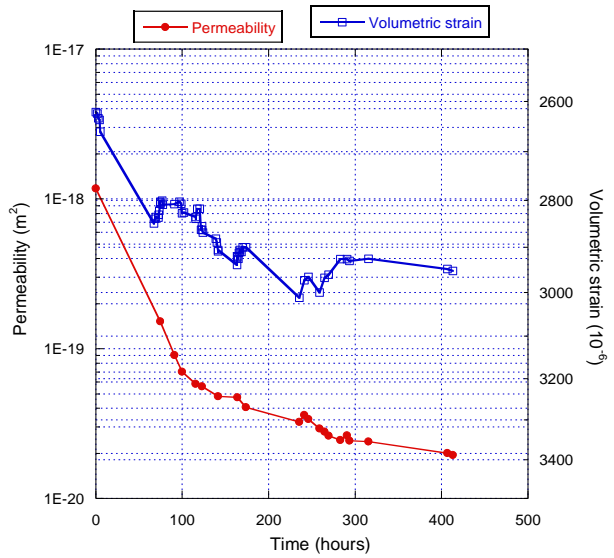


Fig.4.50 changes in K_g and ϵ_v with time at $P_c=20MPa$

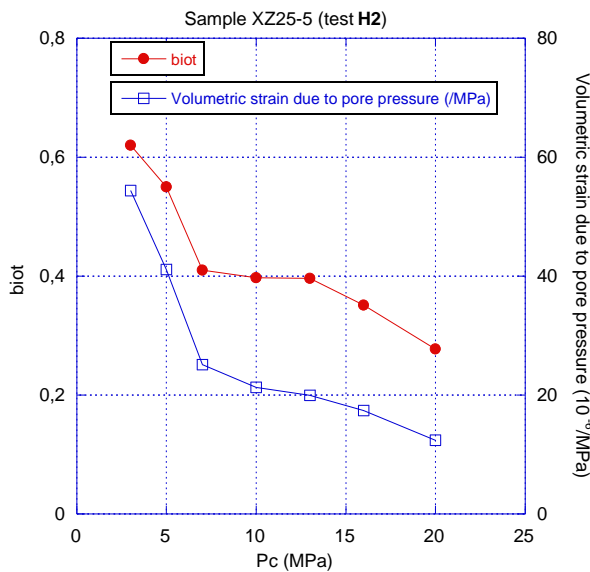


Fig.4.51 Biot and $\Delta\epsilon_v$ due to P_i after uniaxial test

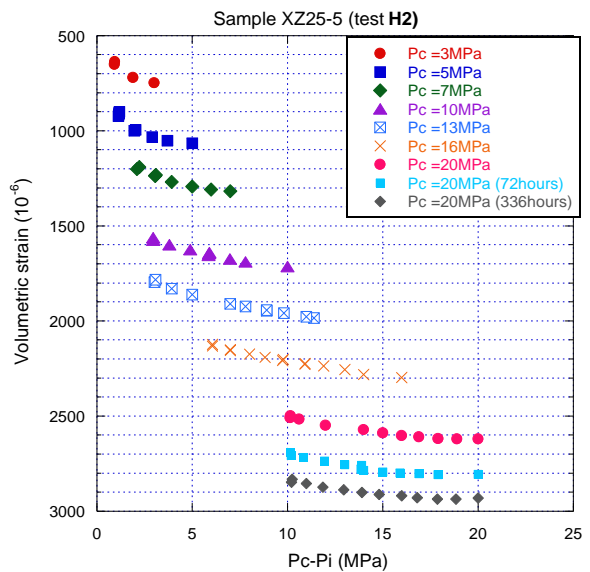


Fig.4.52 ϵ_v as a function of $P_c - P_i$

Increase in confining pressure results in crack closure. This produced a visible decrease in Biot's coefficient (Fig.4.51), which is partially linked to less couplings between gas pressure and skeleton (Fig.4.52). The time effect has shown marginal changes (from 0.28 to 0.23) in the Biot's coefficient. However, the permeability decreased in parallel by two orders of magnitude (see Table 4.19).

4.5.2. Sample XZ25-4

4.5.2.1. Uniaxial test (U1, U2) and hydrostatic tests (H1, H2, H3) for sample XZ25-4

All the tests and scannings performed on sample XZ25-4 are described below:

The first scan was done on this sample at its initial state. Hydrostatic test (**H1**) was then carried out to detect time effects on permeability, porosity and volumetric strain at two confinement levels (see Table 4.4 in §4.3.1). As mentioned in §4.2.4, the first uniaxial test **U1** was performed after test **H1** without scanning between **H1** and **U1**, as the X-ray microtomography equipment was not operational at that time. The following hydrostatic tests **H2** and **H3** were used to heal the damaged specimen. (**H2** test had to be stopped due to *Covid*, hence test **H3** was carried out and the experimental process was similar to test **H2**). The second scan was done after test **H3**. In order to observe the microstructure changes due to uniaxial stress, the second uniaxial test (**U2**) was therefore performed (see Fig.4.3 in §4.2.4) and followed by the third scan.

The experimental steps of test **U1** are the same as for the previous one (sample XZ25-5): the maximum axial stress is 20MPa and four axial unloadings were applied to estimate Young's modulus, as shown in Fig.4.53. The increase in this modulus with the axial load in test **U1** indicates an occurrence of hardening or compaction without noticeable mechanical damage. It is found that Young's moduli in test **U2** were higher than **U1**. This can be mainly attributed to the sample compaction during tests **H2** and **H3**, which were executed between **U1** and **U2**. It can also be underlined that the material had already reached the maximum axial stress point **A** before being unloaded to point **B**. It is thus logical that the loading path **CD** is similar to **AB** (elastic path). This is valid for lateral and longitudinal strains.

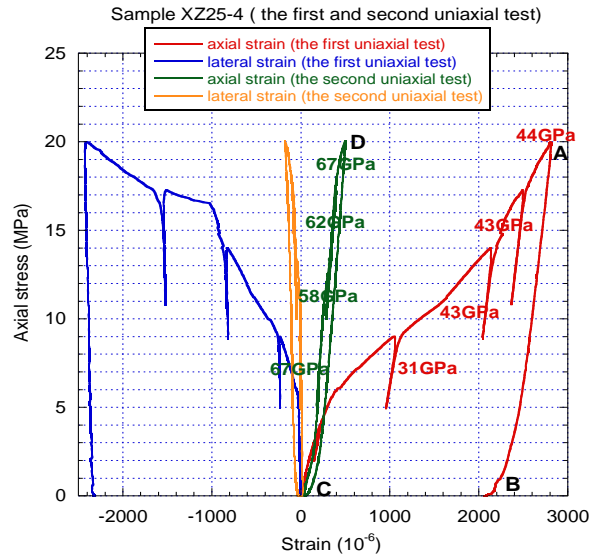


Fig.4.53 Stress-strain curves of uniaxial tests (U1 and U2)

The experimental steps of **H2** are the same as for the sample XZ25-5. The damage due to axial loading was supposed to be significant since the permeability at $P_c=3\text{MPa}$ is now $3.83\text{E-}17\text{m}^2$, almost two orders of magnitude higher than the initial one $9.03\text{E-}19\text{m}^2$ in **H1** (see Point A and C in Fig.4.54). At the same time, the porosity in **H2** had increased to 1.15%, compared to the corresponding value 0.52% in **H1** (see Point B and D in Fig.4.54). The higher permeability and porosity values indicate that multi-cracks, i.e. new pathways, had been produced by axial loading. It can be verified by the micro-observation from X-ray microtomography experiments (see §4.5.2.2).

The permeability exponentially decreased from $3.83\text{E-}17$ to $4.29\text{E-}21\text{m}^2$, by four orders of magnitude, with P_c increasing from 3 to 20MPa, as shown in Fig.4.54. It can be assumed that (on a permeability point of view,) new cracks had been closed at 20MPa confining pressure, as permeability had been reduced to $4.29\text{E-}21\text{m}^2$, lower than the lowest permeability ($5.44\text{E-}20\text{m}^2$) in test **H1**.

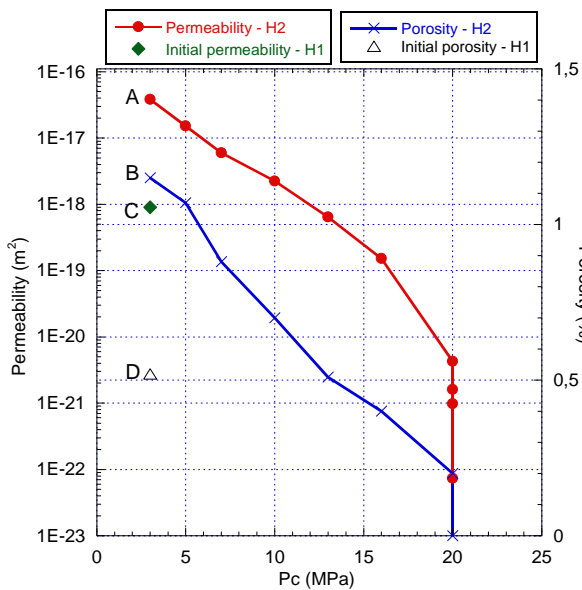


Fig.4.54 Changes in K_g and ϕ with P_c in test **H2**

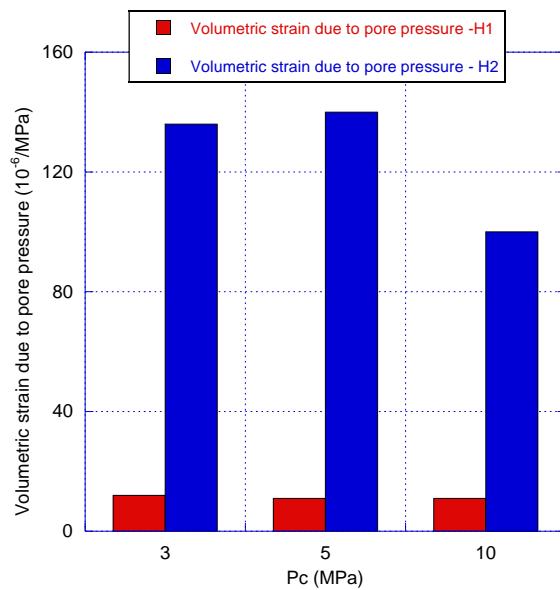


Fig.4.55 $\Delta\varepsilon_v$ due to P_i in tests **H1** and **H2**

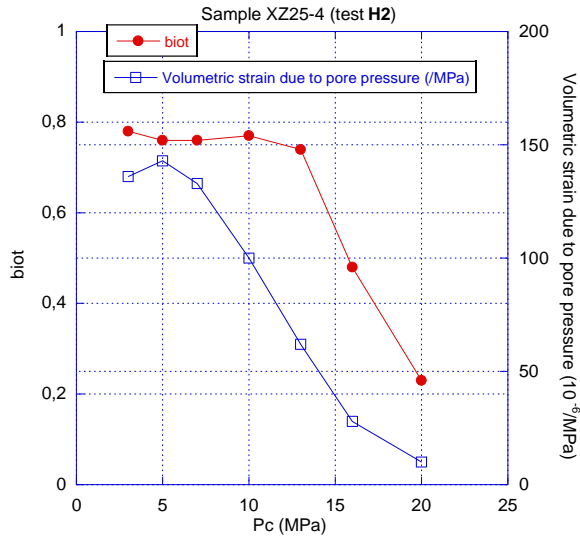


Fig.4.56 Biot and $\Delta\epsilon_v$ due to P_i in test **H2**

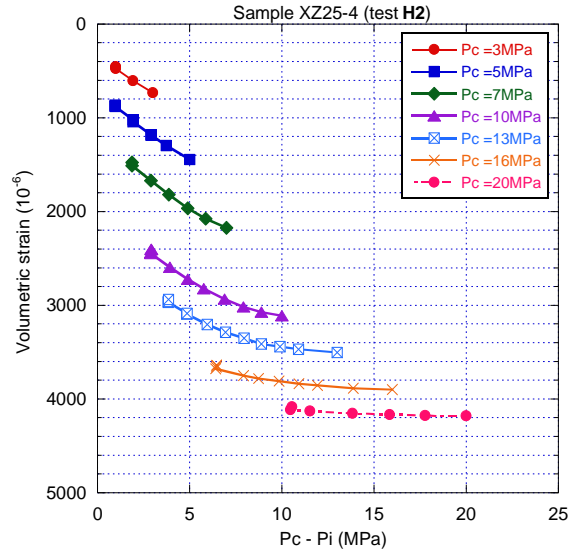


Fig.4.57 ϵ_v as the function of $P_c - P_i$ in test **H2**

Another evidence of the strong damage due to axial loading is the significant increase in the couplings (see in Fig.4.55): $\Delta\epsilon_v$ due to P_i was $133 \cdot 10^{-6}/\text{MPa}$ at $P_c=3\text{MPa}$ in **H2**, while the value was only $12 \cdot 10^{-6}/\text{MPa}$ in test **H1**. This one order of magnitude difference is clearly the ‘cracking signature’, already observed in previous experiments. Fig.4.56, 4.57 and Table 4.21 show that, as they are linked to the cracked state, the coupling effects are dependent on confining pressure in test **H2**:

- Low confinement (from 3 to 7MPa): There were no changes in both the moduli K_b and H , which led to a stable value of ‘apparent’ Biot’s coefficient (0.76).
- Moderate confinement (7 to 13MPa): a parallel increase in H and K_b that results in a constant ratio $b=K_b/H$, as a result ‘b’ varies very little.
- High confinement (from 13 to 20MPa): Biot’s coefficient sharply decreased from 0.74 to 0.23 with P_c , which demonstrates its sensitivity to crack closure. This is mainly due to the ‘H’ increase as K_b increase is (relatively) smaller. As expected, the coupling effects are very weak at 20MPa of confinement, the volumetric strain due to gas pressure ($10 \cdot 10^{-6}/\text{MPa}$) is close to the one before uniaxial test. On a coupling effects point of view, 20 MPa confining pressure is high enough to close cracks produced by axial loading. This kind of phenomenon was also observed on the cracked sample XR02-3 after triaxial loading.

Table 4.21 Variations of porosity (ϕ), biot, moduli K_b and H , $\Delta\varepsilon$ due to P_i , permeability (K) and volumetric strain (ε_v) with P_c for the same sample before and after uniaxial test

XZ25-4	P_c (MPa)	ϕ (%)	biot	K_b (GPa)	H (GPa)	$\Delta\varepsilon_v(P_i)$ $10^{-6}/\text{MPa}$	K (m^2)	$\varepsilon_v(10^{-6})$
Scan 1°								
Test H1 (time effect)	3	0.52			83.33	12	9.03E-19	198
	5	0.2			90.91	11	8.56E-19	413
	5(282hrs)	0			83.33	12	2.85E-19	450
	10	0			90.91	11	5.44E-20	738
Uniaxial test U1 (axial stress maximum 20MPa)								
Test H2	3	1.15	0.76	5.71	7.49	133	3.83E-17	734
	5	1.08	0.76	5.33	6.97	143	1.52E-17	1445
	7	0.88	0.76	5.68	7.5	133	5.94E-18	2173
	10	0.7	0.77	7.67	10	100	2.24E-18	3113
	13	0.51	0.74	12	16.2	62	6.40E-19	3504
	16	0.4	0.48	17.2	36	28	1.51E-19	3905
	20(0hr)	0.2	0.23	22.7	99.5	10	4.29E-21	4173
Test H2 (time effect)	20(26hrs)	0					1.61E-21	4143
	20(31hrs)	0					9.81E-22	4142
	20(96hrs)	0					7.33E-23	4139
Unload to $P_c=1\text{MPa}$, and keep P_c constant at 1MPa for about 70days (from 16 march to 25 may)								
Test H3 (Reload)	3	0	0.65	9.28	14.26	70	5.27E-19	2940
	7	0	0.53	11.49	21.85	46	2.20E-19	3358
	13	0	0.42	18.06	42.71	23	3.43E-20	3841
	20(0hr)	0	0.13	22.31	168.75	6	9.69E-21	4231
Test H3 (time effect)	20(71hrs)	0	0.12		183.18	5	1.50E-23	4291
	20(184hrs)	0	0		∞	0	1.45E-23	4289
	20(209hrs)	0	0		∞	0	0	4306
	20(238hrs)	0	0	22.36	∞	0	0	4304
Test H3 (Unload)	13	0	0.28	18.91	68.36	15	4.67E-22	3929
	7	0	0.57	11.85	20.66	48	2.93E-21	3601
	3	0	0.73	8.85	12.14	82	4.78E-20	3135
Scan 2°								
Uniaxial test U2 (axial stress maximum 20MPa)								
Scan 3°								

Due to *Covid*, this test (**H2**) had to be stopped when time effects were evaluated at $P_c=20$ MPa. The confining pressure was then unloaded and maintained at 1 MPa. As shown in Table 4.21, under $P_c=20\text{MPa}$, the permeability decreased with time by nearly two orders of magnitude while the volumetric strain changed weakly within 96hours. However, it cannot be concluded that the volumetric strain was stabilized at 96 hours. Besides, the permeability had not been measured during the unloading phase. Hence, test **H3** was carried out after 70 days. The experimental process is similar as for test **H2**.

The permeability, volumetric strain, coupling effects and biot were estimated under $P_c=3, 7, 13, 20$ MPa. Then, the time-dependent behavior was recorded at $P_c=20$ MPa, then followed by an unloading.

Results of test **H3**:

The permeability variation in **H3** (due to confining pressure) is quite logical (Fig.4.58) and with a lower value than in **H2**. This simply reflects that the **H2** test led to some irreversible crack closure. The only interrogative point is at $P_c=20$ MPa for which the ‘**H3**’ permeability is slightly higher than the ‘**H2**’ one ($9.69 \text{ v.s. } 4.6\text{E-}21\text{m}^2$). It must be kept in mind that these values are already very low and conclude that they are similar (even biased by some artefact). There was then a significant time effect with a permeability reduction from $9.69\text{E-}21$ to $7.33\text{E-}23\text{m}^2$. This occurred in parallel with a small increase (contraction) in volumetric strain (Fig.4.59). The unloading step logically led to hysteretic effect (Fig.4.58), which follow the compaction phase.

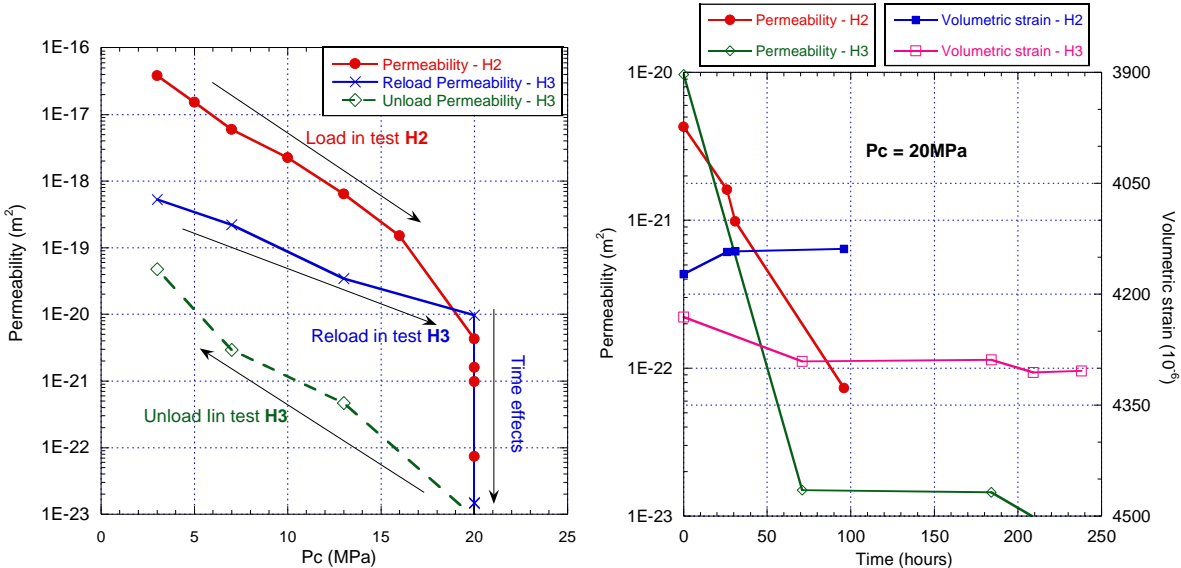


Fig.4.58 Permeability variations as a function of P_c Fig.4.59 Changes in K_g and ϵ_v with time at $P_c=20$ MPa

It is useful to plot the relationship between permeability and volumetric strain (Fig.4.60) obtained in **H2** and **H3**. There is a logical decrease (or increase) in permeability due to loading (or unloading) that is linked to volumetric strain increase/compaction (or decrease/expansion). The irreversible crack closure effect can be seen for these different phases in the comparison (for example) of points **D-E-F**. Both (**H2** and **H3**) observed time effects indicate a sharp permeability reduction at constant volumetric strain. This phenomenon can be interpreted as being sealing.

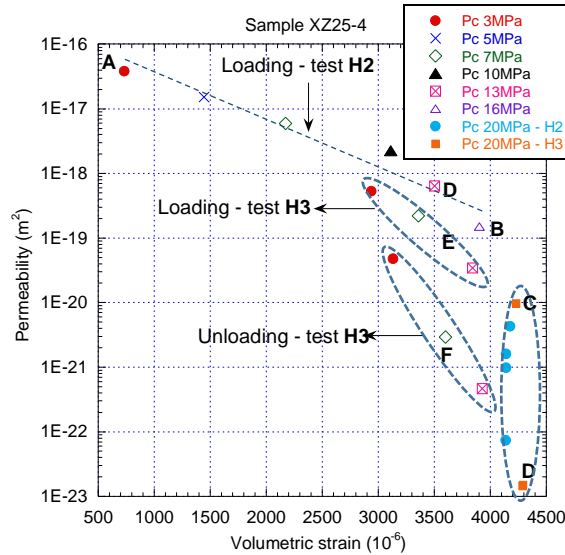


Fig.4.60 K_g v.s. ϵ_v under different P_c after uniaxial test ((H2) and load-unload (H3))

4.5.2.2. Microstructure observations from X-ray microtomography of sample XZ25-4

Scan 1° on this sample was performed to present the initial microstructure (pores and cracks) of this sample. The first uniaxial test (U2) was carried out after hydrostatic test H1 without scanning, followed by hydrostatic tests H2 and H3. Scan 2° was done after test H3 and scan3° was after the second uniaxial test (U2). Therefore, the micro-observation from scan2° to scan3° can be used to present the microstructure changes due to uniaxial stress. The variations of permeability, porosity (and the ones obtained based on micro-CT) and couplings during/between different tests are presented in Table 4.22.

Some comments are directly given on Fig.4.62 and 4.63 to facilitate the analyses. To sum up, the pore/crack changes seen thanks these three scans are as follows:

- Scan 1° to 2°: some initial cracks were partially closed due to test H1/H2/H3, but with virtually no changes in pores volume. This occurred despite the U1 test between H1 and H2. In parallel, new cracks due to test U1 could have been observed in scan 2°. These cracks had induced the changes in porosity, permeability and coupling effects.
- Scan 2° to 3°: Uniaxial test U2 led to an unambiguous generation (or propagation) of cracks, which can provide more pathways for the gas transfer so as to cause an increase in permeability and porosity. They would likely induce some new changes in coupling effects.

New cracks due to U1 were virtually closed during the test H3, as the permeability reached an unmeasurable level ($0m^2$) with time at 20MPa confining pressure. Hence, ‘new’ cracks observed in scan 2° must be attributed to the reopening of cracks generated in U1 during the unloading phase of H3 or due to stress release (see Fig.4.63).

It can be noted that the three scans did not show significant changes in pore volume. However, changes/compaction in pores can be observed after triaxial test on sample XR02-4 and XS01-4. It can

be inferred that pores (with a low resolution) are not very sensitive to hydrostatic stress or uniaxial stress, but only can be compacted under high deviatoric stress. The changes in permeability of sample XZ25-4 should be mainly due to crack closure or opening, rather than to pore compaction.

Table 4.22 Variations of permeability, porosity and couplings of sample XZ25-4 during different tests

XZ25-4	Mechanical loadings	K (m ²)	Porosity (%)	$\Delta\varepsilon_v$ (P _i) 10 ⁻⁶ /MPa	Modulus H (GPa)
Scan 1° (0.3299 %)					
Test H1	P _c = 3MPa	9.03E-19	0.52	12	83.33
	P _c = 10MPa	3.38E-20	0	11	90.91
Uniaxial test U1	$\sigma_{max} = 20\text{MPa}$				
Test H2	P _c = 3MPa	3.82E-17	1.15	133	7.49
	P _c = 10MPa	2.24E-18	0.7	100	10
	P _c = 20MPa	7.33E-23	0		
Test H3 (load-unload)	P _c = 3MPa	5.27E-19	0	70	14.26
	P _c = 7MPa	2.20E-19	0	46	21.85
	P _c = 20MPa	1.45E-23	0	0	+ ∞
	(unload) P _c = 3MPa	4.78E-20	0	82	14.26
Scan 2° (0.215%)					
Uniaxial test U2	$\sigma_{max} = 20\text{MPa}$				
Scan 3° (0.466%)					

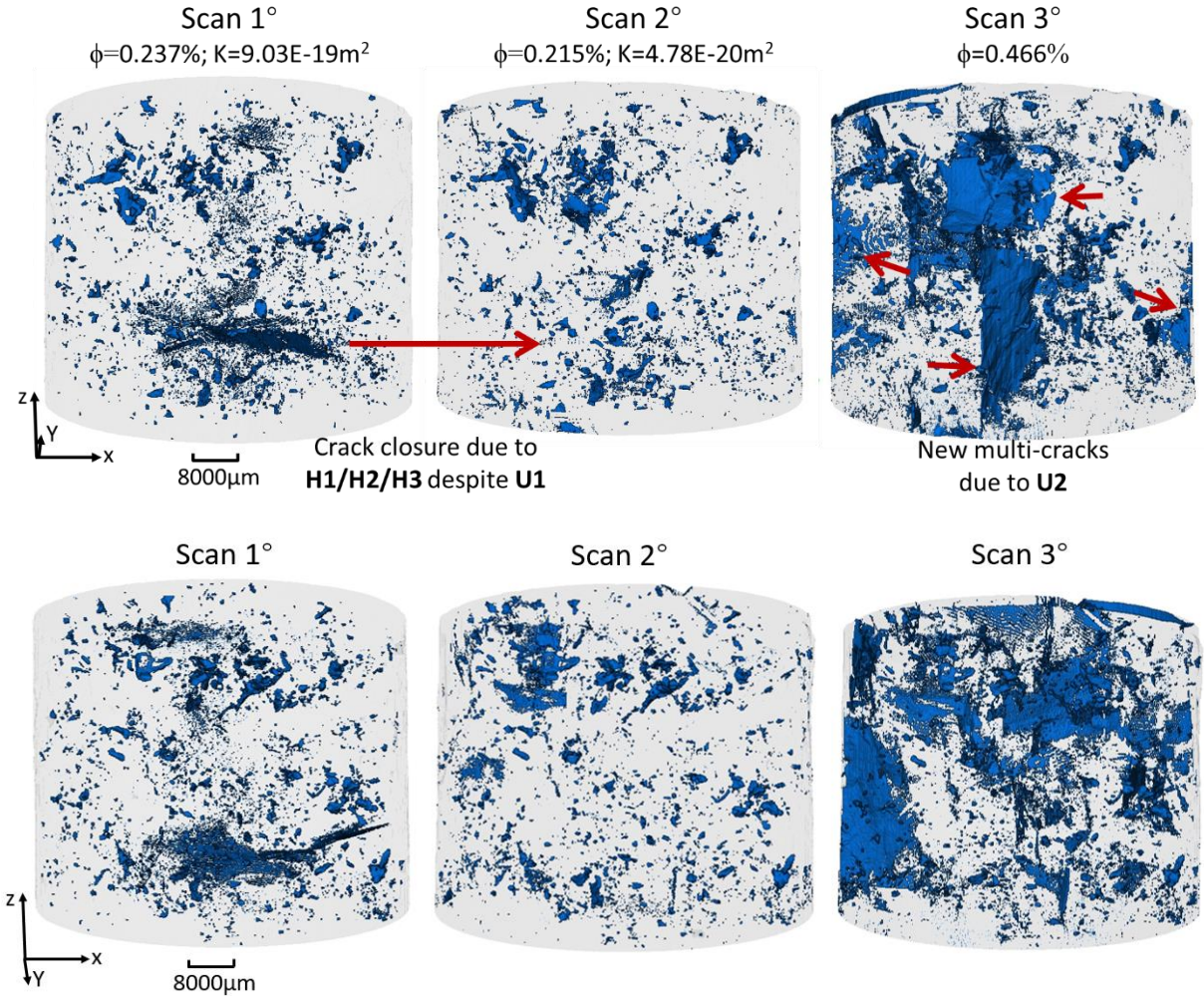
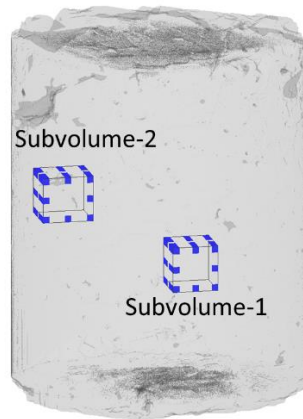
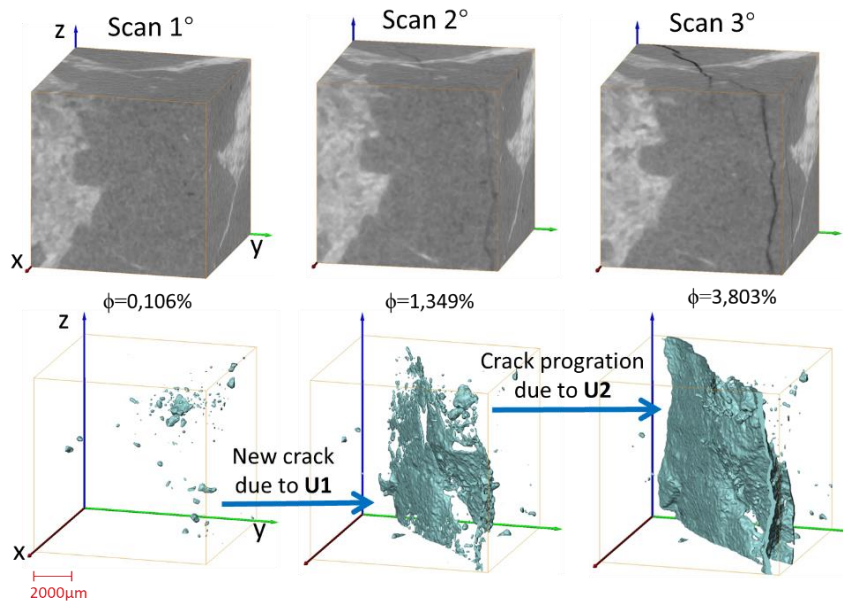


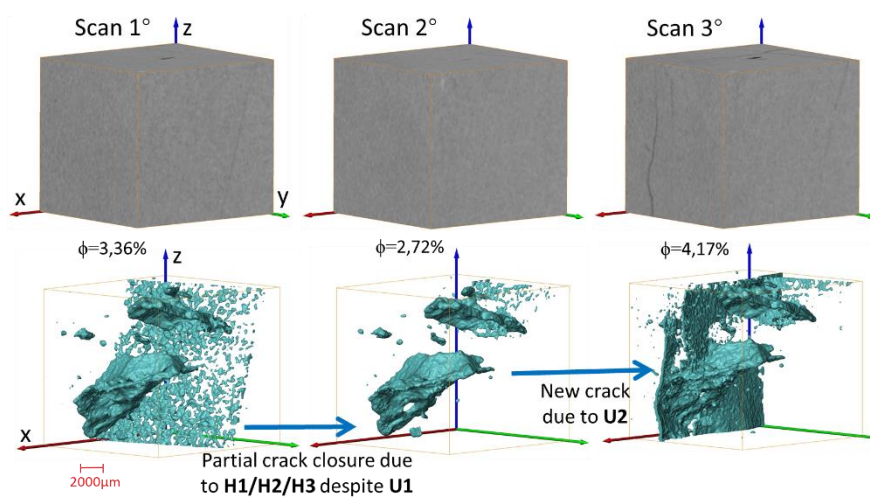
Fig.4.61 The 3D pore space of sample XZ25-4 from different scans



(a) Location of Subvolume-1 and Subvolume-2 of XZ25-4 from scan 1°



(b) Subvolume-1 (10mm×10mm×10mm)



(c) Subvolume-2 (10mm×10mm×10mm)

Fig.4.62 3D sub-volumes and pore space extracted from three scans of sample XZ25-4

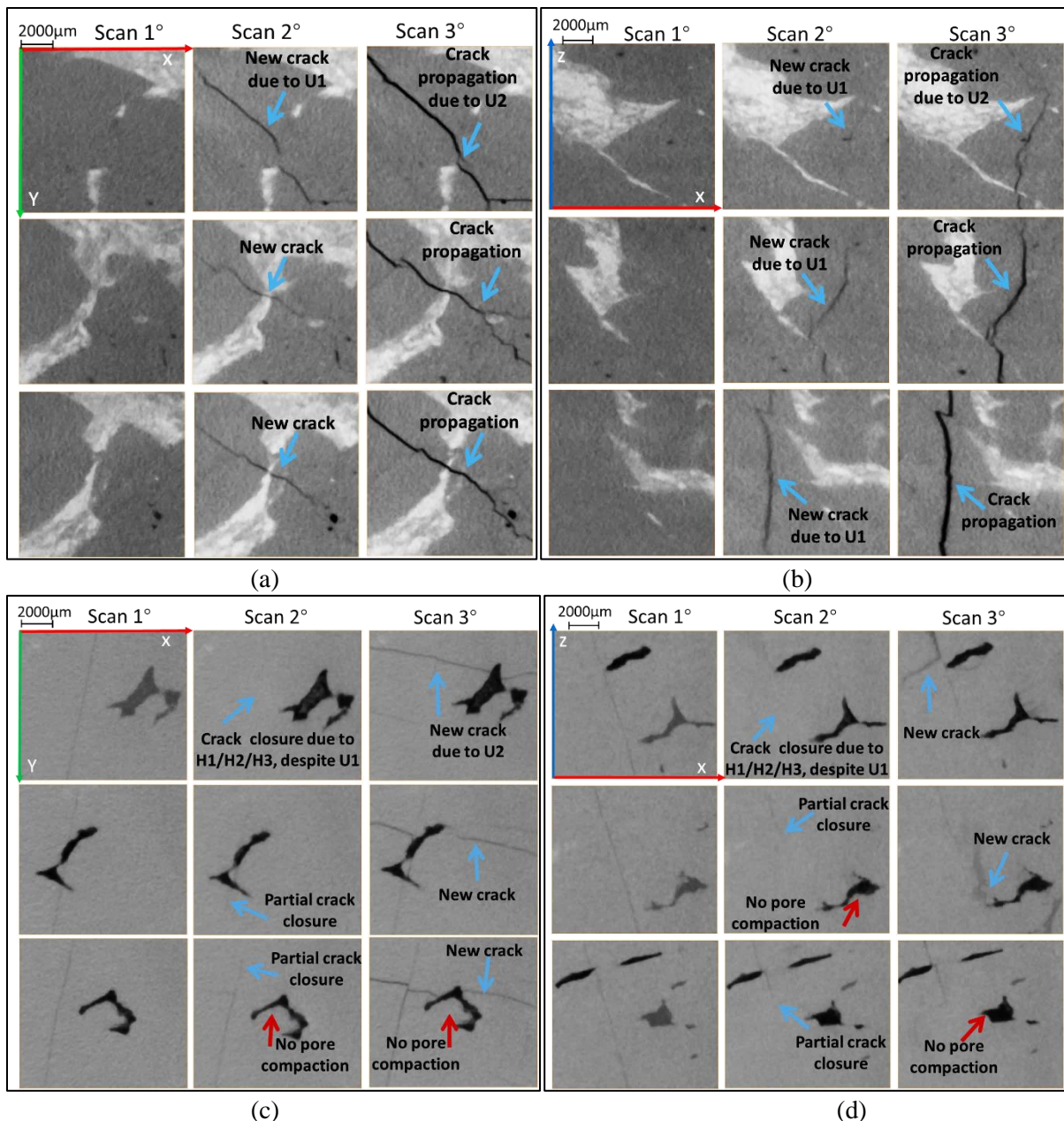


Fig.4.63 Microstructure development (crack: blue arrows; pore: red arrows) of slices in sub-volumes with different scans of sample XZ25-4 ((a) and (b): the horizontal and vertical slices of subvolume-1; (c) and (d): the horizontal and vertical slices of subvolume-2)

4.5.3. Partial conclusion

The uniaxial loading up to 20MPa caused a strong damage on both samples (XZ25-5 and XZ25-4). The initial permeability value at 3MPa confining pressure increased by 2-3 orders of magnitude due to axial loading. In addition to the increase in permeability, there were also a significant increase in skeleton compressibility (decrease in modulus K_b) and an increase in coupling effects (the expansion due to internal gas pore pressure). These measurements revealed the occurrence of strong damage/cracking.

During the sealing/healing process, the permeability decreased not only with P_c , but also significantly decreased with time at $P_c=20\text{MPa}$. After uniaxial test, the initial Biot's coefficient value is high (0.62 for XZ25-5; 0.76 for XZ25-4) and it decreased with confining pressure. This can be linked to crack closure effects. The sensitivity of permeability and Biot's coefficient to confinement support the hypothesis that fluid flows through cracks or boundaries between salt grains and that coupling are only due to (fluid) pressure effect into those cracks.

The sealing phenomenon observed on sample XZ25-4 at $P_c=20\text{ MPa}$ may be a great advantage in the context of long-term storage in salt rock formations. It was also found that permeability, porosity and volumetric strain were irreversible in the unloading phase of test **H2** for XZ25-5 and **H3** for XZ25-4.

Moreover, an important finding from X-ray micro-tomography experiment for sample XZ25-4 is that the changes in permeability during/between different tests should be primarily due to crack closure or opening, rather than to pore compaction, as almost no changes in pores observed from three scans. However, changes (compaction) in pores can be observed after triaxial tests for sample XR02-4 and XS01-4 (in §4.4.4 and 4.4.5). It can be inferred that pores are not very sensitive to hydrostatic stress or uniaxial stress, but can only be compacted under high deviatoric stress.

5. Conclusions and perspectives

5.1. Conclusions

This thesis has contributed to the characterization of fluid transfer properties and (potential) skeleton-fluid couplings of salt rock for the application in a scenario of cavern abandonment and/or hydrogen storage. This experimental study therefore includes mechanical, pore-mechanical and permeability (especially gas) tests with the effect of confinement or triaxial/uniaxial loading. The influences of isotropic stress and time on these two properties were first detected during hydrostatic test. As damage and dilatancy may occur in the DRZ, permeability variation with deviatoric stress was measured in triaxial test. The other purpose of triaxial test was to get damaged sample with cracks, as cracks are suspected to lead to significant coupling effects. Those pre-damaged samples were then tested under hydrostatic loadings to investigate the potential sealing/healing properties and changes in poromechanical coupling due to axial test. Meanwhile, the non-destructive X-ray micro-tomography imaging technique was used to capture the microcrack/pore changes due to these different mechanical loadings (hydrostatic stress and deviatoric/axial stress). The main conclusions drawn from all the experimental results are summarized as follows:

1) Part I

Different behaviors in term of gas permeability were detected for different samples in hydrostatic tests, in a large range of 10^{-16} - 10^{-23} m². The samples (coming from the same site but from two different wells), have very different properties. This may be attributed to a great heterogeneity of salt formation (and/or a damage due to coring). Regardless of the level of permeability, all the recorded porosities were very small (less than 1%). At a microscopic scale, the SBET results confirmed a very small porosity, which is consistent with the porosity measurements. The permeability is not only dependent on confinement but also evolves with time because of the viscous effects even under isotropic loading. In addition, permeabilities measured with argon or hydrogen are close to each other, and argon permeability may be considered as representative of hydrogen permeability. It is well known that tests with hydrogen require safety disposal and precautions. Hence, this result will allow easier gas permeability measurements for the application of hydrogen storage in salt cavern. Klinkenberg effect was also clearly observed. There is an increase in Klinkenberg coefficient with loading, which can reflect crack closure effect.

The existence of fluid-skeleton coupling was verified using gas techniques for different samples, which is an important finding. This simultaneously led to a rough estimation of (apparent) Biot's coefficient, with initial values in a range of 0.31-0.37. The apparent Biot's coefficients were found to be sensitive to confinement and could almost reach '0' at 17MPa. They are lower than usual values

measured for permeable or low permeable sandstones, shales or other sedimentary rocks but they are significant.

2) Part II

The time effects on permeability had been clearly evidenced for both hydrostatic and triaxial tests. Different samples exhibit considerably different time-dependent behaviors. For example, a sealing with time (i.e. significant decrease in permeability but with small changes in volumetric strain) was detected. Another observed phenomenon is a quasi-constant permeability despite a volumetric strain evolution. Sometimes, a mixed behavior of both can also be observed. Time effects on permeability were also observed to be quite different under different levels of deviatoric stress. In the compression phase (usually at low deviatoric stress), the permeability decreased with time due to crack closure/compaction. When sample went into the dilatant phase (usually at high deviatoric stress), the permeability increased with time due to cracking.

The confining pressure plays a crucial role in the permeability variation for triaxial test. The damage/dilatancy due to deviatoric loading is observed to be the most significant at low confinement (2MPa), such as 5 orders of magnitude increase in permeability for sample XZ25-3. At high confinement (10MPa), permeability was slightly increased for XR02-4 and was moderately increased for XS01-4. The uniaxial loading caused a strong damage/cracking, i.e. significant increase in permeability, decrease in modulus K_b and increase in couplings were observed in test **H2**.

After triaxial tests, the dismounting operation brought an increase in permeability between the last value of triaxial test and the beginning one of test **H2**, which can be mainly attributed to the opening of new cracks generated due to deviatoric stress.

For test **H2**, The permeability of damaged samples can recover to the initial one before axial loading. In other words, new cracks caused by axial loading can be closed under isotropic stress and with time. A sealing phenomenon was detected for both the initial and damaged samples (i.e. for tests **H1** and **H2**). Couplings between gas pore pressure and skeleton are much more significant in damaged/cracked samples than initial ones. The sensitivity of permeability and of Biot's coefficient to confinement support the hypothesis that fluid flows through cracks or boundaries between salt grains and that coupling are due to (fluid) pressure effect into those cracks.

The X-ray microtomography results confirm that there were crack (partially) closure but basically no changes in pore due to test **H1**. Two 'antagonistic' effects were observed due to triaxial test: a compaction effect that makes pores smaller (and further crack closure); and cracking effect (which can make higher permeability, stronger coupling effects and more sensitive to confining pressure in **H2**). Moreover, almost no changes/compaction in pore can be found due to uniaxial test. Hence, the changes in permeability during/between different tests on sample XZ25-4 (uniaxial test) should be primarily due

to crack closure or opening. It can be inferred that pores are not very sensitive to hydrostatic stress or uniaxial stress, but only can be compacted under high deviatoric stress. Micro-CT experiments reveal that deviatoric loading leads to a complete change in porous structure.

5.2.Perspectives

The experimental perspectives for this thesis are as bellows:

Brine permeability test was performed for only one sample in this study, as it is very time-consuming. Since the gas transfer properties have been investigated for different samples, the sample, coming from the family with high gas permeability may be used for testing brine permeability, which is suspected to be less time consuming. It is therefore very interesting to compare the gas and brine permeability of the same sample.

The salt porosity recorded in this thesis may not be very accurate, due to its very low value. In further research, we will use a new device from our laboratory for high precision porosity measurement. It then allows to perform a series of porosity measurements such as the initial value (without confinement), the variation in loading-unloading phase, with time effect or even heating effect (200°C).

For the permeability evolution in triaxial test, a ‘stable’ value was supposed to be reached after a several days. It seems crucial to record the permeability evolution with creep during a period of several months. The parallel porosity measurement should also be proposed in triaxial test, as it is a valid evidence to identify the development of connected porous network due to axial loading.

In further study, X-ray micro-tomography under loading may be performed as it can realize the non-destructive observation of the internal microstructure evolution of sample under progressive loading.

References

- [1] Hou Z. Mechanical and hydraulic behavior of rock salt in the excavation disturbed zone around underground facilities. *Int J Rock Mech Min Sci* 2003; 40: 725–738.
- [2] Chen X, Caratini G, Davy CA, et al. Coupled transport and poro-mechanical properties of a heat-treated mortar under confinement. *Cem Concr Res* 2013; 49: 10–20.
- [3] Bérest P, Brouard B. Safety of Salt Caverns Used for Underground Storage Blow Out; Mechanical Instability; Seepage; Cavern Abandonment. *Oil Gas Sci Technol* 2003; 58: 361–384.
- [4] Schoenherr J, Urai JL, Kukla PA, et al. Limits to the sealing capacity of rock salt: A case study of the infra-Cambrian Ara Salt from the South Oman salt basin. *AAPG Bull* 2007; 91: 1541–1557.
- [5] Huang X, Xiong J. Numerical Simulation of Gas Leakage in Bedded Salt Rock Storage Cavern. *Procedia Eng* 2011; 12: 254–259.
- [6] Lomenick TF, Bradshaw RL. Deformation of rock salt in openings mined for the disposal of radioactive wastes. *Rock Mech Felsmech Mec Roches* 1969; 1: 5–29.
- [7] Hunsche U, Hampel A. Rock salt — the mechanical properties of the host rock material for a radioactive waste repository. *Eng Geol* 1999; 52: 271–291.
- [8] Schulze O, Popp T, Kern H. Development of damage and permeability in deforming rock salt. *Eng Geol* 2001; 61: 163–180.
- [9] Karimi-Jafari M. *Sur le comportement transitoire des cavités salines profondes: étude numérique et interprétation des essais in situ*. Dissertation, Ecole polytechnique, 2007.
- [10] Bérest P, Brouard B, Hévin G. A 12-year cavern abandonment test. *EPJ Web Conf* 2010; 6: 22003.
- [11] Schlichtenmayer M, Bannach A, Amro M, et al. *Renewable Energy Storage in Salt Caverns - A Comparison of Thermodynamics and Permeability between Natural Gas, Air and Hydrogen* -. Research Project Report RR2015-1, Germany: Solution Mining Research Institute, Inc. (SMRI), 2015.
- [12] Chan KS, Bodner SR, Munson DE. Permeability of WIPP Salt during Damage Evolution and Healing. *Int J Damage Mech* 2001; 10: 347–375.
- [13] Peach CJ. *Influence of deformation on the fluid transport properties of salt rocks*. Dissertation, University of Utrecht, 1991.
- [14] Stormont JC, Daemen JJK. Laboratory Study of Gas Permeability Changes in Rock Salt During Deformation. *Int J Rock Mech Min Sci* 1992; 29: 325–342.
- [15] Stormont JC. Conduct and interpretation of gas permeability measurements in rock salt. *Int J Rock Mech Min Sci* 1997; 34: 303-e1.
- [16] Alkan H. Percolation model for dilatancy-induced permeability of the excavation damaged zone in rock salt. *Int J Rock Mech Min Sci* 2009; 46: 716–724.

- [17] Labaune P, Rouabhi A, Tijani M, et al. Dilatancy Criteria for Salt Cavern Design: A Comparison Between Stress- and Strain-Based Approaches. *Rock Mech Rock Eng* 2018; 51: 599–611.
- [18] Peach JC, Speirs CJ, Tankink AJ, et al. *Fluid and ionic transport properties of deformed salt rock*. 1987.
- [19] Pusch G, Clausthal T, Alkan H. Gas permeation Models Related to Dilatancy Development under Deviatoric Stress Conditions. *Solut Min Res Inst Fall 2002 Tech Meet Bad Ischl Austria Oct 6 - 9 2002*; 18.
- [20] Xing W, Zhao J, Düsterloh U, et al. Experimental study of mechanical and hydraulic properties of bedded rock salt from the Jintan location. *Acta Geotech* 2014; 9: 145–151.
- [21] Mansouri H, Ajalloeian R. Mechanical behavior of salt rock under uniaxial compression and creep tests. *Int J Rock Mech Min Sci* 2018; 110: 19–27.
- [22] Ding J, Chester FM, Chester JS, et al. Microcrack Network Development in Salt-Rock During Cyclic Loading at Low Confining Pressure. 2017.
- [23] Khaledi K. *Constitutive Modeling of Rock Salt with Application to Energy Storage Caverns*. PhD, Ruhr-Universität Bochum, 2017.
- [24] Tsang C-F, Bernier F, Davies C. Geohydromechanical processes in the Excavation Damaged Zone in crystalline rock, rock salt, and indurated and plastic clays—in the context of radioactive waste disposal. *Int J Rock Mech Min Sci* 2005; 42: 109–125.
- [25] Berest P, Brouard B, Durup JG. Tightness Tests in Salt-Cavern Wells. *Oil Gas Sci Technol* 2001; 56: 451–469.
- [26] Thoms RL, Gehle RM. A brief history of salt cavern use. *Proc 8th World Salt Symp*.
- [27] Yang C, Wang T, Li Y, et al. Feasibility analysis of using abandoned salt caverns for large-scale underground energy storage in China. *Appl Energy* 2015; 137: 467–481.
- [28] Donadei S. Chapter 6 - Compressed Air Energy Storage in Underground Formations. In: *Storing Energy*. 2016, pp. 113–133.
- [29] Han G, Bruno MS, Lao K, et al. Gas Storage and Operations in Single-Bedded Salt Caverns: Stability Analyses. Canada, 2006.
- [30] Ma H, Yang C, Li Y, et al. Stability evaluation of the underground gas storage in rock salts based on new partitions of the surrounding rock. *Environ Earth Sci* 2015; 73: 6911–6925.
- [31] Wei L, Jie C, Deyi J, et al. Tightness and suitability evaluation of abandoned salt caverns served as hydrocarbon energies storage under adverse geological conditions (AGC). *Appl Energy* 2016; 178: 703–720.
- [32] Lux K-H. Design of salt caverns for the storage of natural gas, crude oil and compressed air: Geomechanical aspects of construction, operation and abandonment. *Geol Soc Lond Spec Publ* 2009; 313: 93–128.
- [33] Karami-Jafari M. *Sur le comportement transitoire des cavités salines profondes*. PhD, Ecole polytechnique, 2007.

- [34] Peach CJ. *Influence of deformation on the fluid transport properties of salt rocks*. Dissertation, Facultiet Aardwetenschappen der Rijksuniversiteit Utrecht, 1991.
- [35] Wang T, Yang C, Ma H, et al. Safety evaluation of gas storage caverns located close to a tectonic fault. *J Nat Gas Sci Eng* 2015; 23: 281–293.
- [36] Houben ME, ten Hove A, Peach CJ, et al. Crack healing in rock salt via diffusion in adsorbed aqueous films: Microphysical modelling versus experiments. *Phys Chem Earth Parts ABC* 2013; 64: 95–104.
- [37] Desbois G, Urai JL, de Bresser JHP. Fluid distribution in grain boundaries of natural fine-grained rock salt deformed at low differential stress (Qom Kuh salt fountain, central Iran): Implications for rheology and transport properties. *J Struct Geol* 2012; 43: 128–143.
- [38] Popp T, Kern H. Ultrasonic wave velocities, gas permeability and porosity in natural and granular rock salt. *Phys Chem Earth* 1998; 23: 373–378.
- [39] Cosenza Ph, Ghoreychi M, Bazargan-Sabet B, et al. In situ rock salt permeability measurement for long term safety assessment of storage. *Int J Rock Mech Min Sci* 1999; 36: 509–526.
- [40] Sutherland HJ, Cave SP. Argon Gas Permeability of New Mexico Rock Salt under Hydrostatic Compression. *Int J Rock Mech Min Sci* 1980; 17: 281–288.
- [41] Stormont JC, Howard CL, Daemen JJK. *In situ measurements of rock salt permeability changes due to nearby excavation*. Sandia National Labs., Albuquerque, NM (United States), 1991.
- [42] Dale T, L. Diane H. *WIPP air-intake shaft disturbed-rock zone study*. No. SAND--96-1327C, Sandia National Labs, 1996.
- [43] Brouard B, Bérest P, Durup JG. *In-Situ Salt Permeability Testing*. Albuquerque, New Mexico, USA, 2001, 7–10.
- [44] Wong TE, Batjes DAJ, de Jager J. *Geology of the Netherlands*. Royal Netherlands Academy of Arts and Sciences, 2007.
- [45] Coussy O. *Poromechanics*. New York: John Wiley & Sons, 2004.
- [46] HU D. *Contribution à l'étude du comportement mécanique et hydromécanique d'une roche endommagée*. PhD, Université des sciences et technologies de lille, 2009.
- [47] Urai JL, Spiers CJ. The effect of grain boundary water on deformation mechanisms and rheology of rock salt during long-term deformation. *The Mechanical Behavior of Salt—Understanding of THMC Processes in Salt: Proceedings of the 6th Conference (SaltMech6)*, Hannover, Germany, 22–25 May 2007. Boca Raton, Fla.: CRC Press, 2007.
- [48] Thiemeyer N, Zulauf G, Mertineit M, et al. Microfabrics and 3D grain shape of Gorleben rock salt: Constraints on deformation mechanisms and paleodifferential stress. *Tectonophysics* 2016; 676: 1–19.
- [49] Ji W, Yang C, Liu W, et al. Experimental investigation on meso-pore structure properties of bedded salt rock. *Chin J Rock Mech Eng* 2013; 32: 2036–2044.
- [50] Zhang Z, Jiang D, Liu W, et al. Study on the mechanism of roof collapse and leakage of horizontal cavern in thinly bedded salt rocks. *Environ Earth Sci* 2019; 78: 292.

- [51] Thiemeyer N, Habersetzer J, Peinl M, et al. The application of high resolution X-ray computed tomography on naturally deformed rock salt: Multi-scale investigations of the structural inventory. *J Struct Geol* 2015; 77: 92–106.
- [52] Chen J, Li E, Luo J. Characterization of Microscopic Pore Structures of Rock Salt through Mercury Injection and Nitrogen Absorption Tests. *Geofluids* 2018; 2018: 1–7.
- [53] SHEN X, Zhu C, Arson C. Analysis of microstructure, deformation and permeability of salt/sand mixtures during creep. In: *Poromechanics VI*. 2017: 980--987.
- [54] Renard F, Bernard D, Thibault X, et al. Synchrotron 3D microtomography of halite aggregates during experimental pressure solution creep and evolution of the permeability. *Geophys Res Lett*; 2004, 31 (7).
- [55] Anovitz LM, Cole DR. Characterization and Analysis of Porosity and Pore Structures. *Rev Mineral Geochem* 2015; 80: 61–164.
- [56] De Las Cuevas C. Pore structure characterization in rock salt. *Eng Geol* 1997; 47: 17–30.
- [57] Thommes M, Kaneko K, Neimark AV, et al. Physisorption of gases, with special reference to the evaluation of surface area and pore size distribution (IUPAC Technical Report). *Pure Appl Chem* 2015; 87: 1051–1069.
- [58] Baroghel-Bouny V. *Caractérisation microstructurale et hydrique des pâtes de ciment et des bétons ordinaires et à très hautes performances*. Ecole Nationale des Ponts et Chaussées, 1994.
- [59] Ratigan JL. A finite element formulation for brine transport in rock salt. *Int J Numer Anal Methods Geomech* 1984; 8: 225–241.
- [60] Cosenza P. *Sur les couplages entre comportement mécanique et processus de transfert de masse dans le sel gemme*. PhD, Paris 6, 1996.
- [61] Tanikawa W, Shimamoto T. Klinkenberg effect for gas permeability and its comparison to water permeability for porous sedimentary rocks. *Hydrol Earth Syst Sci Discuss* 2006; 3: 1315–1338.
- [62] Tanikawa W, Shimamoto T. Comparison of Klinkenberg-corrected gas permeability and water permeability in sedimentary rocks. *Int J Rock Mech Min Sci* 2009; 46: 229–238.
- [63] Loosveldt H, Lafhaj Z, Skoczylas F. Experimental study of gas and liquid permeability of a mortar. *Cem Concr Res* 2002; 32: 1357–1363.
- [64] Liu W, Li Y, Yang C, et al. Permeability characteristics of mudstone cap rock and interlayers in bedded salt formations and tightness assessment for underground gas storage caverns. *Eng Geol* 2015; 193: 212–223.
- [65] Firouzi M, Alnoaimi K, Kovscek A, et al. Klinkenberg effect on predicting and measuring helium permeability in gas shales. *Int J Coal Geol* 2014; 123: 62–68.
- [66] Caglayan DG, Weber N, Heinrichs H, et al. Technical Potential of Salt Caverns for Hydrogen Storage in Europe. *Int J Hydrog Energy* 2020; 45: 6793–6805.
- [67] Landinger H, Crotogino F. The role of large-scale hydrogen storage for future renewable energy utilisation. Second International Renewable Energy Storage Conference (IRES II), 2007.

- [68] Maurice S, Bannach A, Amro M. *Renewable Energy Storage in Salt Caverns - A Comparison of Thermodynamics and Permeability between Natural Gas, Air and Hydrogen* -. Research Project Report RR2015-1, Germany: Solution Mining Research Institute, 2015.
- [69] Klinkenber LJ. The permeability of porous media to liquids and gases. In: *Drilling and production practice*. Tulsa. Okla, 1941.
- [70] Knudsen M. Die Gesetze der Molekularströmung und der inneren Reibungsströmung der Gase durch Röhren. *Ann Phys Phys* 1909; 333: 75–130.
- [71] Schaaf SA, Chambre PA. *Flow of Rarefied Gases*. Princeton, New Jersey, Princeton University Press, 1961.
- [72] Kast W, Hohenthanner C-R. Mass transfer within the gas-phase of porous media. *Int J Heat Mass Transf* 2000; 43: 807–823.
- [73] Civan F. Effective Correlation of Apparent Gas Permeability in Tight Porous Media. *Transp Porous Media* 2010; 82: 375–384.
- [74] Dong M, Li Z, Li S, et al. Permeabilities of tight reservoir cores determined for gaseous and liquid CO₂ and C₂H₆ using minimum backpressure method. *J Nat Gas Sci Eng* 2012; 5: 1–5.
- [75] Ziarani AS, Aguilera R. Knudsen's Permeability Correction for Tight Porous Media. *Transp Porous Media* 2012; 91: 239–260.
- [76] Ashrafi Moghadam A, Chalaturnyk R. Expansion of the Klinkenberg's slippage equation to low permeability porous media. *Int J Coal Geol* 2014; 123: 2–9.
- [77] Chen W, Liu J, Brue F, et al. Water retention and gas relative permeability of two industrial concretes. *Cem Concr Res* 2012; 42: 1001–1013.
- [78] Pei Y. *Effets du chauffage sur les matériaux cimentaires - impact du « self-healing » sur les propriétés de transfert*. Dissertation, Ecole Centrale de Lille, 2016.
- [79] Xiao W, Bernabé Y, Evans B, et al. Klinkenberg Effect and Effective Pressure for Gas Permeability of Tight Sandstones. *J Geophys Res Solid Earth* 2019; 124: 1412–1429.
- [80] Popp T, Kern H, Schulze O. Evolution of dilatancy and permeability in rock salt during hydrostatic compaction and triaxial deformation. *J Geophys Res Solid Earth* 2001; 106: 4061–4078.
- [81] Dong J-J, Hsu J-Y, Wu W-J, et al. Stress-dependence of the permeability and porosity of sandstone and shale from TCDP Hole-A. *Int J Rock Mech Min Sci* 2010; 47: 1141–1157.
- [82] Gloyna EF, Reynolds TD. Permeability measurements of rock salt. *J Geophys Res* 1961; 66: 3913–3921.
- [83] Yang C, Daemen JJK, Yin J-H. Experimental investigation of creep behavior of salt rock. *Int J Rock Mech Min Sci* 1999; 36: 233–242.
- [84] Nazary Moghadam S, Mirzabozorg H, Noorzad A. Modeling time-dependent behavior of gas caverns in rock salt considering creep, dilatancy and failure. *Tunn Undergr Space Technol* 2013; 33: 171–185.

- [85] Ma L, Wang M, Zhang N, et al. A Variable-Parameter Creep Damage Model Incorporating the Effects of Loading Frequency for Rock Salt and Its Application in a Bedded Storage Cavern. *Rock Mech Rock Eng* 2017; 50: 2495–2509.
- [86] Deng J, Liu Y, Yang Q, et al. A viscoelastic, viscoplastic, and viscodamage constitutive model of salt rock for underground energy storage cavern. *Comput Geotech* 2020; 119: 103288.
- [87] Stormont JC. *Gas permeability changes in rock salt during deformation*. Dissertation, The University of Arizona, 1990.
- [88] Berest P, Brouard B, de Greef V. *Salt Permeability Testing-The Influence of Permeability and Stress on Spherical Hollow Salt Samples-*. Technical Report 2000-1, Solution Mining Research Institute (SMRI), 2000.
- [89] Li S-Y, Urai JL. Rheology of rock salt for salt tectonics modeling. *Pet Sci* 2016; 13: 712–724.
- [90] de Boer R. Theoretical poroelasticity—a new approach. *Chaos Solitons Fractals* 2005; 25: 861–878.
- [91] Terzaghi K. *Theoretical soil mechanics*. New York, J. Wiley and Sons. 1943.
- [92] Skempton A. Effective stress in soils, concrete and rocks. *Sel Pap Soil Mech* 1984; 1032: 4–16.
- [93] Biot MA. General Theory of Three-Dimensional Consolidation. *J Appl Phys* 1941; 12: 155–164.
- [94] Sherwood JD. Biot poroelasticity of a chemically active shale. *Proc R Soc Lond Ser Math Phys Sci* 1993; 440: 365–377.
- [95] Chen X-T, Davy CA, Skoczylas F, et al. Effect of heat-treatment and hydrostatic loading upon the poro-elastic properties of a mortar. *Cem Concr Res* 2009; 39: 195–205.
- [96] Pei Y, Agostini F, Skoczylas F. The effects of high temperature heating on the gas permeability and porosity of a cementitious material. *Cem Concr Res* 2017; 95: 141–151.
- [97] Hu C, Agostini F, Skoczylas F, et al. Poromechanical Properties of a Sandstone Under Different Stress States. *Rock Mech Rock Eng* 2018; 51: 3699–3717.
- [98] Hu DW, Zhou H, Zhang F, et al. Evolution of poroelastic properties and permeability in damaged sandstone. *Int J Rock Mech Min Sci* 2010; 47: 962–973.
- [99] Vincke O, Longuemare P, Bouteica M, et al. Investigation of the Poromechanical Behavior of Shales in the Elastic Domain. In: *SPE/ISRM Rock Mechanics in Petroleum Engineering*. Society of Petroleum Engineers, 1998.
- [100] Ortega JA, Ulm F-J, Abousleiman Y. The effect of the nanogranular nature of shale on their poroelastic behavior. *Acta Geotech* 2007; 2: 155–182.
- [101] Detournay E, Cheng AH-D. Poroelastic Response of a Borehole in a Non-hydrostatic Stress Field. *International Journal of Rock Mechanics and Mining Sciences & Geomechanics Abstracts*. Pergamon, 1988, 25(3): 171-182.
- [102] Budiansky B, O’connell RJ. Elastic moduli of a cracked solid. *Int J Solids Struct* 1976; 12: 81–97.

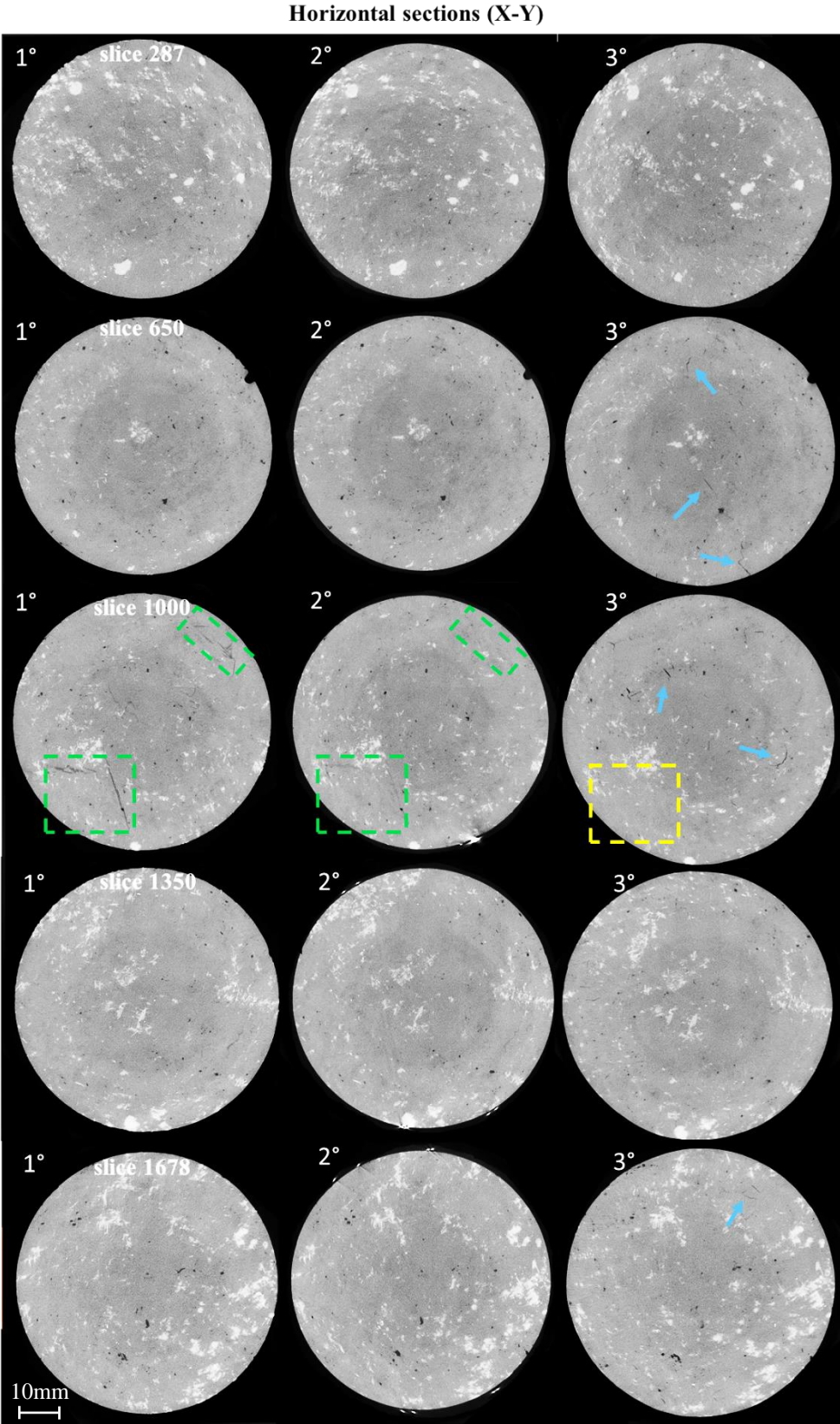
- [103] Alkan H, Cinar Y, Pusch G. Rock salt dilatancy boundary from combined acoustic emission and triaxial compression tests. *Int J Rock Mech Min Sci* 2007; 44: 108–119.
- [104] Munson DE, Holcomb D, DeVries KL, et al. Correlation of theoretical calculations and experimental measurements of damage around a shaft in salt. The 35th US Symposium on Rock Mechanics (USRMS). American Rock Mechanics Association, 1995.
- [105] Shen X, Arson C. Simulation of salt-cavity healing based on a micro–macro model of pressure solution. *Pet Geosci* 2019; 25: 251–257.
- [106] Koelemeijer PJ, Peach CJ, Spiers CJ. Surface diffusivity of cleaved NaCl crystals as a function of humidity: Impedance spectroscopy measurements and implications for crack healing in rock salt. *J Geophys Res Solid Earth*; 117 (B1).
- [107] Peach CJ, Spiers CJ. Influence of crystal plastic deformation on dilatancy and permeability development in synthetic salt rock. *Tectonophysics* 1996; 256: 101–128.
- [108] Liang W, Yang C, Zhao Y, et al. Experimental investigation of mechanical properties of bedded salt rock. *Int J Rock Mech Min Sci* 2007; 44: 400–411.
- [109] Liang WG, Zhao YS, Xu SG, et al. Effect of strain rate on the mechanical properties of salt rock. *Int J Rock Mech Min Sci* 2011; 48: 161–167.
- [110] Popp T, Kern H. Monitoring the state of microfracturing in rock salt during deformation by combined measurements of permeability and P- and S- wave velocities. *Phys Chem Earth Part Solid Earth Geod* 2000; 25: 149–154.
- [111] Billiotte J, Yang D, Su K. Experimental study on gas permeability of mudstones. *Phys Chem Earth Parts ABC* 2008; 33: S231–S236.
- [112] Liu W, Muhammad N, Chen J, et al. Investigation on the permeability characteristics of bedded salt rocks and the tightness of natural gas caverns in such formations. *J Nat Gas Sci Eng* 2016; 35: 468–482.
- [113] Peach CJ, Spiers CJ, Trimby PW. Effect of confining pressure on dilatation, recrystallization, and flow of rock salt at 150°C. *J Geophys Res Solid Earth* 2001; 106: 13315–13328.
- [114] Silberschmidt VG, Silberschmidt VV. Analysis of Cracking in Rock Salt. *Rock Mech Rock Eng* 2000; 33: 53–70.
- [115] Donadio V. *Salt rock deformation and evolution: damage development and healing in rock salt*. MS Thesis, 2017.
- [116] Chan KS, Bodner SR, Munson DE. Recovery and Healing of Damage in WIPP Salt. *Int J Damage Mech* 1998; 7(2): 143–166.
- [117] Miao S, Wang ML, Schreyer HL. Constitutive Models for Healing of Materials with Application to Compaction of Crushed Rock Salt. *J Eng Mech* 1995; 121(10): 1122–1129.
- [118] Carter NL, Kronenberg AK, Ross JV, et al. Control of fluids on deformation of rocks. *Geol Soc Lond Spec Publ* 1990; 54: 1–13.
- [119] Ter Heege JH, De Bresser JHP, Spiers CJ. Rheological behaviour of synthetic rocksalt: the interplay between water, dynamic recrystallization and deformation mechanisms. *J Struct Geol* 2005; 27: 948–963.

- [120] Chen J, Ren S, Yang C, et al. Self-Healing Characteristics of Damaged Rock Salt under Different Healing Conditions. *Materials* 2013; 6: 3438–3450.
- [121] Davy CA, Skoczylas F, Barnichon J-D, et al. Permeability of macro-cracked argillite under confinement: Gas and water testing. *Phys Chem Earth Parts ABC* 2007; 32: 667–680.
- [122] Zhang C-L. Experimental evidence for self-sealing of fractures in claystone. *Phys Chem Earth Parts ABC* 2011; 36: 1972–1980.
- [123] Brodsky NS, Munson DE. Thermomechanical damage recovery parameters for rock salt from the Waste Isolation Pilot Plant. In: *1st North American Rock Mechanics Symposium*. American Rock Mechanics Association, 1994.
- [124] Düsterloh U, Lerche S, Lux K-H. Damage and Healing Properties of Rock Salt: Long-Term Cyclic Loading Tests and Numerical Back Analysis. Springer Berlin Heidelberg, 2013. 341–362.
- [125] Fuenkajorn K, Phueakphum D. Laboratory assessment of healing of fractures in rock salt. *Bull Eng Geol Environ* 2011; 70: 665–672.
- [126] Chan KS, Bodner S, Munson DE, et al. *A constitutive model for representing coupled creep, fracture, and healing in rock salt*. Sandia National Labs., Albuquerque, NM (United States), 1996.
- [127] Zhu C, Arson C. A Model of Damage and Healing Coupling Halite Thermo-mechanical Behavior to Microstructure Evolution. *Geotech Geol Eng* 2015; 33: 389–410.
- [128] Zhu C, Arson C. Damage and healing model of stiffness and permeability for salt rock: microstructure imaging, fabric processes and continuum mechanics. In: *50th US Rock Mechanics/Geomechanics Symposium*. American Rock Mechanics Association, 2016.
- [129] Buffiere J-Y, Maire E, Adrien J, et al. In Situ Experiments with X ray Tomography: an Attractive Tool for Experimental Mechanics. *Exp Mech* 2010; 50: 289–305.
- [130] Viggiani G, Lenoir N, Bésuelle P, et al. X-ray microtomography for studying localized deformation in fine-grained geomaterials under triaxial compression. *Comptes Rendus Mécanique* 2004; 332: 819–826.
- [131] Desbois G, Höhne N, Urai JL, et al. Deformation in cemented mudrock (Callovo–Oxfordian Clay) by microcracking, granular flow and phyllosilicate plasticity: insights from triaxial deformation, broad ion beam polishing and scanning electron microscopy. *Solid Earth* 2017; 8: 291–305.
- [132] Lenoir N, Bornert M, Desrues J, et al. Volumetric Digital Image Correlation Applied to X-ray Microtomography Images from Triaxial Compression Tests on Argillaceous Rock. *Strain* 2007; 43: 193–205.
- [133] Fonseca J, Bésuelle P, Viggiani G. Micromechanisms of inelastic deformation in sandstones: an insight using x-ray micro-tomography. *Géotechnique Lett* 2013; 3: 78–83.
- [134] Thiemeyer N, Pusch M, Hammer J, et al. Quantification and 3D visualisation of pore space in Gorleben rock salt: constraints from CT imaging and microfabrics. *Z Dtsch Ges Für Geowiss* 2014; 165: 15–25.
- [135] Teles A, Lima I, Lopes R. Rock porosity quantification by dual-energy X-ray computed microtomography. *Micron* 2016; 83: 72–78.

- [136] Wang L, Liu J, Xu H, et al. Research on Confining Pressure Effect on Mesoscopic Damage of Rock Salt Based on CT Scanning. In: *GeoShanghai International Conference*. Springer Singapore, 2018: 254–262.
- [137] Hsieh PA, Tracy JV, Neuzil CE, et al. A Transient Laboratory Method for Determining the Hydraulic Properties of ‘Tight’ Rocks--I. Theory. *Int J Rock Mech Min Sci Geomech Abstr* 1981; 18: 245–252.
- [138] Liang Y, Price JD, Wark DA, et al. Nonlinear pressure diffusion in a porous medium: Approximate solutions with applications to permeability measurements using transient pulse decay method. *J Geophys Res Solid Earth* 2001; 106: 529–535.
- [139] Skoczylas Frédéric, Olivier C, Zouber L. Sur la fiabilité des mesures des perméabilités hétérogènes par injection de gaz. Micro-pulse tests. *Rev Fr Génie Civ* 2003; 7: 451–469.
- [140] Fedor F, Hámos G, Jobbik A, et al. Laboratory pressure pulse decay permeability measurement of Boda Claystone, Mecsek Mts., SW Hungary. *Phys Chem Earth Parts ABC* 2008; 33: S45–S53.
- [141] Walder J, Nur A. Permeability measurement by the pulse-decay method: Effects of poroelastic phenomena and non-linear pore pressure diffusion. *Int J Rock Mech Min Sci Geomech Abstr* 1986; 23: 225–232.
- [142] Dana E, Skoczylas F. Gas relative permeability and pore structure of sandstones. *Int J Rock Mech Min Sci* 1999; 36: 613–625.
- [143] Brunauer S, Emmett PH, Teller E. Adsorption of gases in multimolecular layers. *J Am Chem Soc* 1938; 60: 309–319.
- [144] Bamforth PB. The relationship between permeability coefficients for concrete obtained using liquid and gas. *Mag Concr Res* 1987; 39: 3–11.
- [145] Cui A, Wust R, Nassichuk B, et al. A Nearly Complete Characterization of Permeability to Hydrocarbon Gas and Liquid for Unconventional Reservoirs: A Challenge to Conventional Thinking. In: *Unconventional Resources Technology Conference*. Society of Exploration Geophysicists, American Association of Petroleum Geologists, Society of Petroleum Engineers, 2013: 1716–1732.
- [146] Stormont JC. *Gas permeability changes in rock salt during deformation*. Dissertation, The University of Arizona, 1990.
- [147] Khaledi K, Mahmoudi E, Datcheva M, et al. Sensitivity analysis and parameter identification of a time dependent constitutive model for rock salt. *J Comput Appl Math* 2016; 293: 128–138.
- [148] Yuan H, Agostini F, Duan Z, et al. Measurement of Biot’s coefficient for CO_x argillite using gas pressure technique. *Int J Rock Mech Min Sci* 2017; 92: 72–80.
- [149] Latière HJ, Mazerolle F. The X-ray scanner. A tool for the examination of the intravoluminal crystalline state of aluminum. *Eng Fract Mech* 1987; 27: 413–463.
- [150] Goldman LW. Principles of CT and CT Technology. *J Nucl Med Technol* 2007; 35: 115–128.
- [151] Kak AC, Slaney M. Principles of computerized tomographic imaging, 2002.

Appendix: X-ray microtomography observations

A.1. Sample XR02-4



(a)

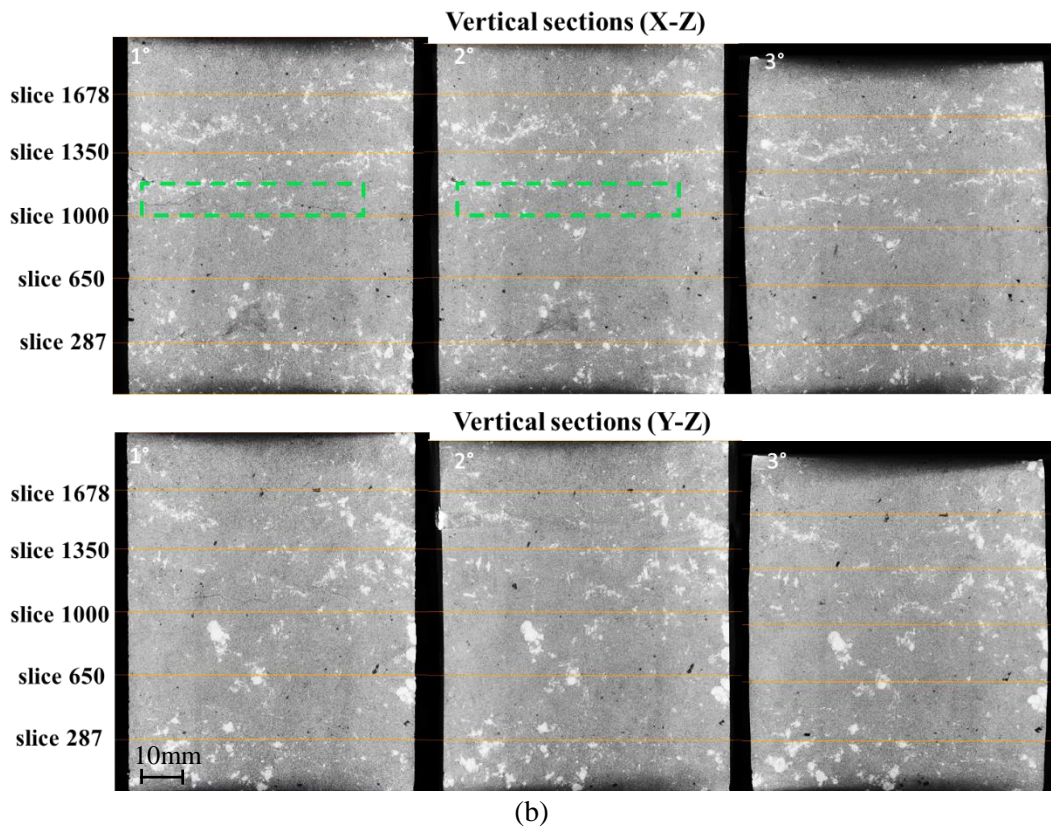
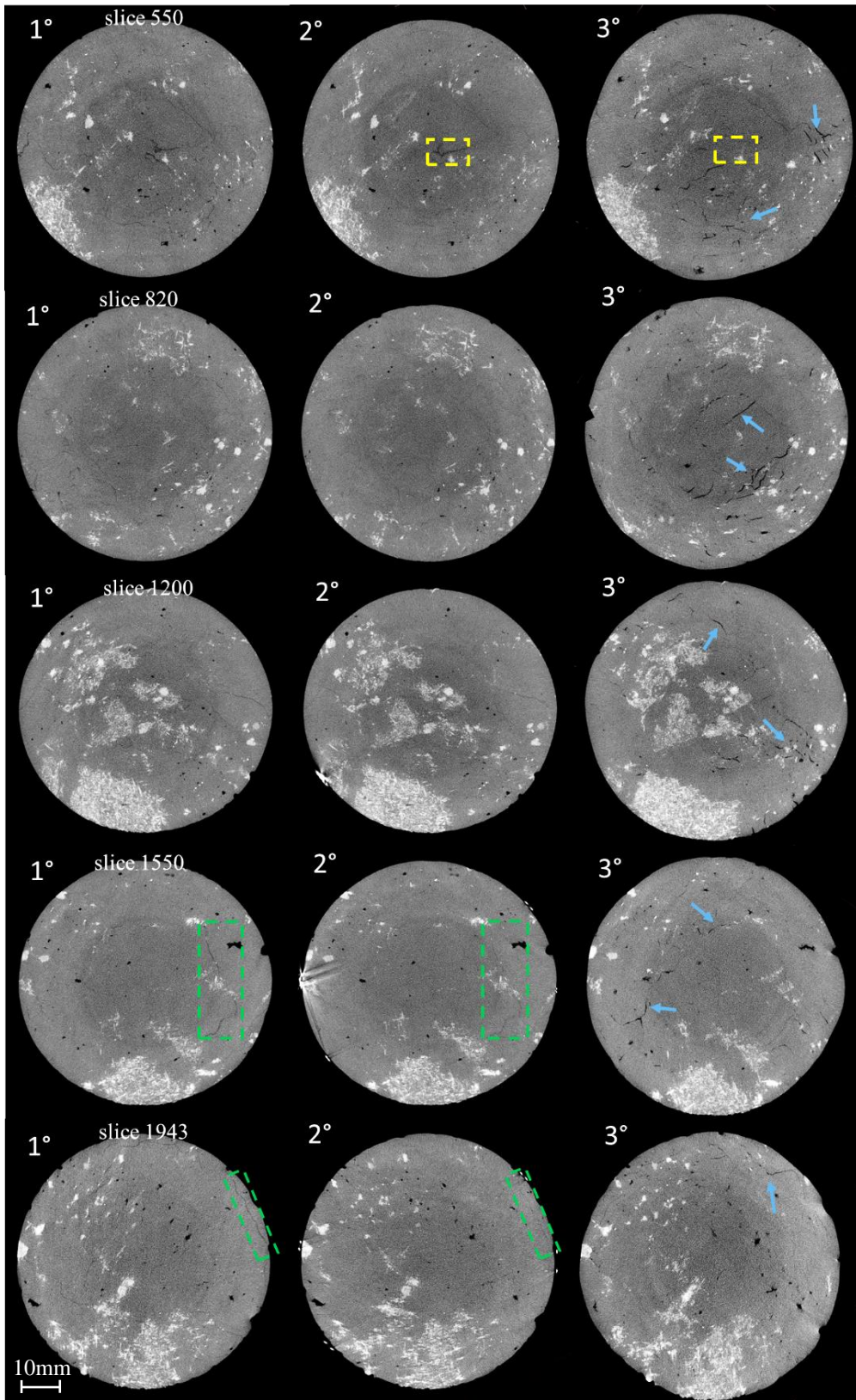


Fig.A.1 Horizontal (a) and vertical (b) tomographic slices of sample XR02-4 from helical scans. Location of horizontal sections indicated by the yellow lines in vertical slices. Cracks closure from the first to second scan due to isotropic stress (green dotted frames). Cracks closure from the second to third scan due to triaxial test (yellow dotted frames). New cracks created by deviatoric loading (blue arrows)

A.2. Sample XS01-4

Horizontal sections (X-Y)



(a)

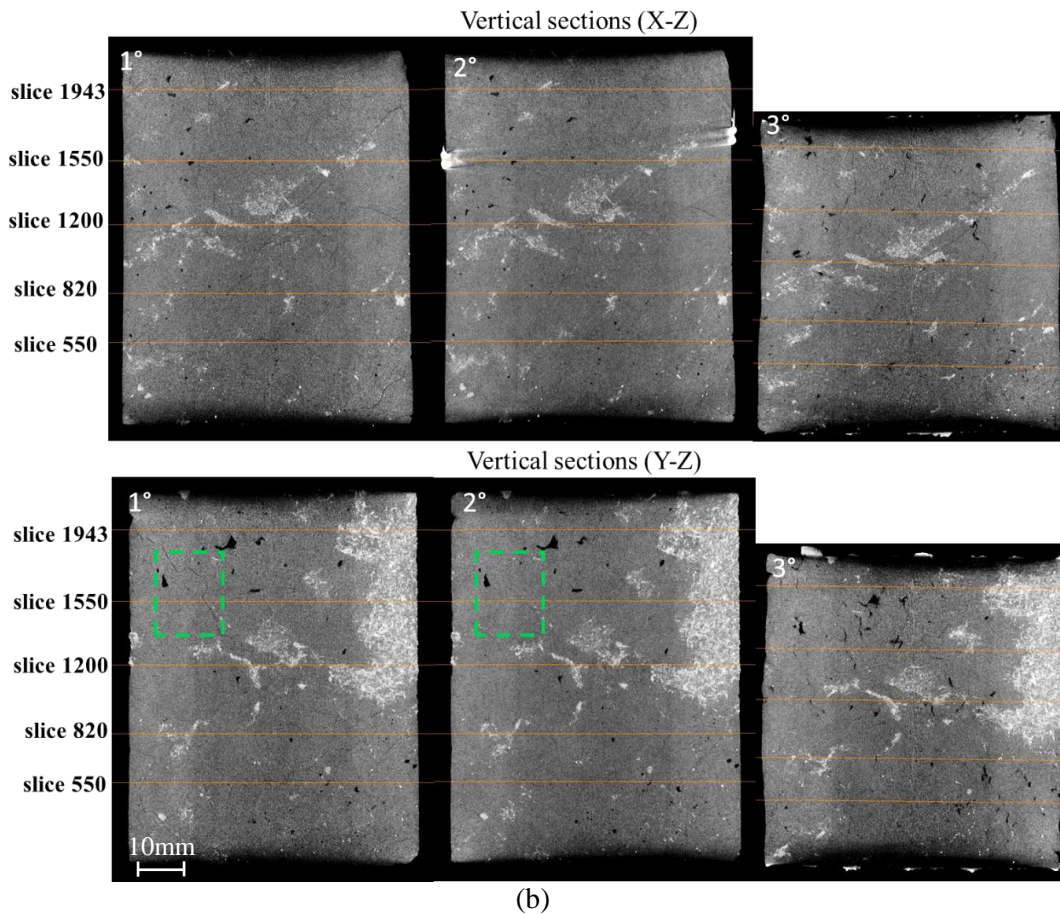
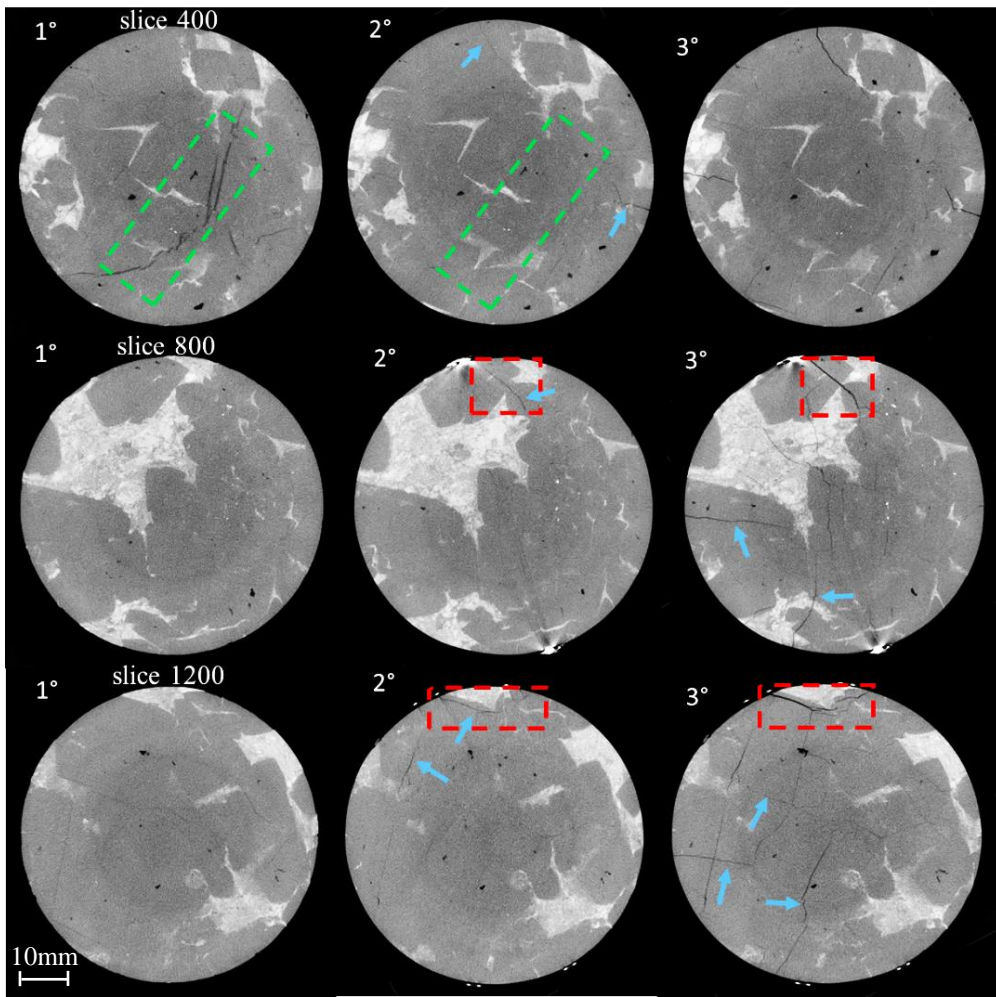


Fig.A.2 Horizontal (a) and vertical (b) tomographic slices of sample XS01-4 from helical scans. Location of horizontal sections indicated by the yellow lines in vertical slices. Cracks closure from scan 1° to 2° due to isotropic stress (green dotted frames). Cracks closure from scan 2° to 3° due to deviatoric stress (yellow dotted frames). New cracks created by deviatoric loading (blue arrows)

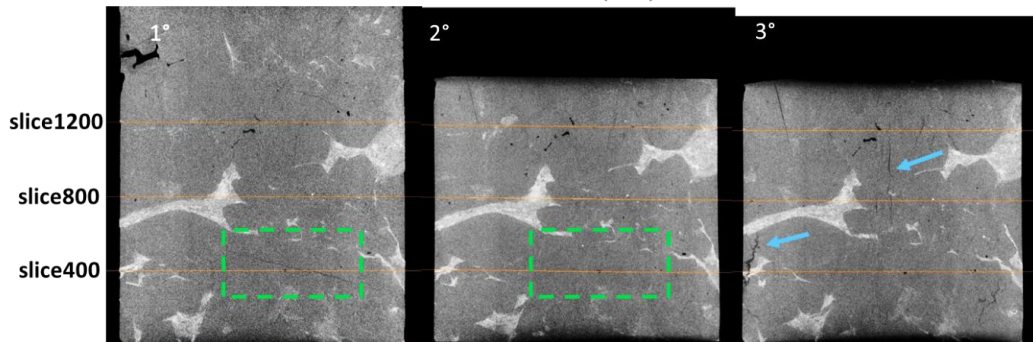
A.3. Sample XZ25-4

Horizontal sections (X-Y)

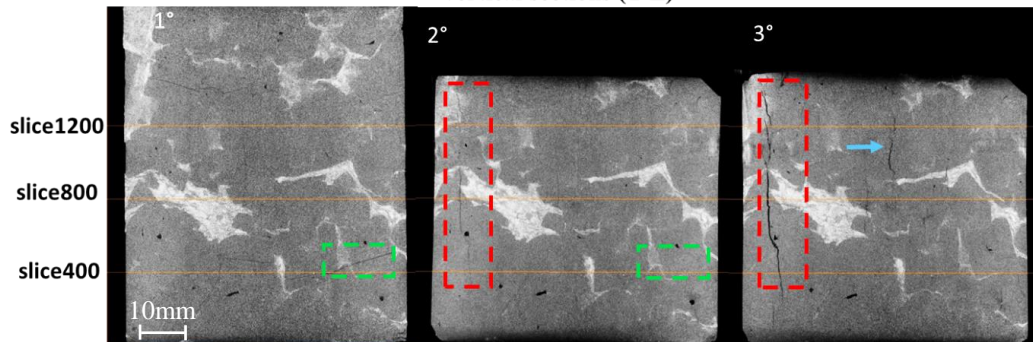


(a)

Vertical sections (X-Z)



Vertical sections (Y-Z)



(b)

Fig.A.3 Horizontal (a) and vertical (b) tomographic slices of sample XZ25-4 from helical scans. Location of horizontal sections indicated by the yellow lines in vertical slices. Cracks closure from scan 1° to 2° due to isotropic stress (green dotted frames). Cracks propagation from scan 2° to 3° (red dotted frames). New cracks created by axial loading (blue arrows)

Étude expérimentale des propriétés de transfert de gaz et des effets de couplage dans des roches salines

Dans le contexte des applications des cavernes de sel, cette étude expérimentale est consacrée à la caractérisation des propriétés de transfert sous des contraintes isotropes et/ou déviatrices, ainsi qu'à une exploration préliminaire du comportement poromécanique de la roche saline. Des tests comparatifs de perméabilité aux gaz avec l'argon et l'hydrogène montrent qu'ils ont des valeurs de perméabilité similaires. Des effets poromécaniques se produisent, mais ils sont faibles et dépendent fortement des niveaux de confinement. De plus, des tests triaxiaux ont été utilisés pour étudier la variation de la perméabilité en fonction du temps et des contraintes déviatoires, et simultanément pour obtenir des échantillons endommagés. Ces échantillons pré-dommagés ont donc été testés à nouveau sous charge hydrostatique pour étudier les effets des dommages et les possibilités d'étanchéité/guérison. Les échantillons endommagés se sont avérés avoir des effets de couplage importants dus à la fissuration. Les effets du temps sur la perméabilité ont également été détectés pour les essais hydrostatiques et triaxiaux. Entre-temps, des expériences de micro-tomographie aux rayons X ont été réalisées pour observer les changements microstructuraux internes avant et après les différents tests. Les résultats soutiennent l'hypothèse selon laquelle les couplages se produisent principalement entre les grains ou les fissures.

Mots clés : roche saline, perméabilité aux gaz, effets du temps, effets de couplage, Micro-tomographie aux rayons X

Experimental investigation of gas transfer properties and stress coupling effects of salt rocks

In the context of salt cavern applications, i.e. cavern abandonment and/or hydrogen storage, this experimental study is dedicated to the characterization of fluid transfer properties under isotropic and/or deviatoric stresses, as well as to a preliminary exploration of poromechanical behavior of salt rock. Comparative gas permeability tests with argon and hydrogen show that they have similar permeability values. Poromechanical effects occur but they are weak and strongly dependent on the confinement levels. Furthermore, triaxial tests were used to investigate permeability variation with deviatoric stress/time, and simultaneously to get damaged samples. Those pre-damaged samples were therefore tested again under hydrostatic loading to investigate damage effects and potential sealing/healing. The damaged samples were found to have significant coupling effects due to cracking. Time effects on permeability were also detected for both hydrostatic and triaxial tests. Meanwhile, X-ray micro-tomography experiments were performed to observe internal microstructural changes before and after various tests. The results support the hypothesis that the couplings mainly occur between grains or cracks.

Keywords: salt rock, gas permeability, time effects, coupling effects, X-ray micro-tomography